Acoustic-Seismic Coupling of Broadband Signals – Support for On-Site Inspections under the Comprehensive Nuclear Test-Ban-Treaty

Dissertation

zur Erlangung des Grades eines
Doktors der Naturwissenschaften

der Fakultät Physik
der Technischen Universität Dortmund

vorgelegt von

Mattes Liebsch

Juli 2017

Erstgutachter:	PD Dr. Jürgen Altmann, Technische Universität Dortmund
Zweitgutachter:	Prof. Dr. Manfred Joswig, Universität Stuttgart
Kontakt zum Author:	mattes.liebsch@tu-dortmund.de

Abstract

In this PhD thesis the process of acoustic-seismic coupling and a method to reduce acoustically induced soil vibrations by applying an acoustic shielding to seismic sensors are investigated.

The research is motivated by the verification of the Comprehensive Nuclear-Test-Ban Treaty: During on-site inspections sensitive seismic measurements can be performed to record seismic aftershocks created in the aftermath of a large, underground, human-caused explosion. This aims to precisely localise the hypocentre of that explosion to verify whether its origin was a nuclear or chemical one. However, these seismic measurements can be disturbed by other seismic signals in the inspection area and thus weak aftershock signals might go undetected. In this work disturbances caused by airborne sources are analysed: When sound waves hit the ground they excite soil vibrations which can mask weak aftershock signals. The findings of this work can be used in the development of new guidelines to improve the sensitivity of seismic on-site inspection measurements.

For this measurements of sound pressure and the acoustically excited soil velocity, recorded with geophones places at the soil surface and in burying depths of up to 0.6 m, in flat terrain with sandy soil, are presented. The acoustic excitation was realised by broadband sound of jet-aircraft overflights, covering a broad range of incidence angles and due to the large distance arriving as plane waves, and of noise artificially produced by a speaker. By evaluating a multitude of overflight events it is shown that the acoustic-seismic coupling coefficient (i.e. the spectral ratio between soil velocity and sound pressure) only depends on the angle of incidence of the acoustic wave and the frequency. Thus, angle-dependent averaging of the coupling coefficient, obtained from the signals of several overflight events, can be performed which significantly improves the signal-to-noise ratio. While previous publications presented only pointwise measurements in this work results for a wide range of angles of incidence and frequencies are presented. In seismic spectral signal frequency bands of increased and decreased soil velocity are observed. These are caused by interfering seismic waves: The directly acoustically excited wave and waves which have been acoustically excited in a certain horizontal distance and which have been reflected within the ground before reaching the sensor.

The seismic response to the broadband acoustic excitation with a range of incidence angles is used to obtain near-surface soil properties e.g. the P-wave velocity and the depth of the reflecting boundary. For this three theoretical models are introduced taking into account contributions of different numbers and types of the interfering waves. While sensors placed at the surface generally lead to the most reliable results, buried sensors are used to verify the models.

Additionally, during several measurements an acoustic shielding is placed over some

sensors. Thus, the sound pressure of the incident acoustic waves is reduced significantly. From the soil velocity recorded with the shielded geophones and the reflection characteristics the horizontal propagation range of acoustically induced seismic signals is estimated. It is shown that treating the process of acosutic-seismic coupling as a local effect is an insufficient approach.

Finally, first suggestions for acoustic shieldings to reduce disturbing signals during sensitive seismic measurements are presented and the applicability during on-site inspections is discussed. An outlook for further research is given: Design and material of a suitable acoustic shielding should be investigated to fulfil requirements of high acoustic damping properties for signals of frequencies of a few Hz.

Contents

List of abbreviations

ADC	analogue-digital converter
BK	Brüel & Kjær
cpa	closest point of approach
CTBT	Comprehensive Nuclear-Test-Ban Treaty
CTBTO	Comprehensive Nuclear-Test-Ban Treaty Organization Until entry into force of the CTBT the organisations' official name is *Preparatory Commission for the Comprehensive Nuclear-Test-Ban Treaty Organization*
DFS	Deutsche Flugsicherung GmbH – German Air Traffic Control
DWD	Deutscher Wetterdienst – German Meteorological Service
FFT	fast Fourier transform
FMO	airport Münster-Osnabrück, Germany, IATA code (designation by the International Air Transport Association): FMO
FWHM	full width at half maximum
GPS	Global Positioning System
IMS	International Monitoring System
LTBT	Limited Test Ban Treaty The name *Limited Test Ban Treaty* is often used as the abbreviated version of the treaties formal name *Treaty Banning Nuclear Weapon Tests in the Atmosphere, in Outer Space and Under Water.*
NPT	Treaty on the Non-Proliferation of Nuclear Weapons
NWS	nuclear weapon state, i.e. a state possessing nuclear weapons
OSI	on-site inspection

RMS root mean square

SAMS Seismic Aftershock Monitoring System

SNR signal-to-noise ratio

TNT Trinitrotoluene – an explosive

UN United Nations

UTC universal time, coordinated

List of parameters and variables

A_i	plane wave in the form $A_i = a_i \cdot e^{\mathrm{i}(\vec{k}\vec{r}-\omega t+\phi_i)}$ with its amplitude a_i, its phase ϕ_i and the angular frequency $\omega = 2\pi f$
a_i	amplitude of the plane wave A_i
$a_{i,\perp}$	vertical component of the amplitude a_i
α	angle of incidence towards the normal to the ground of an acoustic plane wave
$\beta_{\mathrm{P}}, \beta_{\mathrm{P2}}$	angles towards the normal to the ground (or a horizontally aligned underground boundary, respectively) of a seismic P wave in the first soil layer (β_{P}) and in the second soil layer (β_{P2})
$\beta_{\mathrm{S}}, \beta_{\mathrm{S2}}$	angles towards the normal to the ground (or a horizontally aligned underground boundary, respectively) of a seismic SV wave in the first soil layer (β_{S}) and in the second soil layer (β_{S2})
$Cc(f, \alpha)$	acoustic-seismic coupling coefficient, i.e. the ratio between the vertical soil velocity and sound pressure
d	depth of the first underground boundary, separating the first from the second soil layer which are characterised by different elastic properties
$\Delta x, \delta x, \partial x$	path differences in the ground between two waves
$\Delta\phi, \delta\phi, \partial\phi$	phase difference between two waves of which one had to cover the additional path Δx, δx or ∂x, respectively
$D(d, v_{\mathbf{P1}})$	relative root-mean-square deviation between theoretical and experimental data
E	strain tensor
ε_{ij}	symmetric components of the strain tensor E
f	frequency

f_S	sampling frequency/rate
Δf	frequency resolution of a spectrum calculated from N samples with the FFT
$f_{\mathrm{max},k}^{\mathrm{meas}}(\alpha)$	course of the measured frequencies of constructive interference over the angle α
$f_{\mathrm{max},k}^{\mathrm{theo}}(\alpha)$	numerically obtained theoretical course of the frequencies of constructive interference over the angle α
ϕ_i	phase of the plane wave A_i
$\overline{\varphi}$	velocity potential in a fluid
φ	scalar displacement potential in a solid
γ	absorption coefficient in soil
γ_1	proportionality factor between γ and f
k	non-negative integer to indicate the order of interference maxima
$\vec{k}$	wave vector
K	number of data points used in the fit algorithm
λ	wavelength
λ_L, μ	Lamé's constants
M	number of interfering waves
$m_{\Delta\phi,\mathrm{meas}}$	measured proportionality factors between the frequency f and the phase difference of a signal recorded at two sensors $\Delta\phi$
$m_{\Delta\phi,\mathrm{theo}}$	proportionality factors between the frequency f and the theoretical phase difference of two sensors, obtained from the distance $r_\parallel$
$\Delta m_{\Delta\phi}(\alpha)$	difference of the measured and theoretical proportionality factors $\Delta m_{\Delta\phi} = m_{\Delta\phi,\mathrm{meas}} - m_{\Delta\phi,\mathrm{theo}}$ at a certain angle α
N	number of discrete samples in a time interval T
P	stress tensor
p	horizontal slowness of a wave: $p = 1/v_\mathrm{hor}$
p_{ij}	symmetric components of the stress tensor P
ψ, ψ_i	vector potential ψ, and its respective components ψ_i, of the displacement in a solid

$\grave{\mathrm{P}}, \acute{\mathrm{P}}, \grave{\mathrm{S}}, \acute{\mathrm{S}}$	Indices used to specify direction of propagation (i.e. downwards or upwards) and type (P or SV wave) of a seismic wave. A sequence of these indices is used to indicate the respective directions and types of multiply reflected waves.
ρ	density
$r_{\parallel}$	projected distance between two sensors in direction of propagation of an incident acoustic wave
r_{hor}	horizontal propagation range of a seismic wave in the ground
R_{PP}, R	P-P reflection coefficient (ratio between the amplitudes of reflected and incident P wave) at the underground boundary
$R^{\mathrm{s}}_{\mathrm{PP}}, R^{\mathrm{s}}$	P-P reflection coefficient at the free surface
R_{IJ}	reflection coefficients at the underground boundary, namely those of P-S, S-P and S-S reflection
$R^{\mathrm{s}}_{\mathrm{IJ}}$	reflection coefficients at the free surface, namely those of P-S, S-P and S-S reflection
r, Θ, Φ	spherical coordinates
$T_{\mathrm{P}}, T_{\mathrm{S}}$	transmission coefficients at the surface of an acoustic wave exciting seismic P or S waves
θ	dilatation in soil, given by the sum of the principal elements of E
t	time
Δt	time between two samples in a discrete time series (resolution in the time domain).
T	duration of a time interval used for the calculation of a spectrum by the FFT
u, v, w	soil displacement components in x-, y-, and z-direction
v_0	velocity of sound
$v_{\mathrm{P1}}, v_{\mathrm{P2}}$	velocities of P waves in the first and second soil layer
$v_{\mathrm{S1}}, v_{\mathrm{S2}}$	velocities of SV waves in the first and second soil layer
v_{hor}	projected velocity of a plane wavefront along the horizontally aligned ground surface: $v_{\mathrm{hor}} = 1/p$
ω	angular frequency $\omega = 2\pi f$

x, y, z	Cartesian coordinates
z_{S}	burying depth of a geophone in the ground

Chapter 1

Introduction

1.1 Nuclear Disarmament and the Test-Ban Treaty

Even after the end of the Cold War era about 15,000 nuclear weapons still exist globally [1]. On the one hand their total number has decreased over the last decades. On the other hand a new member joined the club of nuclear weapon states (NWSs)[1]: North Korea which performed test explosions of nuclear bombs for the first time in 2006 and again in 2009, 2013 and the two most recent ones in 2016 [3]. The main difference between nuclear weapons and conventional weapons lies in nuclear weapons' enormous energy release of up to several megatons TNT equivalent and the radiation emitted during their explosion. Thus, nuclear weapons are characterised as weapons of mass destruction. The usage of only a fraction of the world's nuclear arsenals could result in tremendous fatalities and would be capable of making vast areas or even the whole world uninhabitable for humankind. The latter would be caused by the radioactive contamination of the hit areas, fallout of contaminated dust transported by wind or even a nuclear winter [4].

Given the enormous power of these weapons and the long-term consequences of their use, scenarios of a war involving the intentional use of nuclear weapons seem very unlikely: The use of a nuclear weapon against another NWS or its military allies would almost certainly result in nuclear retaliation and thus result in fatal consequences for both sites – a scenario called mutually assured destruction. Furthermore, diplomatic and public pressure would make it very unlikely to use these weapons against a non-NWS nowadays.[2] Thus, the main purposes of nuclear weapons seem to be a display of power

[1] The text of the Treaty on the Non-Proliferation of Nuclear Weapons (NPT) [2] recognises the following states as nuclear weapon states: China, France, Russia, the United Kingdom and the United States. Further states (not members to the NPT) possessing nuclear weapons are India, Israel (not declared officially), North Korea and Pakistan. Unlike the NPT, in this work I refer to a state which de facto possesses nuclear weapons as a NWS, i.e. all the states listed here. Consequently, non-NWS refers to a state which does not possess its own nuclear weapons.

[2] It should be noted that such a use was considered several times, e.g. by the United States during the Vietnam War. However, the fact that nuclear weapons have not been used in a war since World War II

and deterrence, i.e. keeping potential opponents from using their nuclear warheads. However, simply giving up one's own nuclear arsenal seems not to be an option, especially if other states refuse to do so as well. So far South Africa has been the only state to completely dismantle its own nuclear weapons which it did under international verification in the 1990s.

The possession of nuclear weapons can be modelled with the help of the prisoners' dilemma [5]: Each NWS has to decide either to keep its nuclear weapons or to abolish them. The former is the most beneficial strategy independent of the actions of the other states: When other states decide to keep their nuclear weapons it is safer to also keep one's own. On the other hand, when they decide to abolish their nuclear weapons, keeping one's own gives oneself a strategic advantage over them – in the extreme case a very substantial one, if one state became the only remaining actor possessing nuclear weapons. On the flip side abolishing nuclear weapons could result in a disadvantage with respect to other NWSs deciding to keep their nuclear weapons. However, if all NWSs decided to abolish their nuclear weapons, the global security level would be increased significantly. Consequently, this outcome would be beneficial to all and thus the most desirable one – but also would require mutual agreement and compliance of all involved actors.

In conclusion, states have an incentive to maintain (or try to acquire) nuclear weapons to feel protected from others and in general to protect their own interests. However, with many actors capable of the use and the counter-use of nuclear weapons – posing the imminent risk of an intended or accidental nuclear exchange – the worldwide level of security is much lower than it would be without nuclear weapons.[3] This contradiction is called the global security paradox or security dilemma.

Already during the research and the development of the first nuclear weapons scientists raised concerns about them. After the actual use of two nuclear bombs during World War II – in Hiroshima on 6th August 1945 and in Nagasaki on 9th August 1945 – and especially since the nuclear arms race during the Cold War era, considerable efforts for a global nuclear disarmament were made by various actors. These include civil and non-governmental organisations' initiatives like the International Campaign to Abolish Nuclear Weapons [7] and the Pugwash Conferences [8], bilateral agreements (for example the Strategic Arms Limitation Talks [9] and the Strategic Arms Reduction Treaty[4] [10] between the United States and the Soviet Union or Russia respectively) as well as

confirms the made statement.

[3] The argument might be raised that there has been no major war between NWSs due to nuclear weapons' effective deterrence, which indicates a high level of global security. However, this is a misleading justification for nuclear weapons, since freeing the world of nuclear weapons need not mean it is open for conventional wars again (discussed e.g. in [6]).

[4] The formal name of the treaty is *The Treaty Between the United States of America and the Union of Soviet Socialist Republics on the Reduction and Limitation of Strategic Offensive Arms.*

multilateral treaties. The most recent one of the latter is the Treaty on the Prohibition of Nuclear Weapons adopted by a United Nations (UN) conference in July 2017 [11]. A more prominent multilateral treaty is the NPT [2] from 1968, the member states of which agree to the following: The five officially recognised NWSs are prohibited from providing other states with nuclear weapons, sharing their knowledge to build them as well as guiding or assisting other states in doing so on their own. All non-NWSs parties to the treaty are prohibited from trying to acquire nuclear weapons but in return should be assisted in the civil use of nuclear power. Furthermore, all member states agree to take serious measures for a complete nuclear disarmament under international control.

If a state attempts to develop nuclear weapons for the first time without help from other NWSs, testing is required. Testing is also required when NWSs strive to improve their nuclear weapons. This is why there were more than 2000 nuclear tests conducted by all NWSs since 1945 [12]. Consequentially, prohibiting such tests is an important step towards nuclear disarmament and the prevention of nuclear proliferation. A first attempt to stop these tests was the Limited Test-Ban Treaty (LTBT) [13] from 1963, which prohibits all nuclear test explosions except underground ones. At that time, it was not possible to distinguish without doubt between the seismic signals of a buried nuclear explosion and those of an earthquake. With advancing knowledge in geoscience, seismology and geophysics these issues could be settled in the following decades clearing the way for a ban of all nuclear tests. Thus, in 1996 the Comprehensive Nuclear-Test-Ban Treaty (CTBT) [14] was adopted by the UN General Assembly. Since then, more than 180 states have signed it and more than 160 also ratified the treaty. However, even though 2016 marked its 20th anniversary it still has not entered into force. This means that it is not binding international law yet, even though with very few exceptions all states have complied with it. In order to enter into force signature and ratification of the treaty by all states listed in Annex II are required: These are all states that operated nuclear programs (regardless whether these were civilian or military ones) in 1996. Among these China, Egypt, Iran, Israel and the United States have not ratified and India, North Korea and Pakistan have neither signed nor ratified the treaty as of July 2017.

To ensure compliance with the treaty good will and trust is not enough. Rather strict international verification with scientifically sound measures is required so that no nuclear explosion will go undetected. For this purpose an organisation was founded to monitor compliance with the treaty by the member states.

1.2 Verification of the Comprehensive Nuclear-Test-Ban Treaty

In 1996 the Comprehensive Nuclear-Test-Ban Treaty Organization (CTBTO)[5] was established, which is tasked among other things with the verification of the CTBT. This organisation sets up the International Monitoring System (IMS) [15], a worldwide sensor network to detect potential nuclear explosions. Additionally, it trains inspectors who can carry out future on-site inspections (OSIs) [16] to check whether an underground explosion that has been detected teleseismically is of nuclear or chemical origin. The IMS and OSIs form the two pillars of the verification regime for the CTBT. While the former is almost completely functional, the latter can only be conducted once the treaty enters into force. An additional task of the CTBTO is to promote the Test-Ban Treaty.

1.2.1 The International Monitoring System

The IMS is a sensor network designed to detect any potential nuclear explosion worldwide with a yield of 1 kt TNT equivalent or more. When completed, the IMS will consist of 321 sensor stations: 50 primary and 120 auxiliary seismic stations, 80 radionuclide stations, 60 infrasound stations and 11 hydro-acoustic stations. Additionally, the IMS facilities include 16 radionuclide laboratories to provide independent analysis of samples collected at the radionuclide stations. About 90 percent of the sensor stations are already certified and operating [17]. A detailed description of the IMS and the used technologies is given in Part I of the Protocol to the CTBT. Additionally, all sensor stations are listed in Annex 1 to the Protocol.

The seismic stations record elastic waves propagating through the Earth and along its surface. It is a major achievement of seismology to be able to distinguish between earthquakes and human-caused explosions. If seismic waves of the same event are recorded at several stations its origin can be localised. Thus, seismic recordings play the most important role in the detection of underground nuclear tests [18].

In radionuclide stations particles are filtered from the surrounding air. These samples are analysed for non-naturally occurring isotopes that might have been released into the atmosphere during or after a nuclear test. The high sensitivity of these stations and the distribution of the radionuclides all over the hemisphere almost certainly ensure the detection of these isotopes. If specific radionuclides are detected, this technology gives unambiguous evidence that an explosion was of nuclear origin [19].

Infrasound stations record low-frequency atmospheric pressure fluctuations which would be caused during atmospheric tests. These signals are reflected at high atmospheric

[5] Until entry into force of the treaty, the organisation's official status is that of an interim organisation. While its official name is *Preparatory Commission for the Comprehensive Nuclear-Test-Ban Treaty Organization*, I refer to it as *Comprehensive Nuclear-Test-Ban Treaty Organization* throughout this work.

layers and at the ground and thus propagate over a long range around the globe [20]. For hydro-acoustic monitoring six hydrophones are positioned in a depth of about 750 m in the oceans and five T-phase geophones are placed at the shores of steep-sloped islands. The former record hydro-acoustic waves and the latter detect seismic waves that are excited when waterborne acoustic energy hits the land. Due to the very long range of underwater sound waves in the so-called Sound Fixing and Ranging Channel – which acts like an underwater waveguide formed by temperature, pressure and salinity gradients – only 11 stations are sufficient to detect signs of underwater nuclear tests worldwide [21].

The importance of seismic monitoring can be understood when taking a closer look at the different possible locations for a nuclear test and the respective probability of the nuclear test to be detected from outside of the territory of the state which conducted the test. When tests are performed in the atmosphere or under water radionuclides released into the atmosphere during the test will be transported over the whole northern or southern hemisphere, respectively. These radionuclides can easily be detected by the radionuclide stations. A test in outer space can be detected by its emitted flash via satellites and electromagnetic pulse as well as by the detection of radiation. However, since the implementation of the LTBT in 1963 most tests were carried out underground the detection of which is more challenging [22]. A human-caused underground explosion can be distinguished from an earthquake e.g. by the spectral characteristics of the seismic signals and the ground-motion directions at the first arrival of the signal at the globally distributed seismic sensors. However, in order to distinguish from a distance whether an explosion was of nuclear or chemical origin the detection of radionuclides by IMS stations is required. The release of those might be prevented if the nuclear test is performed underground at a depth of several hundred metres and beneath layers of clay, rock or other media that can contain the gases. However, gases from the explosion might still escape through cracks in the ground. If no radionuclides can be detected in the aftermath of an underground explosion, the seismic stations will give the best evidence of such a potential nuclear test. Therefore, more than half of the IMS stations are seismic ones forming a dense global network. Considering the fact that the only feasible way to conceal a nuclear test is to do it underground, the importance of these seismic sensors is highlighted.

Additionally, data of the IMS are used for other purposes beside the verification of the CTBT: After the accident in a Fukushima nuclear power plant on 11th March 2011 data from IMS radionuclide stations were used to track the spread of radioactive isotopes around the globe in order to provide information and warning of potential hazards to the public. Accordingly, atmospherically transported radioisotopes like Cs-137 and I-131 as well as noble gas isotopes like Xe-133 were detected one day after the accident at the

radionuclide station RN38 in Takasaki, Japan, after nine days in North America and after less than two weeks in Europe e.g. at the German radionuclide station RN33 near Freiburg [23].
Furthermore, since 2006 seismic data from IMS stations are used for tsunami warning mainly in the region of the Indo-Pacific [24].

1.2.2 On-site-inspections for the CTBT

All of the data collected at IMS stations are transmitted to the International Data Centre of the CTBTO in Vienna, where they are processed. The raw data and the processed ones are then made available to all member states of the treaty for their own analysis. The data are analysed for suspicious events indicating a potential nuclear test: Either an unusually large human-caused explosion or the release of radionuclides. After entry into force of the CTBT each member state can request an OSI in the area where a potential underground nuclear explosion is suspected, indicated by recordings from the IMS or from national technical means. If approved by the Executive Council of the CTBTO, the OSI will commence quickly, as time is of the essence for the verification. The inspection area must not exceed 1000 km^2, as specified by the Protocol to the CTBT, Part II, Article 3. Other specifications of an OSI are also strictly defined in Part II of the Protocol to the CTBT – like its duration (Article 4), the number of inspectors (Article 9) and the approved equipment that can be used by the inspectors (Articles 36 - 40). Until today several extensive OSI field exercises were carried out – the last one in Jordan in December 2014 [25].
The main purpose of an OSI is to gain evidence whether the suspicious event was caused by a nuclear or a chemical explosion. To be able to do this inspectors need to locate the hypocentre of the explosion as precisely as possible and proceed to collect gas samples either directly from the cavity of the explosion or at the surface above it. These gas samples are analysed for short-lived radionuclides which would have been produced during a nuclear explosion. The findings of the inspection are reported to the Executive Council, which then has to decide whether a violation of the treaty was committed. A violation will be reported to the UN, e.g. to the UN Security Council, which will decide about further consequences.
The precision in the localisation of the hypocentre of an underground explosion by the IMS is in the range of ten kilometres. However, during an OSI the aim is to localise it with a accuracy of 0.1 km. To achieve this inspectors can use multiple techniques in the inspection area, as for example overflights, multi-spectral imaging, gamma radiation monitoring as well as magnetic and gravitational field mapping.
An important method is the use of the so-called Seismic Aftershock Monitoring System (SAMS), which uses a local network of seismic sensors placed in the inspection area to

record aftershocks of the explosion. These aftershocks can be caused by a partial or full cave-in of the cavity from the explosion. Cooling and decompression with the associated fracturing in the surrounding rock will also lead to seismic aftershocks. When these aftershock signals are recorded at several SAMS stations, the cavity can be localised using triangulation methods. The number of such aftershocks will decrease rapidly: It is estimated that only one single event of local magnitude M_L = - 2.0 per day can be detected two weeks after the explosion. However, other sources in the inspection area might cause seismic signals of larger magnitude and therefore mask the weak aftershock signals so that they might go undetected.

Acoustically induced disturbances form the motivation for the research performed in this work (see Section 1.3). These signals can be caused by airborne sources such as aircraft or helicopters that are used by the inspectors themselves to monitor the area. Additionally, concerns have been raised that the OSI could be disturbed intentionally e.g. by jet-aircraft overflights or by machinery for road-building. For an effective performance of SAMS measurements during an OSI disturbing seismic signals have to be minimised or prevented.[6]

1.3 About this work

In the present work airborne acoustic signals and the resulting seismic responses are investigated. In order to excite soil vibration by (nearly) plane waves of a wide frequency range between few tens and several hundreds of Hz, the noise from jet aircraft passing overhead was used. The large distance between the aircraft and the sensors of several hundred metres made sure that the incident waves were plane over the range of the used setup of less than 10 m. From the trajectory of the aircraft a wide range of angles of incidence and thus quasi-continuously changing excitation conditions are obtained.

Additionally, the method of acoustically shielding sensors from the directly incident sound waves is presented and measurements with an experimental shielding design are performed and analysed. It is shown that the amplitudes of acoustically induced seismic waves can be reduced significantly. This aims at developing guidelines to improve the sensitivity of SAMS measurements during OSIs for the verification of the CTBT.

The work was carried out in the working group *Physics and Disarmament* at the Technische Universität Dortmund, Germany. Acoustic and seismic research has been conducted by the members of the working group for several disarmament purposes. Among them are investigations of the signals from military land and air vehicles for verification of disarmament and peace agreements [28, 29, 30], and of co-operative

[6] An alternative approach could be to remove such disturbances by post-processing. For periodic signals this can be achieved by fitting and removing of spectral peaks (see [26] for mono-frequent signals and [27] for an extension to signals with frequencies linearly varying in time).

early-warning sensors for ballistic missile launches [31].[7] Other measurements of the working group aimed at monitoring nuclear final repositories with seismic sensors to detect attempts to unauthorisedly acquire fissile material [32, 33]. In the context of the CTBT an article [26] and a PhD thesis have been published [27] which present algorithms to subtract periodic content from SAMS recordings.

The interaction of sound waves with the ground, where they can excite soil vibration, has been investigated in several contexts, such as the seismic recordings of meteor entries [34], thunder [35], sonic booms [36], rocket launches [37] or atmospheric explosions [38] as well as in the field of infrasound seismics [39].
The theoretical background of this field of research is given by the theory of wave propagation at a boundary between a fluid and a solid [40], or in a porous solid with fluid-filled pores [41, 42]. The latter references predict three propagating waves in the air-filled porous ground – one slow, strongly attenuated compressional wave mainly in the air-filled pores (Biot type II, see [41]) and a P and an S wave where the soil matrix and the air move in phase. P waves, which are most important for this work, as well as S waves are caused by the friction of the air in the pores at the grain skeleton, building up as the Type-II wave attenuates over a range on the order of 10 cm [43].
Acoustic-seismic coupling has been investigated systematically in several modes.[8] Studies with variation of the incidence angle used small distances (up to few tens of metres) between a speaker, estimated as a point source, and the sensors. Thus, the wavefronts hitting the ground had significant curvature. Additionally, the source position was fixed or varied among a few locations resulting in pointwise measurements with respect to the incident angle of the acoustic signal [45, 46, 47]. Although in one study geophones had been buried during the measurements, only theoretical explanations for surface sensors are provided [46]. Investigations to determine wave velocities were conducted under laboratory conditions. They used very small samples of porous media with dimensions of millimetres [48] up to tens of centimeters [43]. In [49] measurements and extensive numerical modelling of seismic waves excited by a speaker are presented and the use of acoustic sources for near-surface exploration is discussed.
Plane wavefronts of the acoustic signal as the result of long-range propagation over hundreds of metres to a few kilometres were achieved by explosions at the ground; here the incidence was grazing [44, 50]. One study used explosions at several kilometres altitude [38].
Even though the plane acoustic wave hits the ground in a wide area exciting soil vibrations, theoretical descriptions treat acoustic-seismic coupling as local effect: The

[7] Some of the measurements were performed by the *Bochum Verification Project* at the Ruhr-Universität Bochum, Germany. This work is since 2001 continued in the working group *Physics and Disarmament* at the Technische Universität Dortmund, Germany.

[8] [44] provides references and an overview of the theory.

recorded seismic signal is interpreted as excited directly at the sensor (for geophones placed at the surface) or slantly above it (for buried geophones). Few references (e.g. [46]) consider contributions from a seismic wave reflected once at an underground boundary. In this work it is shown, that seismic waves reflected multiple times within the soil contribute significantly to the recorded soil vibration. Correspondingly, acoustically induced soil vibrations excited in a horizontal distance of several metres around the sensor need to be taken into account. Due to frequency-dependent absorption in the soil the influence of multiply reflected waves decreases with frequency.
Additional to the investigation of the acoustic-seismic coupling process an acoustic shielding was applied to several sensors to investigate the possibilities to reduce acoustically-induced signals during sensitive seismic measurements. The process of the reduction of sound pressure by porous absorbers and reflecting surfaces is treated for example to reduce noise in inhabited areas [51]. No work is known to the author which discusses the reduction of sound pressure to improve the sensitivity of seismic measurements.[9]

1.3.1 General usability

Even though this work is motivated by the verification of the CTBT the findings can be applied to other sensitive seismic measurements: Acoustic signals might lead to disturbing soil vibrations the amplitudes of which can be reduced by a suitable shielding of the sensors.
The process of acoustic-seismic coupling can lead to significant seismic amplitudes. Considering this, also signals in existing recordings might be interpreted as acoustically-induced ones.
Furthermore, to obtain near-surface soil properties the introduced models of the propagation of acoustically induced seismic waves and the associated algorithms can be used. Thus, acoustic sources like aircraft or speakers might find application for the exploration of near-surface soil structures.

1.3.2 Outline of this work

Here the main contents of the chapters of this work are summarised:

Chapter 1: The political background for this work of nuclear disarmament and especially the CTBT is presented. The verification regime of the CTBT by the IMS and OSIs is introduced. The problem of disturbing acoustically-induced seismic sig-

[9] The standard technique in seismology of putting seismic sensors underground uses the distance to reduce disturbances from the surface, including acoustically produced ones. However, this is not easily applicable in the short time for setting up a SAMS.

nals during sensitive OSI measurements is raised which forms the motivation for this work.

Chapter 2: The fundamental equations of wave propagation in a solid and a fluid are given. A model of the layered soil used throughout this work and the respective boundary conditions are presented. Furthermore, different theoretical models to explain the recorded interference pattern of seismic waves are derived.

Chapter 3: The measurement instrumentation and the acoustic sources used during measurements conducted in the frame of the work are presented. The most important measurements near the airport Münster-Osnabrück, Germany (FMO) are described.

Chapter 4: Selected signals of various recorded events are shown in the time and in the frequency domain and their characteristics are discussed. The acoustic-seismic coupling coefficient is introduced as an effective method of the evaluations. The influences of various seismic waves on the recorded signal are estimated. The fit algorithm to compare measured data and theoretical models is introduced. With it near-surface soil properties are obtained. Furthermore, recordings using an acoustic shielding of several sensors from the directly incident acoustic waves are discussed. From this recommendations for the use during an OSI are derived.

Chapter 5: The findings of this work are summarised with respect to advances in the field of acoustic-seismic coupling and regarding their applicability for OSI measurements. An outlook for further research is given including several aspects how measurements and algorithms could be improved.

Appendix: In the appendices the equations of the phase difference between seismic waves (Eq. (2.71)) and of the spectral amplitude distribution of any number of interfering waves (Eq. (2.73)) are derived. Supplementary details on the analysed aircraft overflight events as well as on the sensor setup are presented. The calculation of the background level of the sensors used at the measurement site near the airport FMO is demonstrated. Additional spectrograms of sound pressure and soil velocity of various recorded events as well as plots of theoretically obtained interference amplitude distributions are shown. Finally, an estimate of the damping coefficient in unconsolidated soil is made.

Chapter 2

Theory

The propagation of waves in isotropic, homogeneous media as well as the conditions of reflection and refraction at a boundary between two such media have been investigated and described in detail. A basic understanding of the various waves types, their boundary conditions as well as their interaction is required for this work. Thus, in this chapter the theoretical background is developed, mainly following [40], [41] and [52] using the notation of the former.

Firstly, in Section 2.1 the equations of motion for an infinitesimally small volume element in an isotropic, elastic medium for a solid and a fluid are derived. These equations give a full characterisation of propagating seismic and acoustic waves. Additionally, the applicability of the geometrically obtained approximations for spherical and plane waves are discussed.

In Section 2.2 the soil model used throughout this work is introduced. For this wave propagation at a boundary between homogeneous layers of different elastic properties is discussed. Then the equations necessary to calculate the required reflection and transmission coefficients at these boundaries are provided. These coefficients give also information about the phase jump of the components of seismic waves upon reflection which are discussed afterwards.

Finally, in Section 2.3 the interference of seismic waves is described theoretically. Firstly, a simple model of three interfering P waves is introduced. Then, the model is extended to give a comprehensive description of the complex displacement field caused by various seismic waves propagating in the soil.

2.1 Wave equations in an isotropic, elastic medium

The response of a deformable body upon which an external force is acting can be described as the superposition of translation, deformation and rotation. Consider a small volume element containing two infinitesimally neighbouring points O and Q. The Cartesian coordinates of O shall be x, y, z and the respective components of its displacement (due to

the force acting on the body) shall be u, v and w. The displacement of the neighbouring point Q with the coordinates $x+\Delta x$, $y+\Delta y$, $z+\Delta z$ can be expressed using a Taylor expansion:

$$\begin{aligned} &u+\frac{\partial u}{\partial x}\Delta x+\frac{\partial u}{\partial y}\Delta y+\frac{\partial u}{\partial z}\Delta z,\\ &v+\frac{\partial v}{\partial x}\Delta x+\frac{\partial v}{\partial y}\Delta y+\frac{\partial v}{\partial z}\Delta z,\\ &w+\frac{\partial w}{\partial x}\Delta x+\frac{\partial w}{\partial y}\Delta y+\frac{\partial w}{\partial z}\Delta z. \end{aligned} \tag{2.1}$$

Here terms of higher order have been neglected which represents the assumption of small strains in elastic waves.
Eq. (2.1) can be rewritten to separate the individual components of translation, rotation and deformation:

$$\begin{aligned} u \quad &+(\Omega_y\Delta z-\Omega_z\Delta y)+(\varepsilon_{xx}\Delta x+\varepsilon_{xy}\Delta y+\varepsilon_{xz}\Delta z),\\ v \quad &+(\Omega_z\Delta x-\Omega_x\Delta z)+(\varepsilon_{yx}\Delta x+\varepsilon_{yy}\Delta y+\varepsilon_{yz}\Delta z),\\ \underbrace{w}_{translation} \quad &+\underbrace{(\Omega_x\Delta y-\Omega_y\Delta x)}_{rotation}+\underbrace{(\varepsilon_{zx}\Delta x+\varepsilon_{zy}\Delta y+\varepsilon_{zz}\Delta z)}_{deformation}. \end{aligned} \tag{2.2}$$

The first elements in Eq. (2.2) refer to the translation of the point O. The second summands represent a rotation around an axis through O and the third ones a deformation of the volume element. For the terms of the deformation, the following expressions are introduced:

$$\begin{aligned} \varepsilon_{xx}&=\frac{\partial u}{\partial x}, \quad \varepsilon_{xy}=\varepsilon_{yx}=\frac{1}{2}\left(\frac{\partial u}{\partial y}+\frac{\partial v}{\partial x}\right),\\ \varepsilon_{yy}&=\frac{\partial v}{\partial y}, \quad \varepsilon_{yz}=\varepsilon_{zy}=\frac{1}{2}\left(\frac{\partial v}{\partial z}+\frac{\partial w}{\partial y}\right),\\ \varepsilon_{zz}&=\frac{\partial w}{\partial z}, \quad \varepsilon_{zx}=\varepsilon_{xz}=\frac{1}{2}\left(\frac{\partial w}{\partial x}+\frac{\partial u}{\partial z}\right). \end{aligned} \tag{2.3}$$

Now the strain tensor can be defined:

$$E=\begin{pmatrix} \varepsilon_{xx} & \varepsilon_{xy} & \varepsilon_{xz}\\ \varepsilon_{yx} & \varepsilon_{yy} & \varepsilon_{yz}\\ \varepsilon_{zx} & \varepsilon_{zy} & \varepsilon_{zz} \end{pmatrix} \tag{2.4}$$

with symmetric elements $\varepsilon_{ij}=\varepsilon_{ji}$. The components on the principal axes represent expansion ($|\varepsilon_{ii}|>0$) or compression ($|\varepsilon_{ii}|<0$) parallel to the coordinate axis. The elements ε_{ij} for $i\neq j$ refer to a shear deformation. The sum of the principal elements, the dilatation, given by

$$\theta=\varepsilon_{xx}+\varepsilon_{yy}+\varepsilon_{zz}=\frac{\partial u}{\partial x}+\frac{\partial v}{\partial y}+\frac{\partial w}{\partial z}, \tag{2.5}$$

is independent of the chosen orthonormal system.
Accordingly, the terms of the rotation in Eq. (2.2) are expressed by:

$$\Omega_x = \frac{1}{2}\left(\frac{\partial w}{\partial y} - \frac{\partial v}{\partial z}\right), \quad \Omega_y = \frac{1}{2}\left(\frac{\partial u}{\partial z} - \frac{\partial w}{\partial x}\right), \quad \Omega_z = \frac{1}{2}\left(\frac{\partial v}{\partial x} - \frac{\partial u}{\partial y}\right). \tag{2.6}$$

Thus, the antisymmetric rotation tensor with its elements Ω_{ij} = - Ω_{ji} and its principal elements $\Omega_{ii} = 0$ can be defined.

To describe the forces acting upon an infinitesimal small volume element of a body the traction at point O on all planes passing through it need to be specified. The traction on any plane can be described as the superposition of the components of traction across planes running parallel to three planes perpendicular to each other. For this the planes normal to the Cartesian coordinate axis are used. Thus, the stress tensor P can be defined as the forces, acting upon the respective surfaces of the volume:

$$P = \begin{pmatrix} p_{xx} & p_{xy} & p_{xz} \\ p_{yx} & p_{yy} & p_{yz} \\ p_{zx} & p_{zy} & p_{zz} \end{pmatrix}. \tag{2.7}$$

Here the first index of p_{ij} refers to the plane normal to the coordinate axis i and the second one states the direction of the traction, parallel to the coordinate axis j. Again, the stress tensor is symmetric with $p_{ij} = p_{ji}$.
In elastic theory (corresponding to only infinitesimally small deformations), which is generally used for seismology, the components of the stress p_{ij} are linear functions of all ε_{kl}. Thus, the stress-strain relations, the generalised Hook's Law, is given by

$$p_{ik} = c_{ijkl}\varepsilon_{kl} \tag{2.8}$$

with 36 elastic constants c_{ijkl}. In the special case of an isotropic medium only two elastic constants remain, known as Lamé's constants λ_{L} and μ.[10] Depending on context Lamé's first and second parameter might be given different names – I will refer to the second one μ as rigidity as in [40].

[10] Contrary to the general use in literature, I will use the expression λ_{L} (instead of λ) to distinguish Lamé's first constant from the wavelength λ.

Using Lamé's constants the strain-stress relations can be expressed as:

$$\begin{aligned} p_{xx} &= \lambda_L\theta + 2\mu\frac{\partial u}{\partial x}, \quad p_{xy} = p_{yx} = \mu\left(\frac{\partial u}{\partial y} + \frac{\partial v}{\partial x}\right), \\ p_{yy} &= \lambda_L\theta + 2\mu\frac{\partial v}{\partial y}, \quad p_{yz} = p_{zy} = \mu\left(\frac{\partial v}{\partial z} + \frac{\partial w}{\partial y}\right), \\ p_{zz} &= \lambda_L\theta + 2\mu\frac{\partial w}{\partial z}, \quad p_{zx} = p_{xz} = \mu\left(\frac{\partial w}{\partial x} + \frac{\partial u}{\partial z}\right). \end{aligned} \tag{2.9}$$

With these expressions the equations of motion of the small volume element upon which an external force is acting can be given:

$$\begin{aligned} \rho\frac{\partial^2 u}{\partial t^2} &= (\lambda_L + \mu)\frac{\partial\theta}{\partial x} + \mu\nabla^2 u, \\ \rho\frac{\partial^2 v}{\partial t^2} &= (\lambda_L + \mu)\frac{\partial\theta}{\partial y} + \mu\nabla^2 v, \\ \rho\frac{\partial^2 w}{\partial t^2} &= (\lambda_L + \mu)\frac{\partial\theta}{\partial z} + \mu\nabla^2 w. \end{aligned} \tag{2.10}$$

Here ρ is the density in the material and $\partial/\partial t$ is the time derivative. Thus, the left terms in Eq. (2.10) refer to the respective components of the inertia term of the small volume element. Note, that generally body forces and surface forces acting upon a small volume element would need to be considered. However, for the treatment of seismic waves, body forces play a minor role and therefore they are generally neglected in seismology. Thus, in Eq. (2.10) only the forces acting upon a surface of the volume element are taken into account.

2.1.1 Wave in an ideal elastic fluid

For an ideal fluid the rigidity μ vanishes which strongly simplifies above equations. From Eq. (2.9) one finds, that only the principal elements of the stress tensor are non-zero:

$$p_{xx} = p_{yy} = p_{zz} = \lambda_L\theta = -p,^{11} \tag{2.11}$$

where the value $-p$ is identified with the hydrostatic pressure of the fluid. This means, that in a fluid only a compressional wave can propagate, while shear waves are not possible due to the vanishing shear components: $p_{ij} = 0$ for $i \neq j$.
To obtain the wave equation a velocity potential $\overline{\varphi}$ is defined as follows:

$$\frac{\partial u}{\partial t} = \frac{\partial\overline{\varphi}}{\partial x}, \quad \frac{\partial v}{\partial t} = \frac{\partial\overline{\varphi}}{\partial y}, \quad \frac{\partial w}{\partial t} = \frac{\partial\overline{\varphi}}{\partial z}. \tag{2.12}$$

[11] With $\mu = 0$ the Lamé constant λ_L can be identified with the incompressibility of the fluid.

Using the equation of motion Eq. (2.10) and the definition of the dilatation θ (Eq. (2.5)) one finds (see [53]):

$$\nabla^2 \overline{\varphi} = \frac{1}{{v_0}^2} \frac{\partial^2 \overline{\varphi}}{\partial t^2}. \tag{2.13}$$

For the velocity of the wave in a fluid $v_0 = \sqrt{\lambda_\mathrm{L}/\rho}$ the expression v_0 is used in this work, referring to the velocity of an acoustic wave in air. This is to distinguish it from the velocities of seismic waves which are introduced in Section 2.1.2. The wave equation Eq. (2.13) is not only fulfilled for the three components of the velocity potential but also for the deviations from the static values of pressure and density in the fluid. The first is called sound pressure and will be used throughout this work to characterise acoustic waves propagating in air.
Using the assumption of an ideal gas the temperature dependency of v_0 is given by:

$$v_0 = \sqrt{\frac{c_\mathrm{p}}{c_\mathrm{v}} \frac{RT}{M}}. \tag{2.14}$$

Here $R = 8.3145\,\mathrm{J/(K\ mol)}$ is the molar gas constant [54], T is the absolute temperature and, if the gas under consideration is air, $M = 28.97\,\mathrm{g/mol}$ is the molar mass of air [55]. The ratio between c_p and c_v (i.e. the specific heat capacities at constant pressure and volume, respectively) is approximately $c_\mathrm{p}/c_\mathrm{v} \approx 1.40$. It varies only slightly with temperature. Thus, the wave velocity of sound in air v_0 is approximately proportional to the square root of the temperature:

$$v_0 \approx 20.05 \sqrt{\frac{T}{\mathrm{K}}} \frac{\mathrm{m}}{\mathrm{s}}. \tag{2.15}$$

2.1.2 Waves in a solid elastic body

To derive the wave equations in a solid elastic body a scalar potential φ and a vector potential $\psi(\psi_1, \psi_2, \psi_3)$ are defined for the displacement:

$$\begin{aligned} u &= \frac{\partial \varphi}{\partial x} + \frac{\partial \psi_3}{\partial y} - \frac{\partial \psi_2}{\partial z}, \\ v &= \frac{\partial \varphi}{\partial y} + \frac{\partial \psi_1}{\partial z} - \frac{\partial \psi_3}{\partial x}, \\ w &= \frac{\partial \varphi}{\partial z} + \frac{\partial \psi_2}{\partial x} - \frac{\partial \psi_1}{\partial y}. \end{aligned} \tag{2.16}$$

Eq. (2.16) can also be written in vector form, showing the separation in a pure deformation and a pure rotation more clearly:

$$\begin{pmatrix} u \\ v \\ w \end{pmatrix} = \text{grad } \varphi + \text{curl} \begin{pmatrix} \psi_1 \\ \psi_2 \\ \psi_3 \end{pmatrix}. \tag{2.17}$$

Eq. (2.10) is fulfilled, if the potentials φ and ψ_i are solutions of the wave equations

$$\nabla^2 \varphi = \frac{1}{{v_\mathrm{P}}^2} \frac{\partial^2 \varphi}{\partial t^2} \tag{2.18}$$

and

$$\nabla^2 \psi_i = \frac{1}{{v_\mathrm{S}}^2} \frac{\partial^2 \psi_i}{\partial t^2}. \tag{2.19}$$

The respective wave velocities are given by:

$$v_\mathrm{P} = \sqrt{\frac{\lambda_\mathrm{L} + 2\mu}{\rho}} \quad \text{and} \quad v_\mathrm{S} = \sqrt{\frac{\mu}{\rho}}.^{12} \tag{2.20}$$

In a solid body two types of waves can propagate: The first type are compressional waves, also called primary or P waves, with the wave velocity v_P. The second type are shear waves, also called secondary or S waves, with the respective velocity v_S. For P waves the displacement of a volume element is in the direction of propagation of the P wave. On the contrary, for S waves the displacement is perpendicular to its direction of propagation. Therefore, in seismology two orthogonal S waves are defined using the Earth's surface as a plane of reference: SH waves have a displacement parallel to the surface and SV waves show displacement perpendicular to the propagation direction of the wave as well as to that of the SH waves.
P and SV waves each excite only P and SV wave upon reflection or refraction at a plane, horizontally aligned boundary. SH waves can be treated separately – and since the investigated sources are compressional waves, SH waves play no further role throughout the evaluation presented in this work. Thus, when talking about S waves, I generally imply that the wave is an SV wave.

2.1.3 Approximations for spherical and plane waves

Both compressional and shear waves can also be characterised by the form of their wavefronts, which are the locations of the propagating wave having the same phase. The wave vector $\vec{k}$, generally pointing in the direction of propagation of the wave, is at each point

[12] Note: In literature often the Greek letters α and β are used for v_P and v_S, respectively. I use the letters α and β for angles in this work.

normal to the wavefront. A point source emits waves whose wavefronts are the surfaces of spheres, therefore these wave are called spherical waves. Physical sources with finite dimensions $r' > 0$ can be treated as a point source in a distance $r \gtrsim 4 \cdot \lambda$, depending on the wavelength λ of the emitted wave. This distance is referred to as the far field of the source – here the wavefronts can be assumed to be spherical. A spherical wave has the form

$$u(\vec{r},t) = \frac{1}{r} f_1(r - ct) + \frac{1}{r} f_2(r + ct). \tag{2.21}$$

Here r is the radial distance from the source, expressed in spherical coordinates $\vec{r} = (r, \Theta, \Phi)$ (expressed in Cartesian coordinates r is given by $r^2 = x^2 + y^2 + z^2$). c is the velocity of the wave and f_1 and f_2 are general solutions of the wave equation, representing outgoing and incoming spherical waves. From Eq. (2.21) it is obvious that a spherical wave shows radial symmetry towards its (point) source and can be fully described using only the dependency on r – without any further dependencies on the polar angle Θ or the azimuthal angle Φ of the spherical coordinates.
The emitted power of a spherical wave is distributed equally over a sphere. Thus, conservation of energy requires that the intensity (i.e. the power per area) decreases proportionally to $1/r^2$. Accordingly, the amplitude of a spherical wave decreases proportionally to $1/r$, as indicated in Eq. (2.21).

For many considerations like reflection and refraction it is more convenient to deal with plane wavefronts rather than with spherical ones. A plane wave has the form

$$u(\vec{r},t) = g_1(\vec{k}\vec{r} - \omega t) + g_2(\vec{k}\vec{r} + \omega t) \tag{2.22}$$

with the angular frequency $\omega = 2\pi f = c \cdot |\vec{k}|$. The function g_1 represents a wave propagating in the direction of $\vec{r}$ and g_2 a wave propagating in the opposite direction.
The approximation of a spherical wave (emitted at point O) as a plane one required that the wave properties of a point S on the sphere match those of a point P on a plane (see Fig. 2.1). For this two conditions need to be fulfilled: Firstly, the dimension of interest in radial direction Δr (i.e. parallel to the wave vector $\vec{k}$) needs to be small compared to the distance from the source r: $\Delta r \ll r$. Thus, the decrease of the amplitude of the wave (see Eq. (2.21)) within the distance Δr can be neglected and the approximation $\frac{1}{r} \approx \frac{1}{|r+\Delta r|}$ is valid. Secondly, the phase difference due to the curvature of the spherical wavefront between any point S of interest on a sphere of radius r and the respective point P on a plane tangential to the sphere on a fixed point Q needs to be small. It is geometrically determined by r and the length $r_\perp$ perpendicular to $\vec{k}$, as sketched in Fig. 2.1. The path between S and P is given by

$$\Delta r = \sqrt{r^2 + r_\perp^2} - r, \tag{2.23}$$

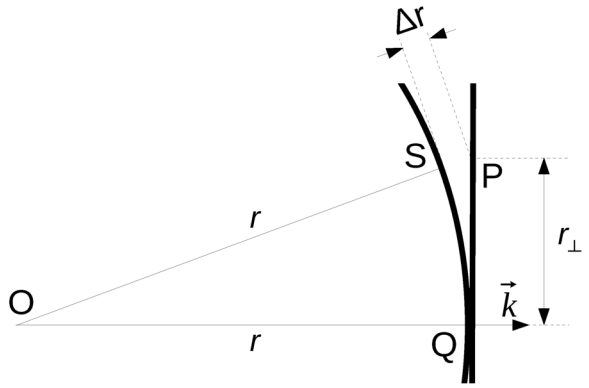

Figure 2.1: Sketch of the deviation of a plane wavefront from a spherical one for spatially separated points Q and P (plane wavefront) respectively S (spherical wavefront). The path Δr between the points S and P leads to a phase difference due to the curvature of the sphere and can be calculated geometrically for given r and $r_\perp$.

leading to the phase difference

$$\Delta\phi = \frac{2\pi f \Delta r}{c} = \frac{2\pi \Delta r}{\lambda}. \tag{2.24}$$

Here f is the frequency, c the velocity and λ the wavelength of the wave. For the presented aircraft measurements the distance between the source and the sensor is large enough and the area of the sensor setup is comparatively small, thus the acoustic signals can be treated as plane waves.

2.2 Wave propagation in a soil layer between two half-spaces

When a plane wave hits a boundary between two media of different elastic properties, reflection and refraction occur. Even if the incident wave is a pure compressional or pure shear wave, upon interaction with the boundary generally both types of waves will be excited in both media. Throughout this work the model of the soil as sketched in Fig. 2.2 is used. With this model P and SV waves propagating within the soil can be fully characterised, i.e. their amplitudes and the phase difference between them can be obtained.
In the model the horizontally aligned soil layer 1 is enclosed by two infinitely extending half-spaces: One is filled with a fluid (i.e. air) above soil layer 1. The lower half-space is the infinitely extending soil layer 2 with different elastic properties than the upper soil layer. Throughout this work variables referring to the first soil layer are indexed with "1" and those referring to the second soil layer with "2".
Two boundaries need to be considered in the model: The first boundary between air and soil layer 1 – the surface – is the plane at $z = 0$ m; the second boundary between the

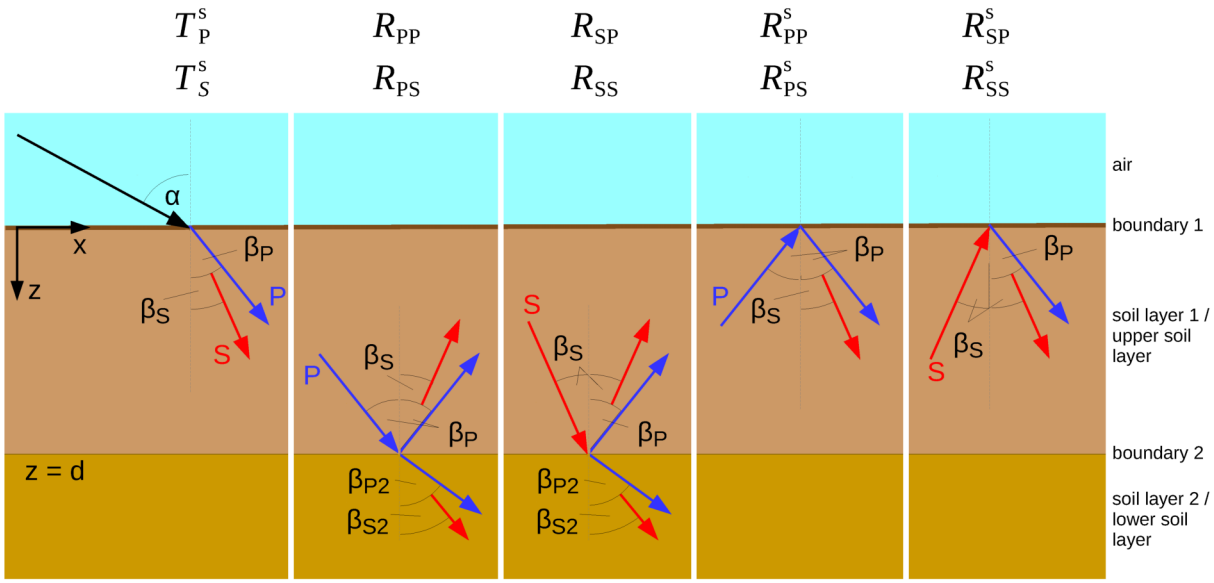

Figure 2.2: Model of layered soil including schemata of types of excited waves: At each boundary P waves (blue) and S waves (red) can be excited in the soil. The ratios between the amplitudes of the incident waves and the excited waves are denoted by the coefficients of transmission T and reflection R, respectively. The first indices of the reflection coefficients refer to the types (i.e. P or S) of the incident waves and the second ones to the types of the reflected waves. The angle from the normal to the surface of the incident acoustic wave (black arrow on the left) is α; the angles of the P and S waves from the normal to the boundaries are β_P and β_S in the first soil layer and β_{P2} and β_{S2} in the second soil layer, respectively.

two soil layers is the plane in depth $z = d$. The P and S waves are excited by acoustic, compressional waves hitting the surface from above.

The velocity of the sound wave in air is denoted with v_0. The angle between the wave vector of the acoustic wave and the normal towards the surface, also referred to as acoustic angle of incidence, is α. In the first soil layer the velocity of P waves is v_{P1} and that of S waves v_{S1} and in the second seismic layer the respective velocities are v_{P2} and v_{S2}. The angles of the seismic waves towards the normal to the boundaries are denoted with β_P and β_S for the refraction at the surface and with β_{P2} and β_{S2} for the refraction at the underground boundary.[13]

Of interest for the evaluations in this work are the amplitude ratios between the acoustically excited P wave (or S wave, respectively) and the incident acoustic wave, denoted with T^s_P and T^s_S.[14] Furthermore, the amplitude ratios between the reflected P and S waves at the underground boundary and the incident seismic waves (P and S waves respectively) are required, denoted with R_{PP}, R_{PS}, R_{SP} and R_{SS}. Here the first index refers to the type of the incident waves and the second index to the type of the reflected waves. The

[13] Since usually only the angles of the waves in the first soil layer are of interest, I simply use β_P (instead of β_{P1}) and β_S (instead of β_{S1}).

[14] The indices "P" and "S" refer to the acoustically excited P and S waves, respectively. The superscript "s" indicates that the transmission coefficients refer to the surface, i.e. the first boundary.

transmitted seismic waves into the second soil layer are generally neglected here. However, their respective wave velocities are required for the calculation of the amplitudes of the reflected waves at the underground boundary. Lastly, the amplitude ratios between the waves excited upon reflection at the free surface and the upwards-propagating seismic waves are needed. They are denoted with $R^{\mathrm{s}}_{\mathrm{PP}}$, $R^{\mathrm{s}}_{\mathrm{PS}}$, $R^{\mathrm{s}}_{\mathrm{SP}}$ and $R^{\mathrm{s}}_{\mathrm{SS}}$, with the superscript "s" indicating that these reflection coefficients refer to the surface.
To obtain the amplitude ratios between the excited and the incident waves, equations taking into account the respective boundary conditions (i.e. continuity or vanishing of certain components of stress and displacement) need to be solved. These are given separately in Section 2.2.2 for a boundary between two solids, in Section 2.2.3 for a free surface and in Section 2.2.4 for a boundary between a fluid and a solid. The amplitude ratios given in these sections refer to the displacement amplitudes of the full wave while the respective vertical components are used for the evaluation (as discussed in Section 4.3.1).
To solve the equations of the boundary conditions the displacement potentials φ and ψ, introduced in Eq. (2.16), are used. Without loss of generality shall the boundary between medium 1 and medium 2 be horizontally aligned and the incident plane wave hits it from above, i.e. its components of the wave vector point in positive x- and z-direction. With the respective wave equations Eq. (2.18) and Eq. (2.19) it can be shown that the potentials in the first medium have the form:

$$\varphi(x,z,t) = a_{\mathrm{inc}} \cdot \mathrm{e}^{\mathrm{i}\omega\left(\frac{\sin(\kappa_{\mathrm{P}})}{v_{\mathrm{P}}}x+\frac{\cos(\kappa_{\mathrm{P}})}{v_{\mathrm{P}}}z-t\right)} + a_{\mathrm{ref}} \cdot \mathrm{e}^{\mathrm{i}\omega\left(\frac{\sin(\kappa_{\mathrm{P}})}{v_{\mathrm{P}}}x-\frac{\cos(\kappa_{\mathrm{P}})}{v_{\mathrm{P}}}z-t\right)} \tag{2.25}$$

and

$$\psi(x,z,t) = b_{\mathrm{inc}} \cdot \mathrm{e}^{\mathrm{i}\omega\left(\frac{\sin(\kappa_{\mathrm{S}})}{v_{\mathrm{S}}}x+\frac{\cos(\kappa_{\mathrm{S}})}{v_{\mathrm{S}}}z-t\right)} + b_{\mathrm{ref}} \cdot \mathrm{e}^{\mathrm{i}\omega\left(\frac{\sin(\kappa_{\mathrm{S}})}{v_{\mathrm{S}}}x-\frac{\cos(\kappa_{\mathrm{S}})}{v_{\mathrm{S}}}z-t\right)}. \tag{2.26}$$

In the second medium only the waves propagating away from the boundary exist, thus both potentials can be written as:

$$\varphi'(x,z,t) = a_{\mathrm{trans}} \cdot \mathrm{e}^{\mathrm{i}\omega\left(\frac{\sin(\kappa'_{\mathrm{P}})}{v'_{\mathrm{P}}}x+\frac{\cos(\kappa'_{\mathrm{P}})}{v'_{\mathrm{P}}}z-t\right)} \tag{2.27}$$

and

$$\psi'(x,z,t) = b_{\mathrm{trans}} \cdot \mathrm{e}^{\mathrm{i}\omega\left(\frac{\sin(\kappa'_{\mathrm{S}})}{v'_{\mathrm{S}}}x+\frac{\cos(\kappa'_{\mathrm{S}})}{v'_{\mathrm{S}}}z-t\right)}. \tag{2.28}$$

Here the coefficients a_{inc} and a_{ref} are identified with the displacement amplitudes of the incident P wave and the reflected P wave in medium 1 and the coefficients b_{inc} and b_{ref} refer to the respective amplitudes of the SV waves. a_{trans} and b_{trans} are amplitudes of the P and SV waves transmitted in the second medium, respectively. All primed terms refer to the second medium. Thus, v_{P} and v_{S} are the wave velocities of P and SV waves in the first

medium and v'_{P} and v'_{S} those in the second one. The angles κ_{P} and κ_{S} are the incidence angles (which equal the reflection angles) in medium 1 of P and SV wave, respectively. The angles κ'_{P} and κ'_{S} are the corresponding angles of refraction in the second medium. ω is the angular frequency of the waves. The trigonometrical expressions in the exponents represent the components in x- and z-direction of the velocities of the compressional and shear waves in the respective medium. The displacements are obtained by solving the respective boundary conditions as demonstrated in the following sections: Depending on the two media (i.e. solid - solid, solid - vacuum or fluid - solid) the equations Eq. (2.25) to Eq. (2.28) are applied to the respective layer of the introduced model.
For the used soil model and therefore for the potentials in Eq. (2.25) to Eq. (2.28) the coordinate system is chosen in such a way that P waves and SV waves do not depend on y, i.e. wave vectors and displacements of incident, reflected and refracted waves are contained in the x-z-plane.

2.2.1 General law of reflection and refraction

The relations between the acoustic angle of incidence, the seismic angles of refraction and reflection (all shown in Fig. 2.2) and the wave velocities of P and SV waves are given by the general laws of reflection and refraction:

$$p = \frac{1}{v_{\mathrm{hor}}} = \frac{\sin(\alpha)}{v_0} = \frac{\sin(\beta_{\mathrm{P}})}{v_{\mathrm{P1}}} = \frac{\sin(\beta_{\mathrm{S}})}{v_{\mathrm{S1}}} = \frac{\sin(\beta_{\mathrm{P2}})}{v_{\mathrm{P2}}} = \frac{\sin(\beta_{\mathrm{S2}})}{v_{\mathrm{S2}}}. \tag{2.29}$$

The common parameter p, referred to in literature as horizontal slowness, can be interpreted as the inverse of the velocity v_{hor} with which a plane wavefront propagates along a horizontally aligned boundary.
Obviously, if the incident and reflected waves have the same type (i.e. P or SV wave), the reflection angle is equal to the incidence one.

2.2.2 Boundary between two solids

The most general case arises when the media on both sides of the boundary support compressional and shear waves as is the case at the underground boundary between the first and the second soil layer (see Fig. 2.2). Boundary conditions require that the components of the displacements u and w as well as the components of the stress tensor p_{zz} and p_{zx} are continuous across the boundary. Expressing p_{zz} and p_{zx} in terms of φ and ψ ($= \psi_2$ in the notation of Eq. (2.16))[15] one finds:

$$p_{zz} = \lambda_{\mathrm{L}} \nabla^2 \varphi + 2\mu \Big(\frac{\partial^2 \varphi}{\partial z^2} + \frac{\partial^2 \psi}{\partial x \partial z} \Big) \text{ and } p_{zx} = \mu \Big(2 \frac{\partial^2 \varphi}{\partial x \partial z} + \frac{\partial^2 \psi}{\partial x^2} - \frac{\partial^2 \psi}{\partial z^2} \Big). \tag{2.30}$$

[15] This is due to the choice of the coordinate system with all waves contained in the x-z-plane. Thus, the partial derivatives $\frac{\partial}{\partial y}$ of the potentials vanish.

The respective expressions for u and w are obtained from Eq. (2.16) by neglecting all terms depending on y due to the suitable choice of the coordinate system:

$$u = \frac{\partial \varphi}{\partial x} - \frac{\partial \psi}{\partial z} \text{ and } w = \frac{\partial \varphi}{\partial z} + \frac{\partial \psi}{\partial x}. \tag{2.31}$$

At the boundary between soil layer 1 and soil layer 2 the four conditions to be solved are: $p_{zz,1} = p_{zz,2}$, $p_{zx,1} = p_{zx,2}$, $u_1 = u_2$ and $w_1 = w_2$. At that boundary only the amplitudes of P or S waves incident from the first soil layer as well as of the waves reflected back upwards are of interest. Using the two potentials in both media for an incident P wave ($b_{\text{inc}} = 0$) the amplitude ratios are obtained. Throughout this work they are refer to as the reflection coefficients at the underground boundary. They are given (as in [56][16]) by:

$$R_{\text{PP}} = \frac{a_{\text{ref}}}{a_{\text{inc}}} = \frac{1}{l_5}\left[\left(m_2 \frac{\cos(\beta_{\text{P}})}{v_{\text{P1}}} - m_3 \frac{\cos(\beta_{\text{P2}})}{v_{\text{P2}}}\right) l_2 - \left(m_1 + m_4 \frac{\cos(\beta_{\text{P}})}{v_{\text{P1}}} \frac{\cos(\beta_{\text{S2}})}{v_{\text{S2}}}\right) l_4 p^2\right] \tag{2.32}$$

and

$$R_{\text{PS}} = \frac{b_{\text{ref}}}{a_{\text{inc}}} = -\frac{2\cos(\beta_{\text{P}})}{v_{\text{S1}}} \frac{p}{l_5}\left(m_1 m_2 + m_3 m_4 \frac{\cos(\beta_{\text{P2}})}{v_{\text{P2}}} \frac{\cos(\beta_{\text{S2}})}{v_{\text{S2}}}\right). \tag{2.33}$$

Corresponding equations are obtained for an incident SV wave ($a_{\text{inc}} = 0$):

$$R_{\text{SP}} = \frac{a_{\text{ref}}}{b_{\text{inc}}} = -\frac{2\cos(\beta_{\text{S}})}{v_{\text{P1}}} \frac{p}{l_5}\left(m_1 m_2 + m_3 m_4 \frac{\cos(\beta_{\text{P2}})}{v_{\text{P2}}} \frac{\cos(\beta_{\text{S2}})}{v_{\text{S2}}}\right) \tag{2.34}$$

and

$$R_{\text{SS}} = \frac{b_{\text{ref}}}{b_{\text{inc}}} = -\frac{1}{l_5}\left[\left(m_2 \frac{\cos(\beta_{\text{S}})}{v_{\text{S1}}} - m_3 \frac{\cos(\beta_{\text{S2}})}{v_{\text{S2}}}\right) l_1 - \left(m_1 + m_4 \frac{\cos(\beta_{\text{P2}})}{v_{\text{P2}}} \frac{\cos(\beta_{\text{S}})}{v_{\text{S1}}}\right) l_3 p^2\right]. \tag{2.35}$$

Here p is the horizontal slowness as introduced in Eq. (2.29). The used coefficients are:

$$\begin{aligned} m_1 &= \rho_2(1 - 2v_{\text{S2}}^2 p^2) - \rho_1(1 - 2v_{\text{S1}}^2 p^2), & m_2 &= \rho_2(1 - 2v_{\text{S2}}^2 p^2) + 2\rho_1 v_{\text{S1}}^2 p^2, \\ m_3 &= \rho_1(1 - 2v_{\text{S1}}^2 p^2) + 2\rho_2 v_{\text{S2}}^2 p^2, & m_4 &= 2(\rho_2 v_{\text{S2}}^2 - \rho_1 v_{\text{S1}}^2) \end{aligned}$$

[16] Many different formulae are found in literature for the various reflection coefficients, both for the amplitude ratios of the displacement and the potentials, respectively. In the primary reference [40] equations for the special case $\lambda_{\text{L}} = \mu$ (and thus $v_{\text{P}} = \sqrt{3} \cdot v_{\text{S}}$) are given. This assumption cannot be made for the underground boundary investigated in this thesis (since v_{P2} is significantly larger than $\sqrt{3} \cdot v_{\text{S2}}$), thus the more general equations is given here (taken from [56]). For the surface boundary the equations from [40] can be used, since $v_{\text{P1}} \approx \sqrt{3} \cdot v_{\text{S1}}$.
Additionally, special care should be taken whether the respective reflection coefficients refer to the displacement or to the potentials. Throughout this work the used coefficients refer to the displacement.

and

$$l_1 = m_2\frac{\cos(\beta_\mathrm{P})}{v_\mathrm{P1}} + m_3\frac{\cos(\beta_\mathrm{P2})}{v_\mathrm{P2}}, \quad l_2 = m_2\frac{\cos(\beta_\mathrm{S})}{v_\mathrm{S1}} + m_3\frac{\cos(\beta_\mathrm{S2})}{v_\mathrm{S2}},$$
$$l_3 = m_1 - m_4\frac{\cos(\beta_\mathrm{P})}{v_\mathrm{P1}}\frac{\cos(\beta_\mathrm{S2})}{v_\mathrm{S2}}, \quad l_4 = m_1 - m_4\frac{\cos(\beta_\mathrm{P2})}{v_\mathrm{P2}}\frac{\cos(\beta_\mathrm{S})}{v_\mathrm{S1}}$$
$$l_5 = l_1 \cdot l_2 + l_3 \cdot l_4 p^2.$$

For the calculation the soil properties (the wave velocities v_P and v_S of P and S wave and the soil density ρ) as well as the angles of the P and S waves towards the normal to the boundary in both soil layers are used.

2.2.3 Reflection at a free surface

When a wave propagating in a solid is reflected at the boundary towards air, the problem can be approximately described as reflection at a free boundary, contrary to one where the second medium shows resistance to deformation. Therefore, due to the large difference in density of both media, the air is treated as vacuum. To calculate the reflection coefficients, the boundary conditions to be fulfilled are: $p_{zz} = p_{zx} = 0$.
Thus, for an incident P wave the reflection coefficients at a free surface are given by (following [40], with $b_\mathrm{inc} = 0$):

$$R^\mathrm{s}_\mathrm{PP} = \frac{a_\mathrm{ref}}{a_\mathrm{inc}} = \frac{4\cot(\beta_\mathrm{P})\cot(\beta_\mathrm{S}) - (1+3\cot^2(\beta_\mathrm{P}))^2}{4\cot(\beta_\mathrm{P})\cot(\beta_\mathrm{S}) + (1+3\cot^2(\beta_\mathrm{P}))^2} \tag{2.36}$$

and

$$R^\mathrm{s}_\mathrm{PS} = \frac{b_\mathrm{ref}}{a_\mathrm{inc}} = \frac{-4\cot(\beta_\mathrm{P})(1+3\cot^2(\beta_\mathrm{P}))}{4\cot(\beta_\mathrm{P})\cot(\beta_\mathrm{S}) + (1+3\cot^2(\beta_\mathrm{P}))^2}. \tag{2.37}$$

The respective equations for an incident SV wave (with $a_\mathrm{inc} = 0$) are:

$$R^\mathrm{s}_\mathrm{SP} = \frac{a_\mathrm{ref}}{b_\mathrm{inc}} = \frac{4\cot(\beta_\mathrm{P})(1+3\cot^2(\beta_\mathrm{P}))}{4\cot(\beta_\mathrm{P})\cot(\beta_\mathrm{S}) + (1+3\cot^2(\beta_\mathrm{P}))^2} \tag{2.38}$$

and

$$R^\mathrm{s}_\mathrm{SS} = \frac{b_\mathrm{ref}}{b_\mathrm{inc}} = \frac{4\cot(\beta_\mathrm{P})\cot(\beta_\mathrm{S}) - (1+3\cot^2(\beta_\mathrm{P}))^2}{4\cot(\beta_\mathrm{P})\cot(\beta_\mathrm{S}) + (1+3\cot^2(\beta_\mathrm{P}))^2}. \tag{2.39}$$

A negative sign of the reflection coefficient corresponds to the same direction of the vertical components of the displacements of incident and reflected waves as will be discussed in detail in Section 2.2.5. For the case of perpendicular incidence ($\beta_\mathrm{P} = 0°$) of a P wave towards a free surface the reflection coefficient has an absolute value of 1: $R^\mathrm{s}_\mathrm{PP}(\beta_\mathrm{P} = 0°) =$ -1. This leads to a doubled displacement amplitude at the surface with respect to that of the incident wave: $a(z = 0\,\mathrm{m},\ \beta_\mathrm{P} = 0°) = a_\mathrm{inc} + a_\mathrm{ref} = 2 \cdot a_\mathrm{inc}$. For the boundary between air and soil and for the full range of acoustic angles of incidence α investigated in this

work $R_{\mathrm{PP}}^{\mathrm{s}}$ is negative. Thus, the vertical components of the displacements of incident and reflected P waves at the free surface superpose always constructively.

2.2.4 Boundary between a fluid and a solid

In a fluid like air the rigidity μ and consequently the shear components of the stress tensor are zero as discussed in Section 2.1.1. Therefore, only compressional waves can propagate in it. When an incident acoustic wave from the air-filled half-space hits the soil surface P and S waves are excited in the soil, representing the second half-space. The better part of the energy is reflected and is not further considered here.
The boundary conditions to be fulfilled require continuity of the displacement in z-direction $w = w'$ and of the zz-component of the stress tensor $p_{zz} = p'_{zz}$. Additionally, the shear components of the stress tensor in the fluid vanish $p_{zx} = p_{zy} = 0$.
The ratios between the amplitudes of incident (compressional) acoustic wave and transmitted P and S waves are given by the transmission coefficients (following [40]):

$$T_{\mathrm{P}}^{\mathrm{s}} = \frac{2\rho_{\mathrm{air}}\cot(\alpha)(1/\sin^2(\beta_{\mathrm{S}}) - 2)}{\rho_{\mathrm{air}}\cot(\beta_{\mathrm{P}})/\sin^2(\beta_{\mathrm{S}}) + \rho_1 \frac{{v_{\mathrm{S}1}}^2}{{v_0}^2}\cot(\alpha)\sin^2(\alpha)\left[(1/\sin^2(\beta_{\mathrm{S}}) - 2)^2 + 4\cot(\beta_{\mathrm{P}})\cot(\beta_{\mathrm{S}})\right]},$$

$$T_{\mathrm{S}}^{\mathrm{s}} = -\frac{4\rho_{\mathrm{air}}\cot(\alpha)\cot(\beta_{\mathrm{P}})}{\rho_{\mathrm{air}}\cot(\beta_{\mathrm{P}})/\sin^2(\beta_{\mathrm{S}}) + \rho_1 \frac{{v_{\mathrm{S}1}}^2}{{v_0}^2}\cot(\alpha)\sin^2(\alpha)\left[(1/\sin^2(\beta_{\mathrm{S}}) - 2)^2 + 4\cot(\beta_{\mathrm{P}})\cot(\beta_{\mathrm{S}})\right]}. \tag{2.40}$$

2.2.5 Phase jump upon reflection at a boundary

Not only the amplitude of the reflected wave (relative to that of the incident one) is of interest, but also the direction of the displacement of a small volume element within the reflected wave compared to its displacement in the incident wave. Depending on this direction of the displacement either the vertical or the horizontal component of the reflected wave experiences a phase jump π with respect to the incident wave. In this section these phase jumps between the respective components of the incident and the reflected waves are discussed.
For the P-P[17] reflection coefficients given in the previous sections the following sign conversion is used (as in [56]): If the scalar product of wave vector $\vec{k}$ and displacement vector has the same sign for the incident wave (directly before the reflection) and for the reflected one (directly after the reflection) the reflection coefficients are positive. This corresponds to the displacement of reflected and incident wave being either both in propagation direction of the respective wave or both in the opposite direction. Thus, the

[17] This is a common nomenclature in seismology e.g. in [56]. It refers to the wave types of incident wave (first letter) and reflected/transmitted wave (second letter).

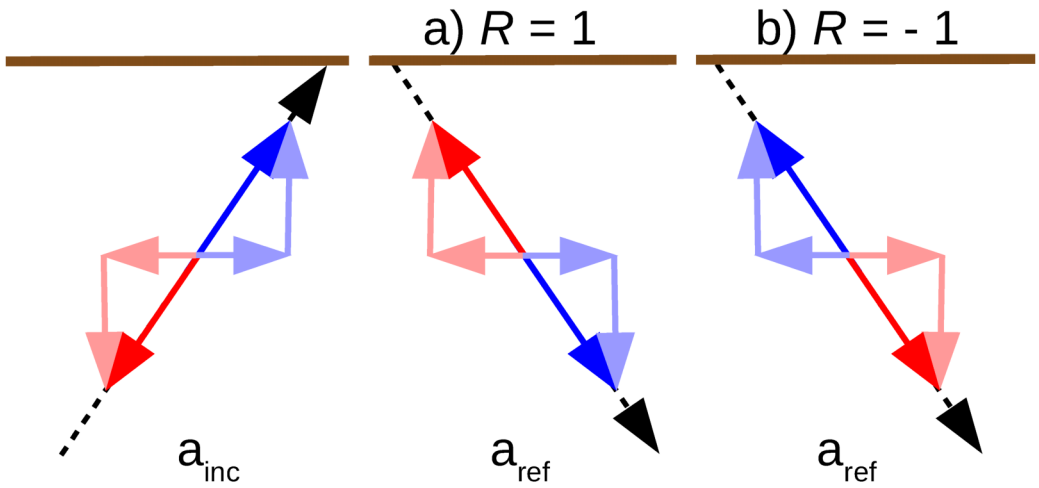

Figure 2.3: Direction of the displacement (and the respective horizontal and vertical components) of a wave before and after reflection at a boundary for the two cases: The horizontal component experiences no phase jump for $R > 0$ (here $R = 1$) or a phase jump of π for $R < 0$ (here $R = -1$). The directions of propagation of the waves are indicated by dashed black arrows. The direction of the displacement before hitting the boundary is indicated by a blue arrow (for the displacement being in direction of propagation of the wave) and red (displacement in the opposite direction). The light blue and light red arrows show the respective horizontal and vertical components of the displacement.

horizontal component of the displacement has the same phase in the incident and the reflected wave, while the vertical component experiences a phase jump of π. In Fig. 2.3 the respective displacement components are sketched (without loss of generality for an upwards-propagating wave) in case a) for $R = 1$.
On the other hand, a negative reflection coefficient indicates a π phase jump of the horizontal displacement component and none of the vertical one. This corresponds to the displacement vectors of incident and reflected wave pointing in opposite directions with respect to the respective wave vectors. This is sketched in Fig. 2.3 in case b) for $R = -1$.

The directions of the displacement components and the resulting phase jumps are illustrated in Table 2.1.
In the used model of the soil (see Fig. 2.2 in Section 2.2) two horizontally aligned boundaries are of interest for the reflection of waves: The first one is the free surface and the second one is the underground boundary between the two soil layers of different elastic properties. For the recorded range of angles of incidence at the former, the P-P reflection coefficient is always negative ($R^{\mathrm{s}}_{\mathrm{PP}} < 0$) and at the latter it is always positive ($R_{\mathrm{PP}} > 0$). With the vertical-component geophones only the vertical component of the soil velocity is recorded. Thus, only the phase jumps of that component $\Delta\phi_{\perp}$ are of interest which are given in the last column of Table 2.1. Therefore, upon reflection of a P wave at the underground boundary a phase jump of π needs to be taken into account. For reflection

	$a_{\text{inc},\parallel}$	$a_{\text{inc},\perp}$	$a_{\text{ref},\parallel}$	$a_{\text{ref},\perp}$	$\Delta\phi_\parallel$	$\Delta\phi_\perp$	
$R > 0$	$\rightarrow$ $\leftarrow$	$\uparrow$ $\downarrow$	$\rightarrow$ $\leftarrow$	$\downarrow$ $\uparrow$	0	π	} underground boundary
$R < 0$	$\rightarrow$ $\leftarrow$	$\uparrow$ $\downarrow$	$\leftarrow$ $\rightarrow$	$\uparrow$ $\downarrow$	π	0	} free surface

Table 2.1: Illustration of the direction of the horizontal and vertical displacement components of incident and reflected waves as well as the corresponding phase jumps for $R > 0$ and $R < 0$. For the presented measurements the former case corresponds to the boundary between the two soil layers, i.e. the underground boundary. Here for each reflection a phase jump of π needs to be taken into account, since the vertical components of the soil velocity are of interest. The case $R < 0$ corresponds to the free surface where no phase jump of the vertical components arises.

of a P wave at the free surface no phase jump arises. And consequently, there is either a phase shift of π or of 0, but of no other value.
In the simple case of perpendicular incidence this can be understood in analogy to acoustics using the impedance Z, defined as the product of wave velocity and density $Z = v \cdot \rho$. Then, the reflection coefficient[18] is defined as

$$R = \frac{Z_2 - Z_1}{Z_2 + Z_1}, \tag{2.41}$$

where the indices refer to the properties of the media before and behind the boundary [53]. A wave impinging on a boundary from a medium of lower impedance towards one of higher impedance ($R > 0$) will experience a phase jump of π upon reflection. This is clearly the case for the underground boundary: Wave velocity and density in the first medium (i.e. the upper soil layer) are smaller than those in the second medium (i.e. the lower soil layer) and thus $Z_2 > Z_1$. If the first medium has the higher impedance (i.e. $R < 0$) the incident and the reflected wave have the same phase at the boundary. This is the case for the reflection of upwards-propagating seismic waves at the free surface where $Z_2 = 0$. If no conversion of waves (i.e. from P to S waves or vice versa) takes place at the boundary Eq. (2.41) can be generalised:

$$R = \frac{Z_2 \cos(\kappa_{\text{trans}}) - Z_1 \cos(\kappa_{\text{ref}})}{Z_2 \cos(\kappa_{\text{trans}}) + Z_1 \cos(\kappa_{\text{ref}})}. \tag{2.42}$$

Here κ_{ref} is the angle of the reflected wave in medium 1 which equals the angle of incidence if no conversion of the wave type occurs. κ_{trans} is the corresponding angle of the wave transmitted into the second medium.
However, generally only for the reflection of SH waves no wave-type conversion occurs

[18] Note that there are different definitions of the reflection coefficient in literature, depending on whether it refers to the amplitude ratio or the intensity ratio of reflected and incident wave. Throughout this work I use the former definition. Using the latter one would result in the square of Eq. (2.41).

[52]. Thus, for reflection of P and SV waves Eq. (2.42) does not hold but the equations derived in Section 2.2.2 and Section 2.2.3 have to by applied.

The phase jumps of the vertical component of the displacement developed in this section refer to P-P reflection only. For the sake of completeness the respective phase jumps $\Delta\phi_\perp$ for all possible reflections are given in Table 2.2, following [56].

	P-P	P-S	S-P	S-S
$R_{ij} > 0$	π	0	0	π
$R_{ij} < 0$	0	π	π	0

Table 2.2: Values of the phase jump $\Delta\phi_\perp$ of the vertical displacement components for reflection of seismic waves at a boundary. The columns state the four possible types of the reflection and the two rows refer to the respective reflection coefficients being either positive or negative. The column of the P-P reflection refers to the case discussed for the vertical and horizontal components above (see Fig. 2.3 and Table 2.1).

On the one hand, if the wave type is conserved upon reflection (i.e. P-P reflection or S-S reflection) a phase jump of $\Delta\phi_\perp = \pi$ between the vertical components of incident and reflected wave is observed for $R > 0$. For $R < 0$ follows $\Delta\phi_\perp = 0$. On the other hand, if the wave type changes upon reflection (i.e. P-S reflection or S-P reflection) the opposite is the case: For $R > 0$ no phase jump is observed between the vertical displacement components while for $R < 0$ the phase jump is $\Delta\phi_\perp = \pi$.

Similar considerations can be made concerning the transmission coefficients (given in Eq. (2.40)) of the acoustic wave exciting P and SV waves at the surface of the soil. When calculating their values (see Section 4.3.4) one finds $T_\mathrm{P}^\mathrm{s} > 0$ and $T_\mathrm{S}^\mathrm{s} < 0$ in the whole investigated range of angles of incidence α. Thus, no phase jump between the vertical components of the incident acoustic and the two transmitted seismic waves arises (see bold entries in Table 2.3). Therefore, also no phase jump between the directly acoustically excited P and SV waves needs to be taken into account.

	P	S
$T_i^\mathrm{s} > 0$	**0**	π
$T_i^\mathrm{s} < 0$	π	**0**

Table 2.3: Values of the phase jump $\Delta\phi_\perp$ of the vertical displacement components for the transmitted P and SV wave at the soil surface, with respect to the incident acoustic wave. The columns state the type of the excited seismic wave and the rows refer to the respective transmission coefficients being either positive or negative. The two bold entries refer to the situations for no phase jump, which is found for the calculated values in Section 4.3.4.

2.3 Wave interference in a layered medium between infinite half-spaces

In the model introduced in Section 2.2 (see e.g. Fig. 2.2) the air above the ground represents one half-space. The ground is described as an upper soil layer of thickness d over an infinite half-space. A plane acoustic wave impinges on the ground with incidence angle α. When it hits the surface seismic P and SV waves are excited in a large area. These waves have a phase difference with respect to each other depending on α and on the lateral distance between their points of excitation. They propagate in the ground and are reflected at both boundaries of the upper soil layer. With seismic sensors mounted at various depths z_S within the upper soil layer ($0\ \mathrm{m} \leq z_\mathrm{S} \leq d$) the soil velocity is recorded. The recordings correspond to the spectral amplitude distribution a_tot caused by interfering seismic waves which were acoustically excited at various locations.
Here several models are introduced to explain the recorded interference patterns: Firstly, in Section 2.3.1 the three P waves which contribute strongest to the seismic signal are identified and their interference is described. In Section 2.3.2 the quasi-infinite number of P waves reflected multiple times within the upper soil layer are taken into account. This model is advanced by introducing frequency-dependent absorption in Section 2.3.3. For a comprehensive picture, in Section 2.3.4 the contributions of waves generated by conversion of P to SV waves and vice versa are described.
Throughout this work I will make use of a intuitive nomenclature for seismic waves often used in seismology (e.g. in [56]): A wave A_i reflected multiple times is indexed by a sequence indicating the wave types and the directions of propagation. Initially, the seismic wave is acoustically created at the surface either as P wave or as SV wave and propagates from there downwards. This is denoted as $A_{\grave{\mathrm{P}}}$ or $A_{\grave{\mathrm{S}}}$, respectively. The grave accent indicates a downwards-propagating wave – according to the assumption made in Section 2.2 that the horizontal component of the wave is in positive x-direction (see Fig. 2.2). When hitting the underground boundary generally a P and an SV wave are reflected which propagates upwards – indicated by the respective subsequent index $\acute{\mathrm{P}}$ or $\acute{\mathrm{S}}$. With each additional reflection at either the surface or the underground boundary another index stating wave type and propagation direction is added to the indices of the name of the wave. Thus, when the wave finally reaches the point of investigation (i.e. the sensor) the sequence of indices indicates the number of times the wave was reflected within the upper soil layer. It also states the wave types and its changes during the propagation through the soil. Furthermore, it tells whether the wave reaches the sensor propagating upwards or downwards.
The full characterisation of a wave A_i is given by

$$A_i = a_i \cdot \mathrm{e}^{\mathrm{i}(\vec{k}\vec{r} - \omega t + \phi_i)}. \tag{2.43}$$

a_i is the amplitude of the wave and ϕ_i its phase. Thus, using the introduced nomenclature, the directly acoustically excited P wave is

$$A_{\grave{\mathrm{P}}} = a_{\grave{\mathrm{P}}} \cdot \mathrm{e}^{\mathrm{i}(\vec{k}\vec{r} - \omega t + \phi_{\grave{\mathrm{P}}})}. \tag{2.44}$$

This wave is used as reference, i.e. its amplitude is taken to be $a_{\grave{\mathrm{P}}} \equiv 1$ and its phase to be $\phi_{\grave{\mathrm{P}}} \equiv 0$. The amplitude of any other wave A_i is given relatively to $a_{\grave{\mathrm{P}}}$ as the product of the respective reflection coefficients. The phase of A_i is obtained from the geometrically determined path differences between the waves A_i and $A_{\grave{\mathrm{P}}}$ using the respective wave velocity for each part of the distance A_i covered in the soil. This is demonstrated exemplarily for the wave $A_{\grave{\mathrm{S}}\acute{\mathrm{P}}} = a_{\grave{\mathrm{S}}\acute{\mathrm{P}}} \cdot \mathrm{e}^{\mathrm{i}(\vec{k}\vec{r} - \omega t + \phi_{\grave{\mathrm{S}}\acute{\mathrm{P}}})}$ (which is acoustically excited as an SV wave, is converted into a P wave upon reflection at the underground boundary and reaches the sensor propagating upwards) in Appendix A.1.
Throughout this work the waves are investigated at fixed locations (i.e. the locations of the sensors in depth z_{S}), thus the term $\vec{k}\vec{r}$ is generally neglected in the expression of the wave (e.g. Eq. (2.43)). The measurand of interest is the spectral amplitude distribution a_{tot} as the result of the interference between several waves A_i. It is independent on the time as shown in Appendix A.2 and thus is determined by the amplitudes of the seismic waves and the phase differences between each pair of them. The phase differences depend on the frequency f and so does $a_{\mathrm{tot}} = a_{\mathrm{tot}}(f)$.

2.3.1 Model of three-wave interference

In this model[19] of wave propagation in the soil (sketched in Fig. 2.4) interference between the three waves with the largest amplitudes is investigated. These are the following waves:

- The wave $A_{\grave{\mathrm{P}}}$ is excited at point D directly by the acoustic wave and reaches the sensor propagating downwards. The wave is described at the location of the sensor by $A_{\grave{\mathrm{P}}} = a_{\grave{\mathrm{P}}} \cdot \mathrm{e}^{\mathrm{i}(\omega t + \phi_{\grave{\mathrm{P}}})}$ (without loss of generality its phase is set $\phi_{\grave{\mathrm{P}}} = 0$).

- The wave $A_{\grave{\mathrm{P}}\acute{\mathrm{P}}}$ was acoustically excited at point C, has propagated into the ground and was reflected at point G which is located at the boundary in depth d. It reaches the sensor propagating upwards and is described by $A_{\grave{\mathrm{P}}\acute{\mathrm{P}}} = a_{\grave{\mathrm{P}}\acute{\mathrm{P}}} \cdot \mathrm{e}^{\mathrm{i}(\omega t + \phi_{\grave{\mathrm{P}}\acute{\mathrm{P}}})}$.

- The wave $A_{\grave{\mathrm{P}}\acute{\mathrm{P}}\grave{\mathrm{P}}}$ was acoustically excited at point B, has propagated into the ground to be reflected at point F in depth d, has propagated upwards to the surface and was reflected a second time at D. It reaches the sensor propagating downwards again and is described by $A_{\grave{\mathrm{P}}\acute{\mathrm{P}}\grave{\mathrm{P}}} = a_{\grave{\mathrm{P}}\acute{\mathrm{P}}\grave{\mathrm{P}}} \cdot \mathrm{e}^{\mathrm{i}(\omega t + \phi_{\grave{\mathrm{P}}\acute{\mathrm{P}}\grave{\mathrm{P}}})}$.

[19] This model was first introduced in [57] using a different nomenclature for the waves. For the sake of consistency throughout this work I will refer to the waves using their type and direction of all parts of their propagation path as introduced in Section 2.3.

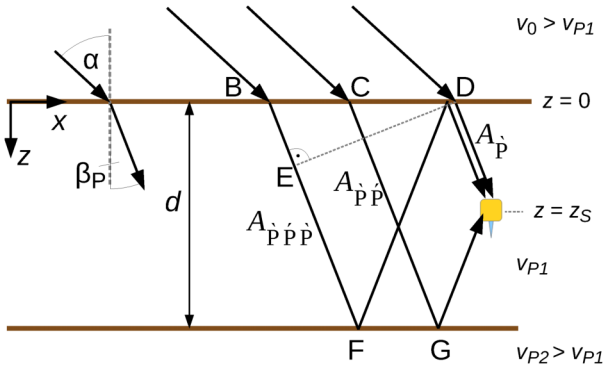

Figure 2.4: Sketch of the acoustically induced P waves propagating within the upper soil layer. The wave $A_{\grave{\mathrm{P}}}$ (excited at point D) reaches the sensor in depth z_S directly. The wave $A_{\grave{\mathrm{P}}\acute{\mathrm{P}}}$ (excited at point C) is reflected at the underground boundary (at point G) in depth d before reaching the sensor propagating upwards. Finally, the wave $A_{\grave{\mathrm{P}}\acute{\mathrm{P}}\grave{\mathrm{P}}}$ (excited at point B) is reflected both at the underground boundary (at point F) and at the free surface (at point D). It reaches the sensor propagating parallelly to $A_{\grave{\mathrm{P}}}$.

As sketched in Fig. 2.4, all seismic waves are excited at the soil surface (at $z = 0$) by the incident, plane acoustic wave. Refraction at the boundary between air and soil changes the angle from α to β_P. Because in the discussed case the wave speed in the upper soil $v_{\mathrm{P}1}$ is lower than the speed of sound v_0, the wave direction is refracted toward the normal. When the acoustic wave arrives at point D, the wavefront of the seismic wave excited at point B reaches point E. Thus, the path difference between both waves is the distance $\Delta x_{\grave{\mathrm{P}},\grave{\mathrm{P}}\acute{\mathrm{P}}\grave{\mathrm{P}}} = \overline{EF} + \overline{FD}$, which can be calculated geometrically using the propagation velocities of the acoustic and seismic waves v_0 and $v_{\mathrm{P}1}$, respectively, for a given angle α and a depth d.

The path differences Δx_{ij} between each pair of the seismic waves are given by

$$\begin{aligned}
\Delta x_{\grave{\mathrm{P}},\grave{\mathrm{P}}\acute{\mathrm{P}}} &= 2(d - z_\mathrm{S})\sqrt{1 - \left(\frac{v_{\mathrm{P}1}}{v_0}\right)^2 \sin^2(\alpha)}, \\
\Delta x_{\grave{\mathrm{P}},\grave{\mathrm{P}}\acute{\mathrm{P}}\grave{\mathrm{P}}} &= 2d\sqrt{1 - \left(\frac{v_{\mathrm{P}1}}{v_0}\right)^2 \sin^2(\alpha)}, \\
\Delta x_{\grave{\mathrm{P}}\acute{\mathrm{P}},\grave{\mathrm{P}}\acute{\mathrm{P}}\grave{\mathrm{P}}} &= \Delta x_{\grave{\mathrm{P}},\grave{\mathrm{P}}\acute{\mathrm{P}}\grave{\mathrm{P}}} - \Delta x_{\grave{\mathrm{P}},\grave{\mathrm{P}}\acute{\mathrm{P}}} = 2z_\mathrm{S}\sqrt{1 - \left(\frac{v_{\mathrm{P}1}}{v_0}\right)^2 \sin^2(\alpha)}.
\end{aligned} \tag{2.45}$$

[20]

A detailed derivation of the geometrically determined path differences can be found in Appendix A.1.

The resulting phase differences $\Delta\phi_{ij} = \phi_i - \phi_j$ are obtained from Eq. (2.24) using the path differences given in Eq. (2.45), a certain frequency f and the wave velocity $v_{\mathrm{P}1}$. Hence,

[20] Using Eq. (2.29) and the relation $\cos(\beta_\mathrm{P}) = \sqrt{1 - \sin^2(\beta_\mathrm{P})}$ it is easy to see that the expressions of the square roots in Eq. (2.45) are equal to $\cos(\beta_\mathrm{P})$. However, to express all equations as a function of the acoustic angle of incidence α (instead of the seismic angles β_P) I will use the terms as given here.

they are given by

$$\begin{aligned}
\Delta\phi_{\grave{\mathrm{P}},\grave{\mathrm{P}}\acute{\mathrm{P}}} &= \frac{1}{v_{\mathrm{P1}}} 4\pi f \cdot (d - z_{\mathrm{S}}) \sqrt{1 - \left(\frac{v_{\mathrm{P1}}}{v_0}\right)^2 \sin^2(\alpha)} + \pi, \\
\Delta\phi_{\grave{\mathrm{P}},\grave{\mathrm{P}}\acute{\mathrm{P}}\grave{\mathrm{P}}} &= \frac{1}{v_{\mathrm{P1}}} 4\pi f \cdot d \sqrt{1 - \left(\frac{v_{\mathrm{P1}}}{v_0}\right)^2 \sin^2(\alpha)} + \pi, \\
\Delta\phi_{\grave{\mathrm{P}}\acute{\mathrm{P}},\grave{\mathrm{P}}\acute{\mathrm{P}}\grave{\mathrm{P}}} &= \Delta\phi_{\grave{\mathrm{P}},\grave{\mathrm{P}}\acute{\mathrm{P}}\grave{\mathrm{P}}} - \Delta\phi_{\grave{\mathrm{P}},\grave{\mathrm{P}}\acute{\mathrm{P}}} = \frac{1}{v_{\mathrm{P1}}} 4\pi f \cdot z_{\mathrm{S}} \sqrt{1 - \left(\frac{v_{\mathrm{P1}}}{v_0}\right)^2 \sin^2(\alpha)}.
\end{aligned} \tag{2.46}$$

The given phase differences take into account a phase jump of π (as discussed in Section 2.2.5) that occurs upon reflection at the boundary in depth d, experienced by the waves $A_{\grave{\mathrm{P}}\acute{\mathrm{P}}}$ and $A_{\grave{\mathrm{P}}\acute{\mathrm{P}}\grave{\mathrm{P}}}$. Thus, the phase jump needs to be considered for $\Delta\phi_{\grave{\mathrm{P}},\grave{\mathrm{P}}\acute{\mathrm{P}}}$ and $\Delta\phi_{\grave{\mathrm{P}},\grave{\mathrm{P}}\acute{\mathrm{P}}\grave{\mathrm{P}}}$, but cancels out for $\Delta\phi_{\grave{\mathrm{P}}\acute{\mathrm{P}},\grave{\mathrm{P}}\acute{\mathrm{P}}\grave{\mathrm{P}}}$.
The resulting signal at the sensor has a time-independent sum amplitude a_{tot} which is derived from the phase-corrected summation of the three waves, given by:

$$\begin{aligned}
a_{\mathrm{tot}} &= \sqrt{|(A_{\grave{\mathrm{P}}} + A_{\grave{\mathrm{P}}\acute{\mathrm{P}}} + A_{\grave{\mathrm{P}}\acute{\mathrm{P}}\grave{\mathrm{P}}})|^2} \\
&= \Big[{a_{\grave{\mathrm{P}}}}^2 + {a_{\grave{\mathrm{P}}\acute{\mathrm{P}}}}^2 + {a_{\grave{\mathrm{P}}\acute{\mathrm{P}}\grave{\mathrm{P}}}}^2 + 2a_{\grave{\mathrm{P}}} a_{\grave{\mathrm{P}}\acute{\mathrm{P}}} \cos(\phi_{\grave{\mathrm{P}},\grave{\mathrm{P}}\acute{\mathrm{P}}}) + 2a_{\grave{\mathrm{P}}} a_{\grave{\mathrm{P}}\acute{\mathrm{P}}\grave{\mathrm{P}}} \cos(\phi_{\grave{\mathrm{P}},\grave{\mathrm{P}}\acute{\mathrm{P}}\grave{\mathrm{P}}}) \\
&\quad + 2a_{\grave{\mathrm{P}}\acute{\mathrm{P}}} a_{\grave{\mathrm{P}}\acute{\mathrm{P}}\grave{\mathrm{P}}} \cos(\phi_{\grave{\mathrm{P}}\acute{\mathrm{P}},\grave{\mathrm{P}}\acute{\mathrm{P}}\grave{\mathrm{P}}}) \Big]^{1/2}.
\end{aligned} \tag{2.47}$$

A detailed derivation of Eq. (2.47) is given in Appendix A.2 together with the more general equation for any number of interfering waves.

Special case: Sensor at the surface ($z_{\mathrm{S}} = 0\,\mathrm{m}$):
In the special case of a sensor placed at the surface ($z_{\mathrm{S}} = 0\,\mathrm{m}$) the propagation paths of the waves $A_{\grave{\mathrm{P}}\acute{\mathrm{P}}}$ and $A_{\grave{\mathrm{P}}\acute{\mathrm{P}}\grave{\mathrm{P}}}$ coincide, thus the phase difference $\Delta\phi_{\grave{\mathrm{P}}\acute{\mathrm{P}},\grave{\mathrm{P}}\acute{\mathrm{P}}\grave{\mathrm{P}}}$ vanishes. The problem is reduced to interference of the two waves $A_{\grave{\mathrm{P}}} = a_{\grave{\mathrm{P}}} \cdot \mathrm{e}^{\mathrm{i}\omega t}$ and $A'_{\grave{\mathrm{P}}\acute{\mathrm{P}}} = (a_{\grave{\mathrm{P}}\acute{\mathrm{P}}} + a_{\grave{\mathrm{P}}\acute{\mathrm{P}}\grave{\mathrm{P}}}) \cdot \mathrm{e}^{\mathrm{i}(\omega t + \phi_{\grave{\mathrm{P}}\acute{\mathrm{P}}})}$. The equation for the sum amplitude is reduced to:

$$a_{\mathrm{tot},z_{\mathrm{S}}=0} = \sqrt{{a_{\grave{\mathrm{P}}}}^2 + (a_{\grave{\mathrm{P}}\acute{\mathrm{P}}} + a_{\grave{\mathrm{P}}\acute{\mathrm{P}}\grave{\mathrm{P}}})^2 + 2a_{\grave{\mathrm{P}}}(a_{\grave{\mathrm{P}}\acute{\mathrm{P}}} + a_{\grave{\mathrm{P}}\acute{\mathrm{P}}\grave{\mathrm{P}}}) \cos(\phi_{\grave{\mathrm{P}}\acute{\mathrm{P}}})}. \tag{2.48}$$

Constructive interference occurs for frequencies at which the path difference between the reflected wave and the direct wave is equal to an integer multiple k of the wavelength. Only in the case of $z_{\mathrm{S}} = 0\,\mathrm{m}$ an analytic expression for the frequencies of constructive interference can be derived using the law of refraction Eq. (2.29):

$$f^{\mathrm{theo,surface}}_{\mathrm{max},k}(\alpha) = \frac{(k + 1/2) v_{\mathrm{P1}}}{2d \sqrt{1 - \sin^2(\alpha) \cdot (v_{\mathrm{P1}}/v_0)^2}}. \tag{2.49}$$

The integer k (with $k \geq 0$) is the order of the constructive interference. The summand $1/2$ originates from the phase jump of π of the vertical component of the seismic waves

when reflected at the boundary to the second layer with a higher impedance. Eq. (2.49) can be applied to destructive interference by replacing the term $(k+1/2)$ by $(k+1)$.

Since seismic waves generally experience a frequency-dependent absorption in the soil an estimate of the absorption is introduced in Section 2.3.3.

2.3.2 Model of a quasi-infinite number of interfering waves

The approach introduced in Section 2.3.1 does not take into account waves reflected multiple times at the boundaries of the first soil layer. However, these waves can contribute significantly to the recorded signals (as will be shown in Section 4.3). Thus, here the equations for the amplitude distribution of multiply reflected, interfering waves are derived. Since main contributions are only expected from P waves (see Section 4.3), in this section only P-P wave reflection is considered. Of the reflection coefficients introduced in Section 2.2 those at the underground boundary and at the free surface are needed. For convenience, I will refer to the one at the underground boundary as R ($R \equiv R_{\mathrm{PP}}$ in Eq. (2.32)) and to the one at the free surface as R^{s} ($R^{\mathrm{s}} \equiv R^{\mathrm{s}}_{\mathrm{PP}}$ in Eq. (2.36)).
Each additional reflection at one of the boundaries reduces the amplitude of the waves arriving at the sensor, either by the factor R or R^{s}. Furthermore, each reflection at the underground boundary results in a phase jump of π of the vertical component of the waves (see Section 2.2.5). Obviously, each pair of reflections increases the horizontal distance between sensor and location of coupling of the acoustic wave into the ground. Therefore, a quasi-infinite number of waves interfere at the sensor that contribute with decreasing amplitude (for increasing horizontal distance of coupling to the ground from the sensor) to the recorded signal. This can be treated in analogy to optics where multiple reflections can occur between two parallel, narrow mirrors e.g. to form a Fabry-Pérot resonator [58]. However, in the present case the sensor is placed between the reflecting boundaries, thus waves propagating in both directions (i.e. down- and upwards) need to be taken into account.
The upwards- and downwards propagating waves, respectively, can be treated as separate sets of waves. The first element in the set of downwards-propagating waves is the direct wave $A_{\grave{\mathrm{P}}}$; the first element in the set of upwards-propagating waves is the wave $A_{\grave{\mathrm{P}}\acute{\mathrm{P}}}$. With respect to the first element, the second elements of both sets each have to cover the additional path, referred to as $\Delta x_{\grave{\mathrm{P}},\grave{\mathrm{P}}\acute{\mathrm{P}}\grave{\mathrm{P}}}$ in Eq. (2.45), of

$$\Delta x = 2d\sqrt{1-\left(\frac{v_{\mathrm{P1}}}{v_0}\right)^2\sin^2(\alpha)}. \tag{2.50}$$

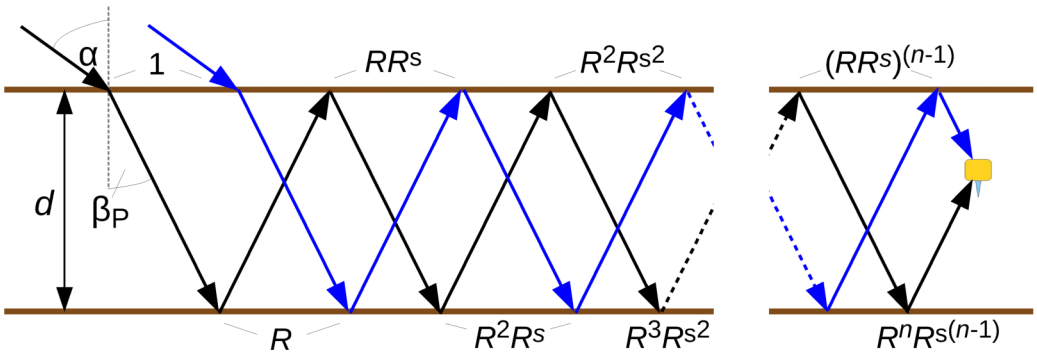

Figure 2.5: Waves reflected multiple times in the first soil layer: Those that reach the sensor propagating downwards are shown in blue; those reaching it propagating upwards are shown in black. The amplitude is reduced by the factor R upon each reflection at the underground boundary and by the factor R^{s} upon each reflection at the free surface. The resulting amplitude is given as the product of the respective reflection coefficients as indicated at each point of reflection. Additionally, each reflection at the underground boundary results in a phase jump of π of the vertical component of the reflected wave.

It results in the phase difference between both waves ($\Delta\phi_{\grave{\mathrm{P}},\grave{\mathrm{P}}\acute{\mathrm{P}}\grave{\mathrm{P}}}$ in Eq. (2.46)) of

$$\Delta\phi = \frac{2\pi f \Delta x}{v_{\mathrm{P1}}} = \frac{1}{v_{\mathrm{P1}}} 4\pi f \cdot d \sqrt{1 - \left(\frac{v_{\mathrm{P1}}}{v_0}\right)^2 \sin^2(\alpha)}. \tag{2.51}$$

The $n-th$ elements of both sets are additionally reflected n times (with respect to the respective first element) both at the underground boundary and at the free surface. This reduces their amplitudes by the factor $(R \cdot R^{\mathrm{s}})^n$. Furthermore, the n-th waves have to cover the additional path inside the first soil layer $\Delta x_n = n \cdot \Delta x$ and thus the resulting phase difference between the first and the n-th element is given by $\Delta\phi_n = n \cdot \Delta\phi$. This is sketched in Fig. 2.5. The n phase jumps of π of the vertical component, resulting from the n reflections at the underground boundary, will be taken into account separately (see Eq. (2.54) and the following).
The path difference between corresponding elements of both sets, e.g. between $A_{\grave{\mathrm{P}}}$ for the downwards- and $A_{\grave{\mathrm{P}}\acute{\mathrm{P}}}$ for the upwards-propagating one ($\Delta x_{\grave{\mathrm{P}},\grave{\mathrm{P}}\acute{\mathrm{P}}}$ in Eq. (2.45)), is

$$\delta x = 2(d - z_{\mathrm{S}}) \sqrt{1 - \left(\frac{v_{\mathrm{P1}}}{v_0}\right)^2 \sin^2(\alpha)}. \tag{2.52}$$

The resulting phase difference ($\Delta\phi_{\grave{\mathrm{P}},\grave{\mathrm{P}}\acute{\mathrm{P}}}$ in Eq. (2.46)) is:

$$\delta\phi = \frac{1}{v_{\mathrm{P1}}} 4\pi f \cdot (d - z_{\mathrm{S}}) \sqrt{1 - \left(\frac{v_{\mathrm{P1}}}{v_0}\right)^2 \sin^2(\alpha)}. \tag{2.53}$$

In Table 2.4 the amplitudes (relative to that of the direct wave $A_{\grave{\mathrm{P}}}$: $a_{\grave{\mathrm{P}}} = 1$), the number of π phase jumps and the resulting phase difference with respect to $A_{\grave{\mathrm{P}}}$ are summarised for the elements of both sets. To improve readability for a P wave propagating n times consecutively downwards and upwards within the upper soil layer the subscript $n\cdot(\grave{\mathrm{P}}\acute{\mathrm{P}})$ is used. Correspondingly, the wave being reflected once more at the free surface after already being reflected n times at both boundaries is referred to as $A_{n\cdot(\grave{\mathrm{P}}\acute{\mathrm{P}})\grave{\mathrm{P}}}$.

A_n	relative amplitude	path difference	π phase jumps	resulting phase difference
$A_{\grave{\mathrm{P}}}$	1	0	0	0
$A_{\grave{\mathrm{P}}\acute{\mathrm{P}}\grave{\mathrm{P}}}$	RR^{s}	Δx	1	$\Delta\phi+\pi$
$A_{2\cdot(\grave{\mathrm{P}}\acute{\mathrm{P}})\grave{\mathrm{P}}}$	$(RR^{\mathrm{s}})^2$	$2\Delta x$	2	$2\Delta\phi$
$A_{3\cdot(\grave{\mathrm{P}}\acute{\mathrm{P}})\grave{\mathrm{P}}}$	$(RR^{\mathrm{s}})^3$	$3\Delta x$	3	$3\Delta\phi+\pi$
		...		
$A_{n\cdot(\grave{\mathrm{P}}\acute{\mathrm{P}})\grave{\mathrm{P}}}$	$(RR^{\mathrm{s}})^n$	$n\Delta x$	n	$n\Delta\phi+n\cdot\pi$
$A_{\grave{\mathrm{P}}\acute{\mathrm{P}}}$	R	δx	1	$\delta\phi+\pi$
$A_{2\cdot(\grave{\mathrm{P}}\acute{\mathrm{P}})}$	$R(RR^{\mathrm{s}})$	$\Delta x+\delta x$	2	$\Delta\phi+\delta\phi$
$A_{3\cdot(\grave{\mathrm{P}}\acute{\mathrm{P}})}$	$R(RR^{\mathrm{s}})^2$	$2\Delta x+\delta x$	3	$2\Delta\phi+\delta\phi+\pi$
$A_{4\cdot(\grave{\mathrm{P}}\acute{\mathrm{P}})}$	$R(RR^{\mathrm{s}})^3$	$3\Delta x+\delta x$	4	$3\Delta\phi+\delta\phi$
		...		
$A_{n\cdot(\grave{\mathrm{P}}\acute{\mathrm{P}})}$	$R(RR^{\mathrm{s}})^{n-1}$	$(n-1)\Delta x+\delta x$	n	$(n-1)\Delta\phi+\delta\phi+n\cdot\pi$

Table 2.4: Waves reflected n times within the upper soil layer: The upper half of the table refers to the set of waves, reaching the sensor propagating downwards, and the lower half to those, propagating upwards (as indicated by the sequences of indices). The second column gives the relative amplitudes with respect to the direct wave $A_{\grave{\mathrm{P}}}$ using the notation $R \equiv R_{\mathrm{PP}}$ and $R^{\mathrm{s}} \equiv R^{\mathrm{s}}_{\mathrm{PP}}$. The third column states the path difference between the waves $A_{\grave{\mathrm{P}}}$ and A_n. In the fourth column the number of π phase jumps of the vertical component is given which cancels out for even numbers. The fifth column shows the resulting phase difference between the waves $A_{\grave{\mathrm{P}}}$ and A_n.

Taking a look at the resulting sum of waves arriving at a sensor using the contributions from Table 2.4 (again $a_{\grave{\mathrm{P}}} = 1$ is used) one finds:

$$
\begin{aligned}
A_{\mathrm{tot}} = \\
\mathrm{e}^{\mathrm{i}\omega t}\Big[&1 + RR^{\mathrm{s}}\mathrm{e}^{\mathrm{i}\Delta\phi}\mathrm{e}^{\mathrm{i}\pi} + R^2R^{\mathrm{s}2}\mathrm{e}^{\mathrm{i}2\Delta\phi}\mathrm{e}^{\mathrm{i}2\pi} + R^3R^{\mathrm{s}3}\mathrm{e}^{\mathrm{i}3\Delta\phi}\mathrm{e}^{\mathrm{i}3\pi} + \ ... \\
&+ R\mathrm{e}^{\mathrm{i}\delta\phi}\mathrm{e}^{\mathrm{i}\pi} + R^2R^{\mathrm{s}}\mathrm{e}^{\mathrm{i}\delta\phi}\mathrm{e}^{\mathrm{i}\Delta\phi}\mathrm{e}^{\mathrm{i}2\pi} + R^3R^{\mathrm{s}2}\mathrm{e}^{\mathrm{i}\delta\phi}\mathrm{e}^{\mathrm{i}2\Delta\phi}\mathrm{e}^{\mathrm{i}3\pi} + R^4R^{\mathrm{s}3}\mathrm{e}^{\mathrm{i}\delta\phi}\mathrm{e}^{\mathrm{i}3\Delta\phi}\mathrm{e}^{\mathrm{i}4\pi} + \ ...\Big].
\end{aligned}
\tag{2.54}
$$

The equality $e^{in\pi} = (-1)^n$ leads to alternating signs of consecutive summands in Eq. (2.54):

$$\begin{aligned} A_{\text{tot}} = e^{i\omega t}\Big[&\left(1 - RR^{s}e^{i\Delta\phi} + R^2R^{s2}e^{i2\Delta\phi} - R^3R^{s3}e^{i3\Delta\phi} + \ ...\right) \\ &- Re^{i\delta\phi}\left(1 - RR^{s}e^{i\Delta\phi} + R^2R^{s2}e^{i2\Delta\phi} - R^3R^{s3}e^{i3\Delta\phi} + \ ...\right)\Big]. \end{aligned} \tag{2.55}$$

The first line corresponds to the waves reaching the sensor propagating downwards and the second line to the waves reaching it propagating upwards. The expressions in parentheses in both lines coincide. It can be noted, that it can be expressed using a geometric series of the form

$$\sum_{n=0}^{\infty} q^n = \frac{1}{1-q}, \tag{2.56}$$

converging for $|q| < 1$. Since for the product of the reflection coefficients holds $|RR^{s}| < 1$ and $|e^{ix}| = 1$ (for any real x), the condition of convergence is fulfilled with $q = -RR^{s}e^{i\Delta\phi}$. Thus, the resulting wave can be expressed as:

$$A_{\text{tot}} = (1 - Re^{i\delta\phi})e^{i\omega t}\sum_{n=0}^{\infty}\left(RR^{s}e^{i\Delta\phi}e^{i\pi}\right)^n = \frac{(1 - Re^{i\delta\phi})e^{i\omega t}}{1 + RR^{s}e^{i\Delta\phi}}. \tag{2.57}$$

The spectral amplitude distribution is now easily obtained as the square root of the multiplication with the complex conjugate:

$$a_{\text{tot}} = \sqrt{A_{\text{tot}} \cdot A_{\text{tot}}^{*}} = \sqrt{\frac{1 + R^2 - 2R\cos(\delta\phi)}{1 + R^2R^{s2} + 2RR^{s}\cos(\Delta\phi)}}. \tag{2.58}$$

For the case of a sensor placed at the surface ($z_{\text{S}} = 0$ m) the phase difference between the first element of the upwards-propagating set of waves and the second element of the downwards-propagating set (i.e. between $A_{\grave{\text{P}}\acute{\text{P}}}$ and $A_{\grave{\text{P}}\acute{\text{P}}\grave{\text{P}}}$) vanishes. The situation is sketched in Fig. 2.6 where the consecutive upwards- and downwards-propagating waves contribute to the signal recorded at the sensor. Hence, $\delta\phi$ (Eq. (2.53)) equals $\Delta\phi$ (Eq. (2.51)) and the resulting spectral amplitude distribution is given by:

$$a_{\text{tot}}(z_{\text{S}} = 0\,\text{m}) = \sqrt{A_{\text{tot}}(z_{\text{S}} = 0\,\text{m}) \cdot A_{\text{tot}}^{*}(z_{\text{S}} = 0\,\text{m})} = \sqrt{\frac{1 + R^2 - 2R\cos(\Delta\phi)}{1 + R^2R^{s2} + 2RR^{s}\cos(\Delta\phi)}}. \tag{2.59}$$

Even though the resulting interference amplitude clearly differs from that obtained with the model of three interfering P waves (see Section 2.3.1) in the special case of $z_{\text{S}} = 0$ m the frequencies of constructive interference (calculated with Eq. (2.49)) coincide for both models.

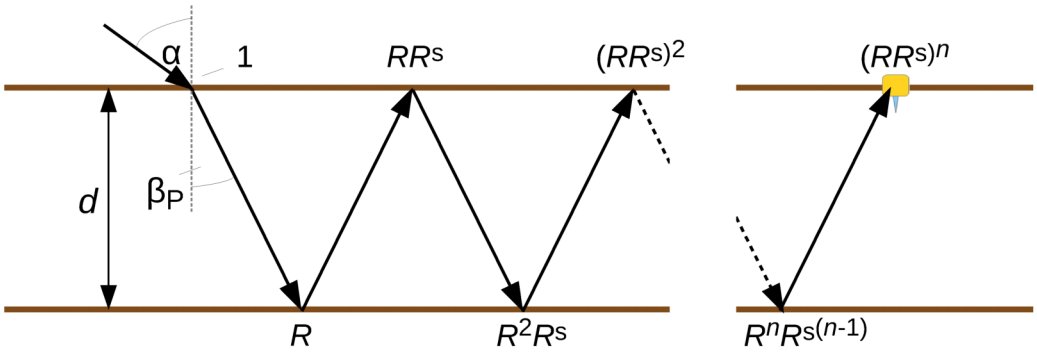

Figure 2.6: Wave reflected multiple times in the first soil layer for $z_S = 0\,\mathrm{m}$. The amplitude after each reflection is given as the product of the respective reflection coefficients as indicated at each point of reflection. Each reflection at the underground boundary results in a phase jump of π of the vertical component of the reflected wave. The signal recorded at the sensor consists of the sum of consecutive upwards- and downwards-propagating waves.

2.3.3 Influence of frequency-dependent absorption

The amplitude a of seismic waves also depends on absorption according to the distance r travelled in the soil:

$$a(r) = a_0 \mathrm{e}^{-\gamma r}. \tag{2.60}$$

Here γ[21] is the absorption coefficient and a_0 is the initial amplitude. Following [59], γ in first approximation is a linear function of the frequency f with the proportionality factor γ_1:

$$\gamma = \gamma_1 \cdot f. \tag{2.61}$$

Note that the distance to be taken into account here differs from Δx given in Eq. (2.50) and from δx given in Eq. (2.52), respectively. Eq. (2.50) and Eq. (2.52) both refer to path differences arising from wavefronts impinging on the ground at different locations taking into account the different propagation velocities in soil and air. Here the total slant distance covered inside the soil is required, i.e. also the amplitude of the direct wave is reduced for $z_S > 0$ m. This can be obtained using the slant distance a wave has to cover for one pair of reflections (at the underground boundary and the surface):

$$\partial x = \frac{2d}{\cos(\beta_P)} \tag{2.62}$$

multiplied by the value n of additional pairs of reflections and adding the respective distance the first waves of both sets $A_{\downarrow 1}$ and $A_{\uparrow 1}$ need to cover to reach the sensor. Thus,

[21] Throughout this work I use the letter γ for the absorption coefficient (often referred to as α in literature) to prevent confusion with α, used in this work as acoustic angle of incidence of the recorded signals.

for the n-th element in both sets one finds:

$$\partial x_{\downarrow,n} = \frac{2nd + z_S}{\cos(\beta_P)} = n\partial x + \frac{z_S}{\cos(\beta_P)} \quad \text{and} \quad \partial x_{\uparrow,n} = \frac{2d(n+1) - z_S}{\cos(\beta_P)} = n\partial x + \frac{2d - z_S}{\cos(\beta_P)}, \tag{2.63}$$

Absorption can be included into the model by multiplying each element of the set of waves with the respective factors $e^{-\gamma \partial x_{\downarrow,n}}$ or $e^{-\gamma \partial x_{\uparrow,n}}$. Thus, the extended form of Eq. (2.57) is obtained as:

$$A_{tot} = \frac{(e^{-\gamma \frac{z_S}{\cos(\beta_P)}} - Re^{i\delta\phi} e^{-\gamma \frac{2d - z_S}{\cos(\beta_P)}}) e^{i\omega t}}{1 + RR^s e^{i\Delta\phi} e^{-\gamma \partial x}}. \tag{2.64}$$

The corresponding spectral amplitude distribution is given by:

$$a_{tot} = \sqrt{A_{tot} \cdot A_{tot}^*} = \sqrt{\frac{e^{-2\gamma \frac{z_S}{\cos(\beta_P)}} + R^2 e^{-2\gamma \frac{2d - z_S}{\cos(\beta_P)}} - 2Re^{-\gamma \partial x} \cos(\delta\phi)}{1 + R^2 R^{s2} e^{-2\gamma \partial x} + 2RR^s e^{-\gamma \partial x} \cos(\Delta\phi)}}. \tag{2.65}$$

2.3.4 Contributions from P-SV and SV-P conversion

So far only P waves contributing to the seismic signal have been considered. In this section the additional influence of SV waves on it are discussed.

Generally, P and SV waves each excite both types of waves upon reflection at a boundary. Thus, the actual seismic signal is much more complex than suggested by the simplified models introduced in the previous sections: Additionally to the P waves (discussed in Section 2.3.1 and Section 2.3.2), it contains contributions from waves that were converted into an SV wave. These include the SV wave created directly by the acoustic wave at the surface, the SV waves reflected multiple times only as SV waves and all waves which propagated as a sequence of P and SV waves. The latter reach the sensor either as a P wave or an SV wave but might have undergone several conversions of wave type before.

In this section at first the phase differences $\Delta\phi_{tot,i}$ at the sensor between the directly, acoustically excited P wave $A_{\grave{P}}$ and an arbitrary wave A_i is developed. Then, the amplitude a_i of the wave A_i is given. With $\Delta\phi_{tot,i}$ and a_i the total amplitude distribution of any number of interfering waves can be calculated.

The path difference between $A_{\grave{P}}$ and an arbitrary wave A_i is obtained geometrically using the angles β_P and β_S for the respective distances covered as P waves and as SV waves (sketched in Fig. 2.7). From this the phase difference is determined using the corresponding wave velocities v_{P1} and v_{S1}. For the time of reference I chose the arrival of the direct wave $A_{\grave{P}}$ at the sensor (point S). Since the phase difference of the plane acoustic wave arriving at different points at the surface is easy to obtain, it is also convenient to consider the phase of $A_{\grave{P}}$ upon arrival at the surface (point D). It is given by $\phi_{A_{\grave{P}},surface} = -2\pi f \cdot \overline{DS}/v_{P1}$ (using that the phase of $A_{\grave{P}}$ at the position of the sensor is set zero).

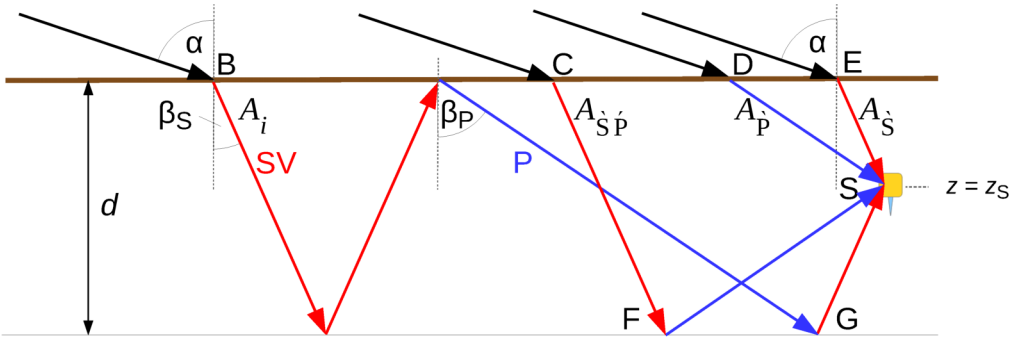

Figure 2.7: Sketch of a plane, acoustic wave hitting the soil surface at $z = 0$ m and exciting various seismic waves. P waves are indicated as blue arrows and SV waves as red arrows. The wave types might change upon reflection at the underground boundary in depth $z = d$ or at the free surface.
For the calculation of the phase difference the directly acoustically excited P wave $A_{\grave{\mathrm{P}}}$ is chosen as reference.

Using this, the phase difference $\Delta\phi_{\mathrm{tot},i}$ between $A_{\grave{\mathrm{P}}}$ and any other wave A_i, arriving at the sensor at a later time than $A_{\grave{\mathrm{P}}}$, can be separated into two parts: The first part is the phase difference between $A_{\grave{\mathrm{P}}}$ at the surface (point D) and A_i at the point where it is reflected the last time, i.e. either at the surface (points D or E) or at the underground boundary (points F or G), see Fig. 2.7. The second part is the phase difference between $A_{\grave{\mathrm{P}}}$ reaching the sensor from the surface and A_i reaching the sensor from either the surface or the underground boundary. Here four different cases can be identified for the wave A_i, depending on its direction (whether it is propagating upwards or downwards) and its wave type (either P or SV wave) when reaching the sensor. The respective distances (between the sensor and either the surface or the underground boundary) of these cases are referred to as $\partial x_{\grave{\mathrm{P}}}$, $\partial x_{\acute{\mathrm{P}}}$, $\partial x_{\grave{\mathrm{S}}}$ and $\partial x_{\acute{\mathrm{S}}}$. The indices P and S state the wave type and the accents illustrate the direction of the wave A_i with the grave accent signifying a downwards-propagating wave and the acute accent an upwards-propagating one.
As an example, in Fig. 2.7 an SV wave $A_{\grave{\mathrm{S}}}$ excited by the acoustic wave at point E is shown together with the direct P wave $A_{\grave{\mathrm{P}}}$ excited at point D (as already shown in Fig. 2.4). A wave $A_{\grave{\mathrm{S}}\acute{\mathrm{P}}}$ is excited at point C as an SV wave which reaches the sensor (point S) propagating upwards after being converted into a P wave upon reflection at the underground boundary. Additionally, an example of an arbitrary, multiply reflected wave A_i is sketched: On the left (at point B) an SV wave is excited by the incident acoustic wave, which is first reflected as an SV wave, then converted upon reflection into a P wave and converted back into an SV wave before reaching the sensor.
The distance $\overline{DS}$ can be identified with $\partial x_{\grave{\mathrm{P}}}$, $\overline{FS}$ with $\partial x_{\acute{\mathrm{P}}}$, $\overline{ES}$ with $\partial x_{\grave{\mathrm{S}}}$ and $\overline{GS}$ with $\partial x_{\acute{\mathrm{S}}}$.
The first part of the total phase difference $\Delta\phi_I$ is given by the sum over all phase

differences arising from the slant propagations through the whole upper soil layer of the wave A_i with respect to the wave $A_{\grave{\mathrm{P}}}$ at point D. Each of them are given by[22]:

$$\begin{aligned}\Delta\phi_{\mathrm{P}} = \Delta\phi_{\grave{\mathrm{P}}} = \Delta\phi_{\acute{\mathrm{P}}} &= 2\pi f\Big[\frac{d}{v_{\mathrm{P1}}}\sqrt{1-\Big(\frac{v_{\mathrm{P1}}}{v_0}\Big)^2\sin^2(\alpha)}\Big],\\ \Delta\phi_{\mathrm{S}} = \Delta\phi_{\grave{\mathrm{S}}} = \Delta\phi_{\acute{\mathrm{S}}} &= 2\pi f\Big[\frac{d}{v_{\mathrm{S1}}}\sqrt{1-\Big(\frac{v_{\mathrm{S1}}}{v_0}\Big)^2\sin^2(\alpha)}\Big],\end{aligned} \tag{2.66}$$

where the indices P and S indicate whether the slant distance $d/\cos(\beta_{\mathrm{P}})$ was covered as P wave or $d/\cos(\beta_{\mathrm{S}})$ as SV wave. Regardless of the direction (i.e. upwards or downwards) the phase differences are the same for the same wave type. Thus, the sum phase difference is given by:

$$\Delta\phi_I = m\cdot\Delta\phi_{\mathrm{P}} + n\cdot\Delta\phi_{\mathrm{S}}. \tag{2.67}$$

Here the integers m and n are the number of times the wave covered the respective slant distances as P wave and as SV wave.
The second part of the phase difference is calculated by

$$\Delta\phi_{II,i} = 2\pi f\Big(\frac{\partial x_i}{v_i} - \frac{\overline{DS}}{v_{\mathrm{P1}}}\Big), \tag{2.68}$$

where ∂x_i corresponds to the four cases for A_i and v_i is the wave velocity of the respective wave type. Note that in the first case of $\partial x_{\grave{\mathrm{P}}}$ the phase difference $\Delta\phi_{II,i}$ vanishes. Therefore, the phase differences of the downwards-propagating waves corresponding to $\partial x_{\grave{\mathrm{P}}}$ and $\partial x_{\grave{\mathrm{S}}}$ are given by

$$\begin{aligned}\partial\phi_{\grave{\mathrm{P}}} &= 0,\\ \partial\phi_{\grave{\mathrm{S}}} &= 2\pi f\Big[\frac{z_{\mathrm{S}}}{v_{\mathrm{S1}}}\sqrt{1-\Big(\frac{v_{\mathrm{S1}}}{v_0}\Big)^2\sin^2(\alpha)} - \frac{z_{\mathrm{S}}}{v_{\mathrm{P1}}}\sqrt{1-\Big(\frac{v_{\mathrm{P1}}}{v_0}\Big)^2\sin^2(\alpha)}\Big].\end{aligned} \tag{2.69}$$

For the waves reaching the sensor propagating upwards the phase differences corresponding to $\partial x_{\acute{\mathrm{P}}}$ and $\partial x_{\acute{\mathrm{S}}}$ are given by

$$\begin{aligned}\partial\phi_{\acute{\mathrm{P}}} &= 2\pi f\Big[\frac{(d-2z_{\mathrm{S}})}{v_{\mathrm{P1}}}\sqrt{1-\Big(\frac{v_{\mathrm{P1}}}{v_0}\Big)^2\sin^2(\alpha)}\Big],\\ \partial\phi_{\acute{\mathrm{S}}} &= 2\pi f\Big[\frac{(d-z_{\mathrm{S}})}{v_{\mathrm{S1}}}\sqrt{1-\Big(\frac{v_{\mathrm{S1}}}{v_0}\Big)^2\sin^2(\alpha)} - \frac{z_{\mathrm{S}}}{v_{\mathrm{P1}}}\sqrt{1-\Big(\frac{v_{\mathrm{P1}}}{v_0}\Big)^2\sin^2(\alpha)}\Big].\end{aligned} \tag{2.70}$$

[22]Note that these phase differences refer to the waves propagating in one direction (i.e. either propagating upwards or downwards) through the whole upper soil layer. This is due to the fact that the wave type might change upon each reflection at a boundary. In contrast, the equations given in Section 2.3.2 refer to a pair of reflections (i.e. the wave propagating downwards and upwards) since only P waves were considered.

For an arbitrary wave A_i being reflected multiple times within the upper soil layer the resulting phase difference with respect to $A_{\grave{\mathrm{P}}}$ is obtained by

$$\Delta\phi_{\mathrm{tot},i} = m \cdot \Delta\phi_{\mathrm{P}} + n \cdot \Delta\phi_{\mathrm{S}} + \Delta\phi_{II,i}. \tag{2.71}$$

Since the phase of $A_{\grave{\mathrm{P}}}$ at the sensor is set zero, $\Delta\phi_{\mathrm{tot},i}$ can be interpreted as the phase of the wave A_i when reaching the sensor.
It is easy to see that $\Delta\phi_{\mathrm{tot},i}$ of a pure P wave with $n = 2$ reproduces Eq. (2.51). For the example of A_i as given in Fig. 2.7 the total phase difference is obtained for $m = 2$, $n = 1$ and $\Delta\phi_{II,i} = \partial\phi_{\acute{\mathrm{S}}}$. The derivation of the phase difference between $A_{\grave{\mathrm{P}}}$ and $A_{\grave{\mathrm{S}}\acute{\mathrm{P}}}$ is given in more detail in Appendix A.1 to show exemplarily the steps to obtain the terms in Eq. (2.66), Eq. (2.69) and Eq. (2.70).

The amplitude a_i of the wave A_i, relative to $A_{\grave{\mathrm{P}}}$, is obtained from the respective reflection coefficients. The four possible combinations of the types of incident and reflected waves lead to four reflection coefficients at the underground boundary (given in Section 2.2.2) and four reflection coefficients at the free surface (given in Section 2.2.3). The general equation for the amplitude of A_i is

$$\begin{aligned} a_i = &(R_{\mathrm{PP}})^{m_{\mathrm{PP}}} \cdot (R_{\mathrm{PS}})^{m_{\mathrm{PS}}} \cdot (R_{\mathrm{SP}})^{m_{\mathrm{SP}}} \cdot (R_{\mathrm{SS}})^{m_{\mathrm{SS}}} \\ &\cdot (R^{\mathrm{s}}_{\mathrm{PP}})^{n_{\mathrm{PP}}} \cdot (R^{\mathrm{s}}_{\mathrm{PS}})^{n_{\mathrm{PS}}} \cdot (R^{\mathrm{s}}_{\mathrm{SP}})^{n_{\mathrm{SP}}} \cdot (R^{\mathrm{s}}_{\mathrm{SS}})^{n_{\mathrm{SS}}} \cdot (T^{\mathrm{s}}_{\mathrm{S}}/T^{\mathrm{s}}_{\mathrm{P}})^{k}. \end{aligned} \tag{2.72}$$

The integers m_{ij} refer to the times the wave is reflected at the underground boundary with the indices i and j stating the type of the incident and the reflected wave, respectively. The integers n_{ij} count the number of corresponding reflections at the free surface. Some of the integers m_{ij} and n_{ij} might be zero. The amplitude of $A_{\grave{\mathrm{P}}}$ is treated to be $a_{\grave{\mathrm{P}}} = 1$. This is accounted for by the term $(T^{\mathrm{s}}_{\mathrm{S}}/T^{\mathrm{s}}_{\mathrm{P}})^k$ using the transmission coefficients from the acoustic wave to either a seismic P or S wave given in Eq. (2.40). If the type of A_i upon first excitation by the acoustic wave is a P wave the integer k equals zero. If it is an SV wave the value is $k = 1$.
Using the phase $\Delta\phi_{\mathrm{tot},i}$ (given by Eq. (2.71)) and the amplitude a_i (given by Eq. (2.72)) of an arbitrary wave A_i reaching the sensor, the total spectral amplitude distribution of M interfering waves can be calculated with

$$a_{\mathrm{tot}} = \left[\sum_{j}^{M}\left({a_j}^2 + \sum_{k\neq j}^{M} a_j a_k \cos(\Delta\phi_{\mathrm{tot},j} - \Delta\phi_{\mathrm{tot},k})\right)\right]^{1/2}. \tag{2.73}$$

The derivation of Eq. (2.73) is presented in Appendix A.2.

Chapter 3

Experimental Work

Several measurement campaigns were performed in the frame of this work during which the sound pressure and the soil velocity caused by various sources were recorded. During these the same sensors, measurement instrumentation and software were used but the setup changed according to the measurement site. During several campaigns sensors were shielded from the incident acoustic signals by a wooden box coated with acoustic damping foam or with mats of damping foam on the ground above the sensors.
In this chapter, firstly, the general setup of the measurement system and its components is outlined and the process of data acquisition is described. Afterwards, the specific sensor setup and the used sources of the measurement near the airport FMO are presented.

3.1 Measurement instrumentation and data acquisition

All data were recorded using up to four analogue-digital converters (ADCs) from Data Translation (DT9841 with 8 channels each, resolution 24 bits) running synchronously. The signals were sampled with 10 kHz with a digital low-pass filter in each channel with corner frequencies of 4530 Hz for all geophones and of 3000 Hz of an additional analogue filter for all microphones, respectively.
For the presented measurements Brüel & Kjær (BK) microphones were used to record the sound pressure: 4166 with preamplifier 2639, 4188 with preamplifier 2639, and 4198 (capsule 4189, preamplifier 2669C). To record the soil velocity geophones of the types SM-6B (Sensor Nederland) and L28 (Sercel) were used. They have an eigenfrequency of 4.5 Hz and produce reliable signals up to several hundred Hz as calibration measurements showed.
To synchronise all data an antenna was used to record GPS time which was converted to DCF77 clock pulses. The pulses were stored in one bit of a binary channel, usually channel 8 (see Table A.1). A sketch of the setup of the used hardware is given in Fig. 3.1.

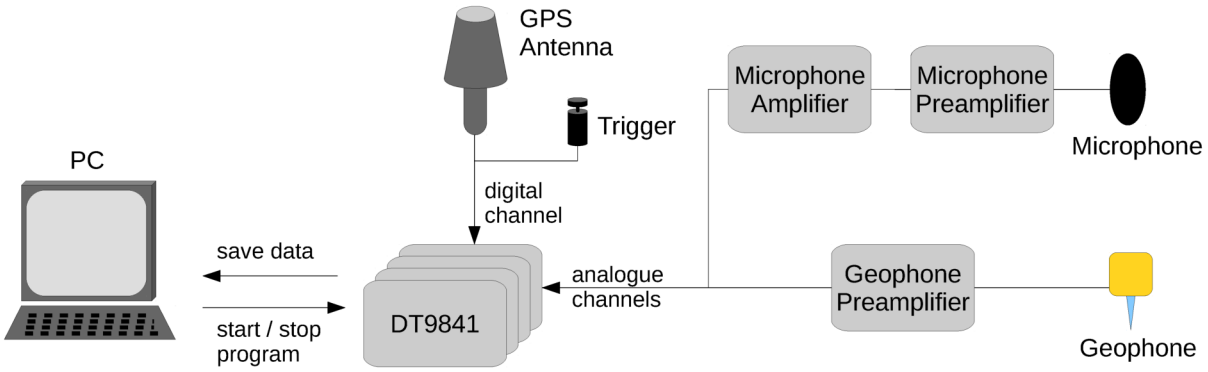

Figure 3.1: Scheme of the used hardware: Sensors (geophones and microphones alike) were placed at the measurement site. Preamplifiers were placed at short distances from the sensors before the signal was transferred via up to 60 m long cables to the base of operation. Here the microphone signal passed an additional amplifier, which contained an internal analogue low-pass filter. Via BNC connector the signals were given into the respective ADC. Up to four of these were connected: The first being the master unit and the others the slave units. The binary channel, containing up to 16 bit signals of which usually only two bits were used for the DCF77 clock pulses and the trigger signal, was part of the master unit. Channels were internally assigned 0 to 7 (for the analogue channels of the master unit), 8 for the binary channel, 9 to 16 for the analogue channels of the first slave unit and respective higher channel numbers for consecutive slave units. A PC program was used to control the recordings and to save the recorded data.

Recording was performed with the measurement program *MessProgrammDT9841* (developed by the working group *Physics and Disarmament*) using library functions provided by the ADC manufacturer. In the program additional information for each channel could be specified like amplification factors, corner frequencies of the used low-pass filters as well as measurement-specific information like the sensor coordinates. The program also controls data flow from the ADCs to the PC: Data blocks of eight channels per ADC are sorted in the correct order and written to the PC's hard drive. The local PC time was used as time stamp for the recorded signals, which however was observed to change relatively with respect to the GPS time of the binary channel. This was observed especially for longer measurements of many hours and when the used hard drive nearly reached its storage capacity. This had usually no effects when only signals recorded at one PC were evaluated. For the synchronisation of signals recorded with two or more PCs or with signals of supplementary measurements the changing time offset had to be taken into account carefully.

Before the measurement the program wrote a preamble file, containing all specified information about the measurement and the channels, to the hard drive. This file was completed after the measurements by a postamble containing the measurement duration, the amount of data recorded as well as additional information optionally input by the

operator.
The evaluations, described in Chapter 4, were performed with the program *Eingabe* (developed by the working group *Physics and Disarmament*) as well as with scripts written in *MATLAB*.

3.2 Acoustic-seismic measurement near the airport Münster-Osnabrück

This measurement site was situated approximately 4 km west-southwest of the airport FMO, in a lateral distance from the runway line of approximately 300 m.[23] Fig. 3.2 shows the location of the measurement site (black x in lower left corner) as well as the airport FMO. The vegetation was sparse grass on a meadow in a bend of the river Ems (closest distance between measurement setup and river approximately 200 m). The site is flat for at least 150 m and without any trees to all directions except for the east and southeast where in 60 m distance a wooded slope rises to about 3 m above the measurement level. The ground consists of sandy soil with no visible layering up to 0.6 m depth. With seismic refraction methods a boundary in a depth of approximately 1.8 m was determined. Additionally, the values of the velocities of the P-wave in the upper layer of $v_{P1} \approx 200\,\mathrm{m/s}$ and in the lower layer of $v_{P2} \approx 1400\,\mathrm{m/s}$ are derived (the high P-wave velocity probably is caused by groundwater in that layer) [60].
The equipment was set up on 13th May 2013 and the measurements presented were done from 14th to 15th May 2013. The air temperature varied between 10°C and 18°C; the sky was mostly overcast with light winds and occasional rain.

3.2.1 Measurement setup

Microphones to record the sound pressure were put at 6.5 cm above ground. Geophones to record the soil velocity were placed at the surface or buried in different depths (0.15 m, 0.30 m, 0.45 m and 0.60 m). In the setup one-dimensional vertical geophones and three-dimensional assemblies (one vertical and two horizontal one-dimensional geophones mounted on the same holder) were used. Of the latter only the vertical components are used for the present evaluation. The geophones were connected to the soil by a conical spike of approximately 7 cm length. Thus, the actual coupling depth to the ground might be slightly larger than the stated values. For burying, quadratic holes of about 25 cm side length were dug. After mounting the geophones or the three-dimensional assemblies, the holes were backfilled, using nearly all the material dug out before. Some efforts were made to compress it, but the original conditions existed only for the soil beneath the

[23] GPS coordinates of the measurement site: 52° 7′ 16″ N, 7° 36′ 16″ E, altitude: 37 m. GPS coordinates of the weather station at the airport Münster-Osnabrück: 52° 7′ 58.1″ N, 7° 41′ 8.2″ E, altitude: 48 m.

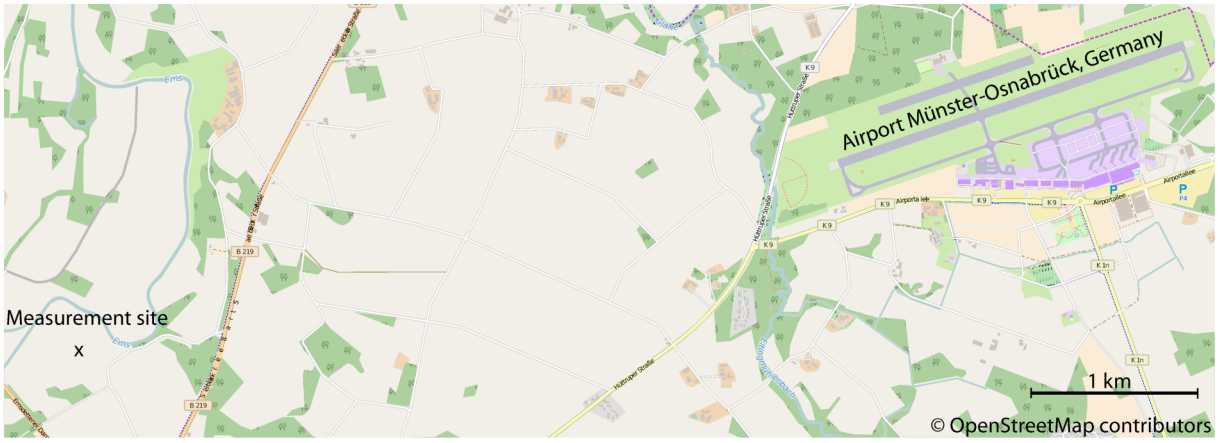

Figure 3.2: Map of the airport Münster-Osnabrück, Germany and its surroundings. The measurement site was located approximately 4 km west-southwest of the runway, marked with a black x. Map licensed under CC BY-SA, ©OpenStreetMap contributors.

geophones. All in all 6 microphone channels and 26 geophone channels were used for the recordings. Fig. 3.3 shows a sketch of the sensor setup including the respective channel numbers.

The local sensor coordinates for each channel are given in Table A.1. The z-axis of this local coordinate system is chosen to point into the ground. Thus, $z = 0\,\mathrm{m}$ refers to the surface of the soil and the burying depths of the geophones have positive z-values. Therefore, the z-coordinates of the microphones above ground (and the occasional mention of the height of the used speaker) are negative.[24]

3.2.2 Acoustic sources used during the measurement

Broadband signals of jet-aircraft:

Taking-off (and occasionally landing) aircraft passed nearly vertically above the setup in altitudes between several hundred metres and up to 1645 m, at lateral distance of few hundred metres. This resulted for most flights at their closest point of approach (cpa) in angles of incidence α of the acoustic signals of approximately 10° to 30° from the normal to the ground surface. In Table A.2 the evaluated aircraft overflights are summarised.

During the aircraft overflights the angle of incidence and distance between source and sensors (and thereby the amplitude of the signal) changed. For all evaluations the position of the aircraft at the time of signal emission was used, taking into account the propagation time of the acoustic signals from the aircraft to the sensors.[25] Trajectories of all overflights, used for the calculation of the respective angles α, were provided by the

[24] It should be obvious that the heights of the aircraft overflying the setup, given in Table A.2, refer to actual heights above the surface. I use positive values in this case since I do not relate them to the local sensor coordinates the z-axis of which points into the ground.

[25] To calculate the propagation time the temperature-dependent sound velocity v_0 was used, given by Eq. (2.15). Effects caused by wind were generally neglected for all evaluations.

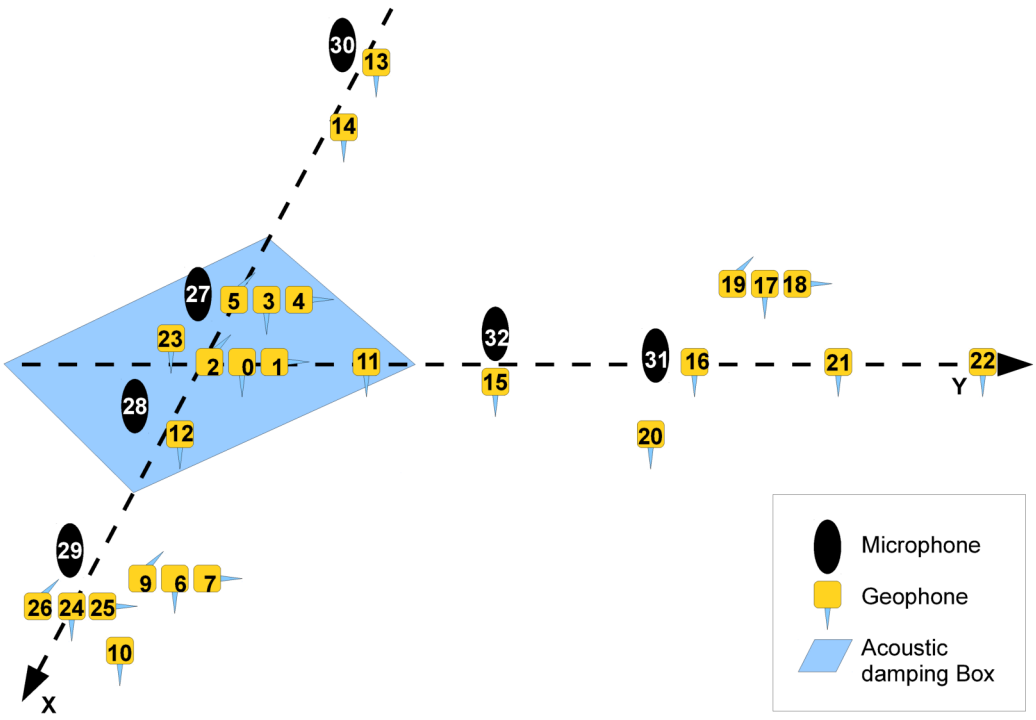

Figure 3.3: Acoustic-seismic measurement setup indicating the positions of the sensors and channel numbers. The size of the sensor array is roughly 4 m in x direction and 8 m in y direction. For the burying depths of the geophones and the precise sensor locations see Table A.1. During several of the overflight events (i.e. overflight numbers 7 to 16, see Table A.2) an acoustic-damping box was placed over several sensors as indicated by the blue area.
The airport FMO is situated approximately 4 km in positive y direction.

German Air Traffic Control (DFS).
The sound pressure recorded during the jet-aircraft overflights originated from mostly two jet engines, mainly excited by the turbulent mixing of the exhaust gases with the air [61]. This resulted for most overflights in a broadband signal with significant sound pressure amplitudes for frequencies from few Hz up to more than 1 kHz. Due to the large distance of the aircraft from the sensors and the relatively small sensor arrangement the aircraft are treated as point sources. This is justified because a fixed phase relation was found between the acoustic signals recorded at each pair of microphones. Also because of the distance, the incident acoustic waves are approximated as plane waves, according to Section 2.1.3.

Noise artificially produced by a speaker:
Artificial acoustic signals were produced with a speaker suspended by a crane at different positions above the ground (sketched in Fig. 3.4). The speaker had twelve membranes to provide a optimal spherical wave-emission characteristic. Via a noise generator and amplifier broadband noise could be replayed by the speaker. The noise signal was supposed to represent pink noise which has equal noise power in every octave and whose power density is inversely proportional to the frequency f. However, the emitted noise signal differed for two reasons from theoretical pink noise. Firstly, in the low frequency range the emitted power was significantly smaller, due to the limited dimensions of the speaker and its membranes. The maximum of the power is recorded for frequencies between 155 Hz and 170 Hz (see the spectrum of the sound pressure in Fig. 4.11, left). Secondly, in the frequency range $200\,\text{Hz} \leq f \leq 750\,\text{Hz}$ the spectral power density is proportional to f^{-4} (instead of f^{-1} for pink noise). Thus, the measurements will be simply referred to as "noise replay". Regardless of the precise spectral characteristics of the noise signal, it represents an acoustic broadband signal which is used as reproducible reference. Thus, the noise replay from the speaker has been used at various measurement sites with and without acoustic shielding of the sensors. Usually it was replayed from several speaker positions for the time of 30 seconds. Thus, the spectral amplitudes of multiple calculated spectra corresponding to the same excitation conditions are averaged to increase signal-to-noise ratio (SNR).

3.2.3 Box used for acoustic shielding

A box (see Fig. 3.5) of the dimensions 1.00 m * 1.00 m * 0.50 m (width * length * height) could be placed over several sensors to reduce the incident sound pressure. Its walls and lid consist of 19 mm thick plywood coated on the inside with acoustic damping foam[26] of thickness 0.1 m. At the measurement site near the airport FMO the sensors were aligned

[26] The used acoustic damping foam has a density of about 120 kg m^{-3} and is suitable for sound insulation as stated by the manufacturer [62].

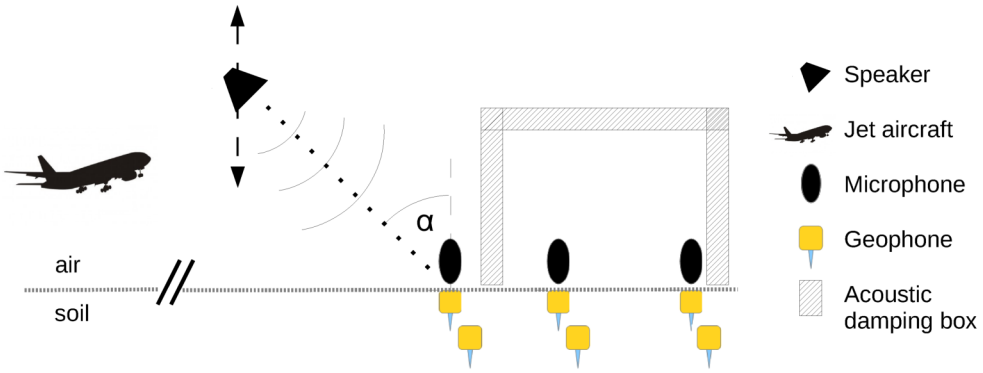

Figure 3.4: Sketch of the acoustic-seismic measurements with the used box to shield some sensors from the incident acoustic signal. The angle of incidence α of the acoustic signals from the normal to the ground surface is indicated. Acoustic signals of jet-aircraft overflights and artificially produced ones by a speaker were recorded.

in such a way that one geophone buried in each of the depths and one at the surface as well as two microphones could fit under the box (see Fig. 3.3). For comparison reasons additional sensors (in all mentioned depths and in different directions from the box) were installed outside of the box in up to 8 m distance. To mitigate seismic excitation by the box itself the damping foam was glued to the plywood in such a way that it protruded by about 2 cm from the bottom of the plywood walls and thus only the damping foam touched the ground. Small slits between box and ground were filled with dirt. A sketch of the setup with the box is given in Fig. 3.4.

Fig. 3.5 (left) shows the open box with two microphones (black wind shields on downward-directed microphones visible) and one geophone at the surface (yellow case) inside. Between the two microphones the rim of a quadratic hole for a buried geophone can be identified – it is backfilled and closed with the sod. The damping foam is glued to the inside of each wall as well as to the lid of the box. In Fig. 3.5 (right) the closed box is shown: Its lid is tightened to the box by four metal clamps.

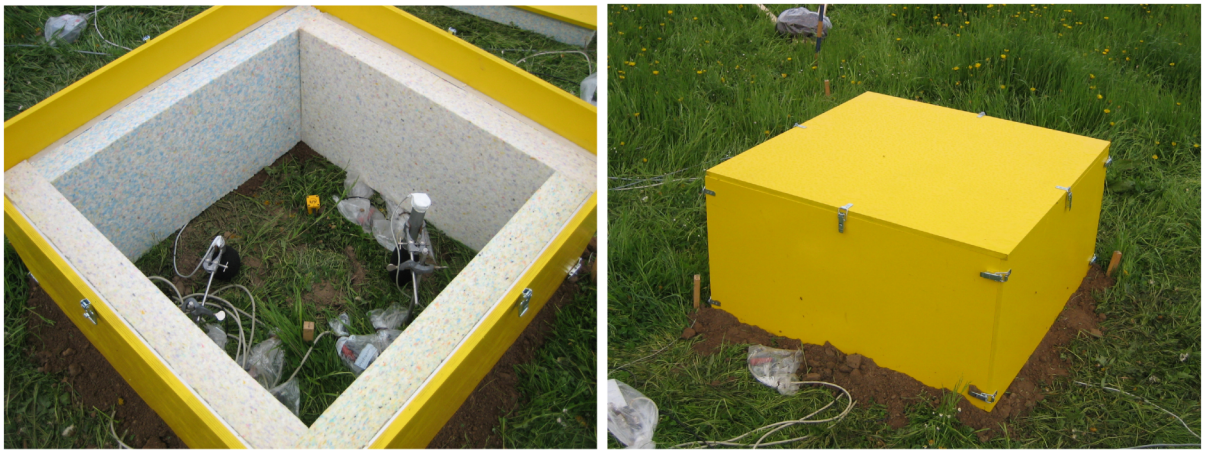

Figure 3.5: Damping box used during the measurements to shield two microphones and several geophones from the incident acoustic signal. Left: Open box consisting of plywood walls coated with damping foam clued on the inside. The black wind shields of two microphones and the yellow case of the surface geophone are visible.
Right: Box closed by the lid (coated with damping foam, respectively) which is tightened to the box by metal clamps.

Chapter 4

Analysis

In this chapter the findings of the measurements are evaluated and discussed. Firstly, in the Introductory assumptions several basic assumptions used throughout the evaluation are stated. The sound pressure and the respective acoustically excited soil velocity of aircraft overflight events and artificial noise replays are shown in Section 4.1 for the time domain and the frequency domain. Afterwards, in Section 4.2 the acoustic-seismic coupling coefficient is introduced which is used as a powerful method to achieve event-independent data.
In Section 4.3 the amplitude ratios between incident and reflected waves are determined which represent the reflection coefficients theoretically introduced in Section 2.2. They are used to obtain the relative amplitudes of seismic waves reflected multiple times within the upper soil layer taking into account that each reflection might change their wave types. The three models of wave interference (introduced theoretically in Section 2.3) are compared and discussed in Section 4.4. Using these models from the recorded interference patterns of seismic waves soil properties are derived. In Section 4.5 the interference pattern recorded with sensors shielded from the incident acoustic waves are investigated. Comparing the interference patterns of sensors placed outside of the acoustic damping box and under it conclusions about the frequency-dependent absorption in the soil can be drawn.
In Section 4.6 the horizontal propagation range of acoustically induced seismic waves is estimated and the findings of this work are discussed with respect to the use for sensitive seismic measurements during OSIs. Finally, in Section 4.7 a brief comparison with recordings of a different measurement site is made and the possibility of constructively superposing Rayleigh waves created by acoustic signals is discussed.

Introductory assumptions

Throughout the evaluation I have to make some general assumptions for the soil at the measurement site. Some soil properties were not determined by measurements thus

values valid for many soils will be used.
The first assumption concerns the ratio between P- and S-wave velocity in the upper soil layer:

$$\frac{v_{\mathrm{P1}}}{v_{\mathrm{S1}}} = \sqrt{3}. \tag{4.1}$$

This is the assumption of a Poisson solid (i.e. $\lambda_{\mathrm{L}} = \mu$ in Eq. (2.20)) which applies to many Earth materials [63].
Secondly, I use assumptions for the ratios of the densities as well as of the S-wave velocities of the first and the second soil layer:

$$\frac{\rho_2}{\rho_1} = 1.25, \quad \frac{v_{\mathrm{S2}}}{v_{\mathrm{S1}}} = 1.15. \tag{4.2}$$

Both assumptions are justified by the usual increase of density and wave velocity with depth in soil. These common values are often used in [64] and also in [40].[27] The usage of different ratios would change the value of the reflection coefficients and therefore the amplitude ratios between P and SV waves as well as these between interference maxima and minima. Therefore, it could also change the frequency of the interference maxima of buried sensors. However, it would not affect the frequencies of the maxima of pure P-wave interference for sensors at the surface. These were used to obtain the best fit results for d and v_{P1}, which are used throughout the evaluation as stated below.

Use of the final results throughout the evaluation

For many of the calculations I use fundamental findings of the evaluation, namely the depth of the underground boundary $d = 2.35\,\mathrm{m}$ and the P-wave velocity in the upper soil layer $v_{\mathrm{P1}} = 230\,\mathrm{m/s}$. For the fit algorithm presented in Section 4.4.1 both were treated as free parameters for all calculations. The graphs given in this chapter were produced afterwards using the final results. So it shall not come as a surprise that d and v_{P1} are used prior to their determination by the fit algorithm, the results of which are presented in Section 4.4.2.

4.1 Characteristics of the investigated signals

During the measurements acoustic and seismic signals produced by various sources were recorded, as described in Section 3.1. In the evaluation mainly the signals caused by jet-

[27] In another approach I estimated the ratio of the densities ρ_2/ρ_1 from the volume of the pores, which are filled with air in the upper soil layer and with water in the second one. Using the values of the pore-volume share of approximately 50 % and the densitiy of the porous soil of $1.2\,\mathrm{g/cm^3}$, given in [65] for sandy soil in the upper layers, this led to $\rho_2/\rho_1 \approx 2.9$. The use of this ratio resulted only in minor changes of the calculated values of the respective reflection coefficients, presented in Section 4.3.3. Thus, I will use the values given in Eq. (4.2) throughout this work.

aircraft take-offs are used but also those of artificially produced noise played by a speaker. Both types of signals were systematically recorded during the measurement campaign near the airport FMO, described in Section 3.2.

Here, firstly, the analysis methods used during the evaluations are specified: In Section 4.1.1 those for the time signals and in Section 4.1.2 those in frequency space. In each section representative signals caused by the various sources are shown and their characteristics are discussed. To give a better understanding of the signal quality additionally the spectral background amplitude at the measurement site near the airport FMO are presented. The calculation of the background spectra is discussed in Appendix A.5.

4.1.1 Time-signal analysis

The time signals recorded with $f_S = 10\,\text{kHz}$ sampling rate are used unprocessed with the signal values for every time point $a(t)$ or as root mean square (RMS) values a_{RMS} in a certain time interval. For the calculation of the RMS values the mean value $\overline{a}$ in the respective time interval was subtracted. Usually one would expect the mean value to be zero, but in some cases a different value was observed: One example of these cases would be, if the voltage of the two 9 V batteries, used as power supply for the geophone preamplifiers, differed. This resulted in a constant offset of the recorded soil velocity. Another example is the measurements of the sound pressure: The used BK microphones recorded considerable infrasound signals caused by wind resulting in a low-frequency modulation of the signal. Thus, data show a non-zero offset which can change for subsequent time intervals.

The RMS value of the signal values of N samples in a time interval of length T is calculated by

$$a_{\text{RMS}} = \sqrt{\frac{1}{N}\sum_{i}^{N}(a_i - \overline{a})^2} \quad \text{with} \quad \overline{a} = \frac{1}{N}\sum_{i}^{N} a_i. \tag{4.3}$$

For a set of statistically distributed measurement data the definition of the standard deviation σ of an underlying Gaussian distribution is used which is also used by the internal *MATLAB*-function *std*. The standard deviation is calculated for RMS amplitudes $a_{\text{RMS},i}$ of n different time intervals during which signals under similar conditions were recorded. Thus, it is given by:

$$\sigma = \sqrt{\frac{1}{n-1}\sum_{i}^{n}(a_{\text{RMS},i} - \overline{a_{\text{RMS}}})^2}. \tag{4.4}$$

The mean value of the n RMS amplitudes $\overline{a_{\text{RMS}}}$ can be calculated following the second equation in Eq. (4.3).

Together with the location of the source the angle of incidence α of the respective acoustic signal at each time can be calculated. This is of special interest for the jet-aircraft

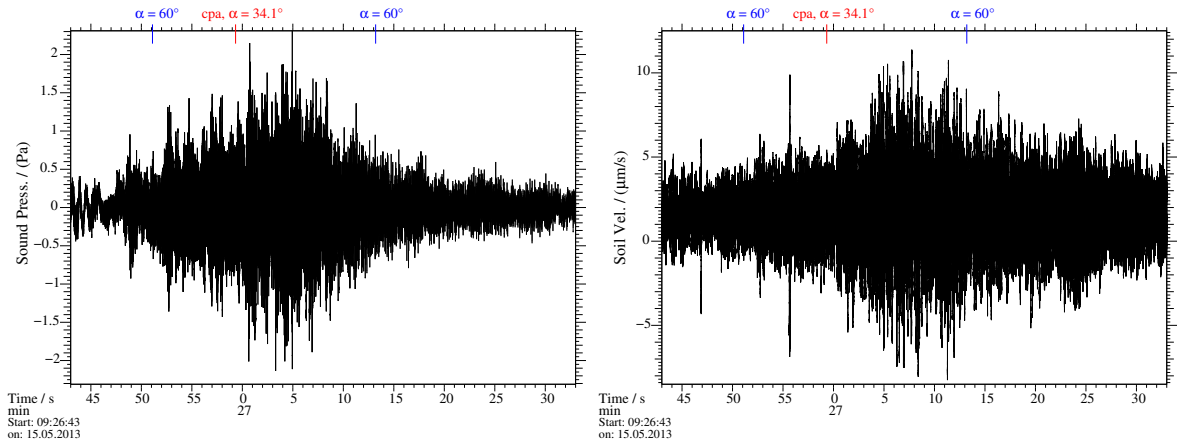

Figure 4.1: Time signals of the jet-aircraft overflight number 13 (see Table A.2). The time when the signal, emitted by the aircraft at its cpa, was recorded is indicated with a red line at the top of each graph. Additionally, the time interval during which the angle of incidence α was smaller than 60° is defined by two blue lines.
Left: Sound pressure, recorded with the microphone of channel 29.
Right: Vertical soil velocity, recorded with a geophone at the surface, channel 24.

overflights: Due to the large distance between sources and sensor the incident signals are treated as plane waves impinging on the soil surface under the angle α. When using the trajectory of the respective aircraft special care has to be taken when synchronising the signals. The acoustic signal emitted by the aircraft had to propagate for several seconds before being recorded at the sensors near the soil surface. The fast moving aircraft had reached a different location by then. Thus, the propagation time of the signal is taken into account when determining the actual location of the source at the time of signal emission.

4.1.1.1 Representative time signals

In this section exemplarily the acoustic and seismic time signals caused by different airborne sources are shown. In Fig. 4.1 the sound pressure (left) and the vertical soil velocity at the surface (right) recorded during the jet-aircraft overflight number 13 (see Table A.2) are shown. Fig. 4.2 shows the corresponding vertical soil velocities recorded with geophones in a depth of 0.30 m (left) and in a depth of 0.60 m (right).
To provide a better comparability, the same y-range of approximately 20 µm/s is used for the graphs of the vertical soil velocity in Fig. 4.1 (right) and Fig. 4.2 (both graphs). This range is adjusted in each graph to compensate for an offset of the data. Thus, the time signals appear centred in the respective graphs.
The jet aircraft (in this case a Boeing 737-800) passed the sensors at its cpa in a distance of approximately 725 m at an angle $\alpha \approx 34°$. The time of the cpa was at 9:26:57 (UTC) while the corresponding signals – taking into account the propagation time of the acoustic signal – were recorded a little more than 2 s later around 9:26:59.

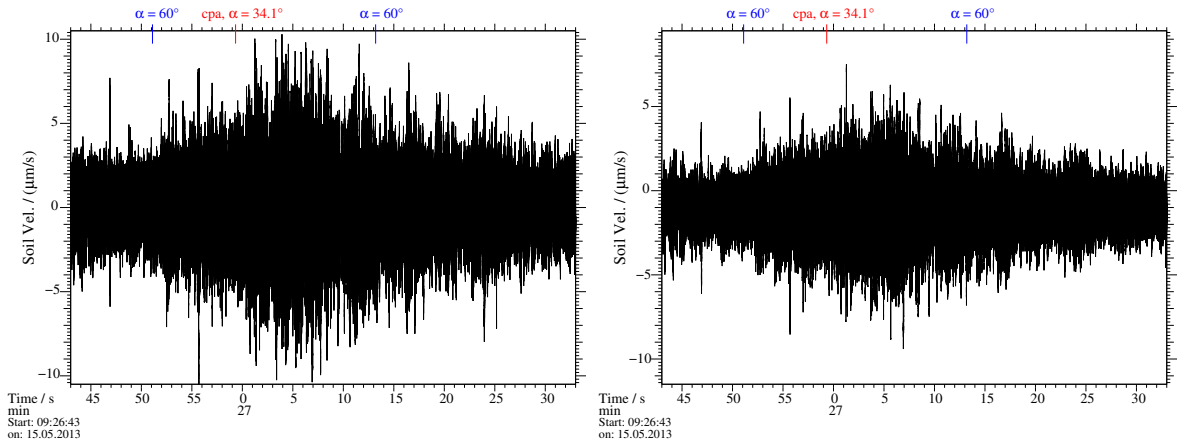

Figure 4.2: Time signals of the vertical soil velocity recorded with buried geophones corresponding to the same aircraft overflight as shown in Fig. 4.1. Left: Geophone in a depth of 0.30 m, channel 6. Right: Geophone in a depth of 0.60 m, channel 13.

The latter time is indicated in the graphs by the red line at the top. The signals reach their maximal amplitudes after the cpa due to the emission characteristics of the aircraft mainly determined by its turbines. Thus, the largest amplitudes of sound pressure and soil velocity are recorded behind the aircraft, i.e. after it had passed the sensor setup. The largest amplitudes of the sound pressure (at the microphone of channel 29) are recorded around 9:27:04 with values of 4.3 Pa (peak to peak) and 0.54 Pa (RMS). For the soil velocity at the surface (channel 24) one finds at 9:27:06 16.4 µm/s (peak to peak) and 2.6 µm/s (RMS). In a depth of 0.30 m at that time slightly larger amplitudes are recorded with 19.3 µm/s (peak to peak) and 2.8 µm/s (RMS). The soil velocity in the depth of 0.60 m has decreased to 14.4 µm/s (peak to peak) and 2.2 µm/s (RMS). The RMS values are calculated for time intervals of 0.8192 s. The particular amplitudes strongly depend on the trajectory of the aircraft, especially its distance from the sensors. In Section 4.2 it is shown how the ratio between the spectral amplitudes of soil velocity and sound pressure – the acoustic-seismic coupling coefficient – can be used to obtain event-independent data.

The start of the time shown in the graphs of Fig. 4.1 and Fig. 4.2 corresponds to a distance between aircraft and sensors of about 1800 m and $\alpha \approx 75°$ and the end of the time to a distance of about 4000 m and $\alpha \approx 72°$. To determine the soil properties (see Section 4.4.2) signals of angles up to 60° were used. The corresponding time interval is defined by two blue lines at the top of the graphs.

The soil velocity recorded in the depth of 0.60 m (Fig. 4.2 right) is visibly smaller than the values recorded at the surface (Fig. 4.1 right) and in a depth of 0.30 m (Fig. 4.2 left). However, few differences can be observed between the soil velocities of the latter two in the time signals alone. The differences will become more obvious when analysing the respective spectral amplitudes in Section 4.1.2.1.

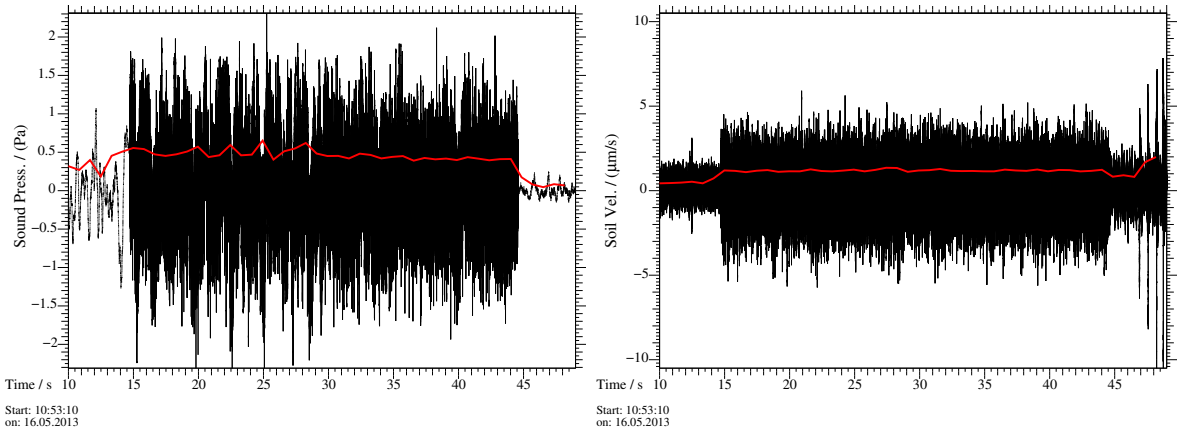

Figure 4.3: Time signals of artificial noise replay by the speaker. The shown data were recorded for the speaker at the position, referring to the used local coordinate system (see Section 3.2.1): x = 0.0 m, y = -1.15 m and in a height of 3.0 m above the surface (z = -3.0 m). As clearly visible in the graphs, the noise replay started around 10:53:15 and ended after about 30 s. Additionally, the RMS values are plotted (red curves) that were calculated for time intervals of 0.8192 s with Eq. (4.3).
Left: Sound pressure, recorded with the microphone of channel 27.
Right: Vertical soil velocity, recorded with a geophone at the surface, channel 23. On the right of the graph four short signals of high amplitude are visible. It is believed that they originate from adjustment work at the crane: This might have caused seismic shocks but no sound, thus they are not observed in the recordings of the sound pressure. These signals were in no way considered for the acoustic-seismic coupling.

In Fig. 4.3 the sound pressure (left) and the vertical soil velocity at the surface (right) of noise replay by a speaker are plotted. The corresponding vertical soil velocities recorded with buried geophones are shown in Fig. 4.4 for the depth of 0.30 m (left) and the depth of 0.60 m (right).

As above, the y-axis of the graphs of the soil velocity shows a range of about 20 µm/s, centred for each signal. Data of both graphs in Fig. 4.4 show a significant offset caused by a difference in the voltage of the batteries used in the geophone preamplifiers. Together with the time signals the RMS values are plotted (red curves; shifted RMS value in Fig. 4.4 (right) in blue). They are calculated with Eq. (4.3) for subsequent time intervals of 0.8192 s, i.e. for 8192 data points. Since the data of the geophone in 0.30 m depth (Fig. 4.4, right) show a large offset, for the plot 20 µm/s was subtracted from the RMS values.

The average amplitude of the sound pressure during the noise replay is approximately 3.4 Pa (peak to peak) and 0.47 Pa (RMS). Differently from the findings of the aircraft overflight presented above, the surface geophone shows smaller amplitudes of the vertical soil velocity than the buried ones. At the surface the soil velocity has an averaged amplitude of 9.0 µm/s (peak to peak) and 1.2 µm/s (RMS). In the depth of 0.30 m one

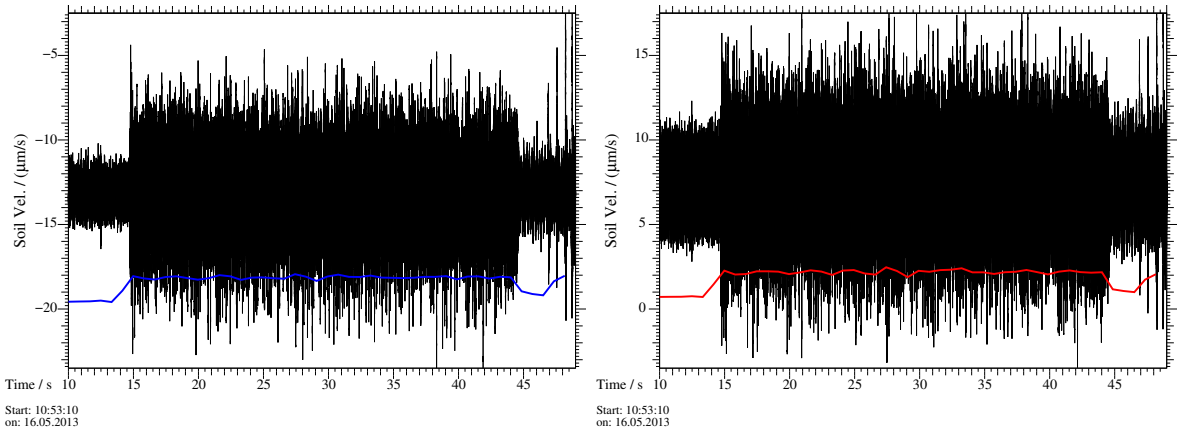

Figure 4.4: Time signals of the vertical soil velocity corresponding to the same time of the noise replay as shown in Fig. 4.3. Left: Vertical soil velocity, recorded with a geophone in a depth of 0.30 m, channel 3. Due to the large offset of the data, for the plot 20 µm/s was subtracted from the RMS values (blue), i.e. the RMS zero line is at -20 µm/s. Right: Vertical soil velocity, recorded with a geophone in a depth of 0.60 m, channel 0.

finds 14.8 µm/s (peak to peak) and 1.9 µm/s (RMS) and in the depth of 0.60 m even 17.2 µm/s (peak to peak) and 2.2 µm/s (RMS). These values are calculated by averaging the respective amplitudes during the whole time of the noise replay.
The increase of the soil velocity with depth (which is not found for the aircraft overflight) is counterintuitive. One reason might be the spherical wavefronts of the signals emitted by the speaker instead of plane waves for the aircraft signal. The spectral analysis of the signals, presented in Section 4.1.2.1, will give additional information. For the buried sensors the background amplitude (before and after the noise replay) is also higher than for the sensor at the surface (see Appendix A.5).

In Fig. 4.5 the sound pressure (left) and the vertical soil velocity at the surface (right) of 40 ms around the start of the noise replay (full replay time in Fig. 4.3) are shown to demonstrate in more detail the correlation between acoustic and seismic time signals. Fig. 4.6 shows the corresponding time signals of geophones buried in the depths of 0.30 m (left) and 0.60 m (right).
The general characteristics of the acoustic time signal are also found in the signals of all seismic sensors. With increasing depth the signals start later due to the increased distance between source and sensors. In all seismic signals, short impulsive disturbances are visible (e.g. at the times of about 694 ms, 700 ms and 704 ms). They are caused by mains hum, which affected the seismic measurements. This is discussed in detail in Section 4.1.2.1.

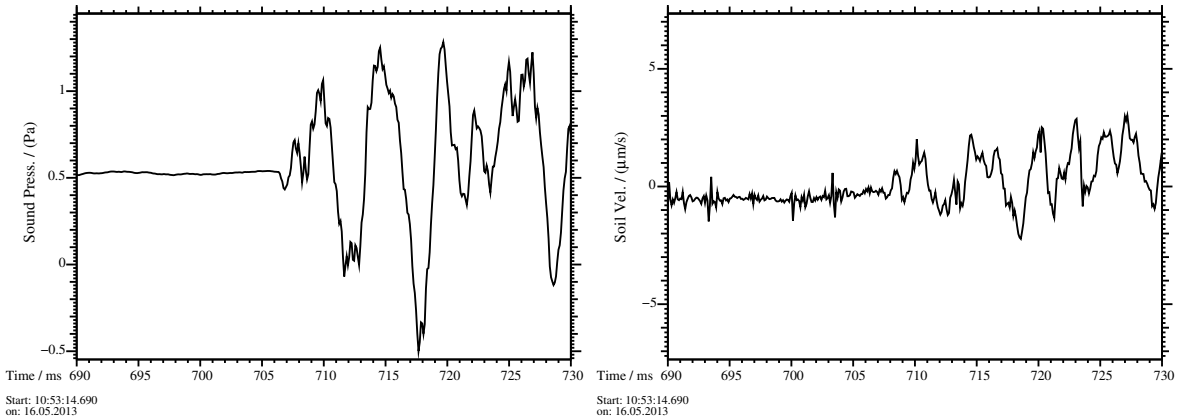

Figure 4.5: Time signals of an interval of 40 ms around the beginning of the noise replay, shown in Fig. 4.3. Left: Sound pressure, recorded with the microphone of channel 27. Right: Vertical soil velocity, recorded with a geophone at the surface, channel 23.

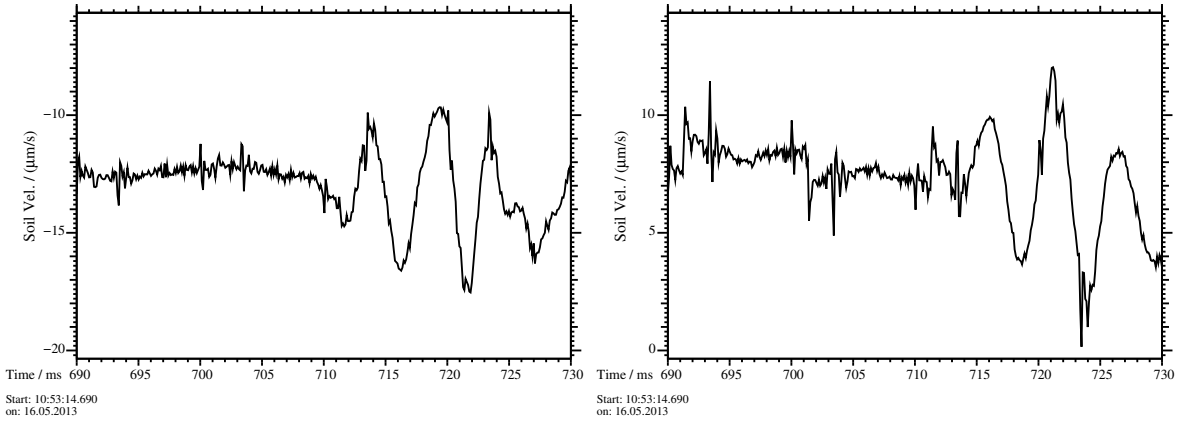

Figure 4.6: Time signals of the vertical soil velocity of an interval of 40 ms around the beginning of the noise replay, shown in Fig. 4.4. Left: Vertical soil velocity, recorded with a geophone in a depth of 0.30 m, channel 3. Right: Vertical soil velocity, recorded with a geophone in a depth of 0.60 m, channel 0.

4.1.2 Analysis in frequency space

With the fast Fourier transform (FFT) time intervals of a signal of N samples can be converted into a frequency spectrum. The theory of the FFT, described e.g. in [66], usually requires that $N = 2^n$ (with the integer $n > 0$). Mathematically the limitation of the time signal to a finite interval T represents its multiplication with a rectangle function (with value 1 in the time interval T and 0 outside) in the time domain. Additionally, the discretisation of the signal is – in mathematical terms – the multiplication with a Dirac comb. Both effects can lead to spectral leakage: The spectrum of e.g. a pure, continuous sine function contains only two δ-peaks at the frequency f of the sine and at its negative value $-f$, while the spectrum obtained for the discretised, finite sine shows a broadening of these peaks and contains oscillations around f and $-f$. To limit the effects of the spectral leakage, additionally a window function can be multiplied to the time signal. In the presented evaluations a Hann window is multiplied to the time signal of each interval before performing the FFT. All spectral values are multiplied by the normalisation factor

$$f_{\text{norm}} = \frac{\sqrt{8/3}}{N}. \tag{4.5}$$

Of this the first component $1/\sqrt{N}$ follows from the periodogram normalisation to make the sum of the N squared spectral magnitude values equal to the mean-square value of the N values of the time signal in the interval used for the FFT. The second component, $\sqrt{8/3}/\sqrt{N}$, is the inverse of the sum over the squares of the N values of the Hann window, to approximately compensate for the decrease of the signal values in the time domain from the multiplication by the window. The precise expression of the Fourier transform of a time signal, multiplied with a rectangle function, a Dirac comb and a Hann window is given in [26] and [27].[28]

Using the FFT a real-valued time signal of length T consisting of N samples is converted to a complex spectrum with N spectral points. The frequencies of the spectrum cover the range $0\,\text{Hz} \leq f < 0.5 \cdot f_S$ with $N/2$ spectral points (neglecting negative frequencies) where f_S is the used sampling rate of the time signal. The sampling rate directly determines how many samples N will be used for the FFT in a chosen time interval T:

$$N = f_S \cdot T. \tag{4.6}$$

In frequency space the resolution of the spectrum is given by

$$\Delta f = \frac{f_S}{N} = \frac{1}{T}. \tag{4.7}$$

[28] Note that in [26] a different sign convention for the FFT and a slightly different normalisation had been used. The equation as used in the evaluation program *Eingabe* is given in [27, p. 41]. However, the normalisation factor in [27, p. 57] has to be corrected to $\sqrt{8}/(N \cdot \sqrt{3})$.

These equations show a fundamental problem of the Discrete Fourier Transform: To obtain a higher resolution in frequency space the number of samples N needs to be increased which will also increase the length of the time interval T. The FFT gives the complex amplitudes of the different frequencies that contribute to a time signal, averaged over the time interval T. The challenge is to find a good ratio between a high frequency resolution and a short time interval used for the FFT. For most evaluations in this work a time interval of $T = 0.8192\,\mathrm{s}$ was used, corresponding to $N = 8192$ samples recorded with a sampling rate of $f_\mathrm{S} = 10\,\mathrm{kHz}$. This leads to a frequency resolution of $\Delta f \approx 1.22\,\mathrm{Hz}$. The FFT was performed using the software *Eingabe* which provides the real and imaginary parts, the values of the spectral amplitude $a(f)$ and the phase $\phi(f)$, defined in Eq. (4.8), as well as the power $a(f)^2$. Additionally, with *Eingabe* single spectra and sequences of spectra can be plotted. For the latter so-called spectrograms consecutive spectra of the length T each were calculated without overlap of the single time intervals.

With the FFT complex spectral values are calculated

$$\tilde{a}(f) = a(f) \cdot \mathrm{e}^{\mathrm{i}\phi(f)} \tag{4.8}$$

with the amplitude

$$a(f) = \sqrt{(\Re(\tilde{a}(f)))^2 + (\Im(\tilde{a}(f)))^2} \tag{4.9}$$

and the phase

$$\phi(f) = \arctan\Big(\frac{\Im(\tilde{a}(f))}{\Re(\tilde{a}(f))}\Big). \tag{4.10}$$

$\Re$ and $\Im$ depict the real and imaginary parts of $\tilde{a}(f)$, respectively. In this work by the term *spectral amplitude* – either in plots or in the discussion – it is referred to the real values $a(f)$. Occasionally, the power $a(f)^2$ is shown in the plots of spectra and spectrograms.

4.1.2.1 Representative spectra and spectrograms

Here the spectra and spectrograms corresponding to the time signals shown in Section 4.1.1.1 are presented.
All spectra were calculated for time intervals of $T = 0.8192\,\mathrm{s}$, corresponding to $N = 8192$ samples. With the sampling rate of $f_\mathrm{S} = 10\,\mathrm{kHz}$ this results in frequencies of the spectra of up to 5 kHz with a spectral resolution of $\Delta f \approx 1.22\,\mathrm{Hz}$. However, the range of all plots is limited to the interval $0\,\mathrm{Hz} \leq f \leq 1000\,\mathrm{Hz}$. Above that upper limit the seismic amplitudes usually have dropped to the background level (or are close to it). Thus, frequencies $f > 1000\,\mathrm{Hz}$ are of no further interest for the evaluations. All plots show the normalised power of sound pressure and vertical soil velocity, respectively.
In Fig. 4.7 and Fig. 4.8 spectra of the aircraft overflight number 13 (see Table A.2) are plotted. The beginnings of the time intervals used for the calculation of the shown

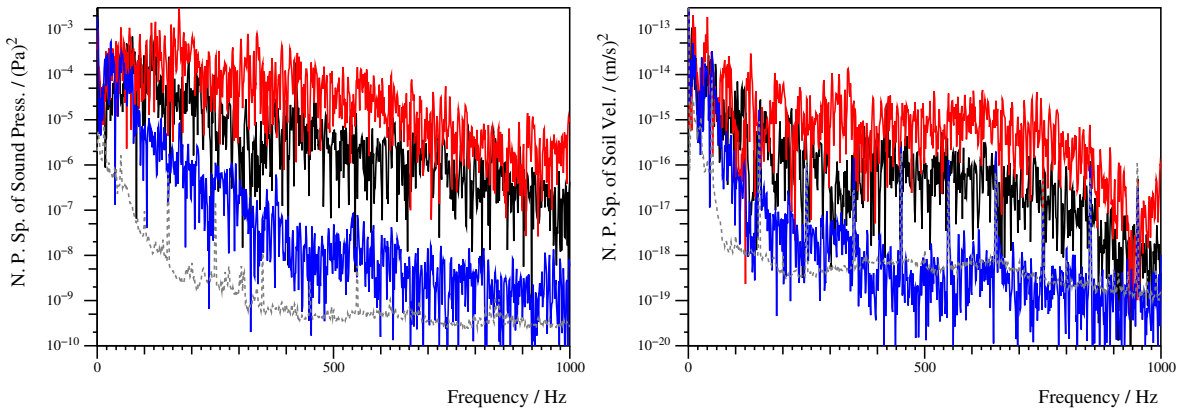

Figure 4.7: Normalised power spectra of jet-aircraft overflight number 13 calculated for the following times, the corresponding incident angles of the signal α and the distances between aircraft and setup r:
Black spectra: 9:26:51 (UTC), $\alpha \approx 60°$, $r \approx 950\,\text{m}$,
red spectra: 9:26:59 (signal of the cpa of the aircraft), $\alpha \approx 34°$, $r \approx 725\,\text{m}$,
blue spectra: 9:27:32, $\alpha \approx 72°$, $r \approx 4000\,\text{m}$.
The dashed, grey spectra depict the averaged background power at each sensor. The plots are limited to the frequency range $0\,\text{Hz} \leq f \leq 1000\,\text{Hz}$.
Left: Sound pressure, recorded with the microphone of channel 29.
Right: Vertical soil velocity, recorded with a geophone at the surface, channel 24.

spectra in each graph are: Black spectra: 9:26:51 (UTC), corresponding to $\alpha \approx 60°$ at a distance of 950 m between sensors and the approaching aircraft; red spectra: 9:26:59, corresponding to the signals of the cpa of the overflight ($\alpha \approx 34°$, distance between aircraft and setup of about 725 m), and blue spectra: 9:27:32, corresponding to $\alpha \approx 72°$ at a distance between departing aircraft and sensors of about 4000 m.

In Fig. 4.7 and Fig. 4.8 the spectra recorded around the cpa (red spectra) show for all sensors and nearly all frequencies the largest spectral amplitudes. For the approaching aircraft (black spectra) the amplitudes are systematically smaller and for the departing aircraft in a distance of about 4000 m (blue spectra) only for low frequencies significant amplitudes are recorded. For the latter at frequencies $f \gtrsim 400\,\text{Hz}$ the soil velocities recorded at all geophones approximately reaches values of the background amplitudes indicated by the dashed, grey spectra. The calculation of the averaged background amplitudes is discussed in Appendix A.5.

In the single spectra strong fluctuations of the amplitudes are visible. This is a usual characteristic of the spectral values. If multiple spectra, corresponding to time signals recorded under similar conditions, are calculated, their spectral values can be averaged. This is demonstrated in Fig. 4.11 for the signals of the noise replay. For a single aircraft overflight excitation conditions (i.e. the angle of incidence α) changed too fast for successful averaging. Sound pressure and soil velocity of different aircraft overflights cannot be averaged due to different trajectories of the aircraft. These resulted in different distances between source and sensor, in different angles of incidence α as well

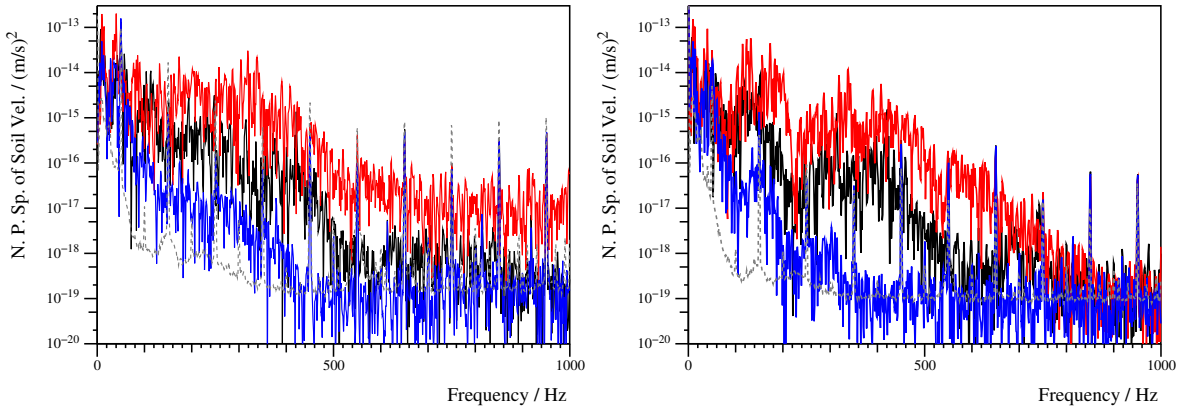

Figure 4.8: Normalised power spectra of the vertical soil velocity recorded with buried geophones for the times as in Fig. 4.7 for the frequency range $0\,\mathrm{Hz} \leq f \leq 1000\,\mathrm{Hz}$. Left: Geophone in a depth of 0.30 m, channel 6. Right: Geophone in a depth of 0.60 m, channel 13.

as different angles from the engines of the aircraft to the sensors. Additionally, each aircraft has a specific sound-emission characteristics. All these are reasons for different recorded amplitudes for each overflight event. However, as shown in Section 4.2, by using the ratio between vertical soil velocity and sound pressure independence of the specific overflight event can be achieved. Thus, the spectral coupling coefficient can be averaged in corresponding intervals of α.

In the spectra of the vertical soil velocity, especially in the blue ones of the sensor buried deepest ($z_S = 0.60\,\mathrm{m}$), narrow spectral peaks are visible at odd multiples of 50 Hz. These stem from mains hum in the used equipment.

Instead of spectra calculated for a single time interval of length $T = 0.8192\,\mathrm{s}$ in Fig. 4.9 and Fig. 4.10 the normalised power spectrograms of the overflight are shown. They represent the time evolution of the spectral amplitudes, i.e. they show spectra of consecutive time intervals. Fig. 4.9 gives the spectral sound pressure (top) and the vertical soil velocity at the surface (bottom) of the overflight shown in Fig. 4.1. In Fig. 4.10 the respective vertical soil velocities recorded with a geophone in depth 0.30 m (top) and that recorded in depth 0.60 m (bottom) are given, corresponding to the time signals in Fig. 4.2.

In the graphs the time 9:26:59 (corresponding to the time when the signals of the cpa were recorded) is marked with a red line at the top. Additionally, the time during which the angle of incidence α of the acoustic signal was smaller than 60° – and which was later used for the determination of the soil properties – is defined by two blue lines.

The acoustic signal emitted by the aircraft is a broadband one with considerable amplitudes for frequencies up to 1 kHz (and even above – not shown here). The largest signal amplitudes were recorded around the cpa. In general the spectral amplitudes decrease with frequency and with increasing angle of incidence α – the latter is

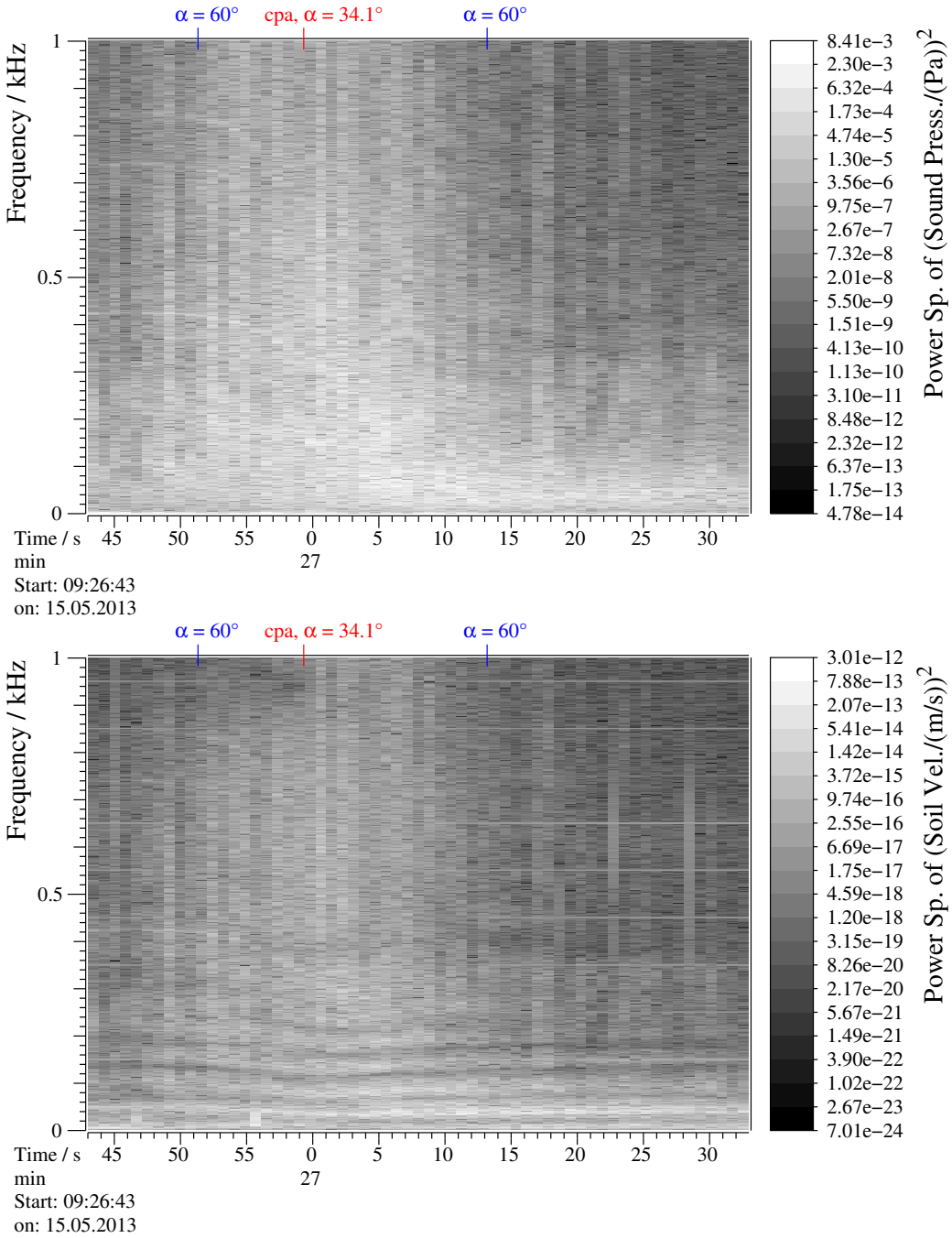

Figure 4.9: Normalised power spectrograms of jet-aircraft overflight number 13. The spectra are recorded for consecutive time intervals of $T = 0.8192\,\mathrm{s}$. The signals of the cpa are recorded at 9:26:59 (red line at the top). The time interval during which α was smaller than 60° (which is used for the fit, see Section 4.4) is marked with blues lines at the top. The plots are limited to the frequency range $0\,\mathrm{Hz} \leq f \leq 1000\,\mathrm{Hz}$.
Top: Normalised power spectrogram for the sound pressure, recorded with the microphone of channel 29.
Bottom: Normalised power spectrogram for the vertical soil velocity at the surface, recorded with the geophone of channel 24.

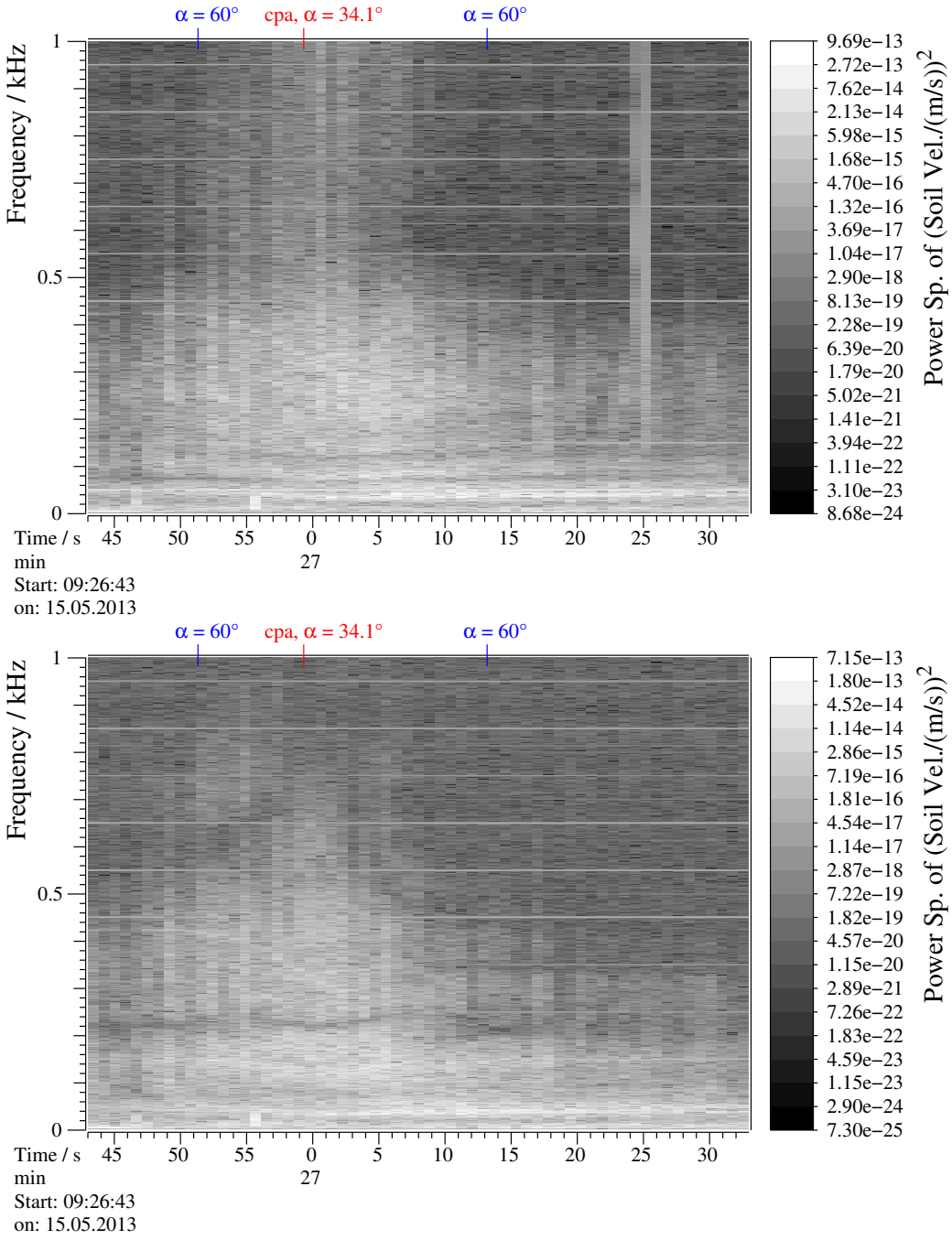

Figure 4.10: Normalised power spectrograms of the vertical soil velocity for a jet-aircraft overflight (as shown in Fig. 4.9) recorded with buried geophones. Top: Geophone in the depth of 0.30 m, channel 6. Bottom: Geophone in the depth of 0.60 m, channel 13.

mainly caused by the increasing distance between aircraft and sensors. The broadband characteristics of the signal hold true for the whole time of the overflight. There is no notable modulation of the spectral amplitudes with frequencies aside from the usual signal fluctuation (see Fig. 4.7, left). As visible in the spectrogram (Fig. 4.9, top) and especially in the single spectra (Fig. 4.7, left) the amplitudes of higher frequencies decrease with increasing distance of the aircraft from the sensor setup. For frequencies of up to about 100 Hz the amplitude of sound pressure hardly changes for distances between aircraft and sensors of up to 4 km.
The spectral amplitudes of the vertical soil velocity in various depths follow the general tendencies of the sound pressure: They decrease with frequency and with increasing α. Additionally, with increasing depth especially the amplitudes of higher frequencies decrease faster. This is due to the frequency-dependent absorption in the soil. The fundamental difference to the spectral amplitudes of the sound pressure lies in a spectral modulation of the soil velocity. This leads to consecutive frequency bands of increased and decreased soil velocity which are visible in the spectrograms of all geophones (Fig. 4.9, bottom, and Fig. 4.10, both graphs). The frequencies of the increased and decreased soil velocity change over time – this change is better explained as a dependency on the angle of incidence α (see also Section 4.2): The frequencies have their smallest values at the cpa (i.e. the smallest values of α for the presented overflight) and they increase with increasing α. These frequency bands are caused by interference of various seismic waves excited at different locations at the surface by the incident, plane, acoustic wave. This interference will be evaluated in detail in Section 4.4 using the theoretical models introduced in Section 2.3.
In the spectrograms of the soil velocity lines at frequencies of 50 Hz and its odd multiples are visible. These are the artefacts caused by mains hum visible as narrow spectral peaks in the plots of the single spectra. Since their frequency does not change over time, they show up in the spectrograms as horizontal lines of constant frequencies and approximately constant amplitude. They might be masked by the acoustically induced soil velocity of stronger amplitude (around the cpa) or at lower frequencies.

In Fig. 4.11 averaged, normalised power spectra of the noise replay (time signals shown in Fig. 4.3 and Fig. 4.4) are plotted: For consecutive time intervals of the length $T = 0.8192\,\mathrm{s}$ single spectra are calculated and their spectral amplitudes are averaged. These spectra are calculated for the time interval from 10:53:15 to 10:53:44, corresponding to 35 consecutive spectra. Fig. 4.11 (left) shows the spectrum of the sound pressure. The right graph shows spectra of the vertical soil velocity recorded with a geophone at the surface (black) and with buried geophones in the depth of 0.30 m (red) and in the depth of 0.60 m (blue).
The spectral power of the sound pressure of the acoustic signal emitted by the speaker

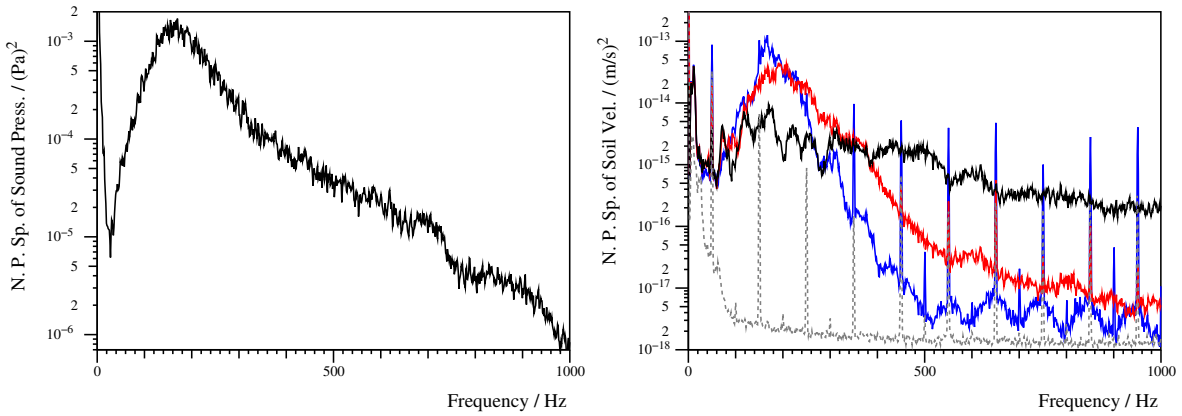

Figure 4.11: Normalised and averaged power spectra of the noise replay, corresponding to the time signals shown in Fig. 4.3 and Fig. 4.4. For time intervals of T = 0.8192 s 35 consecutive spectra are calculated whose spectral amplitudes are averaged.
Left: Power spectrum of the sound pressure, recorded with microphone of channel 27. The background level for all frequencies is significantly smaller than the recorded sound pressure (see Fig. 4.7, left), thus it is not plotted here.
Right: Power spectra of the vertical soil velocity: Black: Geophone at the surface, channel 23; red: Geophone in depth of 0.30 m, channel 3; blue: Geophone in 0.60 m depth, channel 0. The dashed, grey spectrum shows the background level at the geophone in 0.60 m depth.

in the frequency range 200 Hz $\leq f \leq$ 750 Hz shows a monotonous decrease without significant fluctuations proportional to f^{-4}. For lower frequencies it deviates from that proportionality for technical reasons, as stated in Section 3.2.2. The maximal spectral power of the broadband signal is recorded between 155 Hz and 170 Hz.

The spectra of the vertical soil velocities recorded with geophones in various depths show a more complex behaviour. For all geophones several local minima and maxima of the spectral amplitudes can be identified. For many of them the frequency difference between successive local minima or maxima, respectively, is approximately constant. They are caused (as discussed for the signals of the aircraft overflight) by constructive and destructive interference of seismic waves excited at various locations by the acoustic signal. Due to the small distance of few metres between the speaker and the sensors the wavefronts of the acoustic noise signal are spherical. Thus, the treatment of the interference of acoustically excited seismic waves is much more complicated than for the plane waves during the aircraft overflight events. Hence, it is discussed only qualitatively in this thesis.

The spectra of the buried geophones (blue: z_S = 0.30 m, red: z_S = 0.60 m) show the maximal soil velocity around 170 Hz similar to the acoustic spectrum. However, the spectral amplitude decreases much faster with increasing frequency. For the geophone in depth of 0.60 m at around 500 Hz the signal has decreased to the background level (dashed, grey spectrum). The geophone placed at the surface shows no significant

maximum of the soil velocity around 170 Hz. This is believed to be caused by destructive interference of various seismic waves excited at the location of the sensors and in its vicinity.
Again, the lines of the mains hum at 50 Hz (and its odd multiples) are clearly visible in the spectra of the geophones.

There is little variation over time in the sound pressure and the soil velocity during the replay of the broadband noise. For the sake of completeness the spectrograms of the four sensors are shown in Appendix A.6.

4.2 Acoustic-seismic coupling coefficient

Here the acoustic-seismic coupling coefficient is introduced as a fundamental method of the evaluation of the aircraft overflights. It is a measure for the strength of the excited soil vibrations by an acoustic signal. As shown in this section it can be used to achieve independence on a specific recorded event. Thus, the coupling coefficients calculated for different overflight events can be averaged.

Because the coupling from acoustic to seismic waves depends on the frequency f and changes with time t, the coupling coefficient is defined as the ratio of the spectral amplitude of vertical soil velocity over the spectral amplitude of sound pressure[29]:

$$\widetilde{Cc}(f,t) = \frac{SoilVelocity_{\perp}(f,t)}{SoundPress.(f,t)}. \tag{4.11}$$

The calculated coupling coefficient $\widetilde{Cc}(f,t)$ of overflight number 13 of a geophone at the surface, channel 24, and the microphone next to it, channel 29, (respective spectrograms shown in Fig. 4.9) is plotted in Fig. 4.12.
The frequency bands of increased and decreased coupling strength are the result of corresponding frequency bands in the recordings of the vertical soil velocity, as shown in Fig. 4.9 (bottom). The spectral coupling coefficient and the frequencies of the constructive and destructive interference strongly changes as the aircraft passes the setup. To compare and even average different overflight events (as is shown in Section 4.2.1) the trajectories of each overflight is used to calculate the angle of incidence α of the acoustic wave from the normal to the ground surface. Thus, Eq. (4.11) can be re-written replacing the time by the corresponding angle α:

$$\widetilde{Cc}(f,t) \rightarrow Cc(f,\alpha) = \frac{SoilVelocity_{\perp}(f,\alpha)}{SoundPress.(f,\alpha)}. \tag{4.12}$$

[29] For the calculation of the coupling coefficient the sound pressure of the microphone closest to the geophone was used (see sensor setup in Fig. 3.3). Thus, usually only the depth of the geophone is stated.

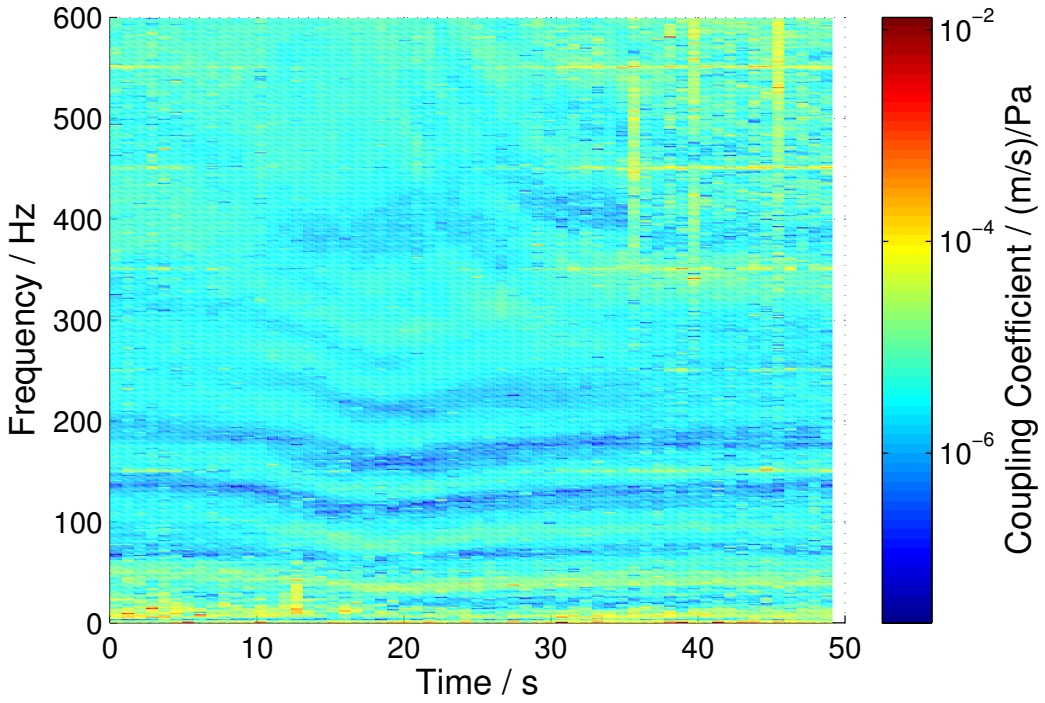

Figure 4.12: Spectral coupling coefficient in (m/s)/Pa over time calculated with Eq. (4.11). The time interval of 50 s, starting 09:26:43 on 15th May 2013 corresponds to the aircraft overflight number 13. The corresponding spectrograms of the sound pressure and the vertical soil velocity are shown in Fig. 4.9. Lines of mains hum are still visible.

The resulting spectrally resolved coupling coefficient $Cc(f,\alpha)$ is given in Fig. 4.13. The whole range of α was divided in small intervals $\Delta\alpha \approx 1.35°$ (see Section 4.2.1). For this plot all spectra recorded at a time corresponding to such an interval $\Delta\alpha$ were averaged. This includes both spectra from the approach towards and the departure from the setup of the aircraft which both cover approximately the same range of angles of incidence.
As shown in Fig. 4.13 the pattern of frequency bands of increased and decreased coupling strength can be correlated to the angle of incidence α. This becomes even clearer when averaging several overflight events.

4.2.1 Averaging of signals of corresponding angle intervals to achieve event-independent values

For 16 aircraft-overflight events the coupling coefficient $Cc(f,\alpha)$ was calculated with Eq. (4.12), using the trajectories of each overflight to obtain the corresponding α. To determine the averaged coupling coefficient data were grouped according to the angle of incidence α of the acoustic signal: For a given frequency all coupling coefficients were averaged that correspond to the same α intervals obtained by dividing the range $11.8° \leq \alpha < 80°$ into 50 equally-spaced intervals, resulting in a resolution of $\Delta\alpha \approx 1.35°$. Additionally, the standard deviation at each data point was calculated for all values used for

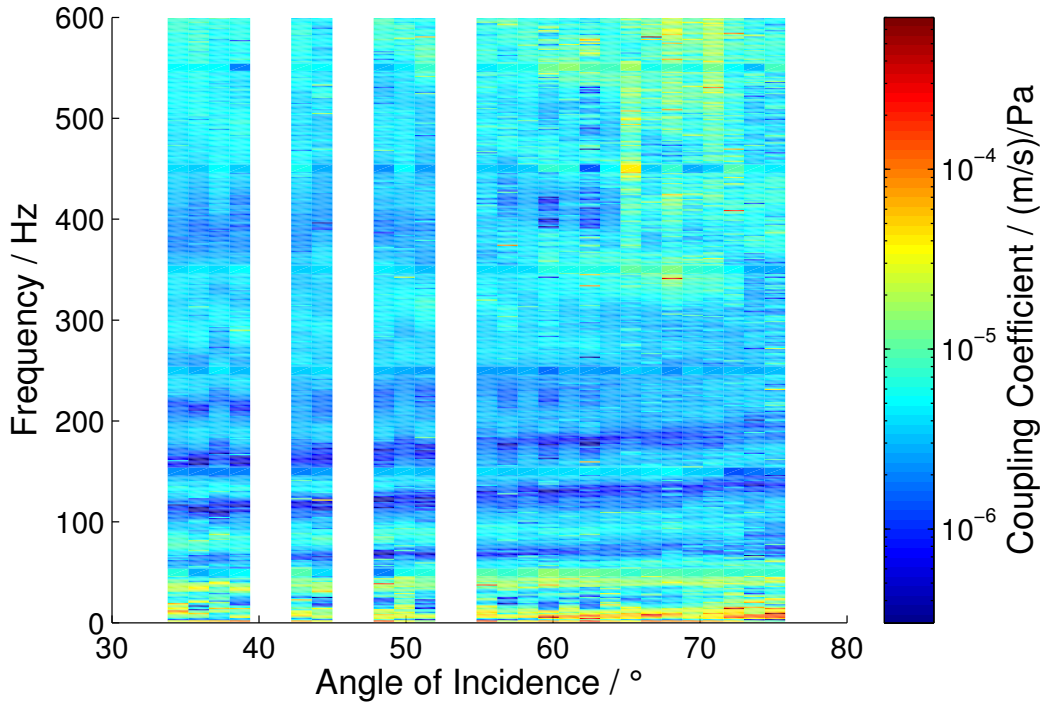

Figure 4.13: Spectral coupling coefficient in (m/s)/Pa of the aircraft overflight number 13, calculated with Eq. (4.12), plotted over the angle of incidence α. Around α approximately 40°, 45° and 53° as well as below 34° no data points are available for this particular overflight. Additionally, lines of mains hum were excluded from the calculation, filling in averages from neighbouring frequencies.

averaging.

The observed pattern of consecutive bands of increased and decreased coupling strength is consistent for all overflights recorded. This is verified by looking at the standard deviation of the 16 overflight events divided by the averaged coupling coefficient for each data point shown in Fig. 4.14. A reversed pattern of frequency bands can be observed: The variation in the measured data between different events is small in all regions where strong signals can be observed – especially for the bands of increased coupling strength. This is indicated by a ratio of standard deviation over averaged coupling coefficient of about 0.1. Stronger fluctuations with a ratio of around 0.5 to 0.7 (and for single points even above 1 up to 5.5) are observed in the frequency bands of decreased coupling strength, for low frequencies and for large angles of incidence. In all these ranges the acoustic and seismic signals are weak and minor fluctuations lead to a large relative standard deviation.

After averaging of 16 jet-aircraft overflights and by using the angle of incidence α to obtain event-independent values the averaged and spectrally resolved coupling coefficient is shown in Fig. 4.15. The pattern of six to seven consecutive frequency bands of increased and decreased coupling strength between about 70 Hz and about 400 Hz can be observed clearly.

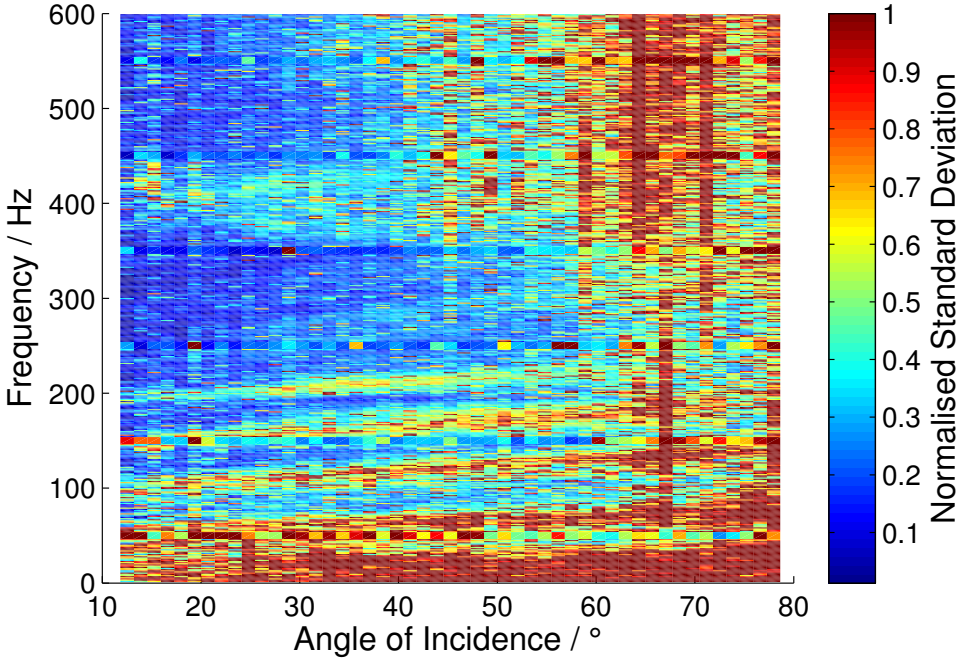

Figure 4.14: Standard deviation of the coupling strength from 16 different overflight events of jet aircraft relative to the averaged coupling coefficient. A reversed pattern of consecutive frequency bands can be seen in such a way that the bands of increased coupling strength show much less variation while the bands of small coupling strength show higher fluctuations due to their small overall signal strengths. The colour scale was limited to the interval [0,1].

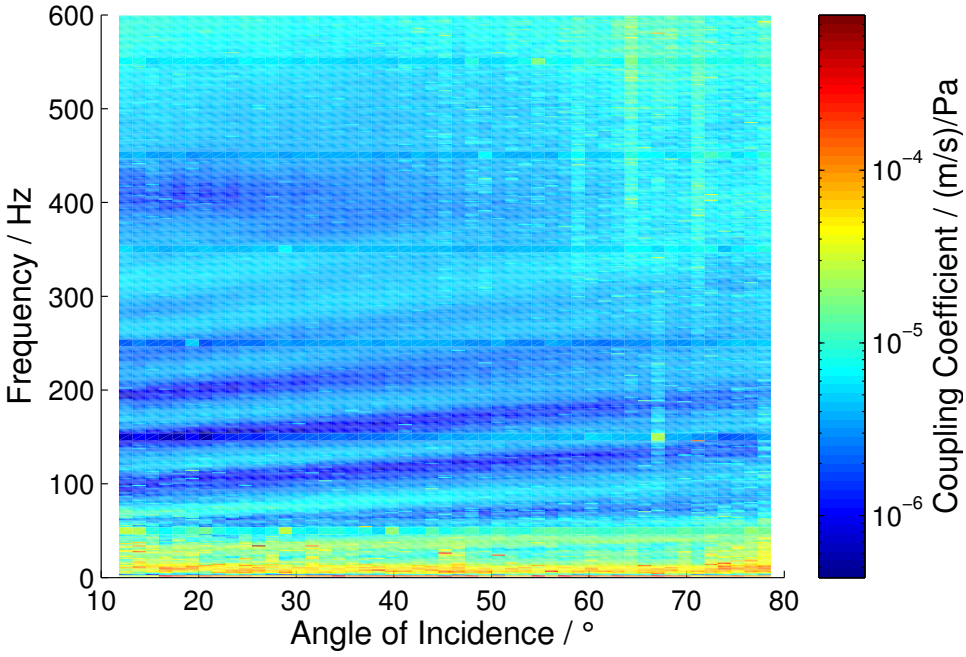

Figure 4.15: Averaged coupling strength in (m/s)/Pa of 16 events of jet aircraft passing nearly overhead for a geophone at the surface (channel 24). The pattern of consecutive frequency bands of increased and decreased coupling coefficient can be seen which is caused by constructive and destructive interference in the ground. Values at odd multiples of 50 Hz are excluded from the plot and replaced by the average from neighbouring frequencies.

4.2.2 Frequency averaging and determination of the frequency course of the bands of increased coupling strength

To determine the frequencies of the bands of increased coupling strength for all angles $f_{\mathrm{max},k}^{\mathrm{meas}}(\alpha)$[30] precisely, small fluctuations in the measured data needed to be corrected. Thus, frequency-distance-weighted smoothing is applied to the data: The spectrally resolved coupling coefficient for each frequency f_i is replaced by a weighted average of the coupling coefficient in the interval $[f_{i-2}, f_{i+2}]$ as given by:

$$\overline{Cc}(f_i,\alpha) = \frac{1}{\delta_i}\left(Cc(f_i,\alpha) + \sum_{j=-2;j\neq 0}^{2} \frac{Cc(f_{i+j},\alpha)}{(|f_i - f_{i+j}|)^{\eta}}\right) \text{ with } \delta_i = 1 + \sum_{j=-2;j\neq 0}^{2} \frac{1}{(|f_i - f_{i+j}|)^{\eta}}.^{31} \tag{4.13}$$

Here $\overline{Cc}(f_i,\alpha)$ is the smoothed value of the coupling coefficient and $Cc(f_i,\alpha)$ corresponds to the value obtained as ratio of the measured vertical soil velocity and the sound pressure at the frequency f_i and for a given α. η is a weighting exponent that was set to $\eta = 0.8$ empirically. Fig. 4.16 shows the spectrum of the coupling coefficient (angle-averaged over 16 overflight events) in blue and the effect of the frequency-distance-weighted smoothing in red to suppress fluctuations. The graph refers to the coupling coefficient obtained from the vertical soil velocity recorded with a geophone at the surface (channel 24) and the sound pressure, recorded with the microphone of channel 29 and the angle $\alpha \approx 17°$.

Now, starting with the spectral coupling coefficient of the smallest angle of incidence ($\alpha \approx 12°$) each local maximum of the coupling coefficient is identified.[32] For subsequent larger angles the respective adjacent local maximum in a small frequency interval around the previously found maximum were determined. This results in the courses of the frequency values $f_{\mathrm{max},k}^{\mathrm{meas}}(\alpha)$, which are shown dotted in Fig. 4.24 for the angles of incidence used for the fit algorithm.

[30] The index k refers to the number of the frequency band of increased coupling strength. Its value is of no importance for any calculation, but it is merely used to specify the particular bands. Thus, the band in Fig. 4.15 starting at $f \approx 70\,\mathrm{Hz}$ at $\alpha \approx 12°$ and reaching frequencies of $f \approx 91\,\mathrm{Hz}$ at $\alpha \approx 60°$ is referred to by $k = 1$. The next band with $f(\alpha \approx 12°) \approx 116\,\mathrm{Hz}$ and with $f(\alpha \approx 60°) \approx 146\,\mathrm{Hz}$ is referred to by $k = 2$. The band of the highest frequencies still visible in Fig. 4.15 starts at $f(\alpha \approx 12°) \approx 316\,\mathrm{Hz}$ and is referred to by $k = 6$.

[31] This equation describes the frequency averaging of the coupling coefficient. In [57] is was falsely stated that it refers to calculations for the vertical soil velocity only.

[32] A manual selection form the list of all found local maxima was necessary: So only those corresponding to the frequency bands caused by interference were further processed. Those corresponding to local maxima due to smaller fluctuation in the measured data were excluded.

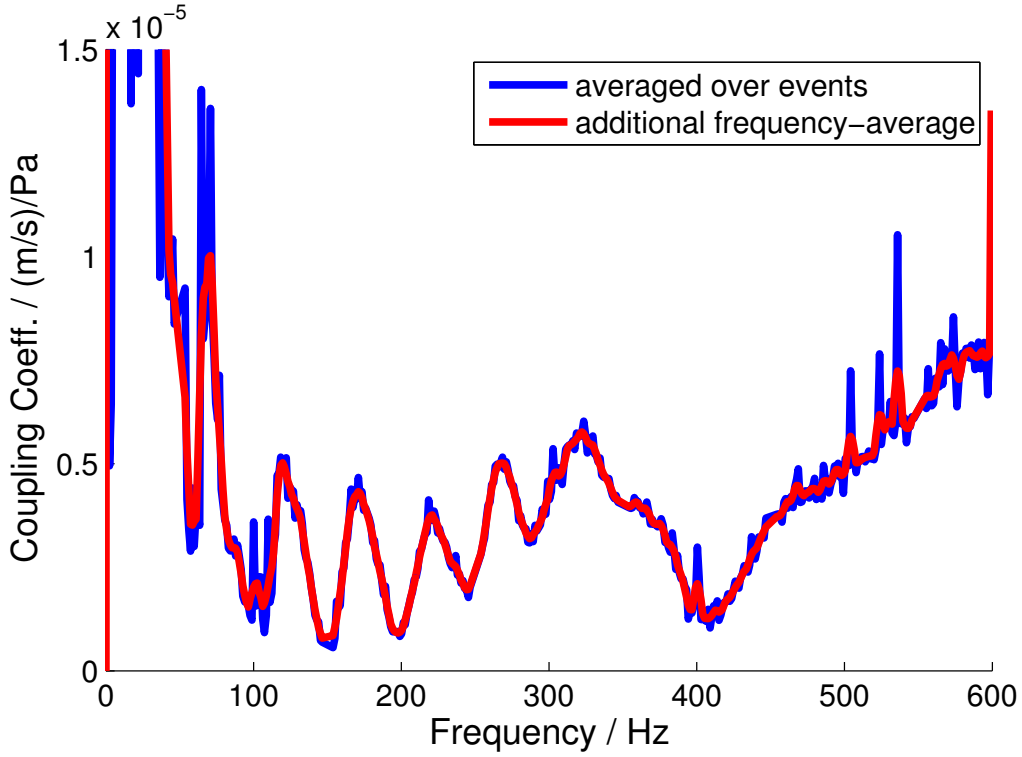

Figure 4.16: Spectrum of the coupling coefficient for a geophone at the surface (channel 24) and an angle of incidence $\alpha \approx 17°$. Blue: Values of 16 overflight events averaged in small angle intervals. Red: Additional application of frequency smoothing to suppress fluctuations.

4.3 Relative amplitudes of P and SV waves

Before using the pattern of interference (see Fig. 4.15), which is caused by various seismic waves, to determine the soil properties in Section 4.4, here the relative amplitudes of the seismic waves reaching the sensor are discussed. They are needed to estimate the influence on the overall seismic signal of P and SV waves, which might have been reflected and undergone conversion of the wave type several times. Thus, the main contributors to the interference can be identified and waves hardly contributing at all can be neglected for the calculations.

Each reflection at one of the boundaries reduces the amplitude of a wave. Thus, the amplitudes of the seismic waves interfering at a sensor can be obtained from the equations of the reflection coefficients at the underground boundary (given in Section 2.2.2) and at the free surface (given in Section 2.2.3). For the calculation of the coefficients at the free surface the velocities of P and S waves in the upper soil layer need to be known. Additionally, for the reflection coefficients at the underground boundary the respective wave velocities in the second soil layer as well as the ratio of the densities of both layers are required. The P-wave velocities were approximatively determined by a seismic refraction survey to be $v_{P1} \approx 200\,\mathrm{m/s}$ and $v_{P2} \approx 1400$ - $1700\,\mathrm{m/s}$ [60]. The high velocity of v_{P2} is believed to be caused by ground water contained below the boundary. Additionally, with the performed fit algorithm (described in Section 4.4.1 and its results given in Section 4.4.2) the P-wave velocity in the first layer v_{P1} was determined much more precisely as $v_{P1} = 228\,\mathrm{m/s}$ ($+2\,\mathrm{m/s}$/$-4\,\mathrm{m/s}$). Thus, for all calculations the more realistic value of $v_{P1} = 230\,\mathrm{m/s}$ will be used here. For v_{P2} the value $v_{P2} = 1400\,\mathrm{m/s}$ is used.

For the other required values the following assumptions are used that were discussed in the Introductory assumptions: The S-wave velocity in the first layer is $v_S = v_P/\sqrt{3} \approx 133\,\mathrm{m/s}$. In the second layer S waves can propagate only in the soil matrix (but not in the contained water), thus the approximation $v_{S2}{=}v_{S1}{\cdot}1.15 \approx 153\,\mathrm{m/s}$ is used. For the ratio of the density of both layers the common value $\rho_2/\rho_1 = 1.25$ is assumed.

In this section, firstly, the influence of the use of vertical-component geophones on the recorded, relative P- and SV-wave amplitudes is discussed in Section 4.3.1. Then the calculations of the reflection coefficients at the free surface (in Section 4.3.2) and at the underground boundary (in Section 4.3.3) are given. The ratio between the amplitudes of acoustically excited P and SV waves are estimated in Section 4.3.4. Finally, in Section 4.3.5 the resulting relative amplitudes of the various seismic waves reaching the sensor are presented.

4.3.1 Vertical and horizontal components of the seismic signals

With the used setup of geophones at several positions the vertical component of the soil velocity together with two horizontal components were recorded. At other positions

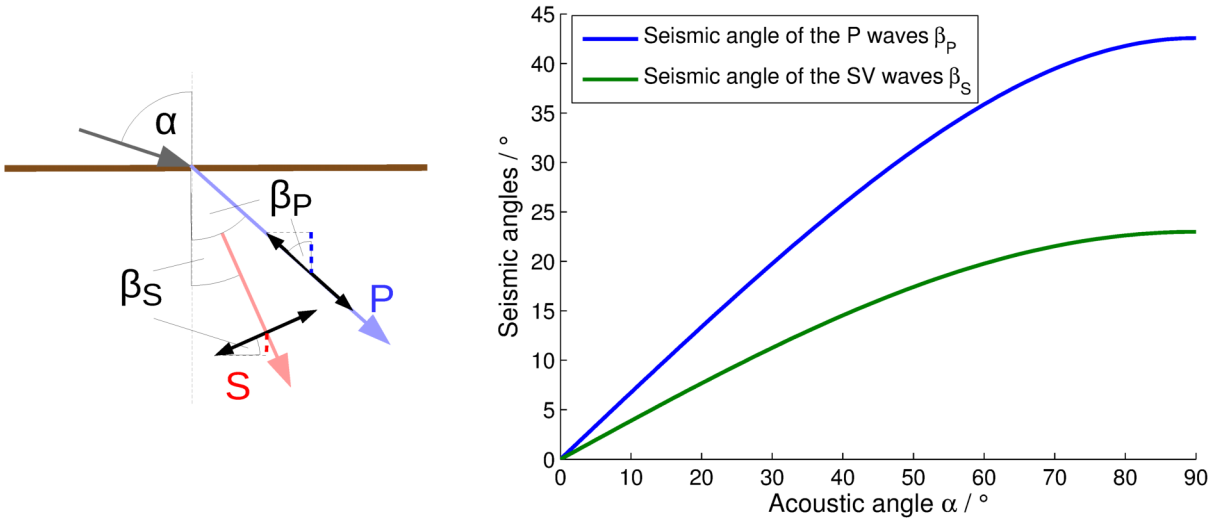

Figure 4.17: Left: Sketch of P (blue) and SV waves (red) excited by an incident acoustic wave (grey). The directions of the displacement of soil particles with respect to the propagation direction of P and SV waves are indicated by the black double arrows. The vertical components of both displacements are indicated by dashed lines. Right: The seismic angles β_P and β_S versus the acoustic angle of incidence α, calculated with Eq. (2.29) for the values $v_0 = 340\,\mathrm{m/s}$, $v_{\mathrm{P1}} = 230\,\mathrm{m/s}$ and $v_{\mathrm{S1}} = 133\,\mathrm{m/s}$.

only a vertical-component geophone was used (see Fig. 3.3 in Section 3.2.1). During the evaluation mainly the vertical components of the soil velocity were used, which has significant implications when talking about the displacement caused by P and SV waves. Due to a smaller velocity of the SV wave v_{S1} than that of the P wave v_{P1}, the wave vector of the SV wave points more steeply into the ground than that of the P wave, i.e. $\beta_\mathrm{S} < \beta_\mathrm{P}$. Furthermore, the displacement of soil particles of a P wave is parallel to its wave vector and that of an SV wave is perpendicular to its wave vector as indicated in Fig. 4.17 (left). With a vertical-component geophone only the vertical projections of the amplitudes of the respective displacement of P and SV waves are recorded which are given by:

$$\begin{aligned} a_{\mathrm{P},\perp} &= a_\mathrm{P} \cdot cos(\beta_\mathrm{P}), \\ a_{\mathrm{S},\perp} &= a_\mathrm{S} \cdot sin(\beta_\mathrm{S}). \end{aligned} \tag{4.14}$$

This means, that the ratio between the recorded (i.e. vertical) and the actual soil-velocity amplitude of SV waves is smaller than that of P waves as long as $\sin(\beta_\mathrm{S}) < \cos(\beta_\mathrm{P})$. Both angles are connected via their respective wave velocities by the general laws of reflection and reflection (Eq. (2.29)). With the used ratio $v_{\mathrm{P1}}/v_{\mathrm{S1}} = \sqrt{3}$ the trigonometric relation is true for angles $\beta_\mathrm{P} < 60°$. As shown in Fig. 4.17 (right) this is fulfilled for the full range of acoustic angles of incidence $0° \leq \alpha \leq 90°$ for the used wave velocities $v_0 = 340\,\mathrm{m/s}$, $v_{\mathrm{P1}} = 230\,\mathrm{m/s}$ and $v_{\mathrm{S1}} = 133\,\mathrm{m/s}$. The maximal seismic angles corresponding to $\alpha = 90°$ are $\beta_\mathrm{max} \approx 42.6°$ and $\beta_{\mathrm{S,max}} \approx 23°$.

The amplitude of SV waves excited upon reflection (shown in Section 4.3.2 and Sec-

tion 4.3.3) and directly by the acoustic wave (Section 4.3.4) is much smaller than that of P waves, at least for smaller α. This effect is amplified by the usage of vertical-component geophones decreasing the relative ratio between P waves and SV waves as given in Eq. (4.14). Thus, SV waves will play a minor role in the interpretation of the recorded interference patterns – and if at all only at higher angles α.
Note that an SH wave has no displacement in vertical direction, thus it cannot be measured with a vertical-component geophone and should not be excited by an incoming (compressional) sound wave in the first place. Thus, in the evaluation SH waves are not considered and the nomenclature S waves refers to SV waves only.

4.3.2 Reflection coefficients at the free surface

An upwards-propagating seismic wave, stemming from reflection at an underground boundary of an acoustically excited seismic wave, shall be reflected at the surface of the soil, treated as free surface. Depending on the type of the seismic wave it impinges on the boundary under the angle β_P (if it is a P wave) or the angle β_S (if it is an SV wave). In both cases upon reflection generally both wave types are excited. Thus, four different reflection coefficients have to be considered resulting from the four combinations of the types of incident and reflected waves. They can be calculated using Eq. (2.36) to Eq. (2.39) in Section 2.2.3. For the used values $v_0 = 340\,\mathrm{m/s}$, $v_{\mathrm{P1}} = 230\,\mathrm{m/s}$ and $v_{\mathrm{S1}} = 133\,\mathrm{m/s}$ the reflection coefficients are plotted in Fig. 4.18 versus the acoustic angle of incidence α.

The first subscript of the reflection coefficients refers to the type of the incident wave towards the free surface and the second one to the type of the reflected wave. Thus, R^s_PP is the amplitude ratio between a reflected P wave and an incident P wave; R^s_PS that between a reflected SV wave and an incident P wave. As becomes obvious from Eq. (2.36) and Eq. (2.39) the values of the reflection coefficients R^s_PP and R^s_SS are identical – even though for perpendicular incidence ($\alpha = 0°$) neither an incident nor a reflected SV wave can exist.
The negative sign of the reflection coefficients in Fig. 4.18 shows that the displacements in the incident and in the reflected wave have the same direction with respect to the propagation directions. Consequently, there is no phase jump between the respective vertical components as was discussed in Section 2.2.5. This is important to keep in mind when evaluating the resulting wave amplitude, shown in Section 4.3.5.

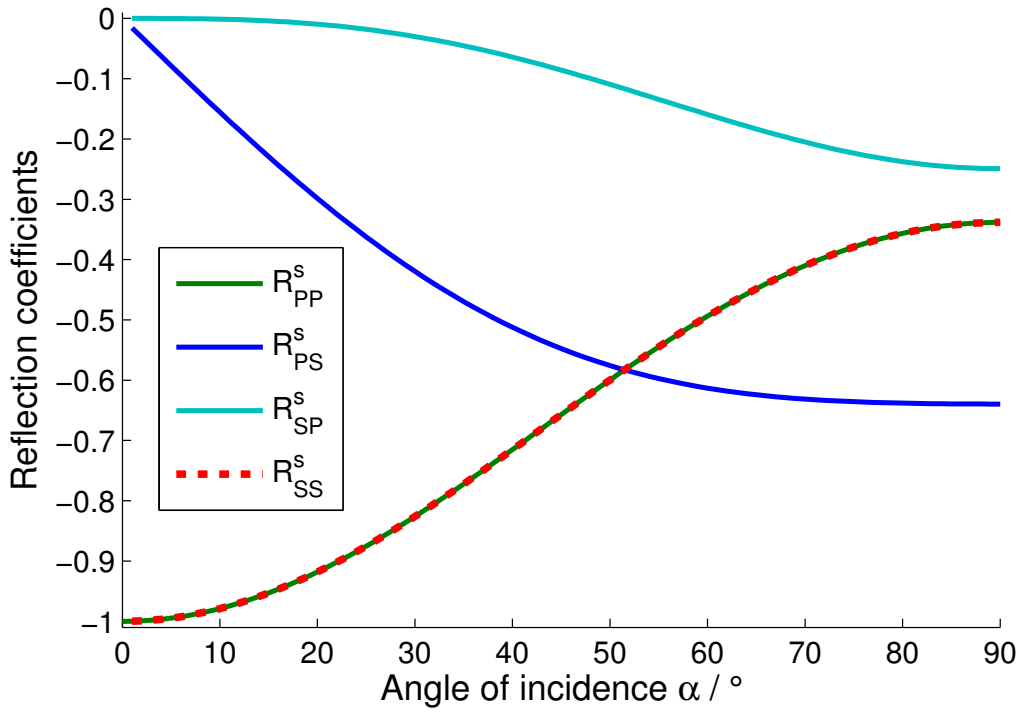

Figure 4.18: Reflection coefficients at the free surface for the full range of acoustic angles of incidence α. The values are calculated with Eq. (2.36) to Eq. (2.39). For the calculation the values $v_0 = 340\,\mathrm{m/s}$, $v_{\mathrm{P1}} = 230\,\mathrm{m/s}$ and $v_{\mathrm{S1}} = 133\,\mathrm{m/s}$ are used. The subscripts of the four coefficients state the types of incident and reflected wave.

4.3.3 Reflection coefficients at the underground boundary

For a seismic wave impinging from above on the boundary between the upper soil layer and the second one, again four reflection coefficients are needed.[33] They are given by Eq. (2.32) to Eq. (2.35) in Section 2.2.2. For the calculation additional to the values of v_0, v_{P1} and v_{S1} the respective wave velocities in the second soil layer are required as well as the ratio of the densities of both layers. Here the following values are used: $v_{\mathrm{P2}} = 1400\,\mathrm{m/s}$, $v_{\mathrm{S2}} = 153\,\mathrm{m/s}$ and $\rho_2/\rho_1 = 1.25$. The real parts of the calculated reflection coefficients are shown in Fig. 4.19.

Here, again, the first subscript refers to the type of the incident wave and the second one to the type of the reflected wave.

At the angle $\alpha_c \approx 14.1°$ the P-P reflection coefficient has the absolute value of nearly $R_{\mathrm{PP}} = 1$. At this critical angle total internal reflection occurs at the boundary for a downwards

[33] For the evaluation the four reflection coefficients for a wave hitting the boundary from below as well as the eight transmission coefficients are of no interest. This holds true since, firstly, no seismic source below the boundary is considered for the explanation of the recordings. The sources of interest are the airborne aircraft whose signals hit the surface and the underground boundary from above. Secondly, the lower soil layer is treated as an infinitely extending half-space. The energy transmitted at the underground boundary does not contribute further to the recorded seismic signals. During the evaluation of the measurements no evidence of an additional, deeper boundary, where seismic waves might have been reflected upwards, was found.

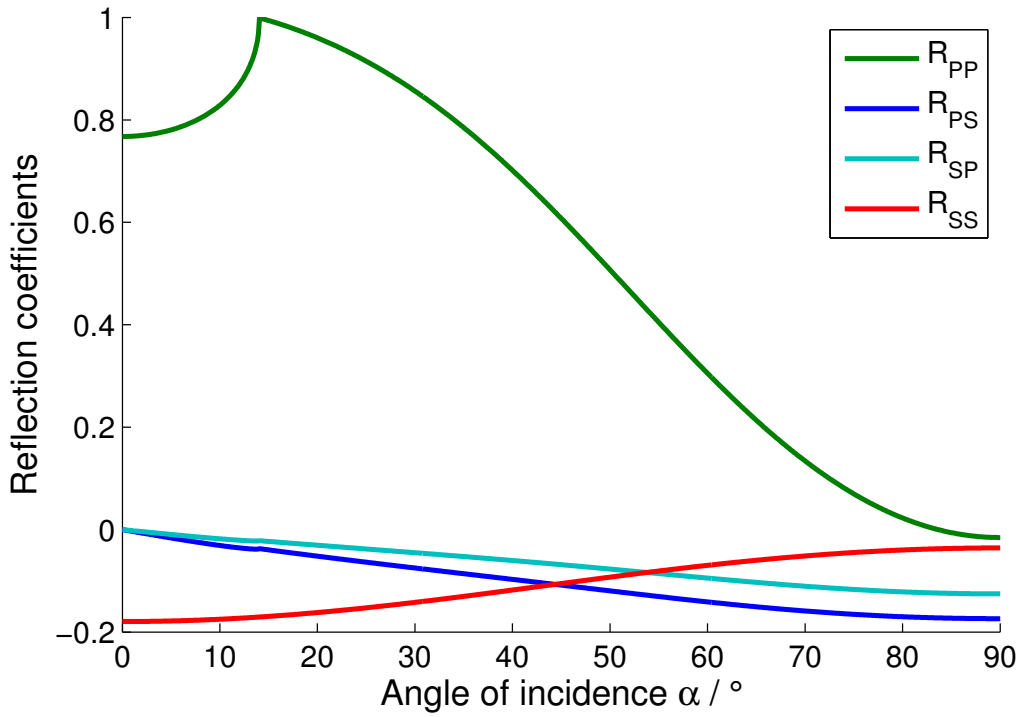

Figure 4.19: Reflection coefficients at the underground boundary versus the acoustic angles of incidence α. The values are calculated with Eq. (2.32) to Eq. (2.35). For the calculation the following values are used: $v_0 = 340\,\mathrm{m/s}$, $v_{\mathrm{P1}} = 230\,\mathrm{m/s}$, $v_{\mathrm{S1}} = 133\,\mathrm{m/s}$, $v_{\mathrm{P2}} = 1400\,\mathrm{m/s}$, $v_{\mathrm{S2}} = 153\,\mathrm{m/s}$ and $\rho_2/\rho_1 = 1.25$.
The subscripts of the four coefficients state the types of incident and reflected wave. The plotted values show the real parts of the reflection coefficients, since above the critical angle of total reflection (e.g. for R_{PP} $\alpha_c \approx 14.1°$) the coefficients are generally complex.

propagating P wave. Thus, no P wave is transmitted into the second soil layer for angles larger than $\alpha_c \approx 14.1°$. However, still an SV wave can be transmitted into the second soil layer, since v_{S2} is smaller than v_{P1} in the investigated case and thus no critical angle for these two velocities exist. Additionally, an SV wave is reflected into the upper soil layer, indicated by the non-zero value of R_{PS}. The critical acoustic angle α_c corresponds to a critical seismic one, which can be calculated by $\beta_c = \arcsin(v_{P1}/v_{P2}) \approx 9.5°$ for the given velocities. The absolute value of R_{PP} for angles $\alpha \lesssim 68°$ is much larger than that of the other three reflection coefficients. This indicates, that the P-P reflection is the dominant contribution to the resulting signal at the sensor as will be shown in Section 4.3.5.
The positive sign of R_{PP} for most α means that the displacement of a small volume element in the incident and in the reflected wave both point in the same direction with respect to the respective wave vectors. Therefore, the vertical component of the displacement undergoes a phase jump of π upon reflection (see also Section 2.2.5). The other three reflection coefficients are negative, indicating no phase jump of the vertical component upon S-S reflection, but a phase jump of π upon P-S reflection as well as upon S-P reflection (see Table 2.2).
The real part of R_{PP} gets negative for angles $\alpha \gtrsim 82.6°$, corresponding to $\beta \gtrsim 42.2°$. For grazing incidence of the P wave ($\beta_P = 90°$) the real part of R_{PP} would approach -1. However, this range of angles β_P is of no interest for the evaluation, since for the acoustically induced seismic signals β_P is limited to $\beta_{max} \approx 42.6°$ (see Fig. 4.17, right).

4.3.3.1 Simple estimate of the P-P reflection coefficient

The calculations presented in the previous sections and especially in Section 4.3.3 use assumptions for the properties of the second soil layer. In [57] an estimate for R_{PP}[34] was presented and it was argued that it is not necessary to know this parameters precisely. Here the made estimate using the simple model of the two-wave interference is outlined (see Section 2.3.1 for a sensor at the surface, $z_S = 0\,\mathrm{m}$) and its applicability is discussed. The soil velocity recorded at the surface is determined by the interference of the waves $A_{\grave{P}}$ with relative amplitude $a_{\grave{P}} = 1$ and the effective wave $A^{surf}_{\grave{P}\acute{P}}$ with relative amplitude $a^{surf}_{\grave{P}\acute{P}} = a_{\grave{P}\acute{P}} + a_{\grave{P}\acute{P}\grave{P}}$ (see Section 2.3.1).[35] The latter amplitude can be expressed using the reflection coefficients R_{PP} and R^s_{PP}: $a^{surf}_{\grave{P}\acute{P}} = R_{PP}(1 + R^s_{PP})$. The maximal amplitude of the interference is given by $a_{max} = a_{\grave{P}} + a^{surf}_{\grave{P}\acute{P}}$ and the minimal one by $a_{min} = a_{\grave{P}} - a^{surf}_{\grave{P}\acute{P}}$. The same equations can be used when evaluating the maxima Cc_{max} and minima Cc_{min} of the coupling coefficient, calculated from the averaged recorded data. Using the ratio $F = Cc_{max}/Cc_{min}$ between the coupling coefficients at the frequencies of maximal

[34] In [57] R_{PP} was referred to simply as R, since wave type conversion of P waves upon reflection was neglected.

[35] Since at the surface the waves $A_{\grave{P}\acute{P}}$ and $A_{\grave{P}\acute{P}\grave{P}}$ have the same phase the vertical components of their displacement sum up reinforcingly. Thus, in order to treat the problem as two-wave interference, the effective wave $A^{surf}_{\grave{P}\acute{P}}$ with the sum amplitude of $A_{\grave{P}\acute{P}}$ and $A_{\grave{P}\acute{P}\grave{P}}$ is used here.

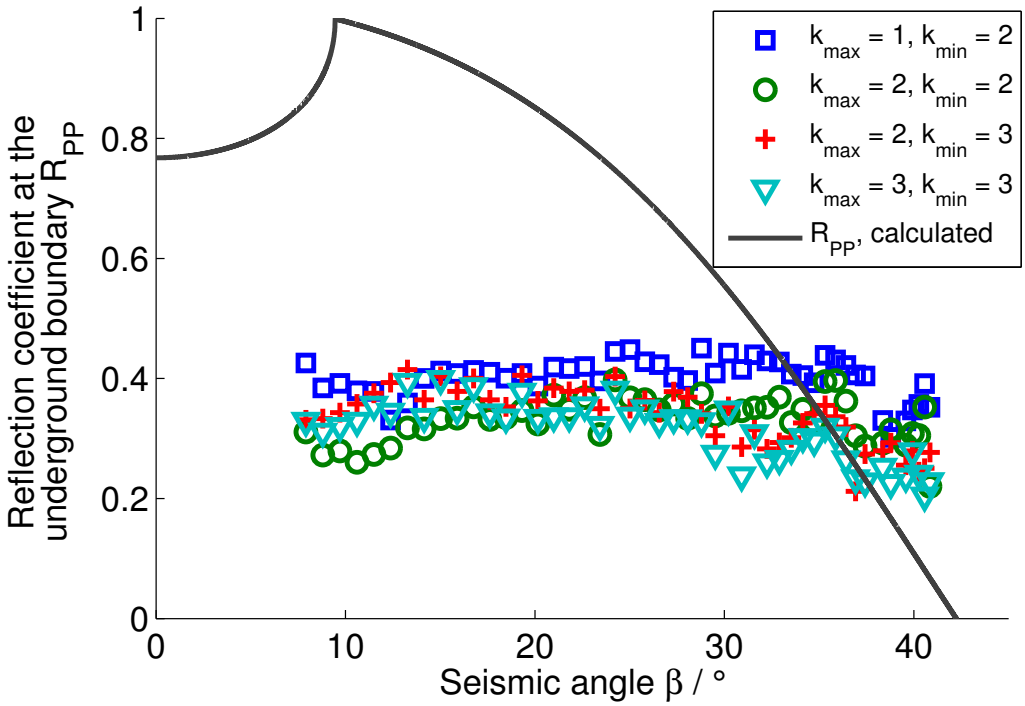

Figure 4.20: Reflection coefficient R_{PP} at the boundary, estimated from the ratio of minimal over maximal coupling strength with Eq. (4.15) (coloured data points) and calculated (black) as in Section 4.3.3, plotted here versus the seismic angle β_{P} as in [57]. For the estimate the ratios $F = Cc_{\max}/Cc_{\min}$ of four pairs of neighbouring frequency bands of local maxima and minima of the coupling strength with the given indices $k_{\max}$ and $k_{\min}$ were used. All estimates result in similar values of R_{PP} for the investigated range of β_{P} with little dependency on the angle and the frequency.

and minimal coupling strength and the calculated values of $R^{\mathrm{s}}_{\mathrm{PP}}$ (see Section 4.3.2), one finds for the reflection coefficient R_{PP}:

$$R_{\mathrm{PP}} = \frac{F-1}{(1-R^{\mathrm{s}}_{\mathrm{PP}})(F+1)}. \tag{4.15}$$

In [57] this calculation was performed for the wide range of angles β_{P} to obtain the angle dependency of $R_{\mathrm{PP}}(\beta_{\mathrm{P}})$. However, the angle dependency of R_{PP} was considered to be so weak that it was neglected. Additionally, multiple pairs of adjacent minima and maxima of the coupling coefficient (at different frequencies) were used. The decrease of R_{PP} with frequency, i.e. for larger indices $k_{\min}$ and $k_{\max}$, was mentioned but not further considered. Thus, the reflection coefficient R_{PP} was assumed to be constant $R_{\mathrm{PP}} = \text{const.} \approx 0.4$ for all made calculations. In Fig. 4.20 R_{PP} is shown for the estimation from the data points as in [57] and for the calculated values from Section 4.3.3.

A strong deviation between the calculated and the estimated values can be observed. The strong angle dependency of the former can indeed not be found for the latter. For the estimate only for large angles β_{P} (corresponding to the acoustic angle α approaching grazing incidence) a slight tendency of decreasing R_{PP} can be observed, which is, however,

significantly smaller than that of the calculated values. Also no maximum of R_{PP} around a critical angle of total reflection can be identified for the estimated values.
Reasons for the deviation can be the following: For the estimate only P waves were taken into account. However, the seismic signal contains contributions from SV waves as will be shown in Section 4.3.5. Furthermore, it was assumed that the amplitudes of maximal and minimal coupling strength are solely given by constructive and destructive interference between two waves, respectively. The seismic background at the measurement site was not taken into account. However, it increases the recorded soil velocity and thus the coupling strength (see Eq. (4.12)). For destructive interference the overall coupling strength is small, thus the background amplitude increases Cc_{min} while it has minor effects on Cc_{max}. This leads to a systematic error in the used ratio F.
Regardless of these limitations of the estimate the simple interference model (Section 2.3.1) with a constant value of R_{PP} can be used to successfully determine the frequencies f_{max} of constructive and f_{min} of destructive interference for a sensor at the surface. This is valid, because these frequencies (see Eq. (2.49) for f_{max} and the modifications of the equation for f_{min}, given in Section 2.3.1) do not depend on the relative amplitudes of the interfering waves. With the use of the more sophisticated calculation of R_{PP} (as has been presented in Section 4.3.3) the relative amplitudes of the coupling strength between destructive and constructive interference can be explained better.
For buried sensors, the waves $A_{\grave{\mathrm{P}}\acute{\mathrm{P}}}$ and $A_{\grave{\mathrm{P}}\acute{\mathrm{P}}\grave{\mathrm{P}}}$ have to be treated separately with their respective relative amplitudes and their phase difference. Thus, the frequencies of maximal and minimal coupling strength depend on the values of the reflection coefficients. The determination of f_{max} for buried sensors, used for the determination of the soil properties presented in [57], is affected by this error. This is another reason for the better results in [57] obtained for surface sensors than those for the buried ones. A comparison of the various interference models is given in Section 4.4.

4.3.4 Transmission coefficients from air to the upper soil layer

A compressional acoustic wave will generally excite a compressional and a shear wave in the soil, when hitting the boundary between the air-fill half-space and the upper soil layer. The amplitudes of P and SV wave are given by the respective transmission coefficients $T_{\mathrm{P}}^{\mathrm{s}}$ and $T_{\mathrm{S}}^{\mathrm{s}}$ calculated with Eq. (2.40) in Section 2.2.4. The amplitude of the wave propagating mainly in the air-fill pores of the soil, i.e. the Biot-type II compressional wave (see [41]), decreases rapidly while its energy is transferred to that of the P and SV waves in the soil matrix. With the use of Eq. (2.40) immediate energy transfer from the sound wave to the seismic waves is assumed.
For the calculation of the transmission coefficients the densities of air and soil are required. For this the approximate values $\rho_{air} \approx 1.2\,\mathrm{kg/m^3}$ and $\rho_{soil} \approx 1.2\,\mathrm{t/m^3}$ [65] are

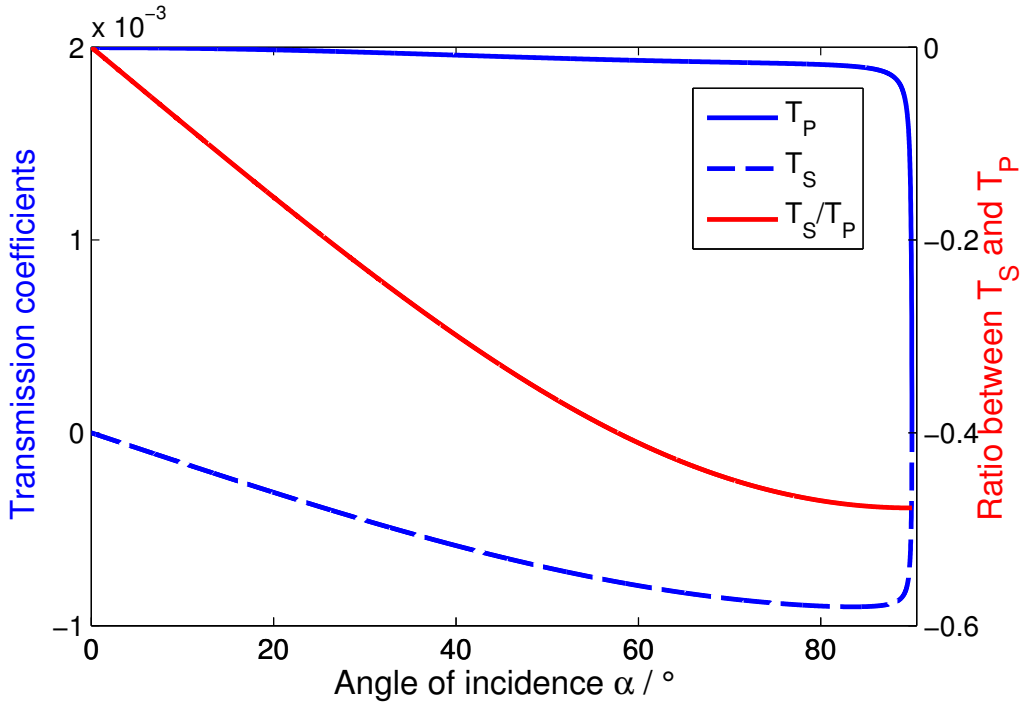

Figure 4.21: Transmission coefficients $T_{\mathrm{P}}^{\mathrm{s}}$ (blue, solid line) and $T_{\mathrm{S}}^{\mathrm{s}}$ (blue, dashed line) from air to the upper soil layer, calculated with Eq. (2.40) for the parameters v_0 = 340 m/s, v_{P1} = 230 m/s, v_{S1} = 133 m/s and $\rho_{air}/\rho_{soil} = 1/1000$. Both transmission coefficients refer to the values of the left y-axis. The red curve shows the ratio between $T_{\mathrm{S}}^{\mathrm{s}}$ and $T_{\mathrm{P}}^{\mathrm{s}}$, referring to the values of the right y-axis.

used, leading to their ratio of $\rho_{air}/\rho_{soil} \approx 1/1000$. The calculated values are plotted in Fig. 4.21 together with their ratio $T_{\mathrm{S}}^{\mathrm{s}}/T_{\mathrm{P}}^{\mathrm{s}}$.

Throughout the evaluation the directly acoustically excited P wave $A_{\grave{\mathrm{P}}}$ is used as a reference and the amplitude of any other wave is given relatively to $A_{\grave{\mathrm{P}}}$. Thus, the term $T_{\mathrm{S}}^{\mathrm{s}}/T_{\mathrm{P}}^{\mathrm{s}}$ has to be considered, depending on the type of the acoustically excited wave (see Eq. (4.16) in Section 4.3.5).

4.3.5 Contributions of arbitrary seismic waves to the seismic signal

As discussed in Section 2.3.4 a seismic wave A_i can be reflected several times within the upper soil layer before reaching the sensor. Upon each reflection its wave type might change. Additionally, each reflection reduces its initial amplitude by the respective reflection coefficient. With the reflection and transmission coefficients given in the previous sections, the resulting amplitude a_i can now be calculated using Eq. (2.72), which is

repeated here:

$$\begin{aligned} a_i =& (R_{\mathrm{PP}})^{m_{\mathrm{PP}}} \cdot (R_{\mathrm{PS}})^{m_{\mathrm{PS}}} \cdot (R_{\mathrm{SP}})^{m_{\mathrm{SP}}} \cdot (R_{\mathrm{SS}})^{m_{\mathrm{SS}}} \\ & \cdot (R^{\mathrm{s}}_{\mathrm{PP}})^{n_{\mathrm{PP}}} \cdot (R^{\mathrm{s}}_{\mathrm{PS}})^{n_{\mathrm{PS}}} \cdot (R^{\mathrm{s}}_{\mathrm{SP}})^{n_{\mathrm{SP}}} \cdot (R^{\mathrm{s}}_{\mathrm{SS}})^{n_{\mathrm{SS}}} \cdot (T^{\mathrm{s}}_{\mathrm{S}}/T^{\mathrm{s}}_{\mathrm{P}})^{k}. \end{aligned} \tag{4.16}$$

In the following calculations the values of reflection coefficients at the free surface R^{s}_{ij} and at the underground boundary R_{ij} obtained in Section 4.3.2 and in Section 4.3.3 are used. The integers m_{ij} and n_{ij} refer to the number of times the wave A_i undergoes the respective reflection. With the term $(T^{\mathrm{s}}_{\mathrm{S}}/T^{\mathrm{s}}_{\mathrm{P}})^k$ it is taken into account whether the type of the first excitation of A_i by the acoustic wave is a P wave or an SV wave: If it is a P wave $k = 0$ and if it is an SV wave $k = 1$ (see also Section 2.3.4).

Due to the use of vertical-component geophones, the respective component of the soil velocity has to be calculated using Eq. (4.14). For this only the wave type of A_i upon arrival at the sensor is of interest, regardless of any previous changes of its wave type.

In Fig. 4.22 (top) the relative amplitudes of selected seismic waves at the sensor are shown calculated with Eq. (4.16). In Fig. 4.22 (bottom) the respective vertical components are given. I will make use of the intuitive nomenclature introduced in Section 2.3 to indicate the types and the direction of the waves A_i that are reflected within the upper soil layer.

In Fig. 4.22 the amplitudes only of some of all possible seismic waves are shown: I have chosen those with the overall largest amplitude in a wide range of α. There are more waves (not shown here), resulting from further P-wave reflections, that have a larger amplitude around α_c than any wave propagating partially as SV wave. The latter (namely $A_{\grave{\mathrm{S}}}$, $A_{\grave{\mathrm{P}}\acute{\mathrm{S}}}$ and $A_{\grave{\mathrm{P}}\acute{\mathrm{P}}\grave{\mathrm{S}}}$) are shown to stress the dominance of the P waves on the seismic signal. These three waves have the largest amplitude of any wave A_i that propagated as an SV wave at any part of its path. Their amplitudes reach significant values only for large angles α, especially when looking at their vertical components (Fig. 4.22, bottom).

The sign of the amplitudes given in Fig. 4.22 results from the multiplication of the values as they were calculated in Section 4.3.2, Section 4.3.3 and Section 4.3.4. It does not represent the direction of the displacement for a conclusion about the resulting interference amplitude. For this the respective phase differences between the waves, following from the path-length differences of both waves at a given frequency, need to be used that are calculated with Eq. (2.71).

As shown in Fig. 4.18 for the reflection of a wave at the free surface all four reflection coefficients are negative. Correspondingly, for the special case of a sensor positioned at the surface there is no phase jump of the vertical component of the displacement between an upwards- and the reflected, subsequently downwards-propagating

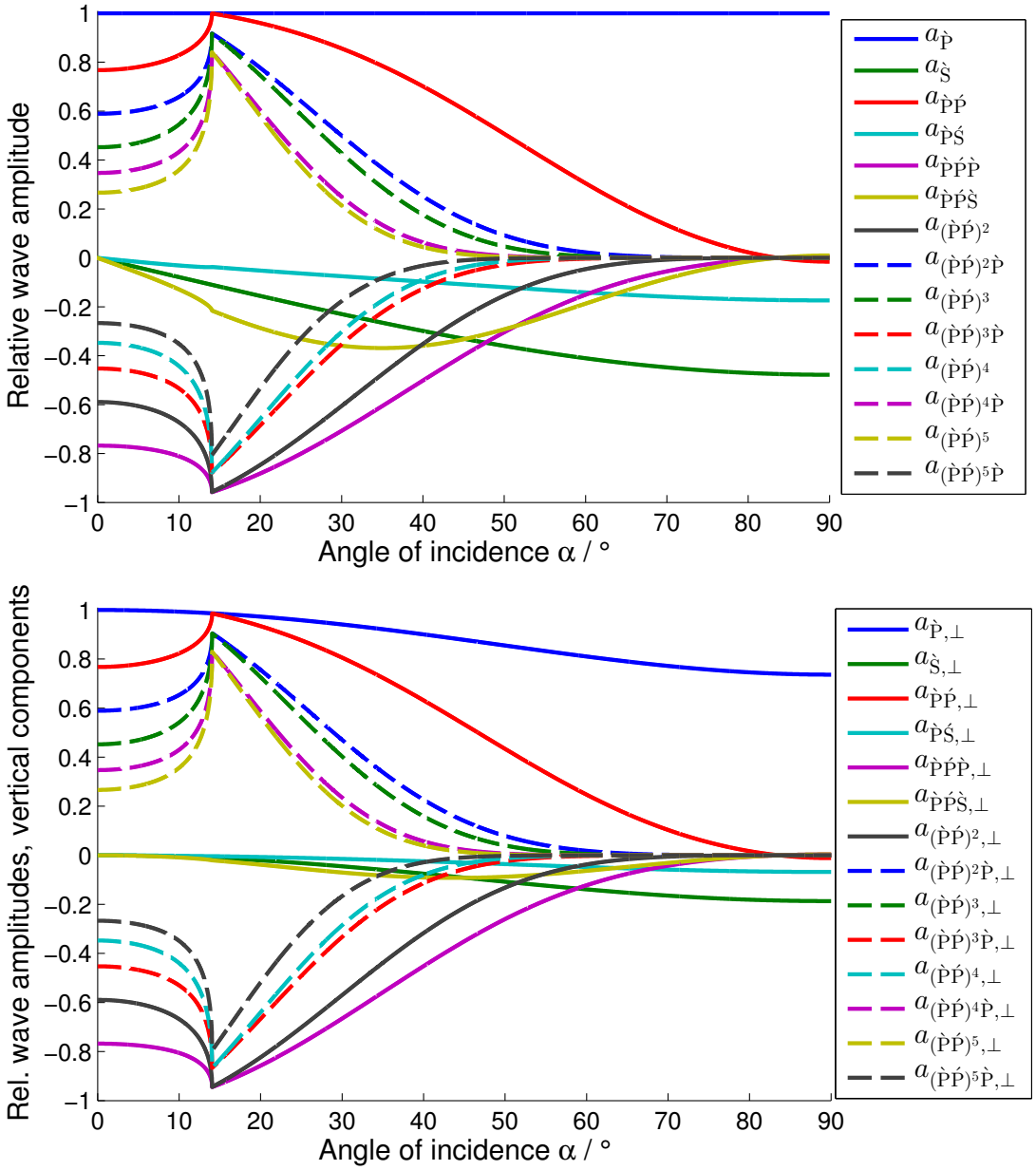

Figure 4.22: Relative amplitudes of selected seismic waves at the sensor, calculated with Eq. (4.16). The plots show the waves which have the highest amplitudes for a wide range of angles α. This includes mainly the waves created by P-P reflection at the free surface and the underground boundary. Additionally, the amplitudes of three waves that covered a part of the path in the soil as SV wave are shown: The directly acoustically excited SV wave $A_{\grave{S}}$, the upwards-propagating SV wave $A_{\grave{P}\acute{S}}$, excited by P-S reflection at the underground boundary and the SV wave $A_{\grave{P}\acute{P}\grave{S}}$, that was excited at the surface by a P wave which passed the upper soil layer in both directions. Their overall amplitude is weak compared to the amplitudes of the pure P waves, especially when looking at the vertical components. They reach significant values only for large α.
Top: Full wave amplitudes calculated with Eq. (4.16), relative to that of $A_{\grave{P}}$.
Bottom: Vertical components, given by the multiplication of the full wave amplitudes with $\cos(\beta_P)$ (if the wave reaches the sensor as a P wave) or with $\sin(\beta_S)$ (if it reaches the sensor as SV wave), see Eq. (4.14).

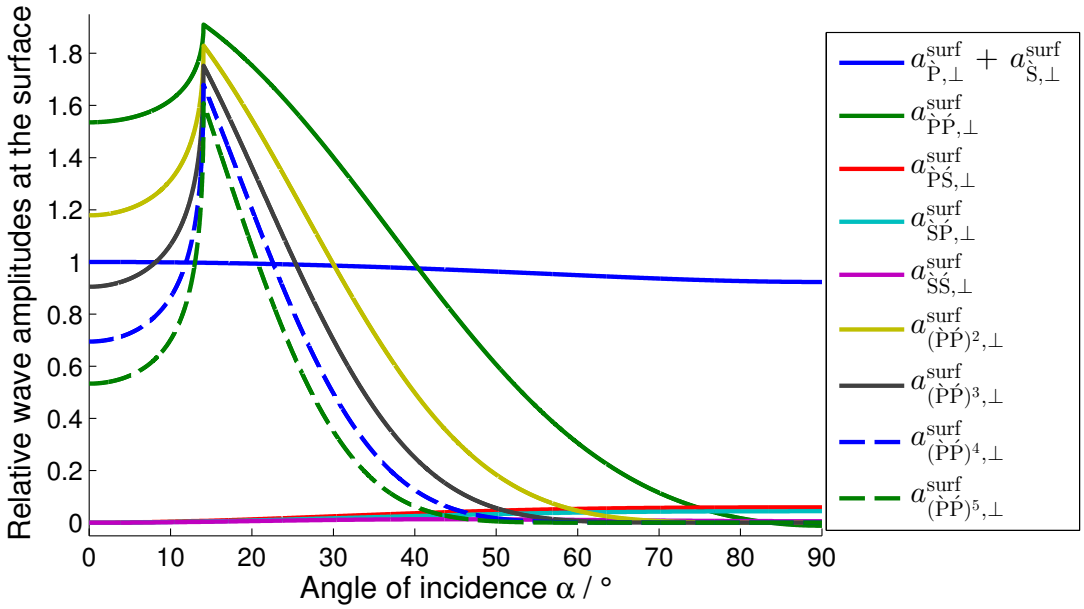

Figure 4.23: Vertical components of the relative, effective wave amplitudes of various seismic waves at a sensors placed at the surface ($z_{\mathrm{S}} = 0\,\mathrm{m}$). The first wave $A_{\grave{\mathrm{P}}} + A_{\grave{\mathrm{S}}}$ refers to the P and the SV wave excited acoustically at the location of the sensor. For all other waves the effective amplitude contains the vertical components of the amplitudes of the wave that propagated through the upper soil layer as indicated by the subscripts and the two waves (P and SV) excited upon its reflection at the free surface.

P wave. Thus, the vertical components of their amplitude can be summed up. The same is true if incident and reflected wave are SV waves. If the wave type changes, there is a phase jump of π between the vertical components of incident and reflected wave, thus the effective amplitude is given by their difference. The phase jumps for the different kinds of reflection were given in Table 2.2 and the values of the reflection coefficients were calculated in Section 4.3.2. Using them the vertical components of the absolute amplitudes for a sensor at the surface are plotted in Fig. 4.23.

The first curve corresponding to the waves $A_{\grave{\mathrm{P}}}$ and $A_{\grave{\mathrm{S}}}$ gives the sum of the vertical components of the amplitudes of the directly acoustically excited P wave and S wave at the location of the sensor. All other curves refer to the effective wave amplitudes at the surface which is given by the sum of the vertical components of the amplitude of a wave that propagated through the upper soil layer as indicated by the sequence of indices and that of the two waves created by the upwards-propagating wave upon reflection at the free surface. The phase jump of π is taken into account for each wave the type of which changed upon reflection. Exemplarily, the amplitude of the wave $A^{\mathrm{surf}}_{\grave{\mathrm{P}}\acute{\mathrm{P}}}$ is given as the sum of the vertical components of the amplitudes of the waves $A_{\grave{\mathrm{P}}\acute{\mathrm{P}}}$, $A_{\grave{\mathrm{P}}\acute{\mathrm{P}}\grave{\mathrm{P}}}$ and $A_{\grave{\mathrm{P}}\acute{\mathrm{P}}\grave{\mathrm{S}}}$ (plotted in Fig. 4.22, bottom) under consideration of the phase jumps between them. Thus, it will not come as a surprise that the effective amplitude at the surface is

larger than 1 for angles α of high reflectivity. It can reach values of twice the amplitude of the incident wave (e.g. for reflection at the free surface of a P wave at perpendicular incidence). The effective amplitude of $A^{\text{surf}}_{\grave{\text{P}}\acute{\text{P}}}$ is calculated by:

$$a^{\text{surf}}_{\grave{\text{P}}\acute{\text{P}},\perp} = R_{\text{PP}} \cdot \left[\cos(\beta_{\text{P}}) + \cos(\beta_{\text{P}}) \cdot R^{\text{s}}_{\text{PP}} - \sin(\beta_{\text{S}}) \cdot R^{\text{s}}_{\text{PS}}\right] \tag{4.17}$$

The factor R_{PP} results from the reflection at the underground boundary. The first summand in the brackets refers to the upwards propagating P wave $A_{\grave{\text{P}}\acute{\text{P}}}$. The second one corresponds to the P wave $A_{\grave{\text{P}}\acute{\text{P}}\grave{\text{P}}}$ created upon reflection at the free surface. The third term gives the amplitude of the SV wave $A_{\grave{\text{P}}\acute{\text{P}}\grave{\text{S}}}$ created as well upon reflection at the free surface. Of all amplitudes the respective vertical components are used, calculated with Eq. (4.14). Since the vertical component of the displacement in the SV wave is in the opposite direction compared to those of the P waves (see Table 2.2), i.e. its phase is shifted by π with respect to the other two waves, the respective summand has a negative sign.

In Fig. 4.23 again it can be noted that the amplitudes of the waves that passed the upper soil layer at least in one direction as an SV wave, i.e. $A^{\text{surf}}_{\grave{\text{P}}\acute{\text{S}}}$, $A^{\text{surf}}_{\grave{\text{S}}\acute{\text{P}}}$ and $A^{\text{surf}}_{\grave{\text{S}}\acute{\text{S}}}$, have very small amplitudes, compared to the waves that propagated as P waves only.

4.4 Comparison of the fit results of the theoretical interference models

In this section the fit of the interference pattern of the averaged coupling coefficient (discussed in Section 4.2) to the theoretically determined frequencies of increased coupling strength is presented. For this the three theoretical models introduced in Section 2.3 will be used and compared. In the first model interference between three P waves is investigated. The second one takes into account multiple reflections of the P waves within the upper soil layer. The comprehensive description of the third model (see Section 2.3.4) uses contributions of any P and SV wave propagating within the upper soil layer. Here only the additional contribution from the directly acoustically induced SV wave is taken into account. Further SV waves are neglected in the scope of this work since their contribution to the overall signal is weak, as is shown in Section 4.3.5.

Firstly, in Section 4.4.1 the fit algorithm is described. Then the case of a sensors at the surface ($z_{\text{S}} = 0\,\text{m}$) is discussed in Section 4.4.2 which leads to identical results for the three theoretical models. From this fit soil parameters, namely the depth of the underground boundary d and the P-wave velocity in the upper soil layer v_{P1}, are obtained. In Section 4.4.3 the results for buried sensors ($z_{\text{S}} > 0\,\text{m}$) of the different models are compared. Finally, in Section 4.4.4 the reliability of the results is discussed.

4.4.1 Description of the used fit algorithm

Using the MATLAB2012a function *fminsearch* the relative root-mean-square deviation $D(d, v_{\mathrm{P1}})$ between theoretical and experimental data for all angles α_i is minimised iteratively. Its minimum is identified with the best fit parameters for d and v_{P1}. $D(d, v_{\mathrm{P1}})$ is given by:

$$D(d, v_{\mathrm{P1}}) = \sqrt{\frac{1}{K} \sum_k \sum_i \left(\frac{f^{\mathrm{theo}}_{\mathrm{max},k}(\alpha_i, d, v_{\mathrm{P1}})}{f^{\mathrm{meas}}_{\mathrm{max},k}(\alpha_i)} - 1 \right)^2}. \tag{4.18}$$

Here $f^{\mathrm{theo}}_{\mathrm{max},k}(\alpha)$ corresponds to the theoretical expressions of the frequencies of maximal coupling strength over α calculated with the respective model for a given pair of (d,v_{P1}). $f^{\mathrm{meas}}_{\mathrm{max},k}(\alpha)$ are the respective frequency courses of the measured data determined as presented in Section 4.2.2. The index k specifies the number of the frequency bands of increased coupling strength. With the index i all angles $\alpha_i \leq \alpha_{\mathrm{max}}$[36] are included in the calculation, leading to the total number K of used data points.

For a sensor at the surface for all presented models the frequencies of the constructive interference can be expressed with Eq. (2.49). For a given angle α the frequency difference between consecutive maxima $f^{\mathrm{theo}}_{\mathrm{max},k}(\alpha)$ and $f^{\mathrm{theo}}_{\mathrm{max},k+1}(\alpha)$ is constant for each k.

For buried sensors Eq. (2.49) cannot be applied to determine the theoretical frequencies of local maxima because the beat between the waves causes the frequencies of maximal amplitude to shift with respect to those at the surface. Thus, the frequency differences between the consecutive maxima $f^{\mathrm{theo}}_{\mathrm{max},k}(\alpha)$ and $f^{\mathrm{theo}}_{\mathrm{max},k+1}(\alpha)$ change with the order of the maximum k. The theoretical frequency courses $f^{\mathrm{theo}}_{\mathrm{max},k}(\alpha)$ have to be determined numerically from Eq. (2.73) and need to be assigned to the corresponding determined $f^{\mathrm{meas}}_{\mathrm{max},k}$. For each iteration of the fit the theoretical spectral amplitude distribution is calculated for the used values of d and v_{P1}. Then the local amplitude maxima of the smallest angle are determined and with a similar algorithm as for the measured data (shown in Section 4.2.2) the courses $f^{\mathrm{theo}}_{\mathrm{max},k}(\alpha)$ are obtained.

4.4.2 Fit results for sensors at the surface

For a sensor at the surface ($z_{\mathrm{S}} = 0\,\mathrm{m}$) the problem of the interference reduces for all three models to that of only two waves A_1 and A_2. However, depending on the applied model, they have different contributions: The first wave A_1 consists of the directly acoustically excited seismic waves and the second one A_2 of the P waves that have been reflected within the upper soil layer. More precisely, the amplitude of wave A_1 in the first and the second model is given by the vertical component of the directly acoustically excited P wave (i.e. wave $A_{\hat{\mathrm{P}}}$). For the third model (taking into account the acoustically

[36] α_{max} refers to the largest angle of incidence used during the fit. It is specified in the sections of the respective fits.

excited SV wave) the amplitude of A_1 is determined by the vertical components of the P wave and of the SV wave, which both are directly acoustically excited, i.e. the waves $A_{\grave{\mathrm{P}}}$ and $A_{\grave{\mathrm{S}}}$. As shown in Fig. 4.21 the transmission coefficients from air to soil have opposite signs for the P wave and the SV wave and thus their ratio is always negative. However, as discussed in Section 2.2.5 (see e.g. Table 2.3) no phase jump between $A_{\grave{\mathrm{P}}}$ and $A_{\grave{\mathrm{S}}}$ arises. Thus, the vertical components of their displacements point in the same direction and their vertical amplitudes sum up reinforcingly.
In the first model the second wave A_2 has the sum amplitude of the vertical components of the upwards- and downwards-propagating, reflected waves (i.e. the waves $A_{\grave{\mathrm{P}}\acute{\mathrm{P}}}$ and $A_{\grave{\mathrm{P}}\acute{\mathrm{P}}\grave{\mathrm{P}}}$). At the surface the vertical displacement components of both waves are in phase (see Table 2.1) and thus the vertical components of their amplitudes sum up reinforcingly. For the second and the third model, the amplitude of A_2 is obtained as a geometric series resulting from the superposition of the quasi-infinite number of P waves acoustically excited at various locations.
The amplitudes a_1 of the waves A_1 and a_2 of the waves A_2 are summarised for all three models in Table 4.1 relative to that of the directly acoustically excited P wave. They are expressed in terms of the P-P reflection coefficients at the free surface $R^{\mathrm{s}}_{\mathrm{PP}}$ (see Fig. 4.18) and at the underground boundary R_{PP} (see Fig. 4.19) as well as of the ratio of the acoustic-seismic transmission coefficients $T^{\mathrm{s}}_{\mathrm{S}}/T^{\mathrm{s}}_{\mathrm{P}}$ (see Fig. 4.21). The terms $\cos(\beta_{\mathrm{P}})$ and $\sin(\beta_{\mathrm{S}})$ stem from the expressions of the respective vertical components.

	model 1, of three P waves	model 2, of multiply reflected P waves	model 3, taking into account the directly excited SV wave
a_1	$\cos(\beta_{\mathrm{P}})$	$\cos(\beta_{\mathrm{P}})$	$\cos(\beta_{\mathrm{P}}) + \lvert T^{\mathrm{s}}_{\mathrm{S}}/T^{\mathrm{s}}_{\mathrm{P}}\rvert \cdot \sin(\beta_{\mathrm{S}})$
a_2	$R_{\mathrm{PP}} \cdot (R^{\mathrm{s}}_{\mathrm{PP}} + 1) \cdot \cos(\beta_{\mathrm{P}})$	$\frac{R_{\mathrm{PP}} \cdot \cos(\beta_{\mathrm{P}})}{1-(R_{\mathrm{PP}} \cdot R^{\mathrm{s}}_{\mathrm{PP}})}$	$\frac{R_{\mathrm{PP}} \cdot \cos(\beta_{\mathrm{P}})}{1-(R_{\mathrm{PP}} \cdot R^{\mathrm{s}}_{\mathrm{PP}})}$

Table 4.1: Amplitudes of the two waves A_1 and A_2 interfering at a sensor at the surface. The models correspond to those theoretically introduced in Section 2.3 and specified at the beginning of Section 4.4.

Each model with its respective amplitudes a_1 and a_2 results in a different ratio of the amplitudes of constructive and destructive interference. Taking into account also the phase differences between the two waves, depending on d and v_{P1}, the spectral amplitude distribution can be calculated. The frequencies of constructive interference between two waves, calculated with Eq. (2.49), do not depend on the amplitudes of these waves. Thus, for each of the models the same theoretical frequencies $f^{\mathrm{theo}}_{\mathrm{max},k}(\alpha)$ are found. This is illustrated in Fig. 4.25 for $d = 2.35\,\mathrm{m}$ and $v_{\mathrm{P1}} = 228\,\mathrm{m/s}$.

Minimizing the relative root-mean-square of the deviation between theoretically determined and measured frequencies of local maxima of the coupling coefficient, the depth of the reflecting boundary d and the soil velocity in the first layer v_{P1} are

determined by the three models:

$$\begin{aligned} d &= 2.35\ \text{m}\ \left(+0.05\ \text{m}/-0.03\ \text{m}\right), \\ v_{\text{P1}} &= 228\ \frac{\text{m}}{\text{s}}\ \left(+2\ \frac{\text{m}}{\text{s}}/-4\ \frac{\text{m}}{\text{s}}\right). \end{aligned} \tag{4.19}$$

This result represents a stable solution for a wide range of starting values and only differs with changed data used for the fit. The relative root-mean-square deviation has a value of $D(d = 2.35\,\text{m},\ v_{\text{P1}} = 228\,\text{m/s}) = 0.0126$, that represents the overall minimum of the deviation. However, in an interval around the solution only slightly larger values are obtained, leading to a range where adequate solutions can be found. The uncertainty values of the results given in Eq. (4.19) refer to values of $D(d, v_{\text{P1}})$ being 50 % larger than the found minimum. They are obtained for v_{P1} for a constant value of d and vice versa. However, the area (in the d-v_{P1}-space) of 50 % increased values of $D(d, v_{\text{P1}})$ is a slant ellipse (see Fig. 4.29), thus the uncertainties of d and v_{P1} depend on each other. This is discussed in detail in Section 4.4.4.

In Fig. 4.24 the frequency-averaged coupling coefficient of a surface sensor (channel 24) is shown together with the data points of the tracked local maxima (black dots), corresponding to the values $k = 2$ to $k = 6$, that were used for the calculation. Data of angles above $\alpha_{\text{max}} > 60°$ were excluded due to low SNR. In certain bands where the tracked maxima deviated strongly from the obvious course more data points were excluded manually from the fit (e.g. for $k = 6$ and $\alpha > 50°$). The band with $k = 1$ (theoretical values shown as dashed line) was excluded, even though it had a good SNR, because the frequency resolution of $\Delta f_{meas} \approx 1.22\,\text{Hz}$ caused an artificially high deviation between measured and theoretical values. Other bands were excluded completely due to low SNR ($k = 0$ and $k \geq 7$). The theoretical frequencies of the maxima calculated for the values given in Eq. (4.19) are shown in Fig. 4.24 (black lines) for the whole range of α.

To compare the three interference models the theoretical spectral amplitude distributions calculated for the values $d = 2.35\,\text{m}$ and $v_{\text{P1}} = 228\,\text{m/s}$ for a sensor at the surface are shown in Fig. 4.25: The left plot shows the spectral amplitude distribution of the three-wave interference, the middle one that of the interference of multiply reflected P waves and the right one that of the interference between multiply reflected P waves and the directly excited SV wave. The spectral amplitude distributions are given relative to the amplitude of the directly acoustically excited wave $A_{\grave{\text{P}}}$, i.e. for all calculations $a_{\grave{\text{P}}} = 1$. Note that the colour scale in Fig. 4.25 is limited to the interval [0,5] for all plots. Thus, also differences of small amplitudes are visible.

The spectral frequency maxima of the consecutive bands of constructive interference are the same for each of the models. They can be analytically determined by Eq. (2.49). However, the amplitudes of the interference maxima differ strongly and so does the ratio between the maxima and minima. For small α the maximal amplitudes of the second and

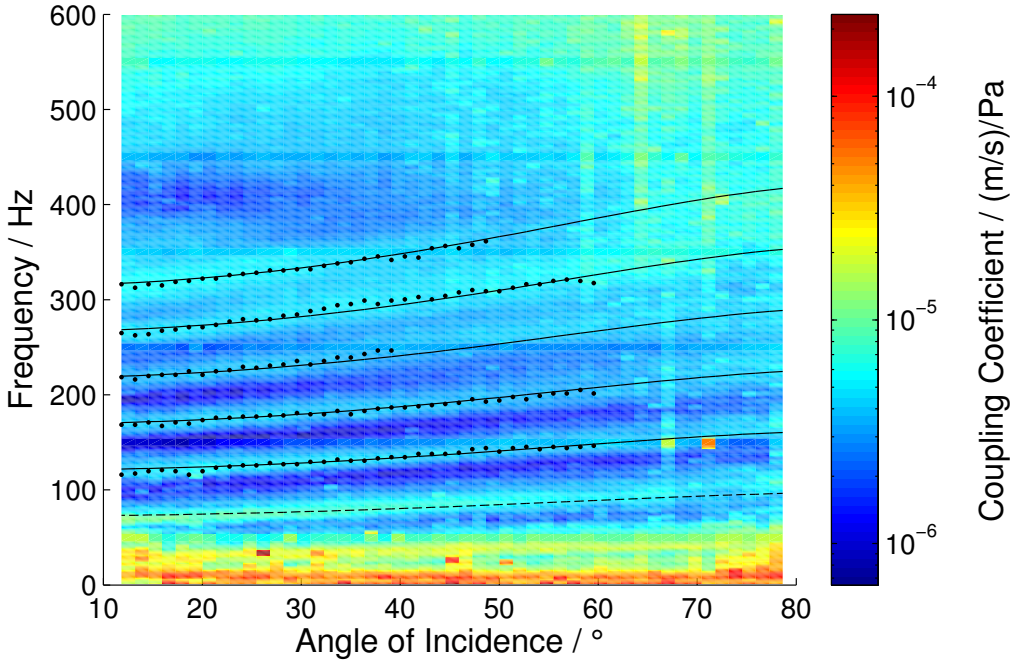

Figure 4.24: Mean coupling coefficient of 16 overflight events measured at the surface (channel 24) showing frequency bands of increased and decreased coupling strength. The local frequency maxima marked with black dots were used for a fit to determine the depth of the reflecting boundary d and the P-wave velocity v_{P1}. The theoretical frequencies of the constructive interference for the obtained values $d = 2.35\,\mathrm{m}$ and $v_{\mathrm{P1}} = 228\,\mathrm{m/s}$ are plotted as well (black lines). The frequency band with $k = 1$ was not used for the fit; its theoretical values are shown with a dashed black line.

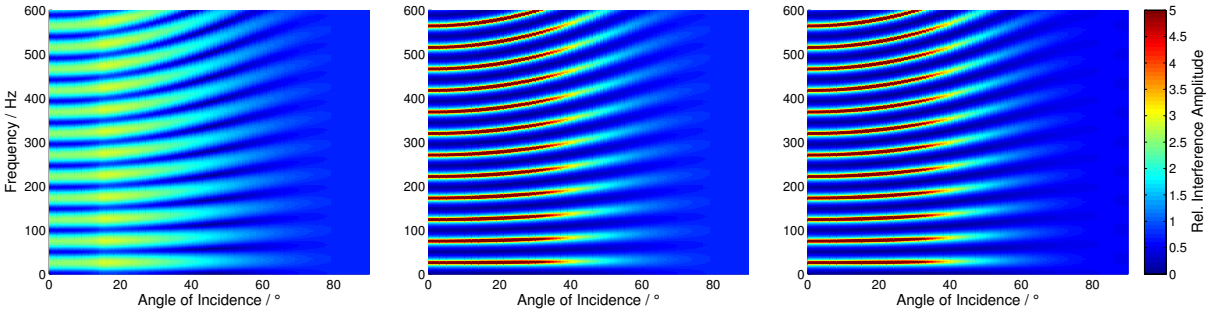

Figure 4.25: Theoretical spectral vertical-amplitude distributions, calculated for the values $d = 2.35\,\mathrm{m}$, $v_{\mathrm{P1}} = 228\,\mathrm{m/s}$ and $z_{\mathrm{S}} = 0\,\mathrm{m}$ for the three different models:
Left: Model 1, of the three-wave interference. Middle: Model 2, of the interference between multiply reflected P waves. Right: Model 3, of the interference of multiply reflected P waves and the directly excited SV wave.
The colour scale is the same for all plots and it is limited to the interval [0,5].

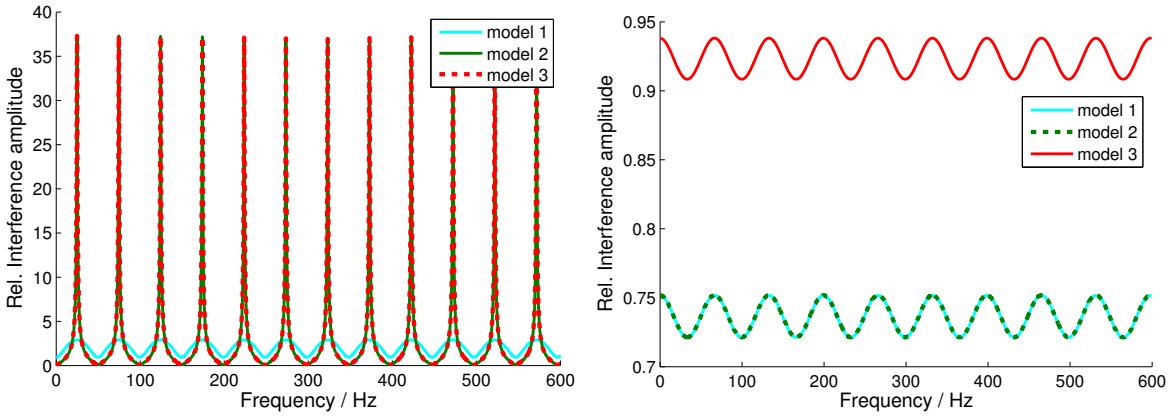

Figure 4.26: Relative interference amplitudes at $\alpha = 14°$ (left) and $\alpha = 90°$ (right). The graphs correspond to the calculated values for the three models: Model 1 of the three-wave interference (blue), model 2 of multiply reflected P waves (green) and model 3 taking into accout the contribution from the directly excited SV wave (red). For $\alpha = 14°$ the values calculated with the second and the third model coincide while for $\alpha = 90°$ the first two models lead to the same values.

the third model are approximately the same and exceed those of the first model by far for certain angles: At the critical angle of total reflection ($\alpha_{crit} \approx 14°$) of the P waves at the underground boundary the relative maximal amplitudes have a value of $a_{\max,1} \approx 2.9$ for the first model, but of $a_{\max,2} \approx a_{\max,3} \approx 37.3$ for the second and the third model (see Fig. 4.26, left). The difference of the relative amplitudes of the latter two models can be neglected for small angles (e.g. at $\alpha_{crit} \approx 14°$ it is about 0.02). For larger angles the relative amplitudes of the first and the second model become the same, while those of the third model are significantly larger. At $\alpha = 90°$ the maximal amplitude is $a_{\max,1} \approx a_{\max,2} \approx 0.75$ for the first and the second model; for the third model $a_{\max,3} \approx 0.94$ is found (Fig. 4.26, right).

At smaller angles the second and the third model lead to the same values. Both models calculate the amplitude distribution of the multiply reflected P waves. The additional contribution from the SV wave used in model three has an insignificant influence for small α as dicussed in Section 4.3. For larger angles the P-P reflection coefficients decrease considerably. Therefore, the influence of P waves reflected several times becomes insignificant and the models one and two yield the same results. On the other hand, the contribution of the direct SV wave reaches its largest values. Thus, the overall interference amplitude obtained with the third model is larger than those obtained with the other two models. This is so, since the amplitude for the third model is determined by the sum between the vertical amplitude components of the directly excited P wave and the directly excited SV wave.

Additionally, for the second and third models which consider P waves reflected multiple times within the upper soil layer, the full width at half maximum (FWHM) of the spectral peaks (i.e. the maxima of the constructive interference) is significantly reduced for high

reflectivity (see Fig. 4.26, left). This can be seen in analogy to a Fabry-Pérot resonator: With increasing number of waves contributing coherently to the interference pattern the FWHM of the spectral peaks decreases. For larger angles α (due to the strongly decreased reflectivity at both boundaries) the spectral peaks are sine-shaped (see Fig. 4.26, right). This indicates, that only few waves contribute to the observed interference pattern.

4.4.3 Comparison of the interference models for buried sensors

As discussed in Section 2.3.1 only for the surface sensor the analytic expression Eq. (2.49) can be used to determine the theoretical values of $f^{\text{theo}}_{\text{max},k}(\alpha)$. For buried sensors ($z_S > 0\,\text{m}$) these values need to be determined numerically from Eq. (2.73). This is performed for the three introduced models of interference. With the algorithm described in Section 4.4.1 the minima of the root-mean-square deviation $D(d, v_{P1})$ between $f^{\text{theo}}_{\text{max},k}(\alpha)$ and $f^{\text{meas}}_{\text{max},k}(\alpha)$ are determined for the values $z_S = 0.15\,\text{m}$, $z_S = 0.30\,\text{m}$, $z_S = 0.45\,\text{m}$ and $z_S = 0.60\,\text{m}$ – in accordance to the fit for $z_S = 0\,\text{m}$ presented in Section 4.4.2. All fits for $z_S = 0.30\,\text{m}$, $z_S = 0.45\,\text{m}$ and $z_S = 0.60\,\text{m}$ were performed for angles up to $\alpha_{\text{max}} = 60°$. The fits for $z_S = 0.15\,\text{m}$ were performed with $\alpha_{\text{max}} = 70°$ which resulted in significantly better results. The corresponding values of d and v_{P1} are compared in Table 4.2 for the three models and for all depths of the used sensors.

z_S / m	model 1		model 2		model 3		data points
	d / m	v_{P1} / (m/s)	d / m	v_{P1} / (m/s)	d / m	v_{P1} / (m/s)	used for fit
0	2.35	228	2.35	228	2.35	228	150
0.15	2.60*	240*	2.42	231	2.41	230	119
0.30	2.23	209*	2.38	225	2.38	225	146
0.45	2.34*	230*	2.25	226	2.24	225	57
0.60	2.14*	210*	2.17	208	2.20	210	55

Table 4.2: Results of the fit for the three models of interference as specified at the beginning of Section 4.4. For sensors in various depths z_S the obtained values of v_{P1} and d are given. Additionally, the numbers of data points used for the respective fits are shown in the last column.
The values in the cells with green margins correspond to fits with the models 2 and 3 which produced better results compared to those obtained from the fit with model 1. For this comparison the fit results for $z_S = 0\,\text{m}$ are used as reference.
The results marked with * differ from those given in [57] (only model 1 is discussed therein).

The fits using multiply reflected waves (models 2) and additionally the direct SV wave (model 3) generally yield better results than those obtained with the fit taking into account only the main contribution of the three strongest P waves (model 1). For this conclusion the results of the fits using the sensors at the surface are used as reference. The results of model 2 and model 3 that are significantly better (i.e. closer to the results of the surface fit) are framed with green in Table 4.2. Only for the fit in the depth $z_S =$

0.45 m slightly better results are obtained with model 1 compared to the fits with model 2 and model 3. All other fits with model 2 or model 3 result in significantly better results (cells with green frame) or comparable results (i.e. the results of d obtained with model 2 and model 3 for $z_S = 0.60\,\mathrm{m}$) with respect to those obtained with model 1. A discussion of the reliability of these results is given in Section 4.4.4.

In the columns of the results of model 1 in Table 4.2 the values for $z_S = 0.15\,\mathrm{m}$, $z_S = 0.45\,\mathrm{m}$ and $z_S = 0.60\,\mathrm{m}$ are marked with *. This indicates that these values differ from the results given in [57] for the corresponding fits. The reason for that deviation is the following: In [57] the reflection coefficient at the underground boundary was estimated to be $R_{\mathrm{PP}}(\alpha) = \text{constant} \approx 0.4$. As shown in Section 4.3.3 for several angles $R_{\mathrm{PP}}(\alpha)$ differs strongly from that value. For all fits presented here $R_{\mathrm{PP}}(\alpha)$ was calculated with Eq. (2.32) using the corresponding soil wave velocities. Thus, the relative amplitudes of the waves reflected at the underground boundary (i.e. $A_{\grave{\mathrm{P}}\acute{\mathrm{P}}}$ and $A_{\grave{\mathrm{P}}\acute{\mathrm{P}}\grave{\mathrm{P}}}$) are different compared to those used in [57]. This also leads to differing theoretically obtained frequency maxima $f^{\mathrm{theo}}_{\mathrm{max},k}(\alpha)$ and consequently do differing fit results.

For the fits outlying points were excluded iteratively to obtain better results. With increasing burying depth of the sensors z_S, generally more data points had to be dismissed due to lower SNR. In Table 4.2 also the number of data points used for the fits is given for each depth. Note that the data points for the fit originate from averaging of 16 overflight events, so the processed number of data is significantly larger.

For sensors at the surface the three models yield identical fit results as is visible in Table 4.2 in the row for $z_S = 0\,\mathrm{m}$ and as already stated in Section 4.4.2. This is so, since the frequencies of constructive interference $f^{\mathrm{theo}}_{\mathrm{max},k}(\alpha)$ are not affected by the different relative amplitudes of the interfering waves for $z_S = 0\,\mathrm{m}$ (see also Fig. 4.26). For $z_S > 0\,\mathrm{m}$ these different relative amplitudes lead to a beat between the waves and thus a modulation of the signal. This also results in different values of $f^{\mathrm{theo}}_{\mathrm{max},k}(\alpha)$ for each of the used models – depending on the order of the maximum k or on the frequency f – as is shown in Fig. 4.27 examplarily for $\alpha = 55°$, $z_S = 0.30\,\mathrm{m}$ and for the results of the surface fit $d = 2.35\,\mathrm{m}$ and $v_{\mathrm{P1}} = 230\,\mathrm{m/s}$.

The beat between the upwards- and downwards propagating interfering waves becomes clearly visible in Fig. 4.27 (top), resulting in an overall minimum of the amplitude of the envelope around 240 Hz for the shown depth $z_S = 0.30\,\mathrm{m}$. The different relative amplitudes of the interfering waves for each model result in a shift of the frequencies of the spectral interference maxima. This is shown in more detail exemplarily for the first spectral maximum (Fig. 4.27, bottom, left) and the fifth one (Fig. 4.27, bottom, right). Generally, the absolute frequency differences between the spectral maxima increase with increasing frequency. More importantly, the frequencies of the maxima calculated with the three models change relatively to each with frequency. For the first spectral maximum model 2 yields the smallest value $f^{\mathrm{theo}}_{\mathrm{max},1}(55°)|_{\mathrm{model\ 2}} \approx 30.7\,\mathrm{Hz}$, the

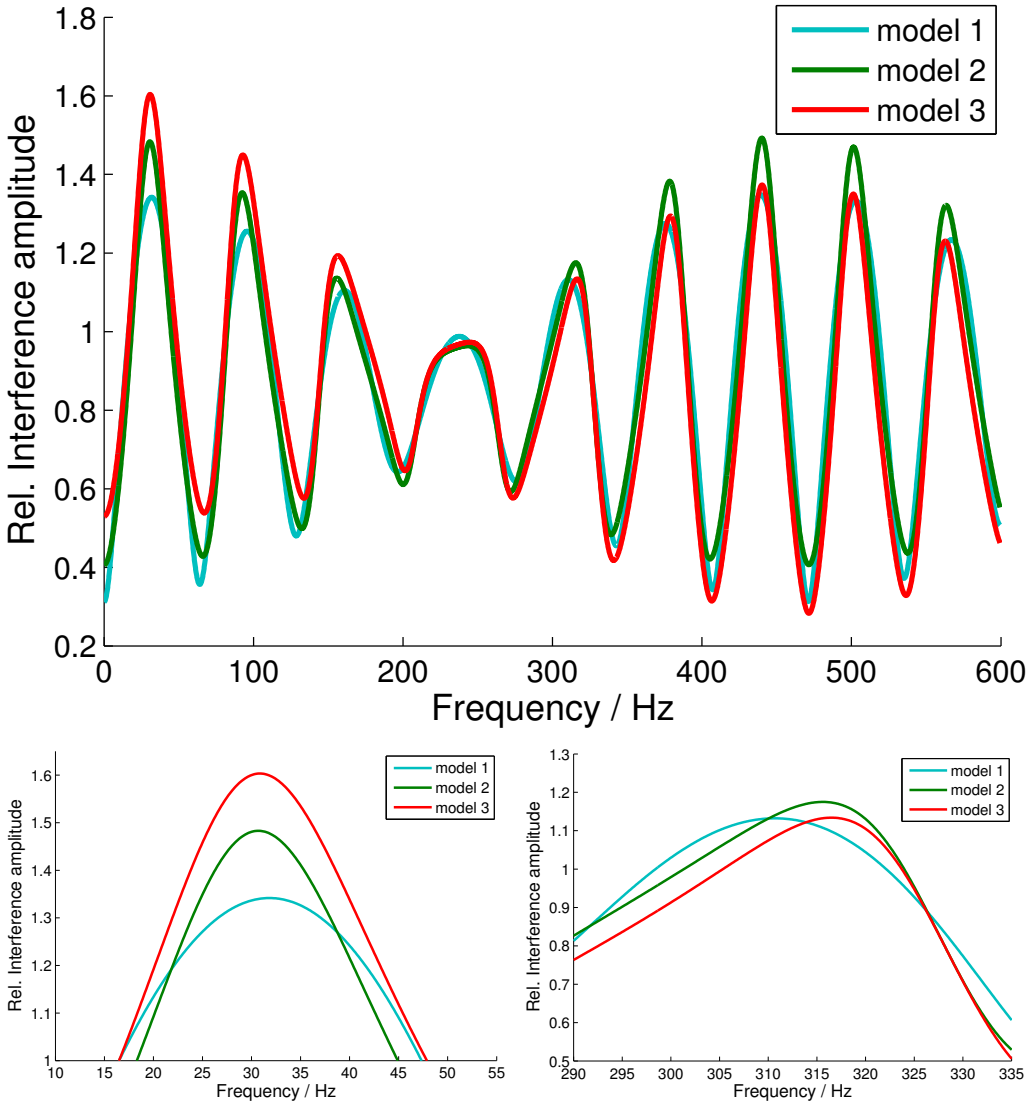

Figure 4.27: Theoretical interference amplitudes (vertical component) for the three models. The graphs are calculated for $\alpha = 55°$, $z_S = 0.30\,\text{m}$, $d = 2.35\,\text{m}$ and $v_{P1} = 230\,\text{m/s}$. Top: Full investigated frequency interval [0 Hz, 600 Hz]. Bottom, left: Detailed plot of the first spectral maximum; frequency interval [10 Hz, 55 Hz]. Bottom, right: Detailed plot of the fifth spectral maximum; frequency interval [290 Hz, 335 Hz].

third model produces a slightly larger value of $f^{\text{theo}}_{\text{max},1}(55°)|_{\text{model 3}} \approx 30.8\,\text{Hz}$ and with the first model the first spectral maxima is found at the frequency $f^{\text{theo}}_{\text{max},1}(55°)|_{\text{model 1}} \approx 31.9\,\text{Hz}$. Looking at the values of the frequencies of the fifth spectral maximum one finds in ascending order: $f^{\text{theo}}_{\text{max},5}(55°)|_{\text{model 1}} \approx 310.6\,\text{Hz}$, $f^{\text{theo}}_{\text{max},5}(55°)|_{\text{model 2}} \approx 315.6\,\text{Hz}$ and $f^{\text{theo}}_{\text{max},5}(55°)|_{\text{model 3}} \approx 316.6\,\text{Hz}$. The relative frequency differences between the maxima of the second and third models are approximately the same for the first and the fifth spectral maxima in this example, but they might change under different conditions. This is clearly the case for the maxima calculated with the first model: While the frequency of the first spectral maximum $f^{\text{theo}}_{\text{max},1}(55°)|_{\text{model 1}}$ is larger (compared to $f^{\text{theo}}_{\text{max},1}(55°)|_{\text{model 2}}$ and $f^{\text{theo}}_{\text{max},1}(55°)|_{\text{model 3}}$), that of the fifth spectral maximum $f^{\text{theo}}_{\text{max},5}(55°)|_{\text{model 1}}$ is significantly smaller than $f^{\text{theo}}_{\text{max},5}(55°)|_{\text{model 2}}$ and $f^{\text{theo}}_{\text{max},5}(55°)|_{\text{model 3}}$. Of course, the frequencies of the bands of increased coupling strength determined from the recorded data $f^{\text{meas}}_{\text{max},k}(\alpha)$ are the same for each fit, regardless of the used model. Thus, the differences in the theoretical values $f^{\text{theo}}_{\text{max},k}(\alpha)$ discussed here are the reason for the differing fit results (see Table 4.2). Using these solutions of each fit the theoretical amplitude distributions calculated for the three models are plotted in Fig. 4.28 exemplarily for $z_S = 0.15\,\text{m}$. Respective graphs for the depths $z_S = 0.30\,\text{m}$, $z_S = 0.45\,\text{m}$ and $z_S = 0.60\,\text{m}$ are shown in Appendix A.7. The upper left graph of Fig. 4.28 shows the averaged coupling coefficient and the data points (black dots) used for the fits. The upper right graph shows the theoretical amplitude distributions calculated with model 1 (for the values $d = 2.60\,\text{m}$ and $v_{P1} = 240\,\text{m/s}$), the lower left graph that calculated with model 2 (for $d = 2.42\,\text{m}$ and $v_{P1} = 231\,\text{m/s}$) and the lower right graph that calculated with model 3 (for $d = 2.41\,\text{m}$ and $v_{P1} = 230\,\text{m/s}$). All these values represent the fit result corresponding to the minimum of the root-mean-square deviation $D(d, v_{P1})$ (see Eq. (4.18)).

The frequencies of the numerically determined interference maxima $f^{\text{theo}}_{\text{max},k}(\alpha)$, which are fitted to the measured data, are plotted as black lines in the three graphs of the theoretical amplitude distribution. These $f^{\text{theo}}_{\text{max},k}(\alpha)$ increase monotonously until they reach a (local) maximum at a certain α. At this angle the reflection coefficient R_{PP} becomes negative (as was stated in Section 4.3.3). The value and sign of R_{PP} and consequently the angle at which the sign changes depend on the soil velocities in the upper and lower soil layer. Thus, the fit result of v_{P1} (from which the other velocities are derived) directly influences this angle. The change of the sign of R_{PP} corresponds to a phase shift of π of waves reflected at the underground boundary. This ultimately causes the $f^{\text{theo}}_{\text{max},k}(\alpha)$ to shift by half of the difference between consecutive $f^{\text{theo}}_{\text{max},i}(\alpha)$ and $f^{\text{theo}}_{\text{max},i+1}(\alpha)$. This is visible in Fig. 4.28 (top, right) for $\alpha \lesssim 78°$. The apparent decrease of the frequencies $f^{\text{theo}}_{\text{max},k}(\alpha)$ (i.e. in Fig. 4.28, top, right for $72° \leq \alpha \leq 78°$) is an artefact of the algorithm to track the frequency of a single interference maximum for increasing α. If the tolerance interval for the tracking of the maxima had been chosen wide enough, $f^{\text{theo}}_{\text{max},k}(\alpha)$ would jump immediately when the sign of R_{PP} changes. This change of the sign of R_{PP} does not

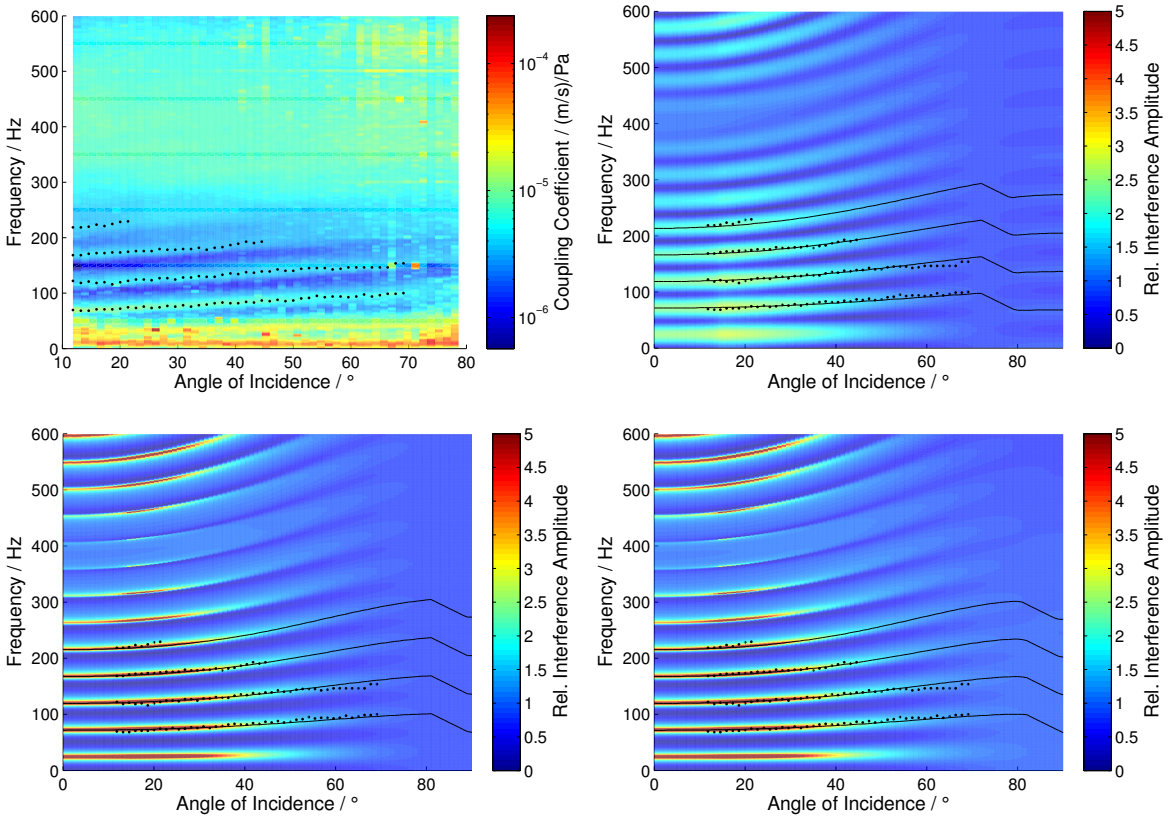

Figure 4.28: Top, left: Mean coupling coefficient measured in depth $z_S = 0.15\,\mathrm{m}$ (channel 10) together with the data points used for the fits (black dots). Top, right: Theoretical spectral amplitude distribution calculated with model 1 for the values $d = 2.60\,\mathrm{m}$ and $v_{P1} = 240\,\mathrm{m/s}$. Bottom, left: Amplitude distribution calculated with model 2 for the values $d = 2.42\,\mathrm{m}$ and $v_{P1} = 231\,\mathrm{m/s}$. Bottom, right: Amplitude distribution calculated with model 3 for the values $d = 2.41\,\mathrm{m}$ and $v_{P1} = 230\,\mathrm{m/s}$. The plots of the theoretical amplitude distribution also show the data points $f^{\mathrm{meas}}_{\mathrm{max},k}(\alpha)$ used for the respective fit (black dots) as well as the numerically determined frequencies of maximal interference amplitude $f^{\mathrm{theo}}_{\mathrm{max},k}(\alpha)$. The colour scale of the three theoretical plots is limited to the interval [0,5].

affect the fit since usually the angle range was limited to $\alpha_{\max} = 60°$. Moreover, $|R_{\mathrm{PP}}|$ approaching 0 corresponds to the vanishing of the reflected wave at the underground boundary. Accordingly, no interference pattern would be observed in the measured data. Additionally, with increasing α the distance between source (i.e. the aircraft) and sensors increases and thus the overall signal amplitude decreases. Both effects lead to a decrease of the ratio between maxima and minima of the interference pattern and ultimately to its vanishing for high α. This can be observed more clearly for increasing depths of the sensors z_{S} and for increasing frequency f.

4.4.4 Reliability of the solution

With the fit algorithm (see Section 4.4.1) the minimum of the relative root-mean-square deviation $D(d, v_{\mathrm{P1}})$, given by Eq. (4.18), is determined. These values are shown in Table 4.3 for each of the used models and for each depth z_{S}.

z_{S} / m	$D(d, v_{\mathrm{P1}})\|_{\text{model 1}}$	$D(d, v_{\mathrm{P1}})\|_{\text{model 2}}$	$D(d, v_{\mathrm{P1}})\|_{\text{model 3}}$	data points used for fit
0	0.0126	0.0126	0.0126	150
0.15	0.0279	0.0287	0.0288	119
0.30	0.0333	0.0333	0.0340	146
0.45	0.0555	0.0415	0.0460	57
0.60	0.0417	0.0344	0.0336	55

Table 4.3: Relative root-mean-square deviation $D(d, v_{\mathrm{P1}})$ between the measured frequencies of maximal coupling strength $f^{\mathrm{meas}}_{\mathrm{max},k}(\alpha)$ and that of the theoretically obtained ones $f^{\mathrm{theo}}_{\mathrm{max},k}(\alpha)$ for each of the used models and all depths z_{S}. The given values are calculated for the fit results d and v_{P1} (see Table 4.2) and represent the respective minimum of $D(d, v_{\mathrm{P1}})$.
In the last column again the numbers of data points used for the fits in the respective depths are given.

The values of $D(d = 2.35\,\mathrm{m},\ v_{\mathrm{P1}} = 228\,\mathrm{m/s}) = 0.0126$ for $z_{\mathrm{S}} = 0\,\mathrm{m}$ are identical for the three used models. Again, this can be understood easily since the theoretical frequency maxima $f^{\mathrm{theo}}_{\mathrm{max},k}(\alpha)|_{z_{\mathrm{S}} = 0\,\mathrm{m}}$ are the same for each model. Additionally, these values represent the overall minimum of $D(d, v_{\mathrm{P1}})$ for all fits. This indicates that the results of the fits for $z_{\mathrm{S}} = 0\,\mathrm{m}$ can be given most credibility. Additional explanations are that at the surface the SNR is best and that here the highest number of points for the fit exists.
For the depths $z_{\mathrm{S}} > 0\,\mathrm{m}$ the values of $D(d, v_{\mathrm{P1}})$ are larger, but still represent very satisfactory results. The reasons for the larger values (compared to those for $z_{\mathrm{S}} = 0\,\mathrm{m}$) are the following: With increasing depth the SNR of the measured data decreased. Thus, the determination of the frequencies of the maxima of the coupling coefficient $f^{\mathrm{meas}}_{\mathrm{max},k}(\alpha)$ is less reliable. This also results in a higher number of outlying data points that had to be excluded from the fitting.

Comparing the values of $D(d, v_{P1})$ at constant z_S for the three models one finds similar results with all models for depths up to $z_S = 0.30\,\text{m}$. For larger depths the values obtained with model 1 are significantly larger than those of the fits with model 2 and model 3. Between model 2 and model 3 only minor differences of the values of $D(d, v_{P1})$ are found – with the slight tendency, that the values calculated for model 2 are smaller than those calculated for model 3. Since the data used for the fits correspond to angles $\alpha \leq 60°$ only minor differences between the two models are expected. This is so, since model 2 and model 3 differ by taking into account SV waves (in the latter) the influence of which increases with increasing α. Only for the fits for $z_S = 0.15\,\text{m}$ $\alpha_{max} = 70°$ is used – and even for these fits hardly a difference between model 2 and model 3 can be observed.
Generally, the found values of d and v_{P1} lead to a good explanation of the measured interference patterns and therefore confirm the used models: By considering only the major contributions of the three P waves already good results are obtained. The evaluation of the signals recorded at the buried sensors shows that additionally waves reflected multiple times within the soil contribute to the seismic signal. In comparison with the additionally performed seismic refraction survey (evaluation in [60]) these values represent a satisfactory result.
However, calculating $D(d, v_{P1})$ at $z_S = 0\,\text{m}$ for a wider range around the obtained solution shows (see Fig. 4.29, top, left) that accepting e.g. values of $D = 0.015$ (representing an increase by 20 % compared to the minimum) leads to solutions in the range from $d = 2.16\,\text{m}$ and $v_{P1} = 212\,\text{m/s}$ to $d = 2.54\,\text{m}$ and $v_{P1} = 242\,\text{m/s}$. Fig. 4.29 (top, left) shows the found solution for $z_S = 0\,\text{m}$ marked with an X together with the contour of 10 %, 20 % and 50 % increased values with respect to the minimum of $D(d = 2.35\,\text{m}, v_{P1} = 228\,\text{m/s}) = 0.0126$. Corresponding calculations were performed for all depths z_S and for all used models for $2.00\,\text{m} \leq d \leq 2.60\,\text{m}$ (with increment 0.01 m) and $200\,\text{m/s} \leq v_{P1} \leq 250\,\text{m/s}$ (with increment 1 m/s). For each model, the solution of the fit (i.e. the minimum of $D(d, v_{P1})$) is displayed together with the range of 20 % increased values relative to the respective minima: Fig. 4.29 (top, right) shows the solution ranges for all z_S obtained with model 1, Fig. 4.29, (bottom, left) that calculated for model 2 and Fig. 4.29, (bottom, right) the corresponding plots for model 3.
For $z_S = 0\,\text{m}$ the position of the solution (dark blue X) and the range of the 20 % increased values of $D(d, v_{P1})$ (dark blue ellipse) are identical in all plots. The results obtained with model 1 at all other depths deviate more strongly from the solution of $z_S = 0\,\text{m}$, which is taken as reference, (see also Table 4.2) than the results of model 2 and model 3. Accordingly, the corresponding solution ranges are wider for model 1 than those of model 2 and model 3. The fit results for $z_S = 0.45\,\text{m}$ resulted in the largest values of $D(d, v_{P1})$ (see also Table 4.3). The solution ranges (black lines) are the widest for all of the three models, compared to the other depths z_S. The fits for $z_S = 0.45\,\text{m}$ used only few data points and only data up to $\alpha \approx 42°$ (see Fig. A.8) while for all other depth angles up to $\alpha_{max} =$

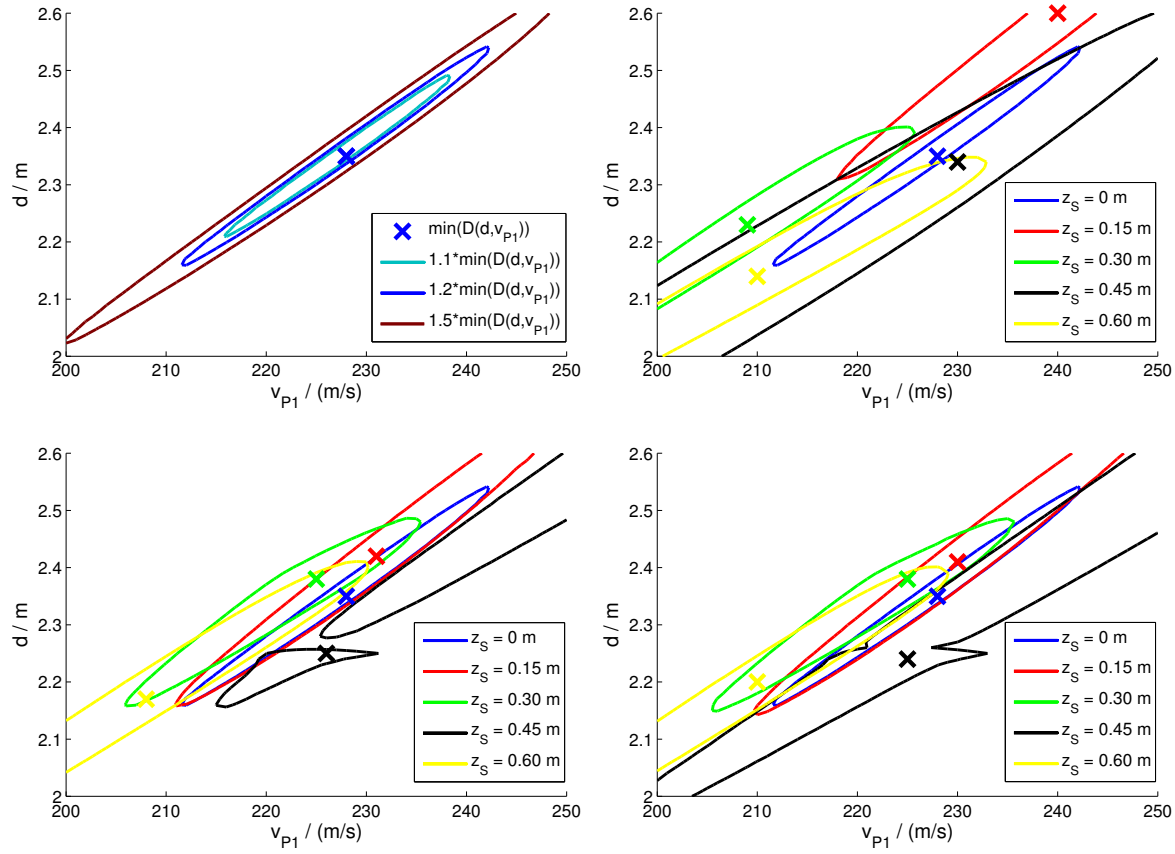

Figure 4.29: Positions of the solution corresponding to the minima of the relative root-mean-square deviation $D(d, v_{\mathrm{P1}})$ between the frequencies of measured and theoretical interference maxima together with an uncertainty range around the solutions. Top, left: Solution of the fit of the surface sensor: The minimum $D(d = 2.35\,\mathrm{m},\ v_{\mathrm{P1}} = 228\,\mathrm{m/s}) = 0.0126$ is marked with a dark blue X. The ranges of 10 %, 20 % and 50 % increased values of $D(d, v_{\mathrm{P1}})$ with respect to the minimum are shown.
Top, right: Solutions obtained with model 1 for all z_{S} with the ranges of 20 % increased values relative to the respective minima. Bottom, left: Solutions obtained with model 2 and the respective ranges of 20 % increased values. Bottom, right: Solutions obtained with model 3 and the respective ranges of 20 % increased values.

60° were used. Additionally, it can be noted, that the ranges of 20 % increased values of $D(d, v_{P1})$ for $z_S = 0.45\,\mathrm{m}$ obtained with model 2 and model 3 show discontinuities around the solution. They result from two local minima in the observed range of the solution. Consequently, the solutions for $z_S = 0.45\,\mathrm{m}$ are given least creadibility.
The parameters d and v_{P1} are not independent but linked by the phase terms in Eq. (2.73) or by Eq. (2.49) (for the special case $z_S = 0\,\mathrm{m}$). Thus, the shape of the solution space can be explained. The found solutions represent stable minima[37] of the relative deviation between measured and theoretical data. However, in a wider range around the solution in which v_{P1} varies approximately linearly with d only slightly larger values of $D(d, v_{P1})$ are obtained – these solutions are nearly as likely as the solution found for the minimum of $D(d, v_{P1})$. A discussion of further improvements and suggestions to enhance reliability is given in Chapter 5.

4.5 Acoustic-seismic coupling with applied acoustic damping

In the previous sections acoustic-seismic coupling has been evaluated and conclusions about the propagation of acoustically-induced seismic waves in the ground have been derived. It is the aim of this work to derive recommendations to reduce or even prevent such disturbing seismic signals during sensitive measurements. Therefore, in this section measurements are presented and discussed during which an acoustic shielding was used to locally reduce the sound pressure hitting the ground.
During ten of the recorded overflight events (i.e. overflights number 7 to 16, see Table A.2) an acoustic damping box was placed over several sensors: Two microphones at the surface and one geophone in each depth $z_S = 0\,\mathrm{m}$, $z_S = 0.15\,\mathrm{m}$, $z_S = 0.30\,\mathrm{m}$, $z_S = 0.45\,\mathrm{m}$ and $z_S = 0.60\,\mathrm{m}$ were shielded by the box from the incident acoustic signals. The characteristics of the box are described in Section 3.2.3 and its setup above the respective sensors is shown in Fig. 3.3.
Firstly, in Section 4.5.1 the effects of the acoustic shielding on the measured signals are presented and consequences for the evaluation are discussed. Then, in Section 4.5.2 the amplitude reduction and the phase shift of the acoustic signal are analysed in detail. In particular, it is demonstrated that the amplitudes of the acoustically-induced seismic disturbances can be reduced strongly in a wide frequency range. Afterwards, in Section 4.5.3 the observed interference patterns under the box are discussed and the theoretical models are applied to explain the findings.

[37] with the exception of the fits for $z_S = 0.45\,\mathrm{m}$ with the models 2 and 3

4.5.1 Physical influence of the acoustic damping on the signal and consequences for the evaluation

When the box is placed over several sensors, the incident acoustic signal is affected in several ways:

- **Reflection:** A share of the energy of the incident acoustic signal is reflected at the solid plywood surface of the box. If reflected at the lid of the box, the direction of the reflected wave is upwards into the air-filled half-space. Thus, the signal does not contribute in any way to the recordings at the sensor. If reflected at the side walls of the box the acoustic signal still hits the soil surface where it excites ground motion. However, the horizontal component of the propagation vector points away from the sensors placed under the box. Thus, the influence on the recorded signal is small and is neglected for the theoretical explanation.

- **Absorption:** Another share of the incident acoustic wave propagates into the plywood and the acoustic damping foam on the inside of the box. In the porous foam a part of the energy of the wave is absorbed. Thus, the amplitude of the acoustic wave penetrating the box and reaching the sensors inside is reduced strongly. The absorption coefficient increases with frequency as discussed in Section 2.3.3. Thus, signals of low frequency (i.e. few tens of Hz) experience only little absorption while those of frequencies of several hundred Hz are nearly completely absorbed.
  The reduction of the amplitude affects only the directly acoustically excited waves $A_{\grave{\mathrm{P}}}$ and $A_{\grave{\mathrm{S}}}$. For waves reflected multiple times (i.e. $A_{\grave{\mathrm{P}}\acute{\mathrm{P}}}$, $A_{\grave{\mathrm{P}}\acute{\mathrm{P}}\grave{\mathrm{P}}}$ and so on) the location of excitation is outside of the box for all angles α and all aircraft trajectories. However, if a seismic wave is acoustically excited close to the box – and therefore the exciting acoustic plane wavefront is disturbed by the latter –, the wavefront of the seismic wave is no longer planar.

- **Phase shift:** Due to different acoustic wave velocities in the plywood and in the damping foam (compared to v_0), the acoustic wave reaching the sensor experiences an effective phase shift $\Delta\phi_{\mathrm{box}}$ with respect to the wave that would reach the sensor undisturbed. $\Delta\phi_{\mathrm{box}}$ depends on the distance which is covered inside of the damping material and thus on α and the orientation of the box with respect to the aircraft trajectories. It is treated as an effective value since in the scope of this work the two phase shifts due to the propagation through the plywood and through the damping foam are not treated separately.

In Section 4.5.2.1 firstly the reduction of the signal amplitude in the time domain and of the spectral amplitude values due to reflection and absorption at the box are presented. The phase shift caused by the box is discussed in Section 4.5.2.2.

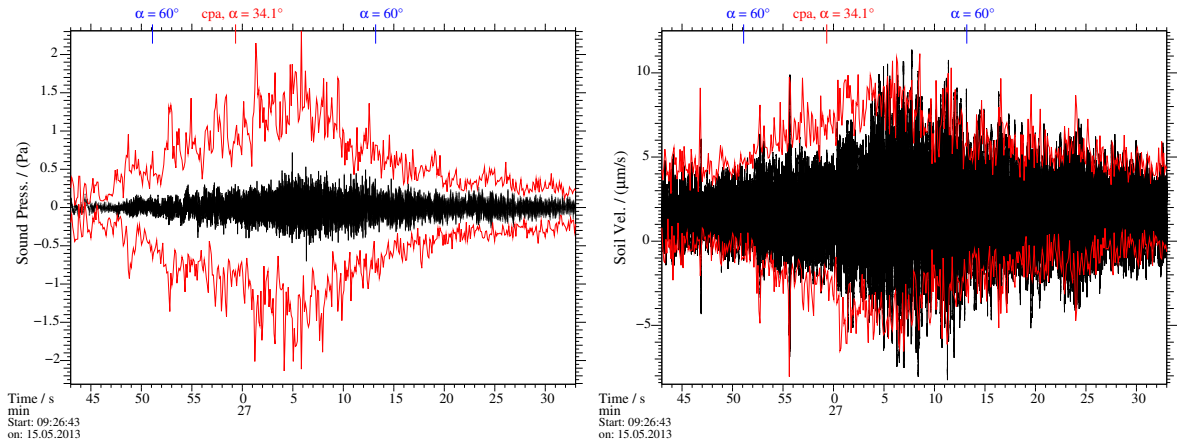

Figure 4.30: Time signals of the jet-aircraft overflight number 13 (see Table A.2). Both graphs show the signal of one sensor which is shielded by the acoustic damping box (black signal) and the envelope of the signal of a corresponding sensor outside of the box (red curves). The time when the signal, emitted by the aircraft at its cpa, was recorded is indicated with a red line at the top of each graph. Additionally, the time interval during which the angle of incidence α was smaller than 60° is defined by two blue lines.
Left: Sound pressure, recorded with the microphone of channel 27 under the shielding box (black signal) and with the microphone of channel 29 outside of the box (red envelope).
Right: Vertical soil velocity at the surface, recorded with the geophone of channel 23 under the box (black signal) and with the geophone of channel 24 outside of it (red envelope).

4.5.2 Signal characteristics with applied acoustic damping

4.5.2.1 Amplitude reduction caused by the box

Fig. 4.30 (left) shows the sound pressure recorded with a microphone under the box (channel 27) during overflight number 13 (black signal). The corresponding soil velocity at the surface, recorded with a geophone under the box (channel 23), is shown in Fig. 4.30 (right) in black. To compare these signals to the respective ones recorded with sensors outside of the box the envelope of the latter are additionally plotted as red curves in Fig. 4.30. The envelope corresponds to the respective minima and maxima of the time signal in time intervals of 0.1 s. The full signals of the sensors outside of the box are shown in Fig. 4.1.

As visible in the time signals the sound pressure is significantly reduced by the box, but only a slight reduction can be observed for the soil velocity: The ratio between the peak-to-peak amplitudes of the signals recorded outside of the box and inside of it is about 4.5 to 5 around the cpa for the sound pressure, but only about 1.6 to 1.7 for the soil velocity. At the beginning and the end of the shown time interval (corresponding to a distance between aircraft and sensor of about 1800 m and about 4000 m, respectively)

this ratio drops to approximately 2 to 2.5 for the sound pressure and to 1 for the soil velocity. The former indicates that the box also reduces background sound-pressure fluctuations. Such signals (especially wind) have a high share of amplitudes at low frequencies. Thus, the reduction factor for the background signals is significantly smaller than that of the aircraft overflights the amplitudes of which range to several hundreds of Hz. The local acoustic shielding reduces the amplitudes of the directly acoustically excited, seismic waves $A_{\grave{\mathrm{P}}}$ and $A_{\grave{\mathrm{S}}}$ but not those of seismic waves excited outside of the box and reflected inside the upper soil layers. Thus, the seismic reduction ratio of the amplitudes at the cpa is smaller than that of the respective acoustic signals. The background soil velocity is determined by sources in a larger area around the sensors and thus approximately the same soil velocities are recorded with geophones outside and inside of the box. The local shielding by the box of the geophones hardly reduces the soil velocity of background signals.
The ratios of the signal amplitudes of geophones buried outside of the box and under it have approximately the same values as for the surface geophones. This can be observed more clearly when evaluating the spectral amplitudes (shown in Fig. 4.31).

Taking a look at the respective spectra in Fig. 4.31 (calculated exemplarily for the cpa of the overflight number 13, the time of which is marked in Fig. 4.30 at the top in red) the reduction of the spectral amplitude can be investigated.[38] All graphs in Fig. 4.31 show spectra of a pair of corresponding sensors – one placed inside of the box (black spectra) and the other one outside of it (red spectra): Spectra of the sound pressure (top, left) and of the soil velocity at the surface (top, right), in the depth of $z_{\mathrm{S}} = 0.30\,\mathrm{m}$ (bottom, left) and in the depth of $z_{\mathrm{S}} = 0.60\,\mathrm{m}$ (bottom, right). The spectrograms of the overflight corresponding to the whole time interval shown in Fig. 4.30 are given in Appendix A.8.
As visible from Fig. 4.31 the reduction of the spectral amplitude by the used box is strongly dependent on the frequency. To characterise it the reduction factors for sound pressure and soil velocity, respectively, can be calculated as the ratio between the amplitude recorded outside of the box and that recorded under it.[39] For the acoustic spectra a reduction can be observed for frequencies larger than $f \approx 30\,\mathrm{Hz}$. The amplitude of the sound pressure is reduced approximately by the factors 3 at 50 Hz, 4.9 at 100 Hz, 10.2 at 250 Hz and 30.8 at 500 Hz. The acoustic damping factor is shown in Fig. 4.32 (blue curve).

[38] In Fig. 4.7 and Fig. 4.8 spectra calculated for different times of sensors outside of the box were compared. In Fig. 4.31 only spectra calculated for the cpa are shown and the comparison between sensors inside and outside of the box is made. The relative spectral amplitudes of the shown pairs of sensors are similar for spectra calculated for different times during the aircraft overflight.

[39] Note that Fig. 4.31 shows power spectra while the reduction factors given here refer to the amplitudes, i.e. the square root of the power values.

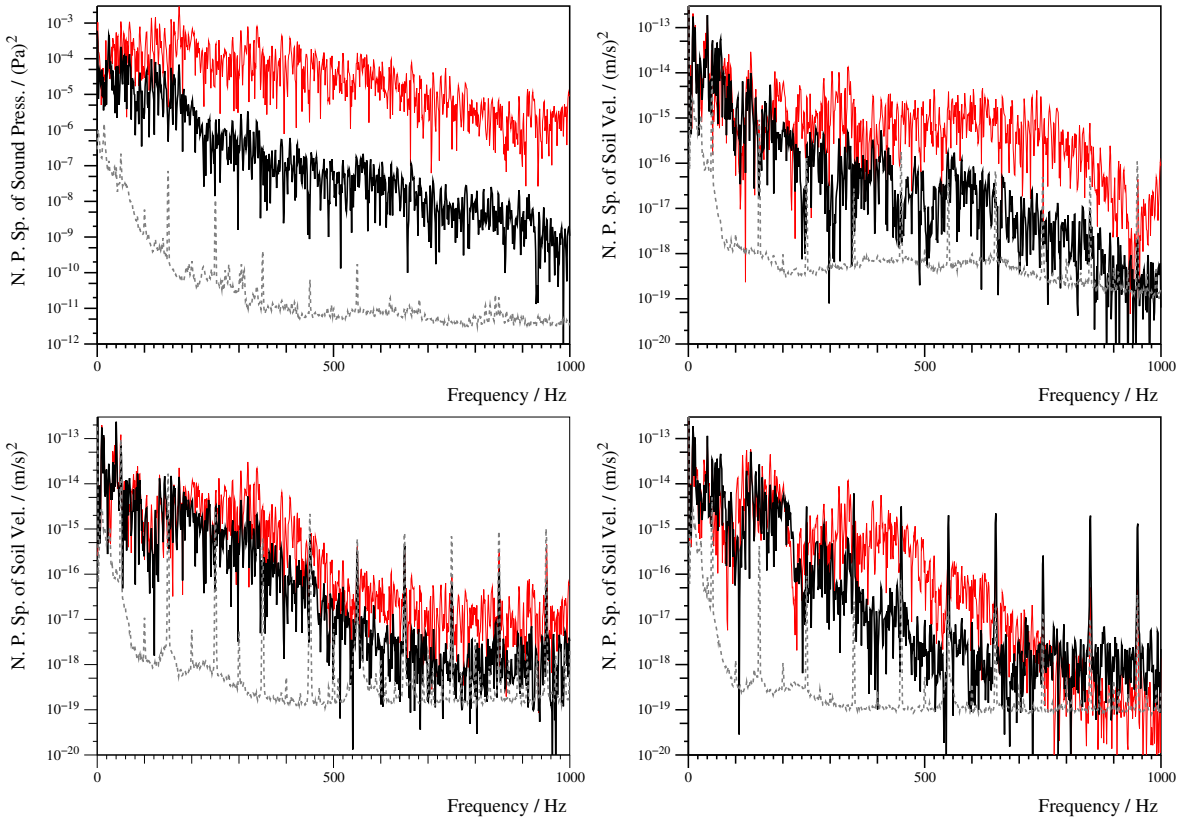

Figure 4.31: Normalised power spectra of jet-aircraft overflight number 13 calculated for the time 9:26:59 (corresponding to the cpa of the aircraft). Black spectra correspond to sensors under the acoustic damping box and red spectra to sensors without shielding – the red spectra were already shown (also in red) in Fig. 4.7 and Fig. 4.8 and are given here again as comparative values. The dashed, grey curves show the background for the respective sensors.
Top, left: Sound pressure, recorded with the microphones of channel 27 (black) and channel 29 (red).
Top, right: Vertical soil velocity, recorded at the surface $z_S = 0\,\mathrm{m}$ with the geophones of channel 23 (black) and channel 24 (red).
Bottom, left: Vertical soil velocity, recorded in the depth $z_S = 0.30\,\mathrm{m}$ with the geophones of channel 3 (black) and channel 6 (red).
Bottom, right: Vertical soil velocity, recorded in the depth $z_S = 0.60\,\mathrm{m}$ with the geophones of channel 0 (black) and channel 13 (red).

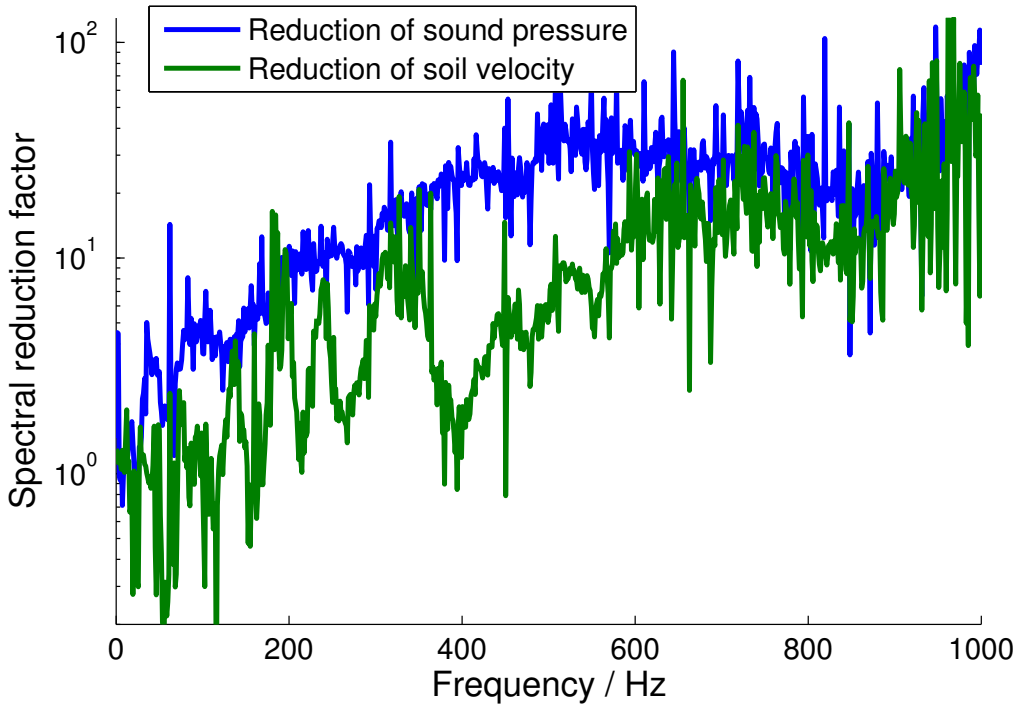

Figure 4.32: Reduction factors of the amplitudes of sound pressure (blue) and soil velocity, recorded at the surface (green).

The seismic reduction factors are much smaller, since not only the local acoustic excitation contribute to the recorded soil velocity but also waves propagating inside of the ground which are excited outside of the box. Thus, up to $f \approx 100\,\mathrm{Hz}$ no significant reduction of the soil velocity is observed. Additionally, the modulation of the spectral amplitudes due to the discussed interference of seismic waves is also found for the reduction factors: The local interference minima and maxima – the frequencies of which do not necessarily match for signals outside and inside of the box – lead to a fluctuation of the reduction factors of about one order of magnitude. Thus, the given reduction factors represent a rough estimate averaged around the stated frequencies. In the scope of this estimate for all burying depths the same reduction factors are found: 1 at 50 Hz, 1 at 100 Hz, 1.6 at 250 Hz and 2.5 at 500 Hz. Furthermore, the discussed fluctuations of the soil velocity lead for some frequencies to an apparent increase of the soil velocity for sensors placed under the box, i.e. a reduction factor smaller than 1.
Exemplarily, the reduction factor of the soil velocity at the surface is shown in Fig. 4.32 (green curve) – the respective factors for the signals of the other depths plotted in Fig. 4.31 show similar values.

4.5.2.2 Additional phase shift introduced by the box

A second – unwanted and disturbing – effect of positioning the damping box above the sensors is an additional phase shift $\Delta\phi_{\mathrm{box}}$ of the acoustic wave penetrating the box. This

phase shift is caused by the smaller effective wave velocity inside of the wall or the lid of the box[40] compared to that in air v_0. $\Delta\phi_{\text{box}}$ depends on the distance the wave has to cover through foam and plywood which is determined by the orientation of the box (see Fig. 3.3) with respect to the direction of incidence of the acoustic signal. Thus, no longer only the angle of incidence α (i.e. the angle towards the normal to the ground) affects the signal but also the azimuthal angle of the acoustic signal. As a consequence for the evaluation averaging of signals of several aircraft overflights of corresponding α is not possible for sensors placed under the damping box.[41] While this was done in the previous evaluations without box as discussed in Section 4.2.1, the spectral evaluation of the interference pattern of acoustically shielded sensors is performed on signals of single overflight events without averaging.[42] In this section it is demonstrated that the phase shift caused by the used damping box varies strongly during the overflight events and thus an averaging of signals cannot be applied.

Since the phase of a signal for a given time and frequency may have any value, it is necessary to look at the phase difference between two sensors. If a correlation between the signals at both sensors exists – that is, both signals agree except for a time shift and an amplitude factor – there is a linear relation between phase difference and frequency. This linear relation is theoretically given by Eq. (2.24) with the proportionality factor

$$m_{\Delta\phi,\text{theo}} = \frac{2\pi r_{\parallel}}{v_0}. \tag{4.20}$$

Here v_0 is the wave velocity of the undisturbed acoustic wave and $r_{\parallel}$ is the projected distance between both sensors in direction of propagation of the wave. Since the wave velocity inside of the foam and the plywood of the box are unknown and the distance covered inside both changes as the aircraft moves, the undisturbed acoustic wave propagating with v_0 is used as reference here. The measured phase difference is the difference of the phases at both sensors which are obtained from the respective complex spectral values with Eq. (4.10).

In Fig. 4.33 for the two microphones of channel 27 and 29 the measured phase differences (blue curves) and those calculated theoretically for the wave speed v_0 (red dashed curves) are shown. The left graph corresponds to overflight number 2 during which the acoustic

[40] The walls and the lid of the box are made of 18 mm plywood and 0.1 m damping foam on the inside. While the wave velocity in the plywood is larger than v_0, it is significantly smaller in the damping foam. The wave velocity during the penetration the box and the corresponding phase shift are treated as effective values in the scope of this work.

[41] Taking into account the angle of incidence α and the azimuthal angle of the acoustic signal with respect to the orientation of the box the signals recorded under the same conditions could be averaged to increase the SNR. From this also characteristics depending on the azimuthal angle could have been derived. However, for the presented measurements too little data are available to achieve this successfully.

[42] If the acoustic shielding would have been hemispherical and centred above the sensor the additional phase shift $\Delta\phi_{\text{box}}$ would be the same for signals incident from any direction. Thus, averaging would have been possible.

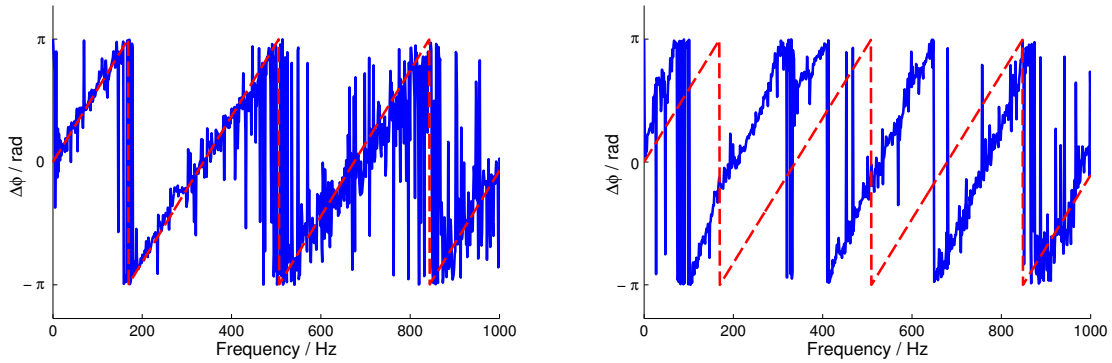

Figure 4.33: Phase difference of the signals recorded at the two microphones of channel 27 and 29 (blue curves) at the angle $\alpha \approx 33°$. The left graph corresponds to overflight number 2 for which no acoustic shielding was used. Thus, the acoustic waves propagated with the velocity v_0 between both microphones. The right plot corresponds to overflight number 9 during which the acoustic damping box was placed over the microphone of channel 27. Thus, the acoustic waves were delayed between both microphones and the effective wave velocity was smaller than v_0.
The red curves show the theoretical phase delay between both sensors calculated with Eq. (2.24) for the wave velocity v_0.

damping box was not used. The right graph corresponds to overflight number 9 during which the acoustic damping box was placed over the microphone of channel 27. The measured phase differences of both events are obtained from spectra recorded at approximately the same angle $\alpha \approx 33°$.

During overflight number 2 (Fig. 4.33, left) the acoustic wave propagated undisturbed between the two microphones. Thus, the measured phase difference follows the theoretically determined one and – disregarding some fluctuations – a clear linear relation can be observed between phase difference and frequency. With increasing frequency the fluctuations of the phase difference become larger indicating a decrease of that correlation. This can be explained by the decreasing spectral amplitude of the acoustic signal and thus a lower SNR.

For overflight number 9 (Fig. 4.33, right) the acoustic damping box placed over the microphone of channel 27 caused an additional phase shift of the acoustic wave. Consequently, the phase difference between the signals recorded at the microphones of channel 27 and channel 29 differs strongly from that calculated for the undisturbed acoustic signal. Still, it shows a clear linear relation between phase difference and frequency for most frequencies. Thus, despite the strong reduction of the spectral amplitude by the box (presented in Section 4.5.2) the correlation between both signals is preserved.[43] The red dashed

[43]Comparing the phase differences of the overflight events without box (Fig. 4.33, left) and that one with the box (Fig. 4.33, right) with increasing frequency stronger fluctuations are found for the former one. This is counter-intuitive since due to the decrease of the sound pressure by the box one would expect smaller correlation between the signals and thus stronger fluctuations in the linear relation in Fig. 4.33 (right). The stronger fluctuations in Fig. 4.33 (left) could be explained by a smaller sound pressure emitted during the respective overflight and due to higher background noise (compared to the overflight

curve shows the theoretical phase difference between the signals recorded at both sensors if the acoustic waves would have propagated undisturbed with the velocity v_0. Since the effective wave velocity while penetrating the box is smaller, the proportionality factor $m_{\Delta\phi,\text{meas}}$ (which is inversely proportional to the wave velocity) is significantly larger than $m_{\Delta\phi,\text{theo}}$ (used as reference).
Now, the difference between the two proportionality factors

$$\Delta m_{\Delta\phi} = m_{\Delta\phi,\text{meas}} - m_{\Delta\phi,\text{theo}} \tag{4.21}$$

can be used to characterise the phase shift by the box for different angles of incidence α and different overflight events. From the measured data $m_{\Delta\phi,\text{meas}}$ is determined as the slope of a linear fit in a suitable frequency interval. For this the phase jumps of 2π are corrected by adding multiples of 2π to the phase difference. The phase difference of outlying points the values of which differed by more than $\pm\pi$ from the averaged one of neighbouring frequencies were iteratively corrected likewise. Then the frequency intervals for the fit were selected manually – the fits usually were performed for intervals of several hundreds of Hz. Frequencies $f > 800\,\text{Hz}$ were not used for these fits due to the general decrease of the SNR. Generally, the assumption is made, that there is only a linear relation between phase and frequency. At some frequencies a deviation from that proportionality can be observed e.g. for overflight number 9 at $f \approx 335\,\text{Hz}$ the phase jumps (see Fig. 4.33, right). These higher order dependencies on the frequency are neglected here.
Thus, for the aircraft overflights for consecutive spectra (calculated for time intervals of $T = 0.8192\,\text{s}$) values of $m_{\Delta\phi,\text{meas}}$ are determined for the two microphones of channel 27 and 29. The values of $m_{\Delta\phi,\text{theo}}$ are obtained from the position of the aircraft at the time of signal emission which determines the respective $r_{\parallel}$ and the wave velocities for each overflight v_0 (stated in Table A.3). Thus, $\Delta m_{\Delta\phi}$ can be calculated with Eq. (4.21). In Fig. 4.34 $\Delta m_{\Delta\phi}$ is plotted for several overflight events: One example of an overflight without box – overflight number 2 (black curve) – and three selected ones during which the box was placed over several sensors: Overflight number 8 (green curve), overflight number 9 (red curve) and overflight number 12 (blue curve). All shown values correspond to the approach of the aircraft towards the sensors – after passing the cpa the orientation of the box also differed for respective α. Correspondingly, approach towards and departure from the sensor setup have to be treated separately as well.
For acoustic waves propagating undisturbed by the box between two sensors the measured phase difference and that calculated theoretically for the wave velocity v_0 show only slight differences (see Fig. 4.33, left). Thus, the difference of the respective proportionality factors between phase difference and frequency $\Delta m_{\Delta\phi}$ is approximately 0 (black curve in Fig. 4.34). When the box is placed over one of the microphones the values of $\Delta m_{\Delta\phi}$

during which the box was placed over one sensor).

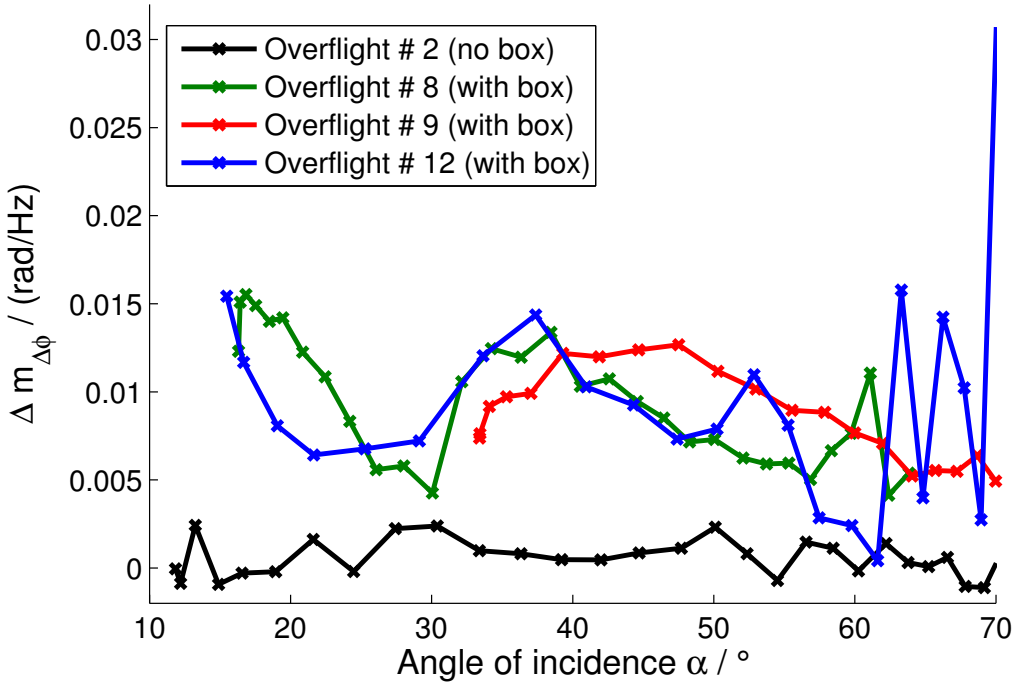

Figure 4.34: Difference of the proportionality factors between phase difference and frequency of measured and theoretical values $\Delta m_{\Delta\phi}$. For overflights during which the damping box was not used, these values are close to 0 for all α (black curve). When the damping box was placed over one of the microphones $\Delta m_{\Delta\phi}$ changes during a single overflight with α as well as for a fixed α between various overflight events (compare green, red and blue curves).

which are a measure for the additional phase shift by the box are significantly larger than 0. More importantly, these values change with α during one overflight and they differ for a given α between overflights during which the box was used. Exemplarily, for α around 20° the values of $\Delta m_{\Delta\phi}$ for overflight number 8 (Fig. 4.34, green curve) are nearly twice as large as that of overflight number 12 (Fig. 4.34, blue curve): At $\alpha \approx 19°$ for overflight number 8 $\Delta m_{\Delta\phi,\#8} \approx 0.014\,\mathrm{rad/Hz}$ and for overflight number 12 $\Delta m_{\Delta\phi,\#12} \approx 0.008\,\mathrm{rad/Hz}$ are found. This means that the additional phase shift by the box is by $(\Delta m_{\Delta\phi,\#8} - \Delta m_{\Delta\phi,\#12}) \cdot f$ larger for the acoustic waves penetrating the box of overflight 8 compared to that of overflight 12. To further exemplify this, for these values the phase shift by the box is at $f \approx 100\,\mathrm{Hz}$ by $0.22 \cdot \pi$, at $f \approx 225\,\mathrm{Hz}$ by $\pi/2$ and at $f \approx 450\,\mathrm{Hz}$ by π larger comparing overflight 8 to overflight 12. Consequently, signals of the various overflight events during which the acoustic damping box was used are not averaged.
The values of $\Delta m_{\Delta\phi}$ show small fluctuations due to an uncertainty in the selection of the fit interval and fluctuations of the phase difference values (see also Fig. 4.33). However, these do not contradict the conclusions made here since the modulation of $\Delta m_{\Delta\phi}$ with α holds despite these fluctuations and the differences in $\Delta m_{\Delta\phi}$ for certain α between the shown overflights with box are clearly observable. For higher α stronger fluctuations occur (e.g. $\alpha \gtrsim 60°$ for overflight 12) which are given no credibility. They are caused by the decreasing correlation of the signals recorded at different sensors due to the low signal amplitude and thus the low SNR at high α and large distances between aircraft and sensors. Therefore, also the fit to determine $m_{\Delta\phi,\mathrm{meas}}$ yielded unreliable results at these angles.

4.5.3 Interference pattern with applied acoustic damping

In Section 4.4 the interference patterns of seismic waves reflected within the upper soil layer are investigated. For this the acoustic-seismic coupling coefficient $Cc(f, \alpha)$ (defined by Eq. (4.12)) is used. Correlating signals by the angle α the coupling coefficients of several aircraft overflights are averaged to increase the SNR.
However, when analysing the interference of seismic waves recorded with sensors placed under the acoustic damping box it is more convenient to use the soil velocity instead of the coupling coefficient: In Section 4.5.2.1 it was shown that the reduction of the amplitude by the used box is much stronger and depends more strongly on the frequency for the sound pressure than for the soil velocity. Thus, if the coupling coefficient (i.e. the ratio between soil velocity and sound pressure) would be used, these differences of the reduction factors would have to be taken into account. Furthermore, due to the phase shift of the acoustic signal (discussed in Section 4.5.2.2) averaging is not possible for the coupling coefficient calculated for signals recorded at sensors under the acoustic damping box. Thus, the advantage of evaluating signals of several overflight events using the cou-

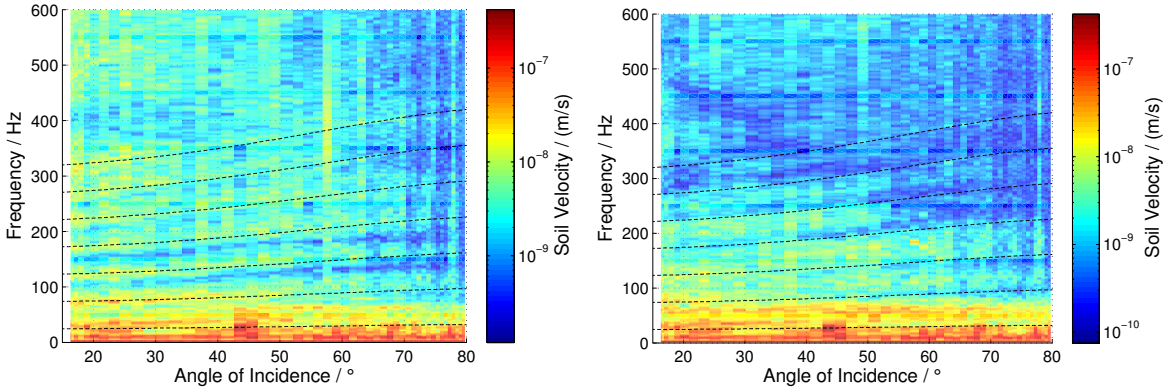

Figure 4.35: Frequency-averaged, vertical soil velocity recorded at the surface during overflight number 8 over the acoustic angle of incidence α:
Left: Geophone not shielded by the acoustic damping box, channel 24.
Right: Geophone placed under the acoustic damping box, channel 23.
Additionally, the theoretical frequencies of maximal interference amplitude $f^{\text{theo}}_{\text{max},k}(\alpha)$ (for $0 \leq k \leq 6$) obtained from the evaluation without shielding box (see Section 4.4) are shown as black dashed lines in both graphs.

pling coefficient does not apply here.

With the use of the soil velocity of single overflight events the interference of the seismic waves can be evaluated. However, since the trajectories of the aircraft and consequently the distance between the aircraft and the sensors varied strongly between the overflights, the recorded soil-velocity amplitudes of different events are not comparable. While the observed interference patterns are consistent for all overflights (see Fig. 4.35 (right) and the additional figures presented in Appendix A.9), the recorded values of the soil velocities differ for each event.

The differences in the soil velocity recorded during overflight 8 at the surface are illustrated in Fig. 4.35: The left graph shows the vertical soil velocity recorded outside of the box (geophone of channel 24) and the right graph that recorded under the box (geophone of channel 23).[44] Additionally, the theoretically obtained frequencies of maximal interference amplitude without acoustic shielding $f^{\text{theo}}_{\text{max},k}(\alpha)$ are plotted as black dashed lines (also shown in Fig. 4.24). Their values are calculated with Eq. (2.49) (which is the special case of Eq. (2.73) for $z_{\text{S}} = 0\,\text{m}$) for $v_{\text{P1}} = 230\,\text{m/s}$, $d = 2.35\,\text{m}$ and $0 \leq k \leq 6$.

The recorded soil velocities of the single overflight show a significantly lower SNR compared to that of the averaged values of the coupling coefficient, e.g. in Fig. 4.24. Still, the frequencies of the interference maxima of the soil velocity at a sensor without acoustic shielding (Fig. 4.35, left) match the theoretically obtained ones. The observed interfer-

[44] The averaged coupling coefficient calculated for the surface geophone of channel 24 is shown in Fig. 4.24. The frequencies of the maxima of the coupling coefficient (in Fig. 4.24) correspond to that of the soil velocity (in Fig. 4.35, left). The frequencies of the maxima of the coupling coefficient calculated for the surface geophone of channel 23 for the overflight event during which the box was not placed over this sensor (overflight numbers 1 to 6) correspond to the respective frequencies obtained for the geophone of channel 24.

ence pattern of the soil velocity recorded at the sensor under the acoustic damping box (Fig. 4.35, right) is more complex: At small α and low frequencies the theoretically obtained frequencies of the maxima $f^{\text{theo}}_{\text{max},k}(\alpha)$ correspond to the recorded ones. However, the frequencies at which maxima of the soil velocity are found shift with increasing α as well as with increasing f. This shift is so significant that maxima of the soil velocity are even found for approximately those frequencies which show interference minima outside of the box. Exemplarily, this can be observed for $f^{\text{theo}}_{\text{max},3}(\alpha)$, starting at $f \approx 170\,\text{Hz}$: For the shown range of α local minima of the soil velocity are observed at these frequencies, while at sensors outside of the box maxima were recorded. For $f^{\text{theo}}_{\text{max},2}(\alpha)$ up to $\alpha \approx 35°$ the recorded interference maxima coincide with the theoretically obtained ones – while for larger α decreased values of the soil velocity are found at $f^{\text{theo}}_{\text{max},2}(\alpha)$. For $f^{\text{theo}}_{\text{max},1}(\alpha)$ similar observations are made with the respective angle $\alpha \approx 45°$.

Additionally, the ratio between interference maxima and minima is strongly decreased compared to that recorded outside of the box. This can be explained easily: The spectral amplitude of the directly acoustically induced seismic signal is reduced by the box. Thus, at frequencies of constructive interference maxima of smaller soil velocity and at frequencies of destructive interference minima of larger soil velocity are observed, compared to the respective interference pattern without box. Similar observation are made for all overflight events during which the acoustic damping box was placed over the respective sensor. Exemplarily, signals recorded during three of these events in various depths z_S are shown in Appendix A.9.

The characteristics of the signal recorded under the damping box can be understood by examining the theoretical expressions of the two sets of upwards- and downwards-propagating, interfering waves: In Eq. (2.55) the first line described the waves propagating downwards and the second line those propagating upwards. With the box placed over the sensors, the directly acoustically excited wave $A_{\grave{\text{P}}}$ is affected (i.e. the first term of the set of downwards-propagating waves). For all angles of incidence α used during the measurements all other waves (i.e. those acoustically excited in a certain horizontal distance from the sensor) reach the sensor being reflected within the upper soil layer without being affected by the box. In Section 4.5.2.1 it was shown that the sound pressure of the acoustic wave that penetrated the box is reduced significantly. Consequently, also the amplitude of the directly acoustically excited wave $a_{\grave{\text{P}}}$[45] is reduced by the reduction factor of the sound pressure. Furthermore, as discussed in Section 4.5.2.2 there is an additional phase shift of that wave $\phi_{\grave{\text{P}},\text{box}}$[46]. Thus, the first term in Eq. (2.55) of the set of the

[45] In the theoretical models the amplitude of the directly acoustically excited wave $A_{\grave{\text{P}}}$ is treated to be $a_{\grave{\text{P}}} \equiv 1$ and the amplitudes of all waves are calculated relatively to $a_{\grave{\text{P}}}$.

[46] In the theoretical models the time of the arrival of $A_{\grave{\text{P}}}$ at the sensor is used as reference. Thus, the phase of that wave $\phi_{\grave{\text{P}}}$ is treated to be 0 (see also Section 2.3.1).

downwards-propagating waves becomes:

$$a_{\grave{\mathrm{P}}} \mathrm{e}^{\mathrm{i}(\omega t+\phi_{\grave{\mathrm{P}}})} \rightarrow a_{\grave{\mathrm{P}},\mathrm{box}}(f,\alpha) \mathrm{e}^{\mathrm{i}(\omega t+\phi_{\grave{\mathrm{P}},\mathrm{box}}(f,\alpha))}. \tag{4.22}$$

According to Section 4.5.2.1 the amplitude $a_{\grave{\mathrm{P}},\mathrm{box}}(f,\alpha)$ changes slightly with α but decreases strongly with f. The dependency of the phase shift $\phi_{\grave{\mathrm{P}},\mathrm{box}}(f,\alpha)$ on the frequency is given by the assumed, linear relation $\phi_{\grave{\mathrm{P}},\mathrm{box}}(f,\alpha) = \Delta m_{\Delta\phi}(\alpha) \cdot f$ (discussed in Section 4.5.2.2). Here a potential dependency of $\Delta m_{\Delta\phi}(\alpha)$ on the frequency was neglected. Thus, the dependency of $\phi_{\grave{\mathrm{P}},\mathrm{box}}(f,\alpha)$ on α is solely given by $\Delta m_{\Delta\phi}(\alpha)$ (see Fig. 4.34).
Due to the strong reduction of the amplitude of the acoustic waves penetrating the box a first approach with $a_{\grave{\mathrm{P}},\mathrm{box}} = 0$ was made. This corresponds to completely neglecting the directly acoustically excited wave $A_{\grave{\mathrm{P}}}$ and therefore also the phase term $\phi_{\grave{\mathrm{P}},\mathrm{box}}$. However, this approach does not explain the observed interference pattern: Using model 1 (introduced in Section 2.3.1) no interference pattern would have been observed at all, since the remaining waves $A_{\grave{\mathrm{P}}\acute{\mathrm{P}}}$ and $A_{\grave{\mathrm{P}}\acute{\mathrm{P}}\grave{\mathrm{P}}}$ are in phase at the surface. The theoretical model 2 (see Section 2.3.2) and model 3 (see Section 2.3.4) yield identical results in this case, since neither a P- nor an SV-wave would be acoustically excited under the box. For angles of high reflectivity at the boundaries the relative amplitude of the wave $A_{\grave{\mathrm{P}}}$ (i.e. $a_{\grave{\mathrm{P}}} = 1$) is much smaller compared to the resulting amplitude of the constructively interfering waves reflected within the upper soil layer (see e.g. Fig. 4.26, left).[47] Thus, neglecting this term would for a wide range of α result in only a minor reduction of the amplitudes of the theoretical interference pattern. Consequently, the interference maxima would be found at the same frequencies under the box as well as outside of it.
The observed shift of the frequencies of the local maxima of the soil velocity can be explained taking into account two assumptions: Firstly, the directly acoustically excited wave under the box contributes to the seismic recordings. This can be implemented in the models with Eq. (4.22) using the reduction factor of the acoustic wave penetrating the box (given in Section 4.5.2.1) and the phase shift of that wave (discussed in Section 4.5.2.2). Secondly, the sum amplitude of the waves reflected in the upper soil layer is significantly larger than $a_{\grave{\mathrm{P}},\mathrm{box}}$ at low frequencies but decreases strongly with increasing f. This is fulfilled when taking into account frequency-dependent absorption in the soil (as theoretically discussed in Section 2.3.3). The absorption coefficient (defined in Eq. (2.61)) is proportional to f with the value of γ_1 in the range of $1 \cdot 10^{-3}$ to $3 \cdot 10^{-3}\,\mathrm{Hz}^{-1}\mathrm{m}^{-1}$ for unconsolidated soil (see [59] and the discussion in Appendix A.10).
In Fig. 4.36 (top) again the soil velocity recorded under the acoustic damping box (surface geophone of channel 23) is shown together with the frequencies of the interference maxima found outside of the box (black dashed lines). Fig. 4.36 (middle) shows the theoretical

[47] As shown in Section 4.3.3 total P-P reflection occurs at $\alpha_c \approx 14.1°$. Up to $\alpha \approx 40°$ the maximal sum amplitude of the multiply reflected waves is more than five times larger than $a_{\grave{\mathrm{P}}}$.

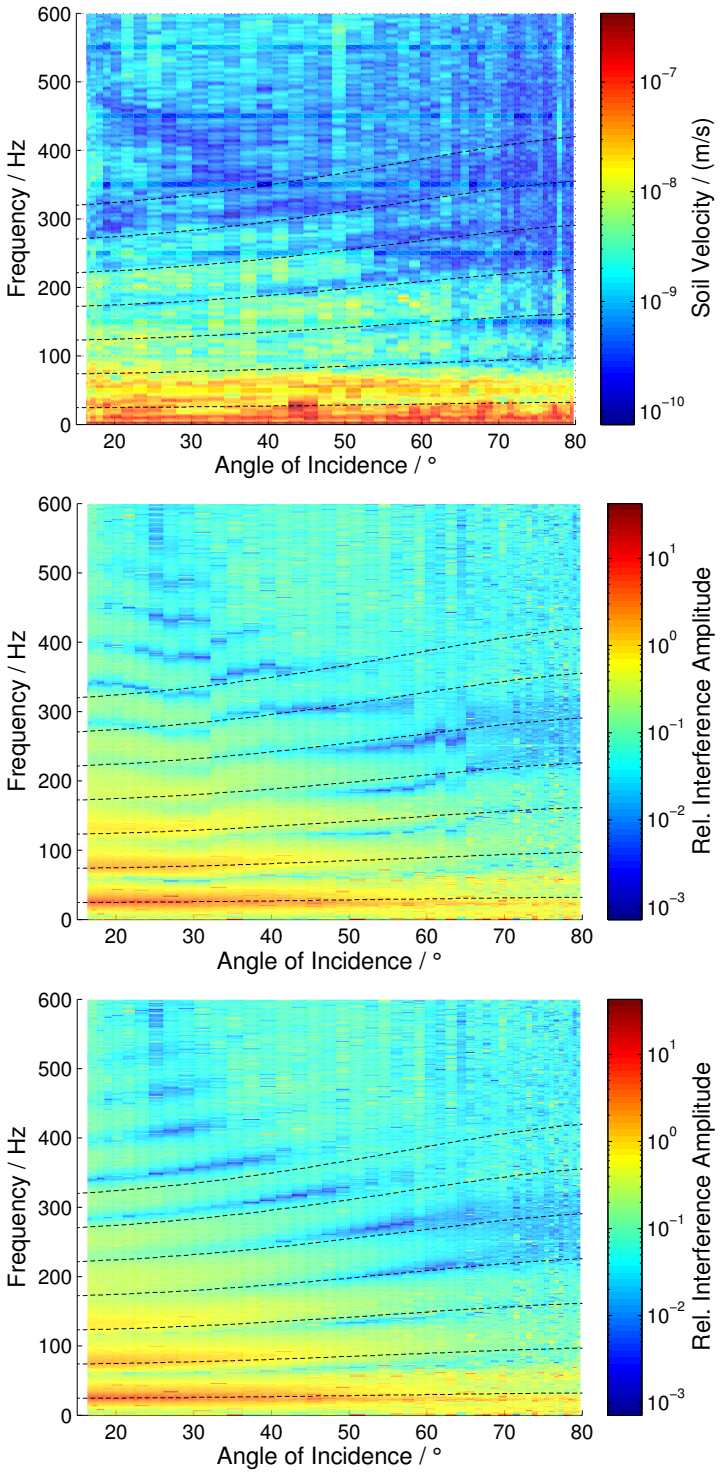

Figure 4.36: Top: Interference pattern of the soil velocity, recorded under the damping box at the surface (geophone of channel 23) during overflight number 8. Middle: Theoretical relative interference amplitude using the acoustic reduction factor (derived in Section 4.5.2.1) as $a_{\grave{\mathrm{P}},\mathrm{box}}$, the phase shift $\phi_{\grave{\mathrm{P}},\mathrm{box}}$ as given in Section 4.5.2.2 and frequency-dependent absorption with the value $\gamma_1 = 0.002\,\mathrm{Hz}^{-1}\mathrm{m}^{-1}$. Bottom: Theoretical relative interference amplitude calculated with a proportionality factor of the phase shift which is assumed to be constant $\Delta m_{\Delta\phi}(\alpha) = 0.015\,\mathrm{rad/Hz}$. The same values as above of $a_{\grave{\mathrm{P}},\mathrm{box}}$ and γ_1 are used.

In all graphs the theoretical frequencies of maximal interference amplitude $f^{\mathrm{theo}}_{\mathrm{max},k}(\alpha)$ (for $0 \leq k \leq 6$) of a sensor outside of the box are shown.

relative soil velocity calculated with model 2: For the amplitude of the directly acoustically excited wave $a_{\grave{\mathrm{P}},\mathrm{box}}(f,\alpha)$ the reduction factor of the acoustic signal (as derived in Section 4.5.2.1) is used. The additional phase shift of that wave $\phi_{\grave{\mathrm{P}},\mathrm{box}}(f,\alpha)$, depending linearly on the frequency f, is calculated by $\phi_{\grave{\mathrm{P}},\mathrm{box}}(f,\alpha) = \Delta m_{\Delta\phi}(\alpha)\cdot f$. The proportionality factor $\Delta m_{\Delta\phi}(\alpha)$ is that obtained by the linear fits presented in Section 4.5.2.2. Its value ranges from approximately 0.004 rad/Hz to 0.016 rad/Hz and changes with α (see Fig. 4.34, green curve of overflight number 8). Since these fits to obtain $\Delta m_{\Delta\phi}(\alpha)$ represent a rough estimate large deviations are observed between $f^{\mathrm{theo}}_{\mathrm{max},k}(\alpha)$ and the frequencies of the calculated interference maxima. Better results are obtained in Fig. 4.36 (bottom): The theoretical relative soil velocity is calculated using the same values of $a_{\grave{\mathrm{P}},\mathrm{box}}(f,\alpha)$ (as derived in Section 4.5.2.1) but an assumed constant proportionality factor $\Delta m_{\Delta\phi}(\alpha)$ = const. = 0.015 rad/Hz for the phase shift $\phi_{\grave{\mathrm{P}},\mathrm{box}}(f,\alpha)$. For both theoretical plots the frequency-dependent absorption coefficient $\gamma = \gamma_1 \cdot f$ with the value $\gamma_1 = 0.002\,\mathrm{Hz}^{-1}\mathrm{m}^{-1}$ is used.

The use of the recorded acoustic reduction factor to calculate the amplitude of the directly acoustically excited wave leads to fluctuations of the theoretical soil velocity at single data points. These can be especially observed at large angles α and at high frequencies (several yellow and dark blue data points in the otherwise light blue area) as well as for the whole range of α at low frequencies (several red data points in the otherwise yellow area).

Using the reduced amplitude of the directly acoustically excited wave $A_{\grave{\mathrm{P}}}$, an additional phase shift of that wave caused by the box and the frequency-dependent absorption of the seismic waves in the soil, the observed interference pattern of a sensor placed under the acoustic damping box can be explained theoretically. For low frequencies the seismic waves multiply reflected within the upper soil layer contribute most strongly to the interference pattern. Thus, the maxima are found at the same frequencies as for a sensor outside of the box (black dashed lines in the graphs of Fig. 4.36). With increasing f the sum amplitude of the multiply reflected waves decreases and the relative influence of the directly acoustically excited wave $A_{\grave{\mathrm{P}}}$ rises. Since the phase of $A_{\grave{\mathrm{P}}}$ is additionally shifted due to the penetration of the box, the frequencies of maximal (and minimal, respectively) interference amplitude shift compared to the respective frequencies $f^{\mathrm{theo}}_{\mathrm{max},k}(\alpha)$.

The phase shift of $A_{\grave{\mathrm{P}}}$ caused by the box calculated with the values of $\Delta m_{\Delta\phi}(\alpha)$ (obtained from the linear fits in Section 4.5.2.2) leads to a shift of the interference maxima[48] large enough to explain the recordings. However, uncertainties in these fits and the negligence of a frequency dependency of $\Delta m_{\Delta\phi}(\alpha)$ lead to artificial fluctuations of the theoretical interference pattern (see e.g. Fig. 4.36 (middle) at $\alpha \approx 30°$). With a constant value of $\Delta m_{\Delta\phi}(\alpha)$ = 0.015 rad/Hz more satisfactory results in explaining the interference pattern are obtained: The frequencies of the recorded (Fig. 4.36, top) and the calculated

[48] Exemplarily, at the frequencies of the theoretical interference maximum $f^{\mathrm{theo}}_{\mathrm{max},3}(\alpha)$, starting at $f \approx$ 170 Hz, in Fig. 4.36 (middle) an interference minimum of the soil velocity is observed for most α.

(Fig. 4.36, bottom) interference maxima and minima, respectively, match.
Better results could be obtained by additionally considering the dependency on the azimuthal angle of the incident acoustic signal and averaging signals recorded under corresponding excitation conditions to increase the SNR.

4.6 Relevance for on-site inspections under the CTBT

In this section the findings of this work are discussed with respect to sensitive seismic measurements with the SAMS conducted during an OSI under the CTBT. To increase the sensitivity of these measurements disturbing signals such as the discussed acoustically excited ones should be reduced or at best be prevented. The presented method of shielding sensors from acoustic signals created by airborne sources can help to achieve this.
The horizontal distance around a sensor from which acoustically-induced soil vibrations contribute to the recorded seismic signal is discussed in Section 4.6.1. From this distance conclusions about the size of a potential acoustic shielding of the sensors are derived. Further requirements for such an shielding for the use during an OSI are discussed in Section 4.6.2. For this the acoustic damping box introduced in this work is briefly compared to another shielding method.

4.6.1 Horizontal propagation range in the ground

As shown in the previous sections the soil vibration recorded at a sensor contains contributions from directly acoustically excited waves at the location of the sensor or above it as well as waves reflected within the upper soil layer. The horizontal propagation range r_{hor} of an acoustically excited seismic signal can be understood as the distance between the surface point vertically above the sensor and the point at which a multiply reflected wave that contributes significantly to the signal has been excited.
Using the models of multiply reflected waves (see Section 2.3.2 and Section 2.3.4) the total signal amplitude a_{tot} is obtained from the summation over the infinite number of reflected waves (see Eq. (2.57) and Eq. (2.58)). The sum amplitude a_M of the directly acoustically excited waves and the first M multiply reflected waves gives the contribution to the total signal caused by this finite number of waves. The ratio between the sum amplitude a_M and the total amplitude a_{tot} (caused by the infinite number of waves) is calculated by:

$$\frac{a_M}{a_{\mathrm{tot}}} = \frac{\sum_{n=0}^{M} a_i}{\sum_{n=0}^{\infty} a_i}. \tag{4.23}$$

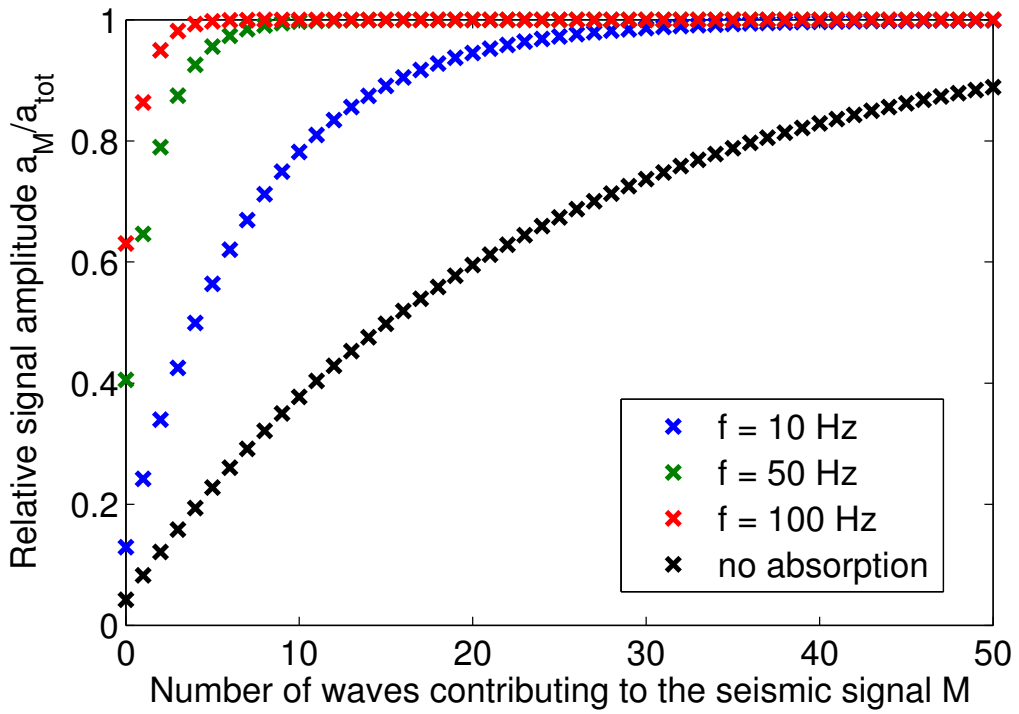

Figure 4.37: Ratio between the sum amplitude a_M and the total signal amplitude a_{tot} over the number of multiply reflected waves M. The ratio at $M = 0$ corresponds to the directly acoustically excited wave.
All curves are calculated for the values of the reflection coefficients at $\alpha_c \approx 14°$. Absorption is considered using the absorption coefficient $\gamma = \gamma_1 \cdot f$ with $\gamma_1 = 0.002\,\text{Hz}^{-1}\text{m}^{-1}$.

In Fig. 4.37 a_M/a_{tot} is plotted over the number of waves M which contribute to the sum amplitude. The black curve corresponds to the case without frequency-dependent absorption. The curves of the calculations taking into account absorption (according to Eq. (2.60) with $\gamma = \gamma_1 \cdot f$ and $\gamma_1 = 0.002\,\text{Hz}^{-1}\text{m}^{-1}$) are shown for the frequencies $f = 10\,\text{Hz}$ (blue), $f = 50\,\text{Hz}$ (green) and $f = 100\,\text{Hz}$ (red). Note that the absolute values of a_{tot} differ for each case since the amplitudes a_i decrease rapidly with increasing frequency when taking into account absorption. The ratio a_M/a_{tot} is used to indicate how many multiply reflected waves contribute to a certain share of the total signal amplitude.
All values are calculated for constructive interference of the M waves. For destructive interference the ratio a_M/a_{tot} converges alternatingly towards 1, while the values $a_M/a_{\text{tot}} < 1$ are identical to the respective values shown in Fig. 4.37.
When absorption is neglected the amplitude of the M-th wave is reduced solely by reflection at the underground boundary and at the free surface. The respective reflection coefficients depend on α (see Section 4.3.2 and Section 4.3.3). Here the calculations are performed using the reflection coefficients of the critical angle of total reflection at the underground boundary $\alpha_c \approx 14°$. At this angle the product of both reflection coefficients has the largest value and thus it results in the largest number M for a given value of

a_M/a_{tot} – for other angles the ratio a_M/a_{tot} would converge faster towards 1.
Without absorption 16 reflected waves are required for the sum amplitude to reach half of the total signal amplitude ($a_M/a_{\text{tot}} \geq 0.5$) and more than 50 waves are needed to reach $a_M/a_{\text{tot}} \geq 0.9$. These numbers decrease when absorption is considered: For $f = 10\,\text{Hz}$ the directly acoustically excited wave and the first four reflected waves nearly contribute to $a_M/a_{\text{tot}} = 0.5$ and for $M = 16$ the value $a_M/a_{\text{tot}} \geq 0.9$ is reached. For $f = 50\,\text{Hz}$ these ratios are reached for $M = 1$ and $M = 4$, respectively. For $f = 100\,\text{Hz}$ the directly acoustically excited wave ($M = 0$) already contributes to about 63 % of the total amplitude while the ratio $a_M/a_{\text{tot}} \geq 0.9$ is obtained for $M = 2$.
For a given ratio a_M/a_{tot} the obtained value M can be used to calculate the respective horizontal propagation range of the M-th wave in the soil:[49]

$$r_{\text{hor}} = (2 \cdot M \cdot d + z_{\text{S}}) \cdot \tan\left(\arcsin\left(\frac{v_{\text{P1}}}{v_0}\sin(\alpha)\right)\right). \tag{4.24}$$

In Table 4.4 the horizontal range r_{hor} around a sensor from which acoustically induced seismic signals affect the measurements calculated with model 2 without and with frequency dependent absorption are given. The values are calculated with Eq. (4.24) for $\alpha_c \approx 14°$, the depth of the reflecting boundary $d = 2.35\,\text{m}$, the velocity of the P wave $v_{\text{P1}} = 228\,\text{m/s}$ and for a sensors placed at the surface $z_{\text{S}} = 0\,\text{m}$. Since r_{hor} of multiply reflected waves depends of the ratio a_M/a_{tot}, exemplarily, the values of $r_{\text{hor},0.5}$ (for the ratio $a_M/a_{\text{tot}} \geq 0.5$) and $r_{\text{hor},0.9}$ (for $a_M/a_{\text{tot}} \geq 0.9$) are given. The respective values of r_{hor} are exemplarily calculated for the frequencies $f = 10\,\text{Hz}$, $f = 50\,\text{Hz}$ and $f = 100\,\text{Hz}$. Since M can take only integer values the given values of r_{hor} refer to the first value M for which the stated ratio a_M/a_{tot} is reached or exceeded.

f / Hz	model 2, no absorption		model 2 with $\gamma_1 = 0.002\,\text{Hz}^{-1}\text{m}^{-1}$	
	$r_{\text{hor},0.5}$ / m	$r_{\text{hor},0.9}$ / m	$r_{\text{hor},0.5}$ / m	$r_{\text{hor},0.9}$ / m
10	12.5	41.5	3.9	12.5
50			0.8	3.1
100			0	1.6

Table 4.4: Horizontal propagation range r_{hor} in the ground of acoustically-induced seismic vibrations calculated for model 2 with as well as without frequency-dependent absorption in the soil. For $f = 100\,\text{Hz}$ the directly acoustically excited wave alone causes more than 50 % of the total signal amplitude (see also red curve in Fig. 4.37), thus the respective value of $r_{\text{hor},0.5}$ is zero.
All values are calculated for $\alpha_c \approx 14°$, $d = 2.35\,\text{m}$, $v_{\text{P1}} = 228\,\text{m/s}$ and $z_{\text{S}} = 0\,\text{m}$.

A reflecting boundary at greater depth will lead to correspondingly larger values of r_{hor} if absorption would be neglected. With absorption the respectively increased slant prop-

[49] The expression of Eq. (4.24) can be understood by looking at a sketch of the propagation of seismic waves, e.g. Fig. 2.4: r_{hor} is the distance between the point at the surface vertically above the sensor and the point B in Fig. 2.4 (for $M = 1$) or the point D (for $M = 0$), respectively.

agation distance through the ground would counteract this effect. The same is true for increased angles α. For different soil parameters (i.e. different relative velocities of P and SV waves in the first two soil layers) the conditions for total reflection and thus the value of α_c will change.
The amplitude ratio calculated with Eq. (4.23) indicates that the first M multiply reflected waves cause at least the specified ratio of the total recorded amplitude. Consequently, the horizontal propagation range corresponds to the area around the sensor that has to be completely acoustically shielded to reduce the amplitudes of acoustically induced signals respectively. Thus, using the results obtained with absorption an area of radius 3.9 m around the sensor has to be shielded to reduce the spectral amplitude of signals of $f = 10\,\mathrm{Hz}$ by the factor 2. A reduction by the factor 10 requires an acoustic shielding of an area with radius 12.5 m.
Thus, it seems prudent to assume that at the site of a potential OSI acoustically induced seismic vibrations can propagate over several metres in the ground and can affect and disturb sensitive seismic measurements. While the soil velocity of acoustically induced signals is strongest for small angles α during the measurements significant signals for α up to 80° were recorded. Depending on the height of an aircraft passing the inspection site – intended or accidentally – sensors in a large area can be blinded by such an overflight.

4.6.2 Acoustic shielding of sensors during an on-site inspection

For the actual use of the an acoustic shielding during an OSI several technical and practical requirements may be of great importance which are not treated in the scope of this work. Since for the detection of seismic aftershock signals mostly signals of frequencies $f \lesssim 100\,\mathrm{Hz}$ are of interest the reduction of disturbing signals of these frequencies is of highest importance. For this a suitable damping material is required. Additionally, the design of the shielding should guarantee good damping properties as well as easy and fast handling during its use by the inspectors. Other practical aspects should be considered like its weight and volume, the time to deploy the shielding during an OSI and the question whether it should be used at all sensor stations or just at selected ones. Another aspect which could be achieved by the shielding is the reduction of disturbing influences of weather (i.e. wind or rain). Thus, the benefits of the achievable enhancement of sensitivity and additional effort of the use of an acoustic shielding should be carefully evaluated.

The acoustic damping box used during this work served mainly experimental purposes. Sensors and equipment were placed inside of the box i.e. between the acoustic shielding and the ground surface. By this the sound pressure of the acoustic signals (outside and inside of the box) could be recorded and thus its reduction by the shielding

could be calculated.[50] Furthermore, geophones could be positioned at the surface to record the soil velocity under the damping box. Thus, the damping material was not placed on the ground directly (except at the bottom of the box walls). However, placing mats of a suitable damping material on top of shallowly buried geophones might be an easy, fast and effective way to achieve an acoustic shielding. To deploy the acoustic shielding it only would have to be placed on the ground above the sensors. No assembling of a box or some other kind of shielding would be required.

In a measurement campaign at a site near the Technische Universität Dortmund, Germany, mats of acoustic damping foam of the thickness 0.1 m of different sizes (about 1.0 m * 1.0 m and 1.7 m * 1.7 m) were placed over buried geophones. In Fig. 4.38 the averaged spectra of the soil velocity caused by the noise replay from a speaker suspended in the air are shown for the two sizes of the foam mats, the acoustic damping box and without acoustic shielding. Each shielding is placed centred over the buried geophones: In Fig. 4.38 (top) the spectra for a geophone in the depth $z_S = 0.15\,\mathrm{m}$ are shown and in Fig. 4.38 (bottom) the respective spectra for a geophone in depth $z_S = 0.30\,\mathrm{m}$.[51]

All curves represent averaged values of consecutive spectra calculated for time intervals of $T = 0.8192\,\mathrm{s}$ each during the replay time of the noise of 30 s. During each measurement the speaker was suspended by a crane in the hight of 3 m above ground centred vertically above the geophone and the middle of the respective shielding. Due to this small distance between the speaker and the surface the wavefronts of the acoustic signal have a significant curvature when hitting the surface. Thus, the wavefronts of the seismic waves reaching the respective sensor are not plane either. This has already been discussed in Section 4.1.2.1 where similar spectra of the soil velocity caused by noise replay have been shown (see Fig. 4.11, right). Thus, the spectrally narrow frequency intervals of reduced soil velocity might be caused by destructively interfering waves excited at various points at the surface around the acoustic shielding. Such frequencies of reduced soil velocity can be observed e.g. for $z_S = 0.15\,\mathrm{m}$ around $f \approx 209\,\mathrm{Hz}$ for the shielding by the foam mat of about $1\,\mathrm{m}^2$ (Fig. 4.38, top: Red curve) or for $z_S = 0.30\,\mathrm{m}$ around $f \approx 133\,\mathrm{Hz}$ and $f \approx 141\,\mathrm{Hz}$ for the foam mat of about $2.9\,\mathrm{m}^2$ (Fig. 4.38, bottom: Green curve).

The soil velocity recorded without acoustic shielding is significantly larger for frequencies $f \gtrsim 240$ Hz (for $z_S = 0.15\,\mathrm{m}$) and $f \gtrsim 190$ Hz (for $z_S = 0.30\,\mathrm{m}$), respectively, compared to all spectra recorded with acoustic shielding. At certain lower frequencies the soil velocity recorded without shielding is even smaller than that recorded with some shieldings. A reason for this might be slight differences of the position of the speaker during these

[50] Currently, the recording of sound pressure is not part of the OSI measurement regime. However, this might be an effective way to identify acoustically induced seismic signals caused by airborne sources. Thus, the efficiency of the signal analysis during an OSI could be increased. It is beyond the scope of this work to recommend such measurements. The possibility of these recordings could be considered in the future if need be.

[51] More details of the respective measurements and their evaluation are given in [67].

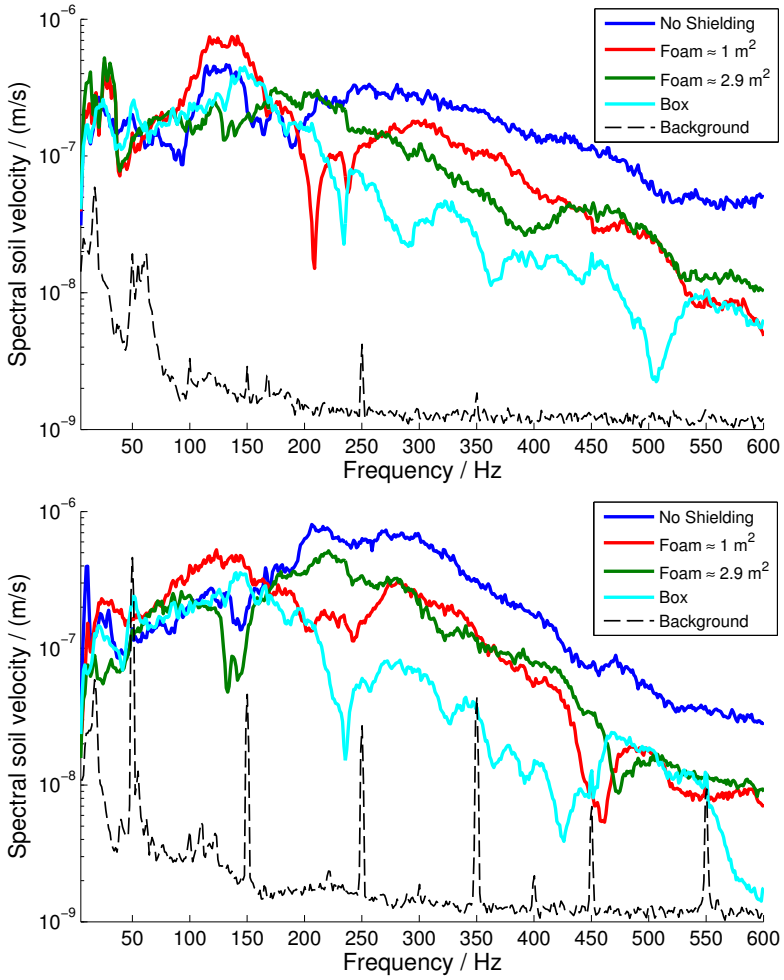

Figure 4.38: Averaged spectral soil velocity caused by noise played by a loudspeaker, recorded with geophones in the depths $z_S = 0.15\,\mathrm{m}$ (top) and $z_S = 0.30\,\mathrm{m}$ (bottom), while different acoustic shieldings were placed above them on the ground. The background spectra of both sensors are shown as dashed black curves.

recordings and thus different conditions for constructive and destructive interference of the seismic waves.
The shielding by the foam mats of the size 1.7 m * 1.7 m results for most frequencies in smaller soil velocities compared to the shielding of the smaller area 1.0 m * 1.0 m. Some exceptions can be found for the discussed narrow frequencies intervals of destructive interference. The used damping box shows for most frequencies the strongest reduction of the soil velocity. This does not come as a surprise since additionally to the damping foam of thickness 0.1 m its walls and lid consist of plywood of thickness 19 mm.

To match the requirements for the use during OSI measurements further research on a suitable damping material is recommended. The presented box as well as the mats of the used thickness show little reduction of the sound pressure for frequencies up to $f \approx 100$ Hz which are of main interest to detect seismic aftershock signals during OSI measurements. Thus, most importantly, a suitable material with high damping properties especially at these low frequencies should be identified. Additionally, the geometry and the dimensions of the damping material i.e. its thickness and the covered area should be part of future research. For large lateral areas a modular setup might be of use. Other kinds of acoustic shielding alignments might be required, i.e. if burying of the geophones is not possible at an inspection site and thus mats of damping material cannot be placed directly on top of them.

4.7 Further aspects of the evaluation

Here two additional aspects of the evaluations are discussed briefly: In Section 4.7.1 the measurements of an interference pattern in the seismic signal recorded at a different site is presented. In Section 4.7.2 the possibility of coherently superposing Rayleigh waves contributing to the seismic recordings is discussed.

4.7.1 Interference pattern observed at another measurement site

The spectral modulation of the recorded soil velocity as well as of the respective coupling coefficient can be explained as interference pattern of seismic waves being reflected within the upper soil layer. The measurements presented and discussed in the previous sections were conducted at the site near the airport FMO (described in Section 3.2). During these measurements several aircraft overflights were recorded systematically. Additionally, with the trajectories of the aircraft (provided by the DFS) the angle of incidence α of the acoustic signals was calculated which was used for the evaluations.
During various other measurement campaigns at different sites broadband acoustic signals

of jet-aircraft overflights were recorded by chance. For these signals the information of the trajectories is not available and thus no evaluations with respect to the angle α are performed. A suitable aircraft overflight was recorded on 12th June 2015 among measurements at a site near the Technische Universität Dortmund, Germany.[52] The aircraft passed the sensor setup at its cpa in a height of few kilometres and at a small angle of incidence α – the positions of the aircraft during the overflight represent estimates made from sight. The acoustic signal was clearly audible. In Fig. 4.39 for the duration of the overflight of 90 s starting at 10:02:00 (UTC) the respective soil velocity (top), recorded in the depth $z_S = 0.45$ m, the sound pressure (middle) and the calculated coupling coefficient (bottom) are shown. For this overflight spectral modulations of the soil velocity are verified – similar to those observed during the measurements near the airport FMO. Thus, it is plausible that similar effects can be expected at various sites which show a layering of the soil near the surface. Therefore, the presented measurements and evaluations are not a specific characteristic of the measurement site near the airport FMO.

In the graphs of the soil velocity (Fig. 4.39, top) and of the sound pressure (Fig. 4.39, middle) tonal components of the overflight can be observed. The frequencies of these signals decrease due to Doppler shift while passing the sensors. Additionally, for the first 20 seconds, subsequent signals of constant frequencies $f \approx 70$ Hz and $f \approx 60$ Hz, respectively, stemming from mono-frequent replay by a speaker are visible. All these signals vanish when calculating the ratio between soil velocity and sound pressure, i.e. the acoustic-seismic coupling coefficient (Fig. 4.39, bottom). Frequency bands of constructive and destructive interference can be best identified in the graph of the soil velocity. The sound pressure shows the characteristic broadband signal which is strongest at the cpa around the time $t = 40$ s. In the graph of the coupling coefficient frequency bands of increased coupling strength can be identified at $f \approx 140$ Hz, $f \approx 215$ Hz and $f \approx 320$ Hz with the respective bands of decreased coupling strength at the intermediate frequencies.[53]

Comparing these findings to the interference patterns observed during the measurements near the airport FMO (see e.g. Fig. 4.15) several differences are obvious: Firstly, in the plots of Fig. 4.39 the SNR as well as the ratios between the interference maxima and minima are smaller. This is mainly caused by the much greater distance between aircraft and sensors and thus by the smaller amplitude of the exciting acoustic signal. Secondly, the frequencies of the interference maxima and minima are nearly constant during the time of the overflight. Due to the large height of the aircraft α changes only slightly during the times in which significant signals are recorded. Thus, only minor changes of the respective frequencies can be expected.

[52] This measurement campaign is the same during which the recordings with the mats of damping foam were performed, see Section 4.6.2.

[53] The frequency bands of increased coupling strength are indicated by black arrows at the times when they are best visible in Fig. 4.39 (bottom). They extend nearly vertically (i.e. at constant frequencies) with time.

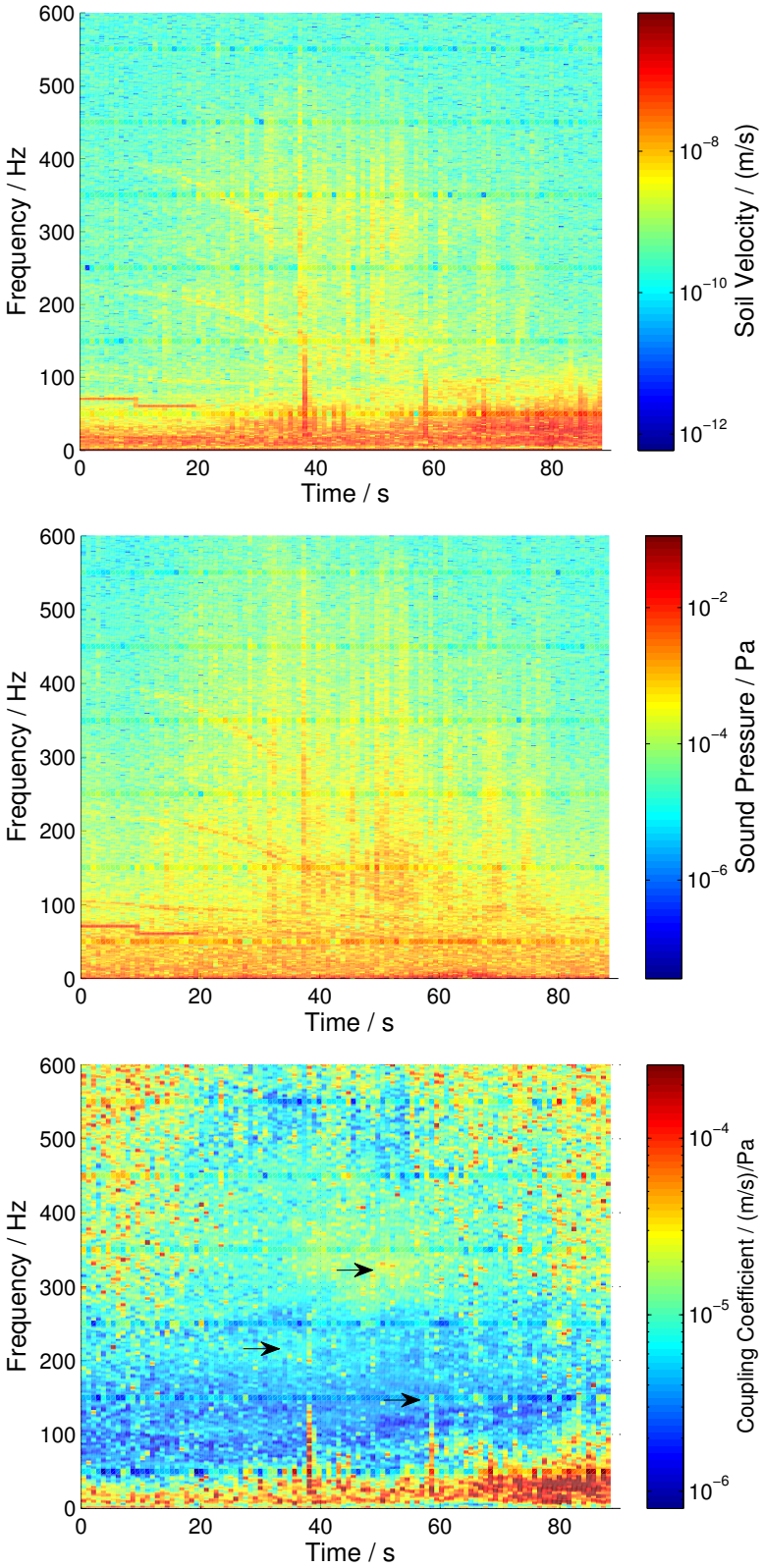

Figure 4.39: Soil velocity (top), sound pressure (middle) and the calculated coupling coefficient (bottom) of a jet-aircraft overflight recorded near the Technische Universität Dortmund, Germany. The soil velocity is recorded in depth $z_S = 0.45\,\mathrm{m}$. Frequency bands of increased coupling strength are highlighted by black arrows.

Finally, constructive and destructive interference are observed at different frequencies compared to the respective frequencies of the measurements near the airport FMO. This is to be expected since wave velocities, depths of reflecting boundaries and reflection coefficients differ at both measurement sites. During this overflight, all geophones were buried in the depth $z_S = 0.45\,\mathrm{m}$. Recordings from different depths would provide useful references, especially since the interference pattern can be observed most clearly in the recordings of a geophone at the surface. However, such recordings are not available for this overflight event.

4.7.2 Influence of coherently superposing Rayleigh waves

During the evaluations the possibility of Rayleigh waves acoustically excited over a long stretch in front of the sensor has been considered. It might have been possible, that under a certain angle of incidence α and for a certain frequency these Rayleigh waves superpose coherently, leading to a significantly larger seismic signal [68]. Rayleigh waves are formed at the soil surface as superposition of upwards- and downwards-propagating P and SV waves [52, 63]. In layered soil they show dispersion: The low-frequency (or long-wavelength, respectively) components of the surface wave, comprising deeper soil layers with usually larger wave velocities, have the highest group velocities.
The constructive superposition of acoustically excited Rayleigh waves would have required that the velocity of the Rayleigh wave is equal to the apparent speed of the sound wave along the ground surface v_{hor}. The Rayleigh-wave speed is typically in the range of $0.90{\cdot}v_{\mathrm{S1}}$ to $0.95{\cdot}v_{\mathrm{S1}}$ [63]. Thus, with a P-wave speed of $v_{\mathrm{P1}} = 228\,\mathrm{m/s}$ and the assumed S-wave speed $v_{\mathrm{S1}} = v_{\mathrm{P1}}/\sqrt{3}$ the Rayleigh-wave velocity in the upper soil layer is approximately $120\,\mathrm{m/s}$. However, v_{hor} is given for a certain angle α and the velocity of the sound wave $v_0 \approx 340\,\mathrm{m/s}$ by:

$$v_{\mathrm{hor}} = \frac{v_0}{\sin(\alpha)} \gtrsim 340\,\mathrm{m/s}. \tag{4.25}$$

Thus, the conditions of the coherent superposition of acoustically excited Rayleigh waves are not fulfilled at the investigated measurement site near the airport FMO.
Larger velocities of Rayleigh waves can be expected for the case of longer-wavelength components comprising the second soil layer. However, if the made interpretation is correct that the high compressional-wave speed there stems from ground water, then the shear- and Rayleigh-wave speeds in the lower layer should not be much above the values of the top ground layer. Thus, the large values of v_{hor} would not be reached by the velocity of these Rayleigh-wave components.

Chapter 5

Conclusion and outlook

In this work acoustic-seismic measurements of jet-aircraft overflights for a wide range of angles of incidence of the exciting acoustic signals and for frequencies up to several hundreds of Hz are presented (Section 4.1). For their evaluation the acoustic-seismic coupling coefficient is introduced in Section 4.2. With it the excited soil vibrations can be analysed independently of the specific characteristics of the exciting acoustic signal. The seismic response to the incident sound waves can be explained to be caused by interference of seismic waves excited locally as well as propagating in the ground and being reflected at an underground boundary and at the surface before reaching the sensor. Three theoretical models using different numbers and types of seismic waves are introduced (Section 2.3) to explain the amplitudes and the frequencies of constructive and destructive interference. The influence of seismic waves, which have taken various paths in the ground before reaching the sensor, on the resulting seismic signal is presented in Section 4.3. It is shown in Section 4.4 that the resulting interference patterns can be used to calculate near-surface soil properties such as the P-wave velocity in the first soil layer, the depth of the underground boundary and the reflection coefficient at that boundary. The recordings with geophones placed at the surface generally lead to the most reliable results. Furthermore, signals from sensor buried in various depths in the ground are analysed and used to verify the theoretical models.
By shielding some sensors from the incident sound waves (presented in Section 4.5) the frequency-dependent absorption coefficient can be estimated. Using these findings the horizontal propagation range of acoustically induced seismic signals in the ground is derived in Section 4.6. Additionally, it is discussed that with a suitable shielding the amplitudes of seismic signals caused by airborne sources can be reduced strongly which could otherwise disturb sensitive seismic measurements.

Due to fluctuations mostly in the seismic recordings the analysis of the interference patterns observed in the calculated coupling coefficients remains challenging. For the presented fits to obtain the soil properties from the recorded interference patterns

only data recorded with one sensor are used, even though data of different sensors in corresponding depths showed very similar characteristics. Thus, better results may be reached by using multiple sensors at different positions as well as in various depths at once in an adapted fit algorithm. With the increase of the amount of analysed data points the computational effort will rise but the SNR and the reliability of the obtained results can be increased significantly. Additionally, for the fits the relative spectral amplitudes of the interference maxima are not taken into account. The beat of the signal of multiple interfering waves causes modulations of the spectral amplitudes which are clearly observable in the measured signal. Their implementation might strongly improve the quality of the results.

Even after averaging of several overflight events the measured coupling strength shows fluctuations which can lead to erroneous determination of the frequencies of constructive interference. Thus, the selection and exclusion of data points for the fit which were mostly done manually for the shown calculations remain critical and can strongly affect the results. Furthermore, for low frequencies (i.e. small orders k of the interference maxima) the frequency resolution of $\Delta f_{meas} \approx 1.2\,\mathrm{Hz}$, given by the used FFT, is in the range of the absolute deviation between measured and fitted data. For this reason the band of $k = 1$ of the surface sensor (with a very good SNR) was excluded from the calculations. Bands of higher frequencies are less affected by the errors caused by the discretisation in frequency space and fluctuations lead to smaller relative deviations. However, the SNR decreases with frequency, so especially for buried sensors only bands at low frequencies could be used for the fit. Probably the centre frequency of the bands could be determined with higher accuracy from a curve fit through the three to five points of the highest spectral values at each angle. Thus, one would not be limited to the frequency resolution of the FFT of the recorded data. Consequently, the interference maxima of low frequencies could be included into the fit algorithm leading to a significant increase of the precision of the calculations.

To calculate the frequencies of maximal interference amplitude for surface sensors the analytic expression Eq. (2.49) can be used giving an advantage in computation effort and in precision. For the numerical calculation of the spectral amplitude distribution with Eq. (2.73) both depend on the steps of discretisation of f. For the used frequency resolution of 1/10 of Δf_{meas} the computation time is in acceptable limits and the relative deviations of the calculated values of the depth of the reflecting boundary d and the P-wave velocity in the first soil layer v_{P1} are less than 1 %. These can be neglected regarding the fluctuations of the measured data discussed above.

A potential source of inconsistencies is the mounting of the geophones buried in dug-out holes. The soil at the bottoms of the holes into which the spikes were pressed was undisturbed, but the backfilling around and above the geophones by the excavated soil could not reproduce the status before digging. An additional modification was

introduced by the relatively massive (about 3.4 kg) holders for the three-dimensional geophone arrangements. Furthermore, the position of the sensors in the ground are assumed to be precisely at the given values $z_S = 0\,\mathrm{m}$, $z_S = 0.15\,\mathrm{m}$, $z_S = 0.30\,\mathrm{m}$, $z_S = 0.45\,\mathrm{m}$ and $z_S = 0.60\,\mathrm{m}$, respectively. However, the geophones have finite dimensions and the spikes with which the geophones were pushed into the ground represent an extended coupling length of the geophones to the ground. Thus, an integration over the full dimension of the spike could increase the precision of the results.
The influence of the acoustic shielding box on the measurement of the soil velocity is not completely clarified. It might be possible, that the box itself causes soil vibrations when hit by an acoustic wave or even wind. The purpose of the protruding damping foam on the bottom of each wall of the box (described in Section 3.2.3) was to mitigate such excitations. During all performed measurement campaigns no clear evidence of soil vibrations caused by a movement of the box were found. However, since no suitable reference is available this influence of the box on the measurement cannot be completely excluded. Furthermore, the box distorts the acoustic wave front of the wave penetrating its walls and lid. Thus, for the measurements of the aircraft overflights, the signals of which have plane wavefronts, the acoustic wave inside of the box has a more complex wavefront. This was not taken into account when treating the seismic wave acoustically excited under the box. With a simpler alignment of the acoustic shielding (e.g. the mats of damping material discussed in Section 4.6.2) of a sufficiently large size the influence of the distorted wavefronts can be diminished.

In the context of the CTBT acoustically excited soil vibrations can disturb sensitive SAMS measurements. If acoustic sensors would be allowed during OSI measurements in addition to seismic ones, this could help to identify acoustic disturbances. However, very faint seismic aftershock signals masked by such disturbances might go undetected nevertheless. While in this work I focus on the excitation of seismic signals by sound waves caused by aircraft the findings can be applied to a other acoustic sources like vehicles. Disturbing, directly seismically induced signals are not treated in the scope of this work. These signals could be artificially created by heavy machinery like from construction work in the inspection area, if the inspected state party intended to disturbed the OSI. To guarantee an effective performance of the SAMS measurements despite such disturbances further research is recommended.
The evaluations in this work show that the acoustically induced soil vibrations propagate within the ground. Their amplitudes decrease due to reflection at boundaries and due to frequency-dependent absorption in the ground. Therefore, the horizontal propagation range in the ground is up to several metres. With increasing frequency of the signals the propagation range decreases. Due to significant signal strengths even for large angles of incidence from the normal to the ground aircraft passing the inspection area – either

helicopters used by the inspectors or even intended aircraft overflights to disturb an OSI – will affect the sensitivity of seismic sensors placed in a wide area. To achieve an effective shielding from disturbing airborne signals an area of many square metres above the sensors would have to be covered with a suitable damping material. Doing so can reduce the spectral amplitude of acoustically induced soil vibrations. Thus, the sensitivity of the SAMS can be increased and the detection probability of weak aftershock signals can be improved.

An example of an acoustic shielding by a plywood box coated with acoustic damping foam is discussed in detail in this work. However, the reduction factor of the sound pressure of the used shielding is low for signals of frequencies up to $f \approx 100\,\mathrm{Hz}$ which are of main interest to detect seismic aftershock signals. Thus, regarding a suitable damping material, its design and its dimensions, further research is recommended. Other practical aspects for the use during an OSI have to be considered as well.

The presented measurements were conducted mainly on sandy soil. Research should be carried out to which extent the findings of this work apply to soil of different characteristics.

Appendix A

Appendix

A.1 Determination of the phase difference of interfering seismic waves

For the interference models presented in Section 2.3 it is essential to determine the phase differences between different pairs of waves. They are required to calculate the total spectral amplitude distribution of the wave interference with Eq. (2.73).
Here the geometrical derivation is demonstrated exemplarily for the phase difference between the directly acoustically excited P wave $A_{\grave{\mathrm{P}}}$ and the wave $A_{\grave{\mathrm{S}}\acute{\mathrm{P}}}$, propagating into the ground as SV wave and being reflected as a P wave at the underground boundary before reaching the sensor propagating upwards (sketched in Fig. A.1).
The wave $A_{\grave{\mathrm{P}}}$ at point D (when hitting the surface) has the same phase as $A_{\grave{\mathrm{S}}\acute{\mathrm{P}}}$ at point B. To reach the sensor wave $A_{\grave{\mathrm{P}}}$ has to cover the distance $\overline{DS}$ with wave velocity v_{P1}. On the other hand, $A_{\grave{\mathrm{S}}\acute{\mathrm{P}}}$ needs to cover the distances $\overline{BC}$ with wave velocity v_{S1} and $\overline{CS}$ with

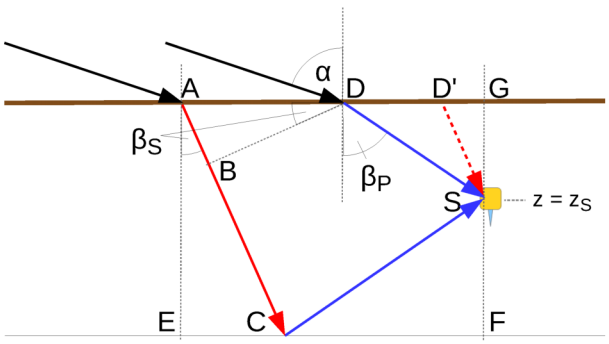

Figure A.1: Sketch of the propagation paths of acoustically excited seismic waves in the layered soil. The direct wave $A_{\grave{\mathrm{P}}}$ (excited at point D) and the wave $A_{\grave{\mathrm{S}}\acute{\mathrm{P}}}$, that is excited at point A as an SV wave and is converted into a P wave upon reflection at the underground boundary before reaching the sensor, are shown.

wave velocity v_{P1}. Thus, the phase difference between both waves is given by:

$$\Delta\phi = 2\pi f\left[\frac{\overline{BC}}{v_{S1}} + \frac{\overline{CS}}{v_{P1}} - \frac{\overline{DS}}{v_{P1}}\right]. \tag{A.1}$$

The distance $\overline{DS}$ is easily obtained from

$$\overline{DS} = \frac{z_S}{\cos(\beta_P)} \tag{A.2}$$

as is the distance $\overline{CS}$

$$\overline{CS} = \frac{(d - z_S)}{\cos(\beta_P)}. \tag{A.3}$$

The distance $\overline{BC}$ is obtained from $\overline{BC}$ = $\overline{AC}$ - $\overline{AB}$. Again, the distance $\overline{AC}$ is easily found

$$\overline{AC} = \frac{d}{\cos(\beta_S)}. \tag{A.4}$$

For the determination of the distance $\overline{AB}$ the right triangle ABD with the angle $\angle ADB$ = β_S has to be used. $\overline{AB}$ is given as $\overline{AB}$ = $\overline{AD}$·sin(β_S) and $\overline{AD}$ is given by $\overline{AD}$ = $\overline{EC}$ + $\overline{CF}$ - $\overline{GD}$. These single distances can be expressed as

$$\overline{EC} = d \cdot \tan(\beta_S), \tag{A.5}$$

$$\overline{CF} = (d - z_S) \cdot \tan(\beta_P), \tag{A.6}$$

$$\overline{GD} = z_S \cdot \tan(\beta_P). \tag{A.7}$$

Now Eq. (A.1) can be re-written as:

$$\begin{aligned}\Delta\phi = 2\pi f\Bigg[&\frac{1}{v_{S1}}\left(\frac{d}{\cos(\beta_S)} - \sin(\beta_S)\left[d \cdot \tan(\beta_S) + (d - z_S) \cdot \tan(\beta_P) - z_S \cdot \tan(\beta_P)\right]\right) \\ &+ \frac{1}{v_{P1}}\frac{(d - z_S)}{\cos(\beta_P)} - \frac{1}{v_{P1}}\frac{z_S}{\cos(\beta_P)}\Bigg].\end{aligned} \tag{A.8}$$

With the law of reflection Eq. (2.29) the relation between the two seismic angles is given:

$$\sin(\beta_S) = \frac{v_{S1}}{v_{P1}}\sin(\beta_P). \tag{A.9}$$

Using the equality tan(β)=sin(β)/cos(β) Eq. (A.8) becomes:

$$\begin{aligned}\Delta\phi = 2\pi f\Bigg[&\frac{1}{v_{S1}}\left(\frac{d}{\cos(\beta_S)} - d\frac{\sin^2(\beta_S)}{\cos(\beta_S)} - (d - z_S)\frac{\sin^2(\beta_P)}{\cos(\beta_P)}\frac{v_{S1}}{v_{P1}} + z_S\frac{\sin^2(\beta_P)}{\cos(\beta_P)}\frac{v_{S1}}{v_{P1}}\right) \\ &+ \frac{1}{v_{P1}}\frac{(d - z_S)}{\cos(\beta_P)} - \frac{1}{v_{P1}}\frac{z_S}{\cos(\beta_P)}\Bigg].\end{aligned} \tag{A.10}$$

Eliminating the parenthesis in the first line and sorting the terms according to their dependencies on β_P or β_S one finds:

$$\Delta\phi = 2\pi f\left[\frac{d}{v_{\mathrm{S1}}}\sqrt{1-\sin^2(\beta_\mathrm{S})}+\frac{(d-2z_\mathrm{S})}{v_{\mathrm{P1}}}\sqrt{1-\sin^2(\beta_\mathrm{P})}\right]. \tag{A.11}$$

Finally, this can be expressed using only the dependency on the acoustic angle α:

$$\Delta\phi = 2\pi f\left[\frac{d}{v_{\mathrm{S1}}}\sqrt{1-\left(\frac{v_{\mathrm{S1}}}{v_0}\right)^2\sin^2(\alpha)}+\frac{(d-2z_\mathrm{S})}{v_{\mathrm{P1}}}\sqrt{1-\left(\frac{v_{\mathrm{P1}}}{v_0}\right)^2\sin^2(\alpha)}\right]. \tag{A.12}$$

It is convenient to notice that the first term in the brackets of Eq. (A.12) represents the phase difference between the wave $A_{\grave{\mathrm{P}}}$ at point D and the wave $A_{\grave{\mathrm{S}}\acute{\mathrm{P}}}$ at point C. This means, it corresponds to the wave $A_{\grave{\mathrm{S}}\acute{\mathrm{P}}}$ having propagated once through the whole upper soil layer as an SV wave. This is the expression $\Delta\phi_\mathrm{S}$ given in Eq. (2.66). If the distance $\overline{AC}$ would have been covered as a P wave (i.e. $A_{\grave{\mathrm{P}}\acute{\mathrm{P}}}$ instead of $A_{\grave{\mathrm{S}}\acute{\mathrm{P}}}$), the respective term $\Delta\phi_\mathrm{P}$ from Eq. (2.66) would have been obtained. Then the phase difference would reproduce that of $\Delta\phi_{\grave{\mathrm{P}},\grave{\mathrm{P}}\acute{\mathrm{P}}}$ in Eq. (2.46) without the phase jump of π.
Similar observations can be made for the second term in the brackets of Eq. (A.12) which corresponds to the phase difference resulting from the respective distances both waves have to cover to reach the sensor. It is the expression $\partial\phi_{\acute{\mathrm{P}}}$ in Eq. (2.70). Consequently, the findings of Eq. (A.12) can be written as $\Delta\phi = \Delta\phi_\mathrm{S} + \partial\phi_{\acute{\mathrm{P}}}$. If the second part of the wave would have been an SV wave (i.e. $A_{\grave{\mathrm{S}}\acute{\mathrm{S}}}$ instead of $A_{\grave{\mathrm{S}}\acute{\mathrm{P}}}$), the term obtained in the derivation would have been the term $\partial\phi_{\acute{\mathrm{S}}}$ from Eq. (2.70).
If an arbitrary wave A_i reaches the sensor propagating downwards, it is of relevance whether the type of the wave during the propagation from the surface to the sensor is a P wave or an SV wave. In the first case, the waves $A_{\grave{\mathrm{P}}}$ and A_i cover the same path $\overline{DS}$ and the resulting phase difference vanishes, corresponding to $\partial\phi_{\grave{\mathrm{P}}} \equiv 0$. In the latter case, the wave A_i reaches the sensor from point D'. The respective phase difference is given as $\partial\phi_{\grave{\mathrm{S}}}$ in Eq. (2.69). Thus, the total phase difference between $A_{\grave{\mathrm{P}}}$ and an arbitrary wave A_i can be written as, reproducing Eq. (2.71):

$$\Delta\phi_{\mathrm{tot},i} = m\cdot\Delta\phi_\mathrm{P} + n\cdot\Delta\phi_\mathrm{S} + \Delta\phi_{II,i}. \tag{A.13}$$

The integers m and n are the number of times the wave A_i passed the whole upper soil layer in one direction as P wave and as SV wave, respectively. The expression $\Delta\phi_{II,i}$ refers to the respective term from Eq. (2.69) or Eq. (2.70) depending of direction and type of the last part of the wave A_i.

A.2 Derivation of the equation of the spectral amplitude distribution

Here detailed descriptions of the calculations leading to the equations of the spectral amplitude distributions of the wave interference, i.e. Eq. (2.47) in Section 2.3.1 as well as the more general equation Eq. (2.73) in Section 2.3.4, are given.
Using model 1 (see Section 2.3.1) each of the waves $A_{\grave{\mathrm{P}}}$, $A_{\grave{\mathrm{P}}\acute{\mathrm{P}}}$ and $A_{\grave{\mathrm{P}}\acute{\mathrm{P}}\grave{\mathrm{P}}}$ has the form $A_j = a_j \cdot e^{\mathrm{i}(\omega t+\phi_j)}$, with the amplitude a_j and the phase ϕ_j. The investigated broadband signals contain a wide range of frequencies, but in a linear problem the superposition can be treated for each frequency separately and therefore it retains the same frequency dependency. Thus, all three waves interfere at the sensor forming a new wave given by the phase-corrected summation of the three single waves: $A_{\mathrm{tot}} = A_{\grave{\mathrm{P}}} + A_{\grave{\mathrm{P}}\acute{\mathrm{P}}} + A_{\grave{\mathrm{P}}\acute{\mathrm{P}}\grave{\mathrm{P}}} = a_{\mathrm{tot}} \cdot e^{\mathrm{i}(\omega t+\phi_{\mathrm{tot}})}$. Its time-independent amplitude a_{tot} is obtained as the square root of the multiplication with its complex conjugate and depends only on the phase differences $\Delta\phi_{jk}$ between the waves A_j and A_k for a given frequency and path difference:

$$a_{\mathrm{tot}} = \sqrt{A_{\mathrm{tot}} \cdot A_{\mathrm{tot}}^*} \tag{A.14}$$

$$= \sqrt{(A_{\grave{\mathrm{P}}} + A_{\grave{\mathrm{P}}\acute{\mathrm{P}}} + A_{\grave{\mathrm{P}}\acute{\mathrm{P}}\grave{\mathrm{P}}})(A_{\grave{\mathrm{P}}} + A_{\grave{\mathrm{P}}\acute{\mathrm{P}}} + A_{\grave{\mathrm{P}}\acute{\mathrm{P}}\grave{\mathrm{P}}})^*} \tag{A.15}$$

$$\begin{aligned} =&\Big(a_{\grave{\mathrm{P}}} \cdot e^{\mathrm{i}\omega t} + a_{\grave{\mathrm{P}}\acute{\mathrm{P}}} \cdot e^{\mathrm{i}(\omega t+\phi_{\grave{\mathrm{P}}\acute{\mathrm{P}}})} + a_{\grave{\mathrm{P}}\acute{\mathrm{P}}\grave{\mathrm{P}}} \cdot e^{\mathrm{i}(\omega t+\phi_{\grave{\mathrm{P}}\acute{\mathrm{P}}\grave{\mathrm{P}}})}\Big)^{1/2} \\ &\cdot \Big(a_{\grave{\mathrm{P}}} \cdot e^{-\mathrm{i}\omega t} + a_{\grave{\mathrm{P}}\acute{\mathrm{P}}} \cdot e^{-\mathrm{i}(\omega t+\phi_{\grave{\mathrm{P}}\acute{\mathrm{P}}})} + a_{\grave{\mathrm{P}}\acute{\mathrm{P}}\grave{\mathrm{P}}} \cdot e^{-\mathrm{i}(\omega t+\phi_{\grave{\mathrm{P}}\acute{\mathrm{P}}\grave{\mathrm{P}}})}\Big)^{1/2} \end{aligned} \tag{A.16}$$

$$\begin{aligned} =&\Big({a_{\grave{\mathrm{P}}}}^2 + {a_{\grave{\mathrm{P}}\acute{\mathrm{P}}}}^2 + {a_{\grave{\mathrm{P}}\acute{\mathrm{P}}\grave{\mathrm{P}}}}^2 + 2a_{\grave{\mathrm{P}}}a_{\grave{\mathrm{P}}\acute{\mathrm{P}}}\cos(\phi_{\grave{\mathrm{P}}\acute{\mathrm{P}}}) + 2a_{\grave{\mathrm{P}}}a_{\grave{\mathrm{P}}\acute{\mathrm{P}}\grave{\mathrm{P}}}\cos(\phi_{\grave{\mathrm{P}}\acute{\mathrm{P}}\grave{\mathrm{P}}}) \\ &+ 2a_{\grave{\mathrm{P}}\acute{\mathrm{P}}}a_{\grave{\mathrm{P}}\acute{\mathrm{P}}\grave{\mathrm{P}}}\cos(\phi_{\grave{\mathrm{P}}\acute{\mathrm{P}}} - \phi_{\grave{\mathrm{P}}\acute{\mathrm{P}}\grave{\mathrm{P}}})\Big)^{1/2}. \end{aligned} \tag{A.17}$$

In Eq. (A.15) the symbol * refers to the complex conjugate of the waves, affecting only the exponential terms. From Eq. (A.16) to Eq. (A.17) the relation $e^{(\mathrm{i}\phi)} \cdot e^{(-\mathrm{i}\phi)} = 2\cos(\phi)$ was used. The time dependency, given by the term $e^{(\mathrm{i}\omega t)}$, cancels out in the multiplication with its complex conjugate: $e^{(\mathrm{i}\omega t)} \cdot e^{(-\mathrm{i}\omega t)} = 1$.

The same calculation can be applied to any number M of interfering waves A_j. Eq. (A.16) will then become:

$$a_{\mathrm{tot}} = \sqrt{\left(\sum_j^M a_j \cdot e^{\mathrm{i}(\omega t+\phi_j)}\right) \cdot \left(\sum_k^M a_k \cdot e^{-\mathrm{i}(\omega t+\phi_k)}\right)}. \tag{A.18}$$

Thus, the more general equation for the spectral amplitude distribution of M interfering

waves is given by:

$$a_{\mathrm{tot}} = \left[\sum_{j}^{M}\left({a_j}^2 + \sum_{k\neq j}^{M} a_j a_k \cos(\Delta\phi_{\mathrm{tot},j} - \Delta\phi_{\mathrm{tot},k})\right)\right]^{1/2}. \tag{A.19}$$

Here the phase differences $\Delta\phi_{\mathrm{tot},j}$ and $\Delta\phi_{\mathrm{tot},k}$ between the respective wave and the reference wave $A_{\grave{\mathrm{P}}}$ are used. The inner sum takes into account the phase differences between a certain pair of waves A_m and A_n. The terms of the phase difference are symmetric due to the cosine: $\cos(\Delta\phi_{mn}) = \cos(\Delta\phi_{nm})$. The factor 2 (compare to Eq. (A.17)) of the term $2a_m a_n \cos(\Delta\phi_{mn})$ will be reproduced when performing the outer sum for both values $j = m$ and $j = n$.

A.3 List of the local sensor coordinates

Sensor	Ch.	x / m	y / m	z / m	Sensor	Ch.	x / m	y / m	z / m
Geo11_v	0	0.00	0.00	0.60	Geo21_v	17	-0.45	5.50	0.30
GeoE_h$_\perp$	1	0.00	0.00	0.60	GeoP_h$_\perp$	18	-0.45	5.50	0.30
GeoF_h$_\parallel$	2	0.00	0.00	0.60	GeoQ_h$_\parallel$	19	-0.45	5.50	0.30
Geo4_v	3	-0.45	0.00	0.30	Geo13_v	20	0.45	5.50	0.45
GeoC_h$_\perp$	4	-0.45	0.00	0.30	Geo15_v	21	0.00	5.90	0.15
GeoD_h$_\parallel$	5	-0.45	0.00	0.30	Geo19_v	22	-0.45	8.00	0.30
Geo3_v	6	1.74	0.00	0.30	Geo5_v	23	0.00	0.23	0.00
GeoH_h$_\perp$	7	1.74	0.00	0.30	Geo20_v	24	1.93	0.23	0.00
binary	8	-	-	-	GeoL_h$_\perp$	25	1.98	0.24	0.00
GeoJ_h$_\parallel$	9	1.74	0.00	0.30	GeoM_h$_\parallel$	26	1.88	0.24	0.00
Geo9_v	10	2.15	0.00	0.15	BK1	27	-0.23	0.00	-0.065
Geo2_v	11	0.00	0.45	0.15	BK5	28	0.23	0.00	-0.065
Geo6_v	12	0.45	0.00	0.45	BK2	29	1.87	0.00	-0.065
Geo1_v	13	-2.20	0.00	0.60	BK6	30	-1.98	0.00	-0.065
Geo7_v	14	-1.75	0.00	0.45	BK3	31	0.22	5.50	-0.065
Geo8_v	15	-0.45	3.00	0.30	BK4	32	-0.22	3.00	-0.065
Geo10_v	16	0.00	5.50	0.60					

Table A.1: Local coordinates of the sensors used during the measurements near the airport FMO. Sensors are named "BK" for Brüel & Kjaer microphones and "Geo" for 4.5-Hz geophones with attached numbers for vertical or capital letters for horizontal geophones and their orientation: "v" (vertical), "h$_\parallel$" (horizontal and parallel to the runway line of the airport FMO, sensor facing in positive y direction) and "h$_\perp$" (horizontal and perpendicular to the runway line, sensor facing in positive x direction). Column 2 states the channel number. The burying depth of the geophones z refers to the depth of the dug hole in which the geophones were pushed into the soil with a conical spike of approximately 7 cm length, thus the actual coupling depth to the ground might be slightly larger than the stated values. Channel 8 recorded GPS time converted to DCF77 clock pulses.

A.4 Table of aircraft overflights

#	Aircraft Type	Lat. Dist./m	Height/m	Vel./(m/s)	α/ °	Turbines
1	Embraer ERJ 190-100	350	760	89.7	24.8	2
2	Boeing 737-800	355	540	112.7	33.3	2
3	Embraer ERJ 190-100	384	807	93.0	25.5	2
4	Bombardier BD-100 Challenger 300	278	1315	99.4	11.8	2
5	Bombardier Regional Jet CRJ-700	288	714	95.4	21.9	2
6	Dassault Falcon 7X	418	1645	103.9	14.4	3
7	Embraer ERJ 190-100	420	740	84.3	29.5	2
8	Gulfstream Aerospace Gulfstream 5	452	1543	88.1	16.3	2
9	Boeing 737-800	465	707	104.0	33.4	2
10	Embraer ERJ 190-100	368	820	90.2	24.3	2
11	Boeing 737-800	413	630	103.7	33.2	2
12	Bombardier Regional Jet CRJ-700	220	800	93.0	15.5	2
13	Boeing 737-800	409	600	106.9	34.1	2
14	Bombardier Regional Jet CRJ-700	375	910	92.9	22.4	2
15	Bombardier Regional Jet CRJ-700	494	851	92.1	30.1	2
16	Embraer ERJ 190-100	352	795	66.2	23.8	2

Table A.2: Overview of the evaluated overflight events, recorded on 14th and 15th May 2013 near the airport FMO. Column 1 gives the event number of the overflights. The values of lateral distance, height, ground speed of the aircraft (columns 3 - 5) as well as the angle of incidence of the acoustic signal α (column 6) refer to the aircraft at its cpa. All presented overflight events are takeoffs.

Overflight #	Temperature / K	v_0 / (m/s)
1	9.7	337.1
2	11.8	338.4
3	12.1	338.5
4	11.6	338.3
5	11.6	338.
6	12.3	338.7
7	12.0	338.5
8	12.0	338.5
9	11.3	338.1
10	12.4	338.7
11	12.4	338.7
12	12.4	338.7
13	17.8	341.9
14	15.7	340.7
15	14.3	339.8
16	15.0	340.3

Table A.3: Temperature for each overflight and the corresponding sound velocity calculated with Eq. (2.15). The temperature was recorded each hour at the weather station of the airport FMO by the German Meteorological Service (DWD) who provided the data for the evaluation. For each overflight event the respective previously recorded temperature is used.

A.5 Calculation of the background level at the used sensors

During the measurement campaign at the airport FMO soil velocity and sound pressure induced by airborne sources were recorded. Exemplary time signals of an aircraft overflight and artificial noise replay are shown in Section 4.1.1.1 and their respective spectral values in Section 4.1.2.1. Various other seismic and acoustic sources in the vicinity of the measurement site generated a background for the recorded data. The background level of the microphones is mainly determined by wind in the low-frequency range. Rarely other disturbing acoustic signals were audible at the site. Geophones recorded additional seismic signals in the vicinity of the measurement site. These could be generated for example by agricultural machinery or vehicles passing a bridge in a distance of about 500 m to the west from the sensor setup. Additionally, movement of the operators at the measurement site and especially adjustment work at the crane for the speaker caused significant soil vibrations. For all recordings great care was taken to minimise these disturbing signals. Occasionally, measurements of the noise replay were repeated if during the replay time signals of another source were detected.

The background level at each sensor was calculated separately. A time of two minutes in the night of 16th May 2013 from 0:58:00 to 1:00:00 (UTC) was chosen during which

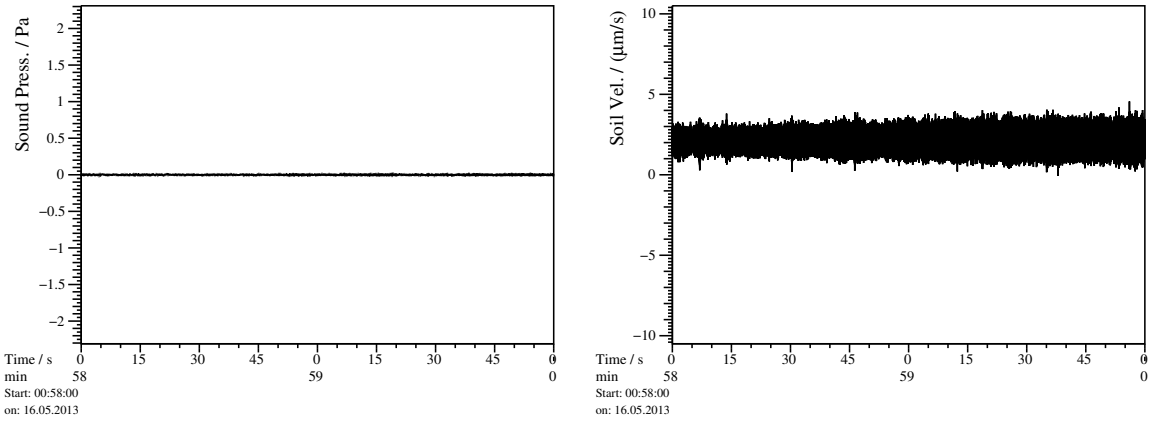

Figure A.2: Time signals of the acoustic and seismic background at the measurement site, recorded for two minutes in the night of 16th May 2013 from 0:58:00 to 1:00:00 (UTC).
Left: Sound pressure, recorded with the microphone of channel 29.
Right: Vertical soil velocity, recorded with a geophone at the surface, channel 24.

only very few and weak disturbing signals were recorded. In Fig. A.2 the time signals of the sound pressure, recorded with microphone of channel 29 (left) and the soil velocity, recorded at the surface with geophone of channel 24 (right) are shown. For both plots the same y-ranges as for the time signals of the aircraft overflight and the noise replay in Section 4.1.1.1 are used.

The time signals are used to obtained averaged spectra of the background signals: Single spectra are calculated for consecutive time intervals of $T = 0.8192\,\mathrm{s}$ and their spectral amplitudes are averaged as plotted in Fig. A.3 and Fig. A.4. The averaged, normalised power spectrum of the sound pressure (microphone channel 29) is given in Fig. A.3 (left). Those of the vertical soil velocity in various depths z_S are shown in Fig. A.3, right (geophone channel 24, at the surface), in Fig. A.4, left (geophone channel 6, $z_\mathrm{S} = 0.30\,\mathrm{m}$) and in Fig. A.4, right (geophone channel 13, $z_\mathrm{S} = 0.60\,\mathrm{m}$).

In all background spectra of the geophones clearly sharp spectral peaks at 50 Hz and its odd multiples are visible, which are caused by mains hum. They were also recorded at times of lower signal amplitude during the aircraft overflights. Thus, frequency intervals of 50 Hz (and its odd multiples) ± 2 Hz were excluded from most calculations during the evaluation.

Additionally, such peaks are visible in the acoustic background spectrum (Fig. A.3, left). Furthermore, in the seismic background spectra peaks of much lower magnitude are visible at frequencies of the even multiples of 50 Hz. Both are usually too weak to be detected during the measurements and thus were not further considered during the evaluation.

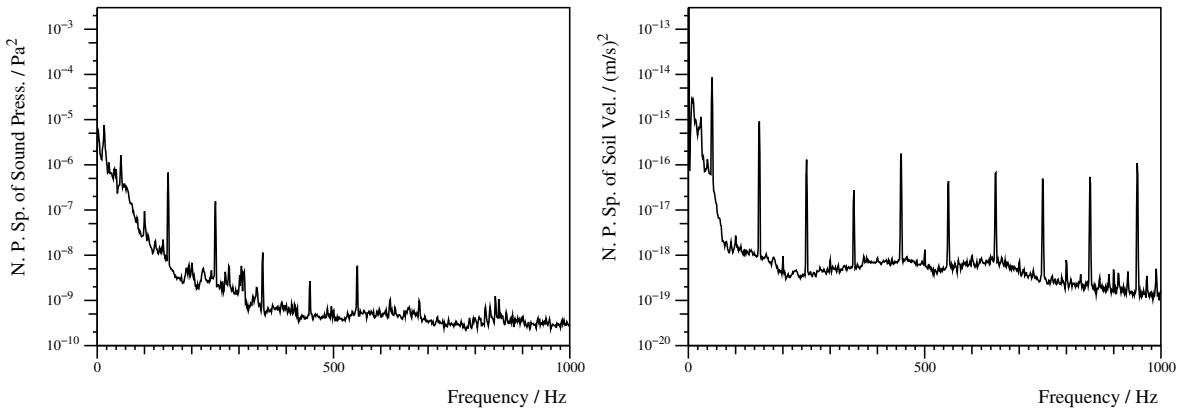

Figure A.3: Averaged, normalised power spectra of the background signals recorded for two minutes in the night of 16th May 2013 from 0:58:00 to 1:00:00 (UTC).
Left: Sound pressure, recorded with the microphone of channel 29.
Right: Vertical soil velocity, recorded with a geophone at the surface, channel 24.

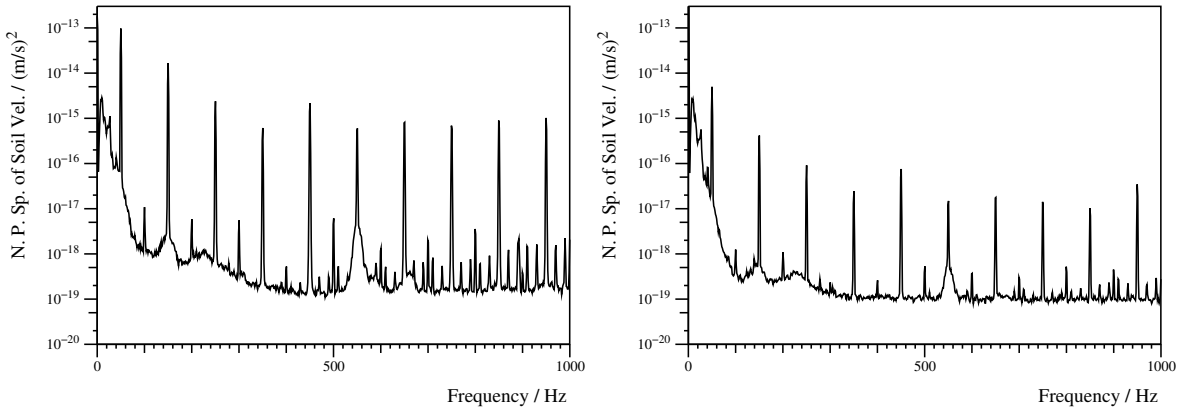

Figure A.4: Averaged, normalised power spectra of the background signals recorded for two minutes in the night of 16th May 2013 from 0:58:00 to 1:00:00 (UTC).
Left: Vertical soil velocity, recorded with a geophone in the depth $z_S = 0.30\,\mathrm{m}$, channel 6.
Right: Vertical soil velocity, recorded with a geophone in the depth $z_S = 0.60\,\mathrm{m}$, channel 13.

A.6 Spectrograms of broadband noise replay by a speaker

Here I show the spectrograms of the artificially produced noise played for 30 seconds by the speaker. They show the replay time as well as about 5 s before and after the replay, as already shown in corresponding time signals (Fig. 4.3 and Fig. 4.4 in Section 4.1.1.1). Using only the time of the noise replay averaged spectra were calculated which are shown in Fig. 4.11 in Section 4.1.2.1.

Fig. A.5 (top) shows the spectrogram of the sound pressure, recorded with the microphone of channel 27 and Fig. A.5 (bottom) that of the vertical soil velocity at the surface, recorded with the geophone of channel 23. In Fig. A.6 the vertical soil velocity for buried geophones are shown: A geophone in the depth of 0.30 m, channel 3 (top) and a geophone in the depth of 0.60 m, channel 0 (bottom).

Over the whole time of the noise replay the spectral amplitudes show approximately the same values, thus averaging of the single spectra led to the good results shown in Fig. 4.11.

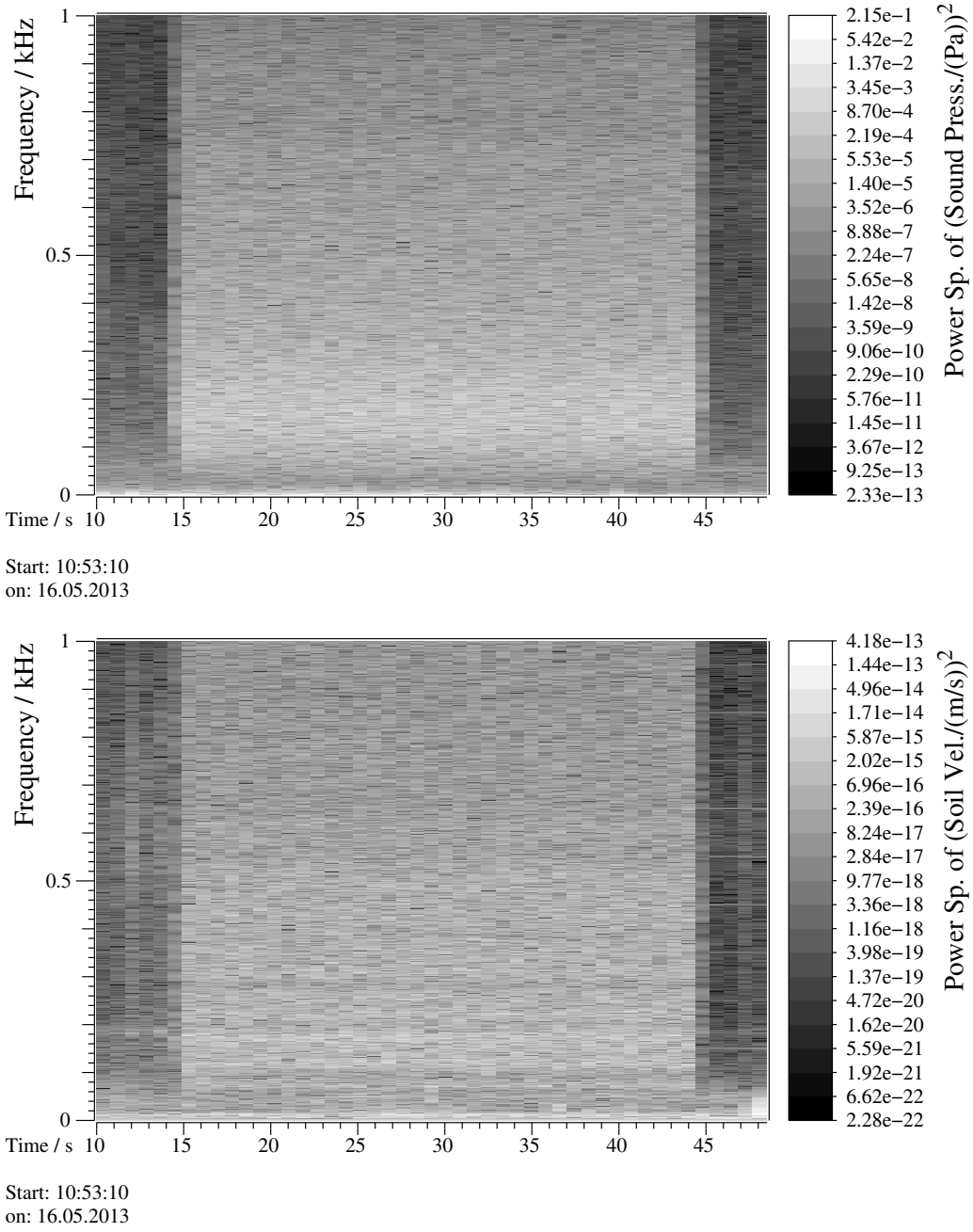

Figure A.5: Normalised power spectrograms of broadband noise replay corresponding to the time signal shown in Fig. 4.3.
Top: Sound pressure, recorded with the microphone of channel 27.
Bottom: Vertical soil velocity, recorded with a geophone at the surface, channel 23.

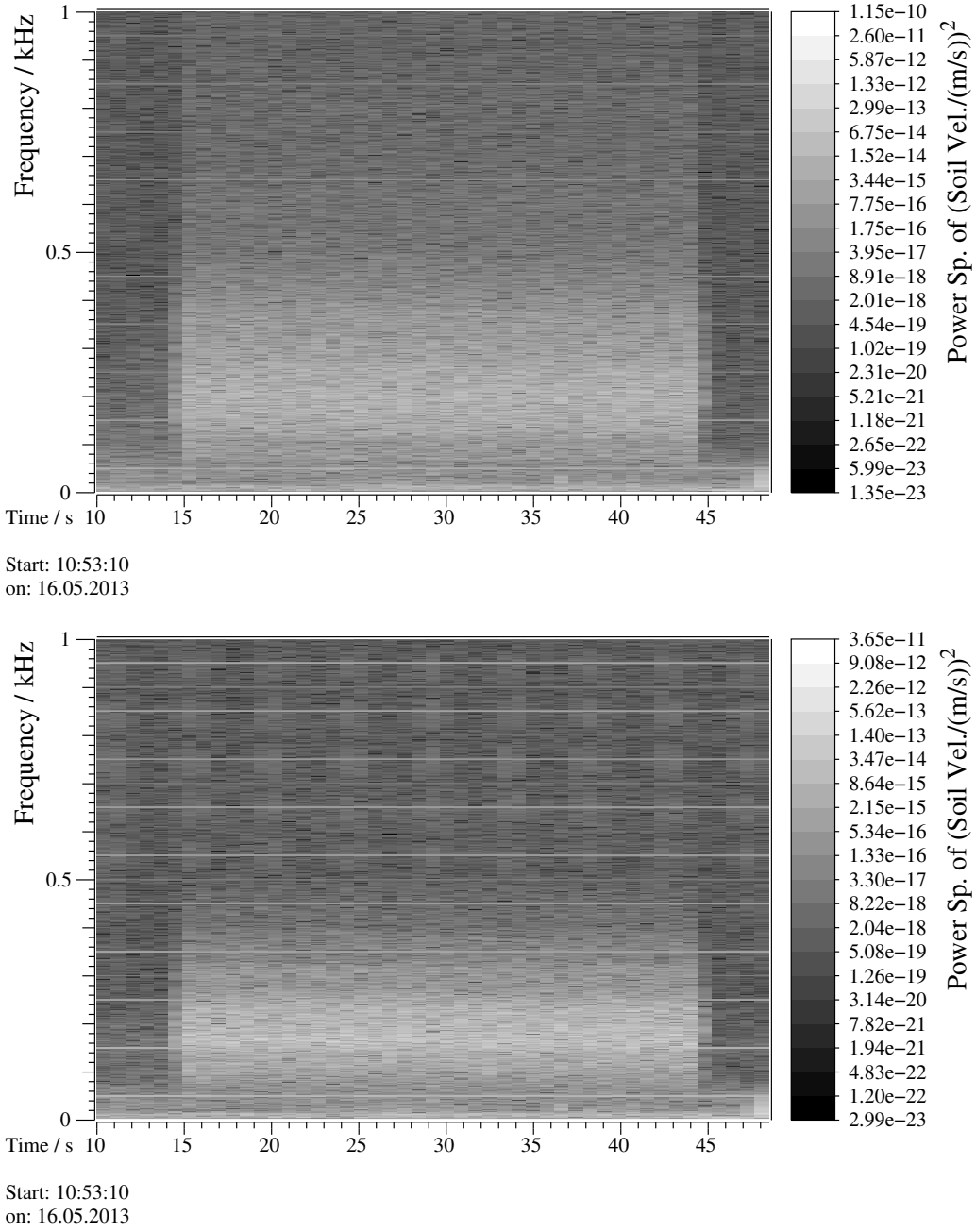

Figure A.6: Normalised power spectrograms of the vertical soil velocity recorded with buried geophones of broadband noise replay corresponding to the time signal shown in Fig. 4.4. Top: Geophone in the depth of 0.30 m, channel 3. Bottom: Geophone in the depth of 0.60 m, channel 0.

A.7 Additional fit results of buried sensors

In Section 4.4.3 the fit results of the three used interference models for buried sensors ($z_S > 0\,\mathrm{m}$) are discussed. The results for each fit are summarized in Table 4.2. The comparison between measured data and theoretically obtained amplitude distributions is shown exemplarily for $z_S = 0.15\,\mathrm{m}$ in Fig. 4.28. Here the corresponding plots for $z_S = 0.30\,\mathrm{m}$ (Fig. A.7), $z_S = 0.45\,\mathrm{m}$ (Fig. A.8) and $z_S = 0.60\,\mathrm{m}$ (Fig. A.9) are shown. All plots were generated for the parameters d and v_{P1} corresponding to the minimum of the root-mean-square deviation $D(d, v_{P1})$ as given in Table 4.2. The models of interference used for the fit are the following (see also Section 4.4): Interference between the three P waves $A_{\grave{P}}$, $A_{\grave{P}\acute{P}}$ and $A_{\grave{P}\acute{P}\grave{P}}$ which generally show the largest amplitudes (model 1); interference between the quasi-infinite number of P waves reflected within the upper soil layer (model 2); interference between the quasi-infinite number of P waves and the directly acoustically excited SV wave $A_{\grave{S}}$ (model 3).

Each graph shows the averaged coupling coefficient together with the data points used for the fit as black points (top, left). The theoretically obtained amplitude distributions (vertical components) as well as the data points used for the fit and the theoretical frequency maxima $f^{\mathrm{theo}}_{\mathrm{max},k}(\alpha)$ (corresponding to the data points) are shown for each model: Model 1 – top, right; model 2 – bottom, left and model 3 – bottom, right.

In the plots of the theoretical amplitude distributions in the depths $z_S = 0.30\,\mathrm{m}$ (Fig. A.7) and $z_S = 0.45\,\mathrm{m}$ (Fig. A.8) it can be observed that some interference maxima with separate frequencies at small α merge into a single interference maximum at larger α. This confluence of the theoretical $f^{\mathrm{theo}}_{\mathrm{max},k}(\alpha)$ is an artefact of the tracking algorithm (described in Section 4.2.2) and the change of the relative amplitudes of the interfering waves: With the algorithm the frequency of each local maximum at the lowest value of α is obtained. For subsequent larger α the frequency of maximal amplitude in a small interval around the found frequency of the previous value of α is determined. However, a change of the relative amplitudes of the interfering waves, caused by the angle dependency of the reflection coefficients, leads to a shift of the frequencies of the interference maxima with respect to each other. If the spectral distance between two maxima becomes too small both merge into a single effective maximum at a certain α. For the subsequent α the algorithm will determine the maximal amplitude values in the given frequency interval around the previously found frequencies of both maxima (which actually might be the value at one boundary of these intervals) until the frequency of the real maximum is found. This has little influence on the fit results to determine d and v_{P1} since hardly any effected data points are used for the fits.

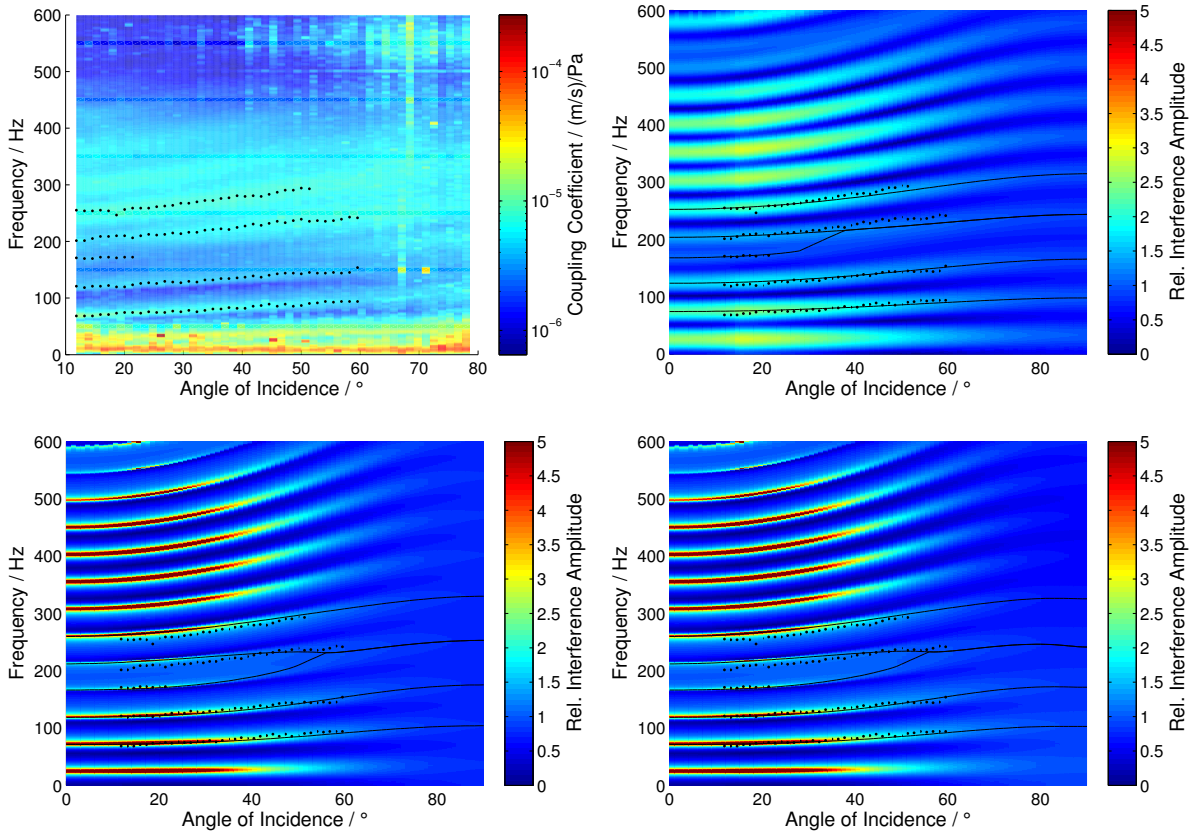

Figure A.7: Top, left: Mean coupling coefficient measured in depth $z_S = 0.30\,\mathrm{m}$ (channel 6) together with the data points used for the fits (black dots). Top, right: Theoretical spectral amplitude distribution calculated with model 1 for the values $d = 2.23\,\mathrm{m}$ and $v_{P1} = 209\,\mathrm{m/s}$. Bottom, left: Amplitude distribution calculated with model 2 for the values $d = 2.38\,\mathrm{m}$ and $v_{P1} = 225\,\mathrm{m/s}$. Bottom, right: Amplitude distribution calculated with model 3 for the values $d = 2.38\,\mathrm{m}$ and $v_{P1} = 225\,\mathrm{m/s}$. The plots of the theoretical amplitude distribution also show the data points $f^{\mathrm{meas}}_{\mathrm{max},k}(\alpha)$ used for the respective fit (black dots) as well as the numerically determined frequencies of maximal interference amplitude $f^{\mathrm{theo}}_{\mathrm{max},k}(\alpha)$ (black lines) for the values $1 \leq k \leq 5$. The colour scale of the three theoretical plots is limited to the interval [0,5].

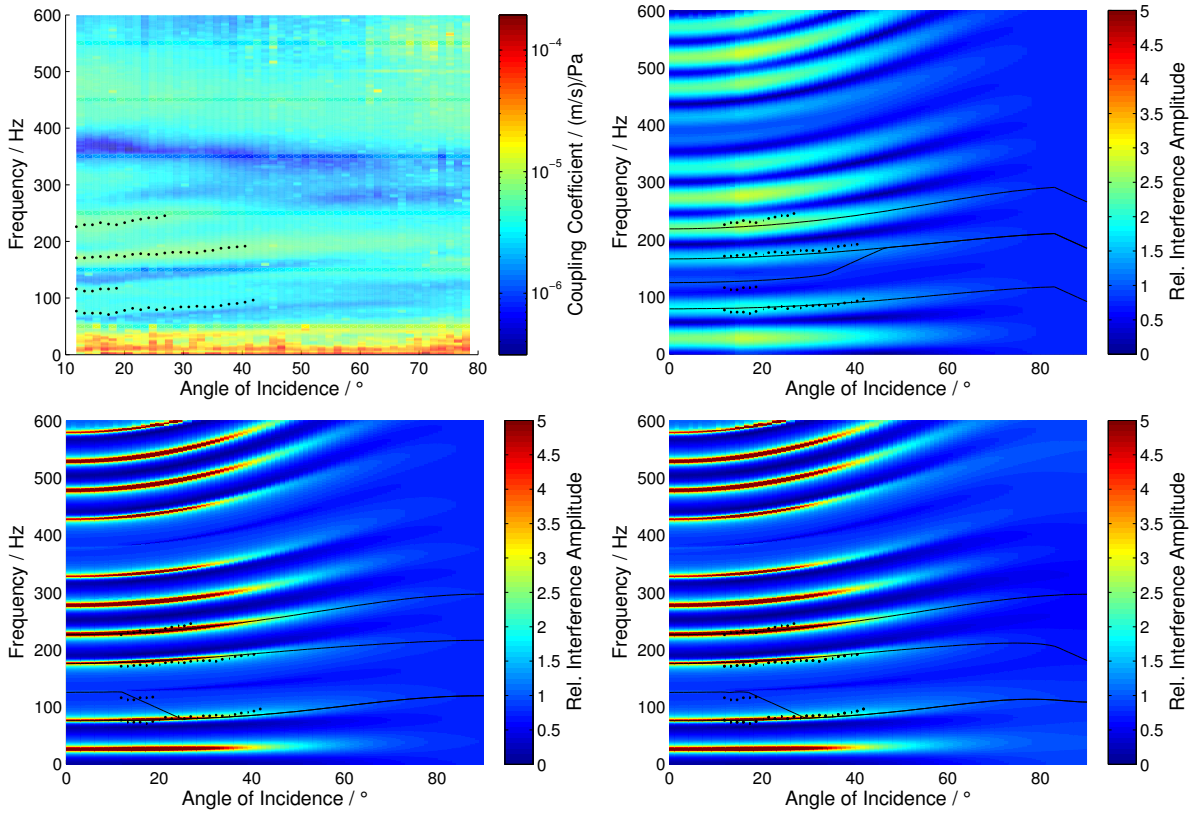

Figure A.8: Top, left: Mean coupling coefficient measured in depth $z_S = 0.45\,\mathrm{m}$ (channel 20) together with the data points used for the fits (black dots). Top, right: Theoretical spectral amplitude distribution calculated with model 1 for the values $d = 2.34\,\mathrm{m}$ and $v_{P1} = 230\,\mathrm{m/s}$. Bottom, left: Amplitude distribution calculated with model 2 for the values $d = 2.25\,\mathrm{m}$ and $v_{P1} = 226\,\mathrm{m/s}$. Bottom, right: Amplitude distribution calculated with model 3 for the values $d = 2.24\,\mathrm{m}$ and $v_{P1} = 225\,\mathrm{m/s}$. The plots of the theoretical amplitude distribution also show the data points $f^{\mathrm{meas}}_{\mathrm{max},k}(\alpha)$ used for the respective fit (black dots) as well as the numerically determined frequencies of maximal interference amplitude $f^{\mathrm{theo}}_{\mathrm{max},k}(\alpha)$ (black lines) for the values $1 \leq k \leq 4$. The colour scale of the three theoretical plots is limited to the interval [0,5].

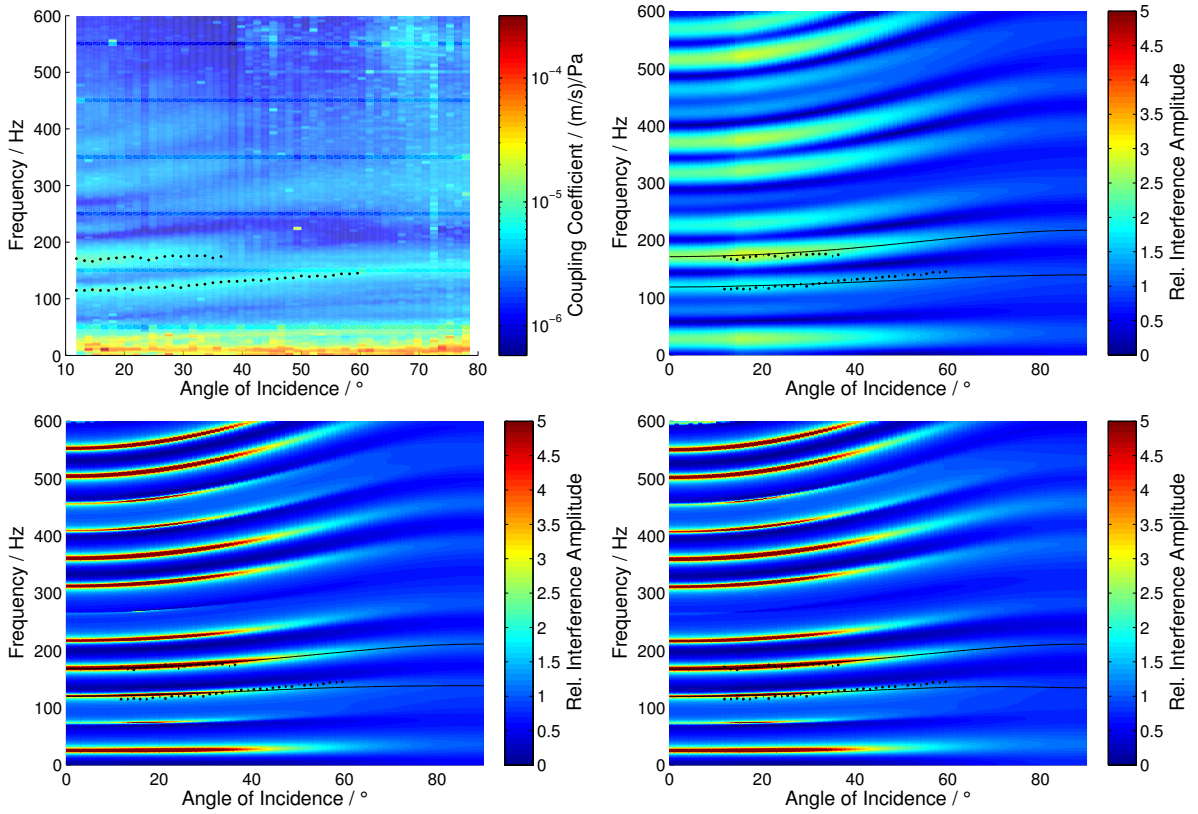

Figure A.9: Top, left: Mean coupling coefficient measured in depth $z_S = 0.60\,\mathrm{m}$ (channel 13) together with the data points used for the fits (black dots). Top, right: Theoretical spectral amplitude distribution calculated with model 1 for the values $d = 2.14\,\mathrm{m}$ and $v_{P1} = 210\,\mathrm{m/s}$. Bottom, left: Amplitude distribution calculated with model 2 for the values $d = 2.17\,\mathrm{m}$ and $v_{P1} = 208\,\mathrm{m/s}$. Bottom, right: Amplitude distribution calculated with model 3 for the values $d = 2.20\,\mathrm{m}$ and $v_{P1} = 210\,\mathrm{m/s}$. The plots of the theoretical amplitude distribution also show the data points $f^{\mathrm{meas}}_{\mathrm{max},k}(\alpha)$ used for the respective fit (black dots) as well as the numerically determined frequencies of maximal interference amplitude $f^{\mathrm{theo}}_{\mathrm{max},k}(\alpha)$ (black lines) for the values $k = 2$ and $k = 3$. The colour scale of the three theoretical plots is limited to the interval [0,5].

A.8 Spectrograms recorded with acoustically shielded sensors

Here the spectrograms of sensors placed under the acoustic damping box are shown. The signals were recorded during the jet-aircraft overflight number 13. The evaluation of these signals is presented in Section 4.5.2.1.

In Fig. A.10 (top) the spectrogram of the sound pressure, recorded with microphone of channel 27, is shown. Spectrograms of the soil velocity are recorded with geophones placed in different depths: $z_S = 0\,\mathrm{m}$ (Fig. A.10 (bottom)), $z_S = 0.30\,\mathrm{m}$ (Fig. A.11, top) and $z_S = 0.60\,\mathrm{m}$ (Fig. A.11, bottom). In each graph the time when the signal from the cpa of the overflight is recorded is indicated by a red line at the top of the graph. Additionally, the times during which the angle of incidence of the acoustic signal α was smaller than 60° is marked with blue lines at the top.

Corresponding spectrograms recorded at sensors outside of the box are shown in Fig. 4.9 and Fig. 4.10.

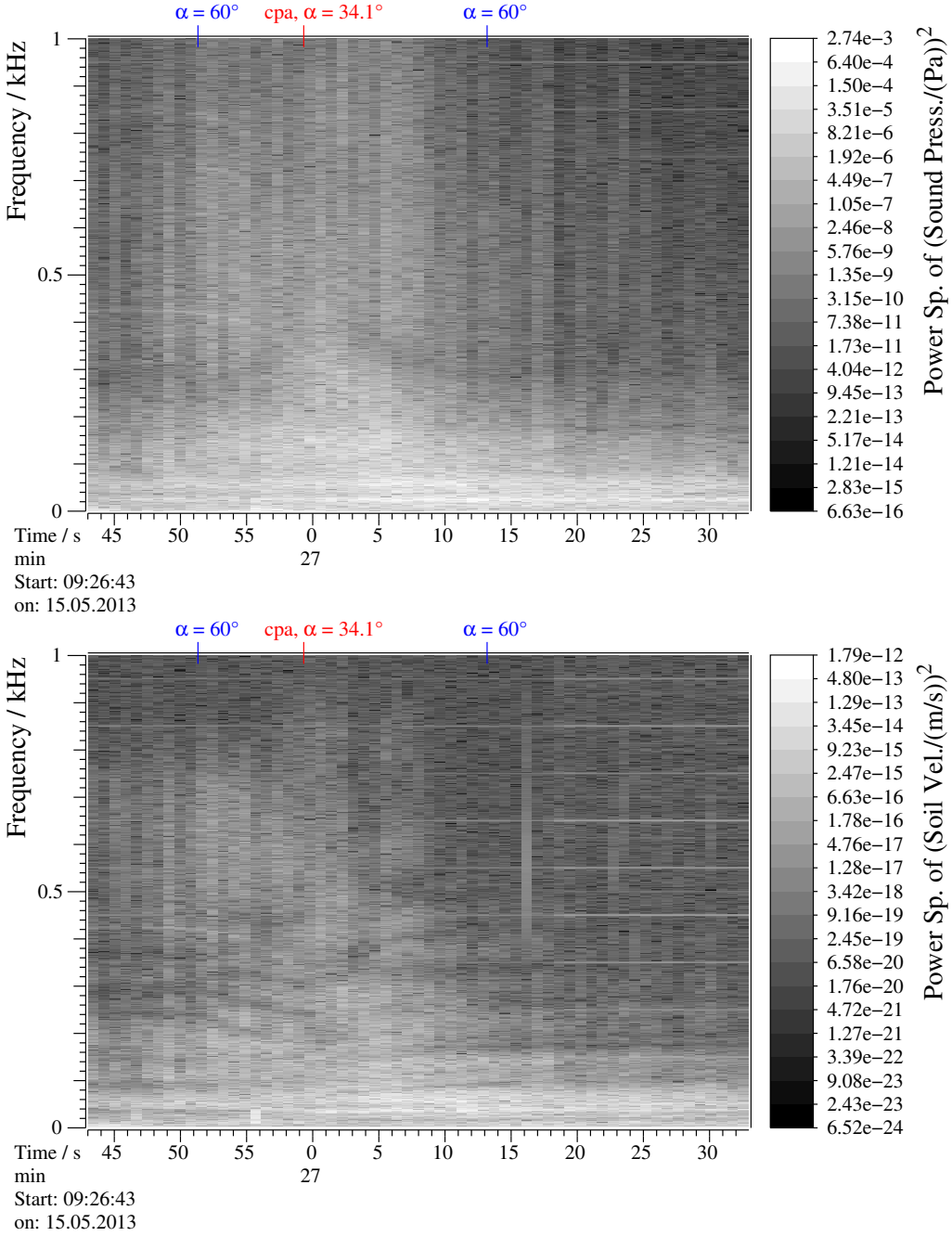

Figure A.10: Normalised power spectrograms of the jet-aircraft overflight number 13. The corresponding time signals are shown in Fig. 4.30.
Top: Sound pressure, recorded with the microphone of channel 27.
Bottom: Vertical soil velocity, recorded with a geophone at the surface, channel 23.

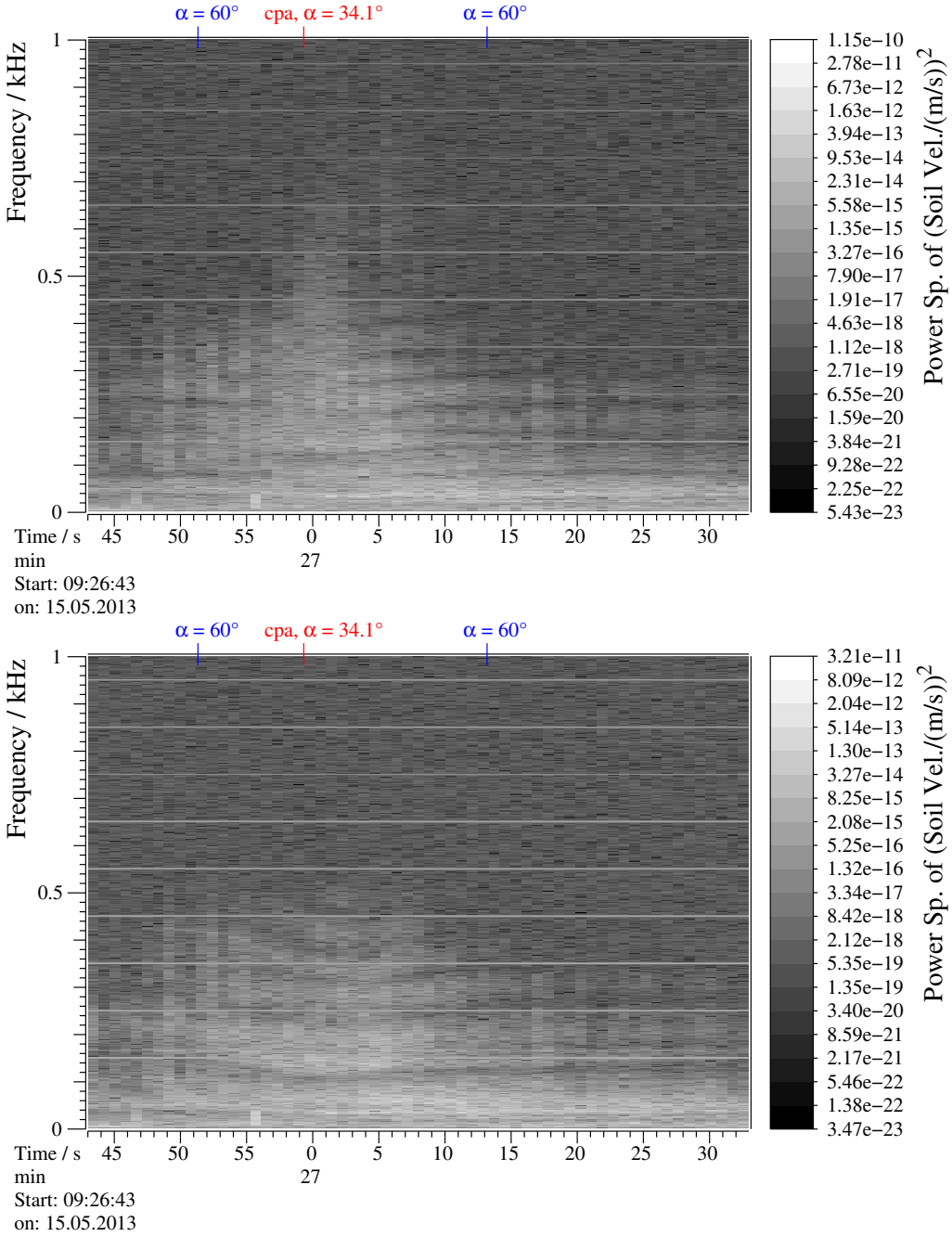

Figure A.11: Normalised power spectrograms of the jet-aircraft overflight number 13. Top: Geophone in the depth of 0.30 m, channel 3. Bottom: Geophone in the depth of 0.60 m, channel 0.

A.9 Interference patterns recorded with and without acoustic shielding

In Section 4.5.3 the interference patterns of the soil velocity recorded at sensors placed under the acoustic damping box are discussed. Here plots of the frequency-averaged, vertical soil velocity of additional aircraft overflight events are presented. Fig. A.12 shows the soil velocity recorded at the surface (geophone of channel 23). The soil velocity recorded with buried sensors under the box is shown in Fig. A.13 for $z_S = 0.30\,\mathrm{m}$ and in Fig. A.14 for $z_S = 0.60\,\mathrm{m}$. Due to different trajectories for each overflight the angle of incidence α of the acoustic signal reaches different minimal values at the cpa. For the sake of comparison the same abscissae $15° \leq \alpha \leq 80°$ are used for all plots.

The absolute values of the soil velocity vary at the same sensor from overflight to overflight. Furthermore, the SNR is much smaller compared to that of the interference patterns of the averaged coupling coefficient of sensors placed outside of the box (see Section 4.4.2 and Section 4.4.3). Nevertheless, for a given depth z_S at all overflight events the frequencies, at which increased values (and decreased values, respectively) of the soil velocity are observed, are approximately the same. Deviations in the interference patterns between overflight events can be explained by a different phase shift of the directly acoustically excited wave $A_{\hat{D}}$ caused by the acoustic damping box as discussed in Section 4.5.2.2. The frequencies of the observed maxima deviate strongly from the theoretically obtained ones $f^{\mathrm{theo}}_{\mathrm{max},k}(\alpha)$[54] for sensors not shielded by the box (shown in each plot as black dashed lines). This is discussed in detail in Section 4.5.3.

During overflight number 12 a narrow spectral line of increased soil velocity can be observed (clearly visible in Fig. A.12, top but also in Fig. A.14, middle). Its frequency rises from $f \approx 435\,\mathrm{Hz}$ at $\alpha \approx 22°$ to $f \approx 490\,\mathrm{Hz}$ at $\alpha \approx 60°$ and drops again to $f \approx 470\,\mathrm{Hz}$ at $\alpha \approx 75°$. It can be observed in the sound pressure signals at all microphones as well as in the signals of the soil velocity: For geophones placed at the surface or buried outside of the box its amplitude is large enough to be clearly visible compared to the other characteristics of the signal. For the geophones buried under the box, its amplitude is significantly smaller. This signal might be caused by a tonal turbine component of that aircraft while changing thrust. Using the coupling coefficient (i.e. the ratio between soil velocity and sound pressure) this signal can be nearly suppressed.

The confluence of the theoretical interference maxima $f^{\mathrm{theo}}_{\mathrm{max},k}(\alpha)$ (i.e. in Fig. A.13 for the values $k = 3$ and $k = 4$ and in Fig. A.14 for the two cases $k = 1$ and $k = 2$ as well as $k = 4$ and $k = 5$) is an artefact of the determination of the values of $f^{\mathrm{theo}}_{\mathrm{max},k}(\alpha)$. This is discussed in Appendix A.7.

[54] The values of $f^{\mathrm{theo}}_{\mathrm{max},k}(\alpha)$ are calculated for each depth z_S using the fit results of model 2 (given in Table 4.2).

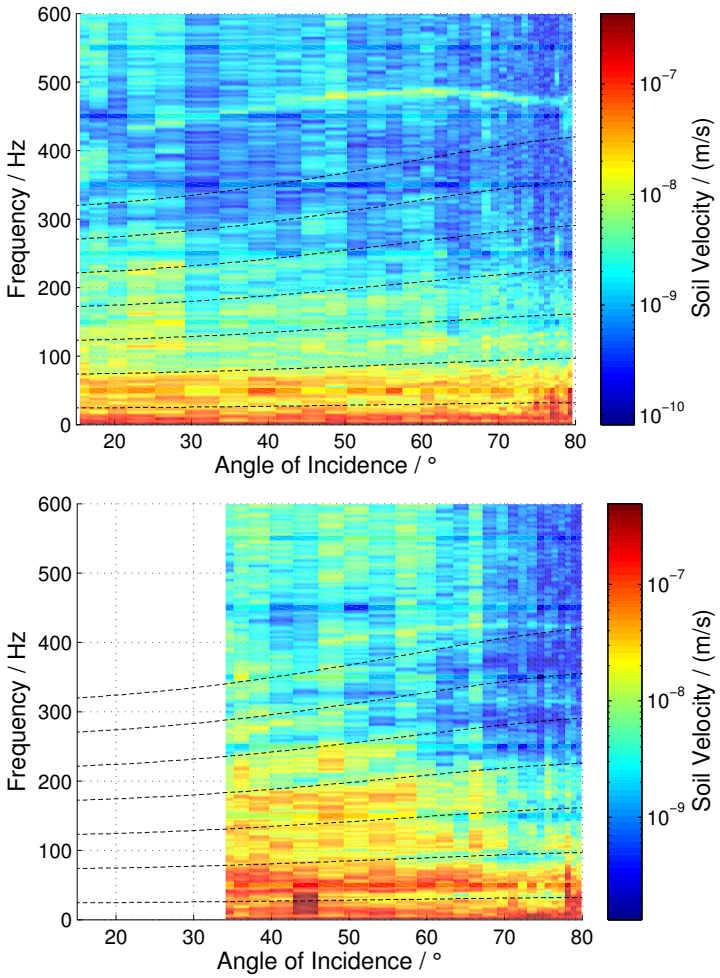

Figure A.12: Frequency-averaged, vertical soil velocity recorded at the surface geophone of channel 23, placed under the acoustic damping box:
Top: Soil velocity recorded during overflight number 12.
Bottom: Soil velocity recorded during overflight number 13.
The theoretical frequencies of maximal interference amplitude $f^{\text{theo}}_{\text{max},k}(\alpha)$ (for $0 \leq k \leq 6$) obtained from the evaluation without shielding box (see Section 4.4) are shown as black dashed lines in both graphs.

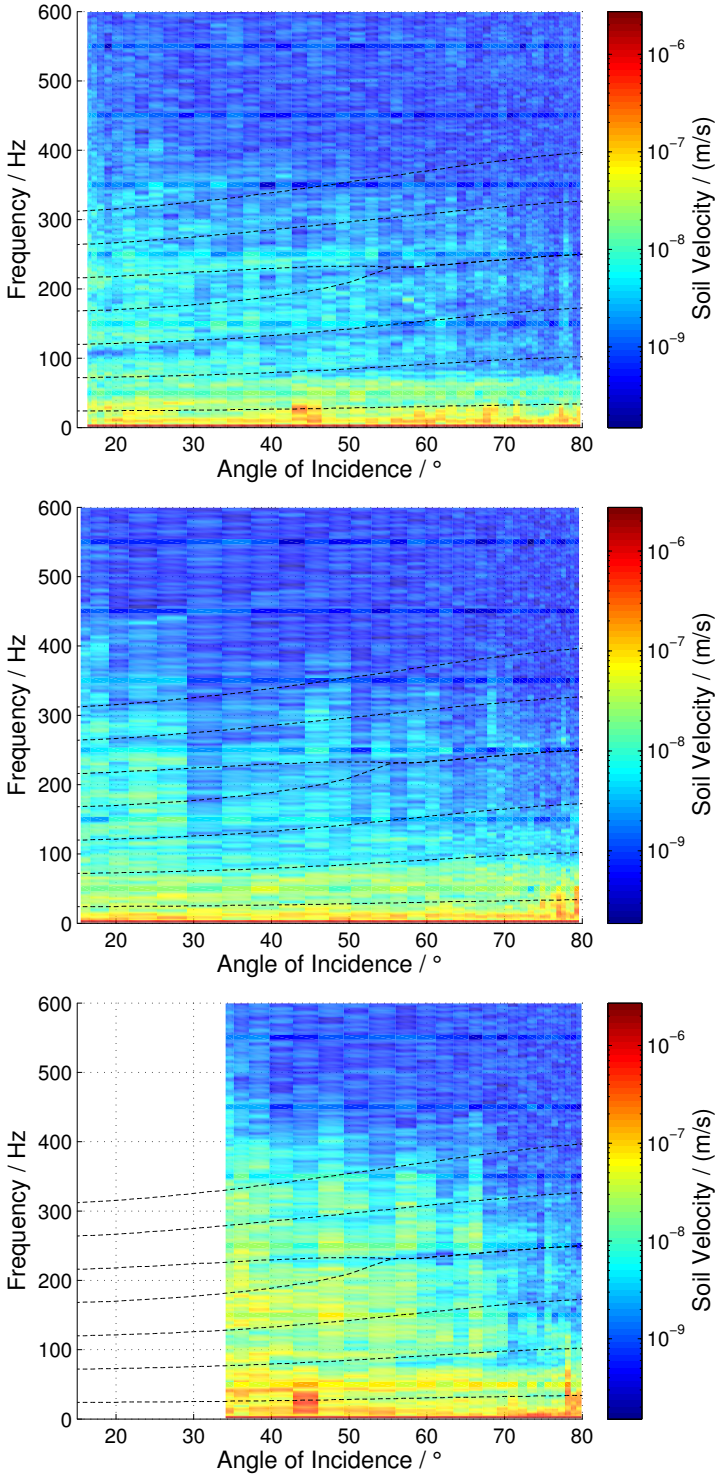

Figure A.13: Frequency-averaged, vertical soil velocity recorded in the depth z_S = 0.30 m with geophone of channel 3, placed under the acoustic damping box: Soil velocity recorded during overflight number 8 (top), overflight number 12 (middle) and overflight number 13 (bottom).
The theoretical frequencies of maximal interference amplitude $f^{\text{theo}}_{\text{max},k}(\alpha)$ for $0 \leq k \leq 6$ (also shown in Fig. A.7) obtained from the evaluation without shielding box are shown as black dashed lines in both graphs. The fit results of model 2 for $z_S = 0.30$ m are used to calculate $f^{\text{theo}}_{\text{max},k}(\alpha)$: $d = 2.38$ m and $v_{P1} = 225$ m/s.

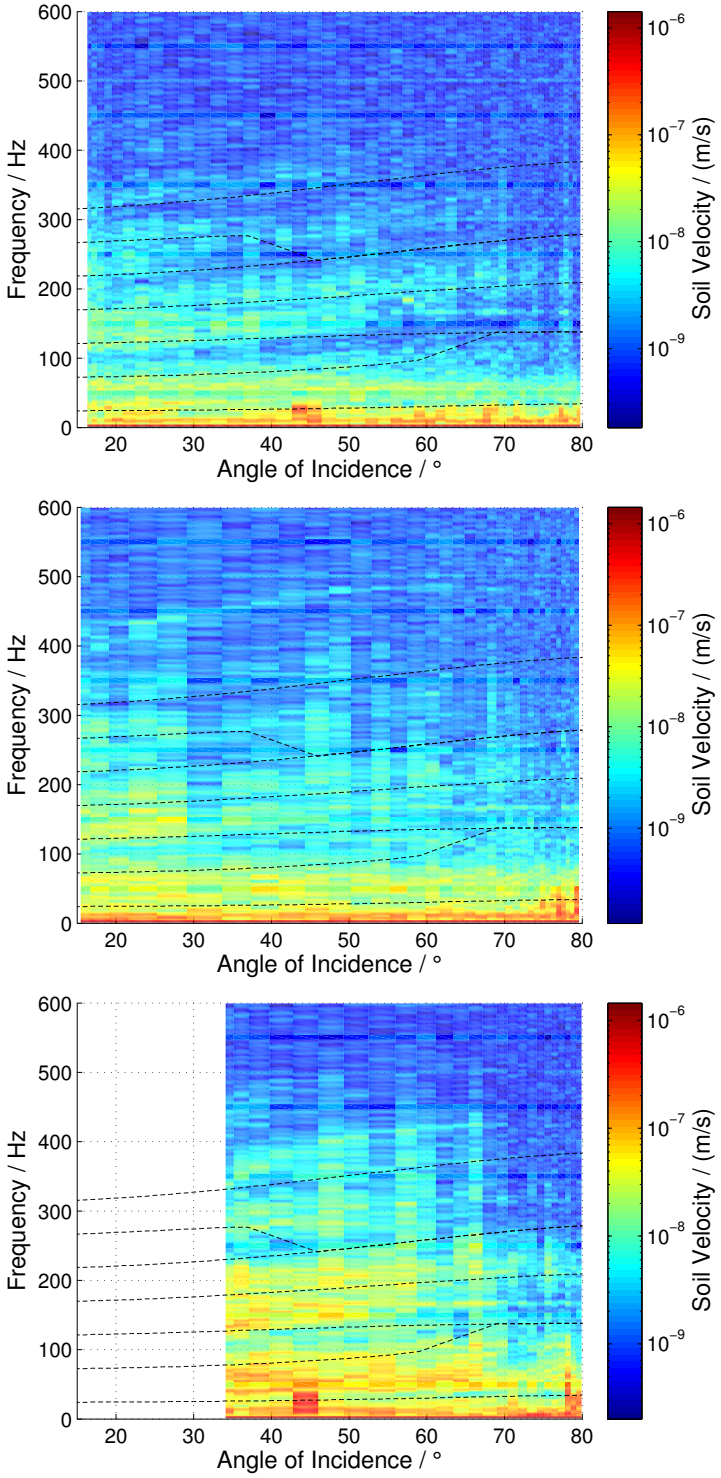

Figure A.14: Frequency-averaged, vertical soil velocity recorded in the depth z_S = 0.60 m with geophone of channel 0, placed under the acoustic damping box: Soil velocity recorded during overflight number 8 (top), overflight number 12 (middle) and overflight number 13 (bottom).
The theoretical frequencies of maximal interference amplitude $f^{\text{theo}}_{\text{max},k}(\alpha)$ for $0 \leq k \leq 6$ (see also Fig. A.9) obtained from the evaluation without shielding box are shown as black dashed lines in both graphs. The fit results of model 2 for $z_S = 0.60$ m are used to calculate $f^{\text{theo}}_{\text{max},k}(\alpha)$: $d = 2.17$ m and $v_{P1} = 208$ m/s.

A.10 Estimate of the absorption coefficient

The values in Table A.4 and Table A.5 of the absorption coefficients γ at certain frequencies f are taken from the graph given in [59, page 183]. From these values the linear factor γ_1 between γ and f is derived (see also Eq. (2.61)), which is used in Section 4.5.3 to include the absorption into the model of interference. Table A.4 states values for unconsolidated sediments and Table A.5 gives values for slightly consolidated sediments.

f / Hz	γ / m^{-1}
33	$1.0{\cdot}10^{-1}$
38	$5.5{\cdot}10^{-2}$
42	$2.0{\cdot}10^{-2}$
60	$1.7{\cdot}10^{-1}$
65	$3.2{\cdot}10^{-2}$
90	$1.4{\cdot}10^{-1}$
130	$3.9{\cdot}10^{-2}$
150	$6.5{\cdot}10^{-1}$
170	$2.5{\cdot}10^{-1}$
180	$1.6{\cdot}10^{-1}$

Table A.4: Absorption coefficient γ at certain frequencies for unconsolidated sediments, taken from [59].

f / Hz	γ / m^{-1}
10	$1.0{\cdot}10^{-5}$
24	$1.3{\cdot}10^{-4}$
24	$3.0{\cdot}10^{-4}$
24	$1.8{\cdot}10^{-3}$
25	$1.8{\cdot}10^{-4}$
25	$2.3{\cdot}10^{-4}$
43	$1.0{\cdot}10^{-3}$
50	$6.0{\cdot}10^{-4}$
70	$2.3{\cdot}10^{-2}$
90	$7.8{\cdot}10^{-4}$
90	$1.5{\cdot}10^{-3}$
105	$5.0{\cdot}10^{-4}$
110	$2.5{\cdot}10^{-1}$
170	$1.6{\cdot}10^{-2}$
$1.8{\cdot}10^{4}$	2.8
$3.5{\cdot}10^{4}$	11
$1{\cdot}10^{6}$	300

Table A.5: Absorption coefficient γ at certain frequencies for slightly consolidated sediments, taken from [59]. The last three entries are not used for the estimate of γ_1 since the frequencies are much larger than those under investigation in this work.

The values obtained by a linear fit are in the range of

$$\gamma_1^{unconsolidated} \approx (2 \pm 1) \cdot 10^{-3}\,\mathrm{m}^{-1}\mathrm{Hz}^{-1} \tag{A.20}$$

for unconsolidated sediments and in the range of

$$\gamma_1^{slightly\ cons.} \approx (3 \pm 2) \cdot 10^{-4}\,\mathrm{m}^{-1}\mathrm{Hz}^{-1} \tag{A.21}$$

for slightly consolidated ones. Since all data obtained from log-log graphs in [59] contain errors (smaller ones at the lower end of each decade and larger ones at the upper end), the obtained values of γ_1 represent rough estimates which are, however, sufficient to develop a good understanding of the effects of absorption on the recorded data.
Fig. A.15 shows plots of the spectral amplitude distributions at a surface sensor ($z_S = 0\,\mathrm{m}$) using model 2 and taking into account absorption in the soil. The coefficients used are $\gamma_1 = 2{\cdot}10^{-3}\,\mathrm{m}^{-1}\mathrm{Hz}^{-1}$ (top), $\gamma_1 = 1{\cdot}10^{-3}\,\mathrm{m}^{-1}\mathrm{Hz}^{-1}$ (middle) and $\gamma_1 = 0.5{\cdot}10^{-3}\,\mathrm{m}^{-1}\mathrm{Hz}^{-1}$ (bottom). As can be seen when comparing the graphs with Fig. 4.15 as well as in Fig. A.16 with the value $\gamma_1 = 1{\cdot}10^{-3}\,\mathrm{m}^{-1}\mathrm{Hz}^{-1}$ (corresponding to unconsolidated sediments) a good agreement with the recorded data can be reached.
In Fig. A.16 the normalised spectra at $\alpha = 25°$ for the three used values of γ_1 are plotted together with the corresponding spectrum recorded with the surface geophone channel 24 (normalised to the maximum for $f > 100\,\mathrm{Hz}$).

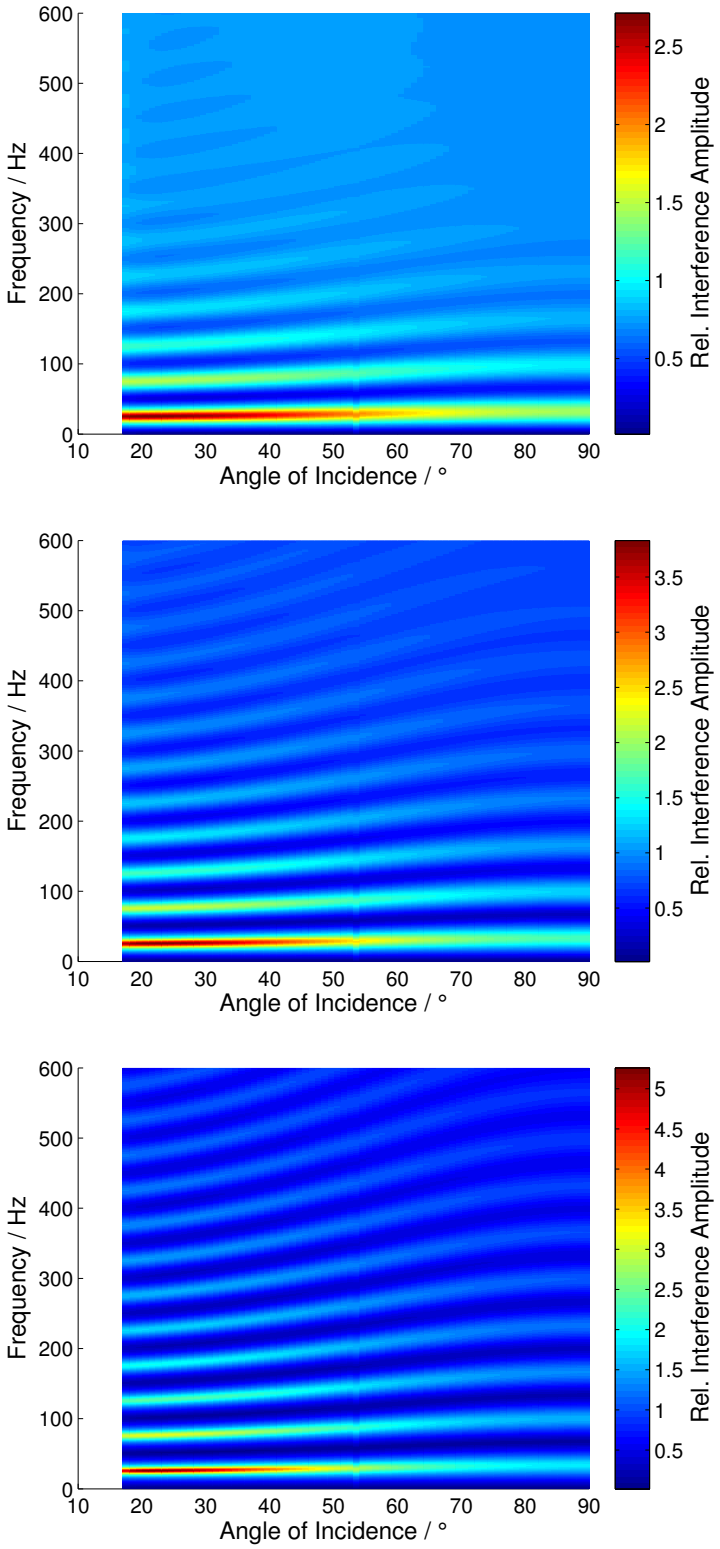

Figure A.15: Theoretical interference patterns including frequency-dependent absorption. From top to bottom: Strong absorption with $\gamma_1 = 2{\cdot}10^{-3}\,\mathrm{m^{-1}Hz^{-1}}$, medium absorption with $\gamma_1 = 1{\cdot}10^{-3}\,\mathrm{m^{-1}Hz^{-1}}$ and weak absorption with $\gamma_1 = 0.5{\cdot}10^{-3}\,\mathrm{m^{-1}Hz^{-1}}$. These values roughly refer to absorption coefficients found in unconsolidated sediments. Note the different colour scale of all graphs.

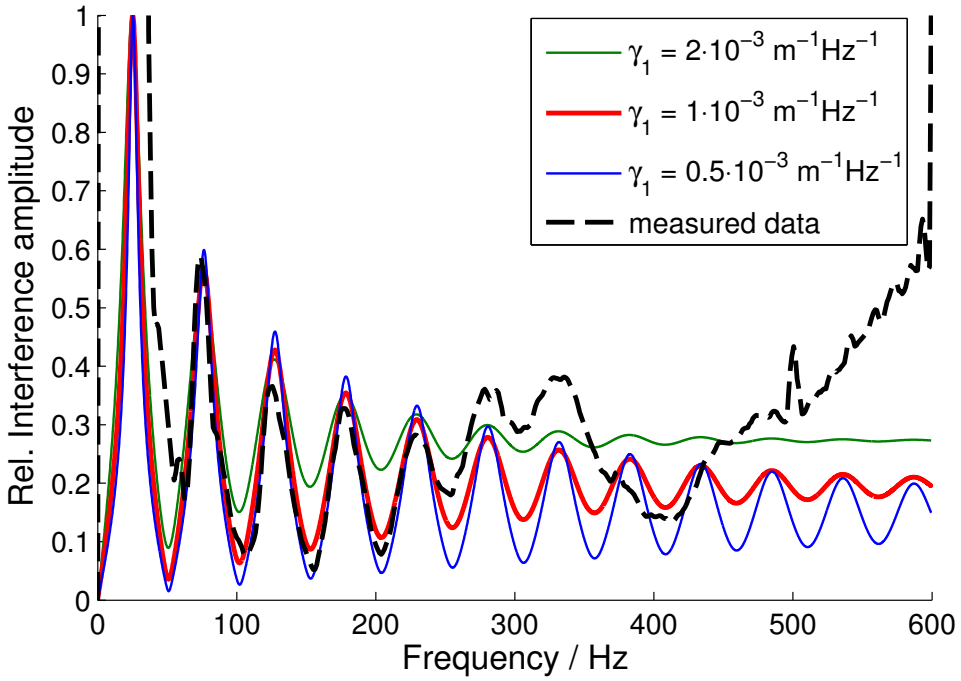

Figure A.16: Normalised spectra calculated theoretically for various absorption values γ_1 and the corresponding spectrum of the coupling coefficient recorded at the surface sensor channel 24 (dashed black) normalised to the maximum for $f > 100\,\mathrm{Hz}$. For the value $\gamma_1 = 1{\cdot}10^{-3}\,\mathrm{m^{-1}Hz^{-1}}$ the ratios between minima and maxima in the interval $75\,\mathrm{Hz} \leq f \leq 250\,\mathrm{Hz}$ match the recorded data well.

Bibliography

[1] SIPRI Yearbook 2015, accessed: 2016-06-06.
URL https://global.oup.com/academic/product/sipri-yearbook-2015-9780198737810?cc=fi&lang=en&# 1.1

[2] Treaty on the Non-Proliferation of Nuclear Weapons (NPT), accessed: 2016-12-17.
URL http://www.state.gov/t/isn/trty/16281.htm 1, 1.1

[3] DPRK announced nuclear test in sept. 2016, accessed: 2016-12-27.
URL https://www.ctbto.org/the-treaty/developments-after-1996/2016-sept-dprk-announced-nuclear-test/ 1.1

[4] A. Robock, L. Oman, G. L. Stenchikov, Nuclear winter revisited with a modern climate model and current nuclear arsenals: Still catastrophic consequences, Journal of Geophysical Research 112 (D13107) (2007). doi:10.1029/2006JD008235. 1.1

[5] S. J. Brams, Superpower Games. Applying Game Theory to Superpower Conflict, Yale University Press, New Haven and London, 1985. 1.1

[6] D. Atwood, E. J. Munro (Eds.), Security in a World without Nuclear Weapons: Visions and Challenges, Geneva Centre for Security Policy, 2013. 3

[7] International Campaign to Abolish Nuclear Weapons, accessed: 2016-06-06.
URL http://www.icanw.org/ 1.1

[8] Pugwash Conferences on Science and World Affairs, accessed: 2017-07-19.
URL https://pugwash.org/ 1.1

[9] Strategic Arms Limitation Talks (SALT I), accessed: 2016-12-18.
URL http://www.state.gov/t/isn/5191.htm 1.1

[10] The Treaty Between the United States of America and the Union of Soviet Socialist Republics on the Reduction and Limitation of Strategic Offensive Arms (START), accessed: 2016-12-18.
URL http://www.state.gov/t/avc/trty/146007.htm 1.1

[11] Draft treaty on the prohibition of nuclear weapons, accessed: 2017-07-08.
URL http://www.undocs.org/en/a/conf.229/2017/L.3/Rev.1 1.1

[12] History of nuclear testing: world overview, accessed: 2016-12-17.
URL http://ctbto.org/nuclear-testing/history-of-nuclear-testing/world-overview/ 1.1

[13] Treaty Banning Nuclear Weapon Tests in the Atmosphere, in Outer Space and Under Water, accessed: 2016-06-06.
URL http://disarmament.un.org/treaties/t/test_ban/text 1.1

[14] Comprehensive Nuclear-Test-Ban Treaty, accessed: 2016-05-03.
URL https://www.ctbto.org/fileadmin/content/treaty/treaty_text.pdf 1.1

[15] Building the International Monitoring System, accessed: 2016-10-30.
URL https://www.ctbto.org/?id=285 1.2

[16] On-site inspections - the final verification measure, accessed: 2016-10-30.
URL https://www.ctbto.org/verification-regime/on-site-inspection/the-final-verification-measure/ 1.2

[17] Station profiles of the IMS, accessed: 2016-10-30.
URL https://www.ctbto.org/verification-regime/station-profiles/ 1.2.1

[18] Seismic monitoring of the CTBT, accessed: 2016-10-30.
URL https://www.ctbto.org/verification-regime/monitoring-technologies-how-they-work/seismic-monitoring/ 1.2.1

[19] Radionuclide monitoring of the CTBT, accessed: 2016-10-30.
URL https://www.ctbto.org/verification-regime/monitoring-technologies-how-they-work/radionuclide-monitoring/ 1.2.1

[20] Infrasound monitoring of the CTBT, accessed: 2016-10-30.
URL https://www.ctbto.org/verification-regime/monitoring-technologies-how-they-work/infrasound-monitoring/ 1.2.1

[21] Hydro-acoustic monitoring of the CTBT, accessed: 2016-10-30.
URL https://www.ctbto.org/verification-regime/monitoring-technologies-how-they-work/hydroacoustic-monitoring/ 1.2.1

[22] History of nuclear testing: 1945 - today, accessed: 2016-12-17.
URL https://www.ctbto.org/nuclear-testing/history-of-nuclear-testing/nuclear-testing-1945-today/ 1.2.1

[23] Fukushima-related measurements by the CTBTO, accessed: 2016-10-31.
URL https://www.ctbto.org/?id=3234 1.2.1

[24] CTBT verification spin-offs for disaster warning and science, accessed: 2016-12-27.
URL https://www.ctbto.org/verification-regime/spin-offs-for-disaster-warning-and-science/ 1.2.1

[25] Integrated Field Exercise IFE14, Jordan, accessed: 2016-10-31.
URL https://www.ctbto.org/specials/integrated-field-exercise-2014/ 1.2.2

[26] F. Gorschlüter, J. Altmann, Suppression of periodic disturbances in seismic aftershock recordings for better localisation of underground explosions, Pure and Applied Geophysics 171 (3) (2014) 561–573. doi:10.1007/s00024-012-0617-y. 6, 1.3, 4.1.2, 28

[27] F. Gorschlüter, Sinusoids with linear frequency shift in time series – precise characterisation and removal, Ph.D. thesis, Technische Universität Dortmund, Germany (2014). doi:10.17877/DE290R-7019. 6, 1.3, 4.1.2, 28

[28] J. Altmann, Acoustic and seismic signals of heavy military vehicles for co-operative verification, Journal of Sound and Vibration 273 (4) (2004) 713 – 740. doi:10.1016/j.jsv.2003.05.002. 1.3

[29] J. Altmann, S. Linev, A. Weiss, Acoustic-seismic detection and classification of military vehicles - developing tools for disarmament and peace-keeping, Applied Acoustics 63 (10) (2002) 1085–1107. doi:10.1016/S0003-682X(02)00021-X. 1.3

[30] R. Blumrich, J. Altmann, Aircraft sound propagation near to the ground: Measurements and calculations, ACUSTICA - acta acustica 85 (1999) 495–504. 1.3

[31] J. Altmann, Acoustic-seismic detection of ballistic-missile launches for cooperative early warning of nuclear attack, Science & Global Security 13 (3) (2005) 129–168. 1.3

[32] J. Altmann, Seismic monitoring of an underground repository in salt - results of the measurements at the gorleben exploratory mine, ESARDA Bulletin 50 (2013) 61–78. 1.3

[33] J. Altmann, Modelling seismic-signal propagation at a salt dome for safeguards monitoring, ESARDA Bulletin 52 (2015) 60–79. 1.3

[34] F. Anglin, R. Haddon, Meteoroid sonic shock-wave-generated seismic signals observed at a seismic array, Nature 328 (6131) (1987) 7027–7034. 1.3

[35] M. E. Kappus, F. L. Vernon, Acoustic signature of thunder from seismic records, Journal of Geophysical Research: Atmospheres 96 (D6) (1991) 10989–11006. doi:10.1029/91JD00789. 1.3

[36] J. E. Cates, B. Sturtevant, Seismic detection of sonic booms, The Journal of the Acoustical Society of America 111 (1) (2002) 614–628. 1.3

[37] V. M. McCarty, I. Dalins, Frequency shift in air-coupled surface waves originated by rocket launches, Journal of Geophysical Research 76 (29) (1971) 7027–7034. 1.3

[38] I. O. Kitov, J. R. Murphy, O. P. Kusnetsov, B. W. Barker, N. I. Nedoshivin, An analysis of seismic and acoustic signals measured from a series of atmospheric and near-surface explosions, Bulletin of the Seismological Society of America 87 (6) (1997) 1553–1562. 1.3

[39] P. Lognonné, Seismic waves from atmospheric sources and atmospheric/ionospheric signatures of seismic waves, in: A. Le Pichon, E. Blanc, A. Hauchecorne (Eds.), Infrasound Monitoring for Atmospheric Studies, Springer Netherlands, Dordrecht, 2009, Ch. 10, pp. 281–304. doi:10.1007/978-1-4020-9508-5_10. 1.3

[40] W. M. Ewing, W. S. Jardetzky, F. Press, Elastic waves in layered media, McGraw-Hill, New York, 1957. 1.3, 2, 2.1, 16, 2.2.3, 2.2.4, 4

[41] M. A. Biot, Theory of propagation of elastic waves in a fluid-saturated porous solid. I. low-frequency range, The Journal of the Acoustical Society of America 28 (2) (1956) 168–178. doi:10.1121/1.1908239. 1.3, 2, 4.3.4

[42] J. M. Sabatier, H. E. Bass, L. N. Bolen, K. Attenborough, V. Sastry, The interaction of airborne sound with the porous ground: The theoretical formulation, The Journal of the Acoustical Society of America 79 (5) (1986) 1345–1352. doi:10.1121/1.393662. 1.3

[43] C. J. Hickey, J. M. Sabatier, Measurements of two types of dilatational waves in an air-filled unconsolidated sand, The Journal of the Acoustical Society of America 102 (1) (1997) 128–136. doi:10.1121/1.419770. 1.3

[44] D. G. Albert, S. Taherzadeh, K. Attenborough, P. Boulanger, S. N. Decato, Ground vibrations produced by surface and near-surface explosions, Applied Acoustics 74 (11) (2013) 1279–1296. doi:10.1016/j.apacoust.2013.03.006. 1.3, 8

[45] H.-C. Shin, S. Taherzadeh, K. Attenborough, W. R. Whalley, C. W. Watts, Non-invasive characterization of pore-related and elastic properties of soils in linear Biot-Stoll theory using acoustic-to-seismic coupling, European Journal of Soil Science 64 (3) (2013) 308–323. doi:10.1111/ejss.12000. 1.3

[46] J. M. Sabatier, H. E. Bass, L. N. Bolen, K. Attenborough, Acoustically induced seismic waves, The Journal of the Acoustical Society of America 80 (2) (1986) 646–649. doi:10.1121/1.394058. 1.3

[47] H. E. Bass, L. N. Bolen, D. Cress, J. Lundien, M. Flohr, Coupling of airborne sound into the earth: Frequency dependence, The Journal of the Acoustical Society of America 67 (5) (1980) 1502–1506. doi:10.1121/1.384312. 1.3

[48] V. Kunigelis, M. Senulis, Acoustic investigation of air-filled porous materials, Acta Acustica United with Acustica 88 (1) (2002) 14–18. doi:10.1121/1.419770. 1.3

[49] W. Weniger, Numerische Simulation und Anwendungen von Luftschallseismik mit gesteuerten Quellen, Ph.D. thesis, Westfälische Wilhelms-Universität Münster, Germany (1994). 1.3

[50] C. Madshus, F. Løvholt, A. Kaynia, L. R. Hole, K. Attenborough, S. Taherzadeh, Air-ground interaction in long range propagation of low frequency sound and vibration-field tests and model verification, Applied Acoustics 66 (5) (2005) 553–578. doi:10.1016/j.apacoust.2004.09.006. 1.3

[51] C. M. Harris, Handbook of acoustical mesurements and noise control, 3rd Edition, McGraw-Hill, New York, 1991. 1.3

[52] G. Müller, Theory of elastic waves, (Scientific Technical Report STR 07/03), Deutsches GeoForschungsZentrum GFZ, Potsdam, 2007. doi:10.2312/GFZ.b103-07037. 2, 2.2.5, 4.7.2

[53] L. Landau, E. Lifshitz, Fluid mechanics, in: Course of Theoretical Physics, Vol. 6, Pergamon Press, Oxford, 1987. doi:10.1016/B978-0-08-033933-7.50016-7. 2.1.1, 2.2.5

[54] National Institute of Standards and Technology - universal physical constants, accessed: 2017-06-26.
URL http://physics.nist.gov/cuu/Constants/ 2.1.1

[55] The Engineering ToolBox - air - molecular mass, accessed: 2017-06-26.
URL http://www.engineeringtoolbox.com/molecular-mass-air-d_679.html 2.1.1

[56] K. Aki, G. Richards, Quantitative seismology, theory and methods, Vol. 1, Freeman, New York, 1980. 2.2.2, 16, 2.2.5, 17, 2.2.5, 2.3

[57] M. Liebsch, J. Altmann, Acoustic-seismic coupling for a wide range of angles of incidence and frequencies using signals of jet-aircraft overflights, Journal of Sound and Vibration 385 (2016) 202–218. doi:10.1016/j.jsv.2016.09.007. 19, 31, 4.3.3.1, 34, 4.20, 4.3.3.1, 4.3.3.1, 4.2, 4.4.3

[58] E. Hecht, Optik, Oldenbourg Wissensch.Vlg, 2005. 2.3.2

[59] J. Schön, Petrophysik - physikalische Eigenschaften von Gesteinen und Mineralen, Stuttgart Enke, 1983. 2.3.3, 4.5.3, A.10, A.4, A.5, A.10

[60] H. Meinert, Seismische Signale aus Pulsanregung – Auswertung der Messung beim Flughafen Münster-Osnabrück, B.S. Thesis, Fakultät Physik, Technische Universität Dortmund, Germany, unpublished (2014). 3.2, 4.3, 4.4.4

[61] H. Harvey, E. Hubbard, Aeroacoustics of Flight Vehicles: Theory and Practice, Vol. 1 Noise Sources, Woodbury NY: Acoustical Society of America, New York, 1995. 3.2.2

[62] Produktinformationen: Verbundschaumstoff zur Schalldämmung - data sheet of the used acoustic damping foam, accessed: 2017-06-26.
URL http://www.schaumstofflager.de/store-pdf-info.php?pID=2307 26

[63] T. Lay, T. C. Wallace, Modern global seismology, Academic Press, San Diego, 1995. 4, 4.7.2

[64] O. Koefoed, Reflection and transmission coefficients for plane longitudinal incident waves, Geophysical Prospecting 10 (3) (1962) 304–351. doi:10.1111/j.1365-2478.1962.tb02016.x. 4

[65] H.-P. Blume, F. Scheffer, G. W. Brümmer, P. Schachtschabel, R. Horn, E. Kandeler, I. Kögel-Knabner, R. Kretzschmar, K. Stahr, B.-M. Wilke, Lehrbuch der Bodenkunde, Spektrum Akademischer Verlag, 2010. 27, 4.3.4

[66] E. O. Brigham, The Fast Fourier Transform: An Introduction to Its Theory and Application, Prentice-Hall, Inc., Englewood Cliffs, New Jersey, 1974. 4.1.2

[67] P. Bagge, Acoustic-Seismic Coupling, DAAD RISE Internship Report, University of South Florida, US and Technische Universität Dortmund, Germany, unpublished (2015). 51

[68] F. Press, M. Ewing, Ground roll coupling to atmospheric compressional waves, Geophysics 16 (3) (1951) 416–430. doi:10.1190/1.1437684. 4.7.2

Acknowledgement

This work would not have been possible without the support and input of many people. Firstly, I thank my supervisor PD Dr. Jürgen Altmann for countless fruitful discussions and constructive reviews as well as his participation in most measurements. His dedication to the field of scientific disarmament research has been a great inspiration to me. Secondly, I want to thank Prof. Dr. Manfred Joswig for accepting my request to be the second supervisor of this work and for constructive discussions about the contents of this thesis.

Special thanks go to Prof. Dr. Dieter Suter for accepting the working group *Physics and Disarmament* as a part of his chair *Experimental Physics III* at the Technische Universität Dortmund. Furthermore, I express my gratitude to all colleagues at this chair, especially Felix Gorschlüter (a former PhD student at the working group *Physics and Disarmament*), Anja Sapsford for technical support and Angelika Sommer for help with all administrative issues. I also gratefully acknowledge all students who wrote a Bachelor or Master thesis or did an internship at the working group *Physics and Disarmament*. They participated in several measurements and contributed to the research and the scientific discussions of the working group.

I thank the CTBTO for providing funding for my research through a collaborative project in 2011 and 2012 as well as through the *Research Award for Young Scientists and Engineers* granted to me from 2013 to 2014.

I am grateful to the DFS for providing the trajectories of the aircraft flights recorded near the airport FMO. I also thank the DWD for providing the hourly measured metrological data like temperature at the airport FMO. Particular thanks go to the Rudolph family in Greven, Germany, who allowed us to perform measurements on their property and supported the measurements with additional logistics.

My thanks go the colleagues at the Ruhr-Universität Bochum, Germany, for their support of my research, especially to Peter Salzsieder of the Institute of Communication Acoustics, who provided a speaker and corresponding equipment for several measurements.

I am deeply grateful to Prof. Annakaisa Korja and professor emeritus Pekka Heikkinen of the Institute of Seismology at the University of Helsinki for giving me the opportunity to stay at their institute as a visiting scientist in 2016. Among the colleagues there I particularly want to thank Pasi Lindblom for his continuous support of my work and for providing his insights as an OSI inspector.

I thank my friends and former fellow students, especially Martin Schaffer, Fabian Stutzki and Alexander Winkler for constructive discussions and Lucas Bitzer for advice and partially reviewing this work.

Furthermore, my appreciation goes to all employees at the universities I worked at, who are generally not visible in scientific research: The cleaners of the university buildings,

the chefs and other employees in the canteens, the technicians and mechanics working in the workshops. Without them and their rarely acknowledged work scientific work as the presented thesis would not be possible.
Finally, I want to express my deepest gratitude to my family for their continuous support of my studies: To my parents for providing encouragement and financial support, to my parents-in-law and my grandparents-in-law for logistically supporting the writing of this work and of course to my wife and to my daughter. My wife provided her insight about the political background of this thesis and reviewed the introduction while my daughter had to suffer through all the times I was not available to her. Without both of them this thesis might have been finished two years earlier – or never at all.

Mattes Liebsch
July 2017